NUMERICAL STUDIES ON QUANTIZED VORTEX DYNAMICS IN SUPERFLUIDITY AND SUPERCONDUCTIVITY

TANG QINGLIN

NATIONAL UNIVERSITY OF SINGAPORE

2013

NUMERICAL STUDIES ON QUANTIZED VORTEX DYNAMICS IN SUPERFLUIDITY AND SUPERCONDUCTIVITY

TANG QINGLIN
(B.Sc., Beijing Normal University)

A THESIS SUBMITTED
FOR THE DEGREE OF DOCTOR OF PHILOSOPHY
DEPARTMENT OF MATHEMATICS
NATIONAL UNIVERSITY OF SINGAPORE
2013

DECLARATION

I hereby declare that this thesis is my original work and it has been written by me in its entirety. I have duly acknowledged all the sources of information which have been used in the thesis.

This thesis has also not been submitted for any degree in any university previously.

Tang Qiglin

Tang Qinglin

26 March 2013

Acknowledgements

It is my great honor to take this opportunity to thank those who made this thesis possible.

First and foremost, I owe my deepest gratitude to my supervisor Prof. Bao Weizhu, whose generous support, patient guidance, constructive suggestion, invaluable help and encouragement enabled me to conduct such an interesting research project.

I would like to express my appreciation to my collaborators Asst. Prof. Zhang Yanzhi and Dr. Daniel Marahrens for their contribution to the work. Specially, I thank Dr. Zhang Yong for reading the draft. My sincere thanks go to all the former colleagues and fellow graduates in our group, especially Dr. Dong Xuanchun and Dr. Jiang Wei for fruitful discussions and suggestions on my research. I heartfeltly thank my friends, especially Zeng Zhi, Xu Weibiao, Feng Ling, Yang Lina, Qin Chu, Zhu Guimei and Wu miyin, for all the encouragement, emotional support, comradeship and entertainment they offered. I would also like to thank NUS for awarding me the Research Scholarship which financially supported me during my Ph.D candidature. Many thanks go to IPAM at UCLA and WPI at University of Vienna for their financial assistance during my visits.

Last but not least, I am forever indebted to my beloved girl friend and family, for their encouragement, steadfast support and endless love when it was most needed.

Tang Qinglin

March 2013

Contents

Summary

Quantized vortices, which are the topological defects that arise from the order parameters of the superfluid, superconductors and Bose–Einstein condensate (BEC), have a long history that begins with the study of liquid Helium. Their appearance is regarded as the key signature of superfluidity and superconductivity, and most of their phenomenological properties have been well captured by the Ginzburg-Landau-Schrödinger equation (GLSE) and the Gross-Pitaevskii equation (GPE).

The purpose of this thesis is twofold. The first is to conduct extensive numerical studies for the vortex dynamics and interactions in superfluidity and superconductivity via solving GLSE on different bounded domains in $\mathbb{R}^2$ and under different boundary conditions. The second is to study GPE both analytically and numerically in the whole space.

This thesis mainly contains two parts. The first part is to investigate vortex dynamics and their interaction in GLSE on bounded domain. We begin with the stationary vortex state of the GLSE, and review various reduced dynamical laws (RDLs) that govern the motion of the vortex centers under different boundary conditions and prove their equivalence. Then, we propose accurate and efficient numerical methods for computing the GLSE as well as the corresponding RDLs in a disk or rectangular domain under Dirichlet or homogeneous Neumann boundary condition (BC). These methods are then applied to study the various issues about the quantized vortex phenomena, including validity of RDLs, vortex interaction, sound-vortex interaction, radiation and pinning effect introduced by the inhomogeneities. Based on extensive numerical results, we find that any of the following factors: the value of ε, the boundary condition, the geometry of the domain, the initial location of the vortices and the type of the potential, affect the motion of the vortices significantly. Moreover, there exist some regimes such that the RDLs failed to predict correct vortex dynamics. The RDLs cannot describe the radiation and sound-vortex interaction in the NLSE dynamics, which can be studied by our direct simulation. Furthermore, we find that for GLE and CGLE with inhomogeneous potential, vortices generally move toward the critical points of the external potential, and finally stay steady near those points. This phenomena illustrate clearly the pinning effect. Some other conclusive experimental findings are also obtained and reported, and discussions are made to further understand the vortex dynamics and interactions.

The second part is concerned with the dynamics of GPE with angular momentum rotation term and/or the long-range dipole-dipole interaction. Firstly, we review the two-dimensional (2D) GPE obtained from the 3D GPE via dimension reduction under anisotropic external potential and derive some dynamical laws related to the 2D and 3D GPE. By introducing a rotating Lagrangian coordinate system, the original GPEs are re-formulated to the GPEs without the angular momentum rotation. We then cast the conserved quantities and dynamical laws in the new rotating Lagrangian coordinates. Based on the new formulation of the GPE for rotating BECs in the rotating Lagrangian coordinates, we propose a time-splitting spectral method for computing the dynamics of rotating BECs. The new numerical method is explicit, simple to implement, unconditionally stable and very efficient in computation. It is of spectral order accuracy in spatial direction and second-order accuracy in temporal direction, and conserves the mass in the discrete level. Extensive numerical results are reported to demonstrate the efficiency and accuracy of the new numerical method. Finally, the numerical method is applied to test the dynamical laws of rotating BECs such as the dynamics of condensate width, angular momentum expectation and center-of-mass, and to investigate numerically the dynamics and interaction of quantized vortex lattices in rotating BECs without/with the long-range dipole-dipole interaction.

List of Tables

List of Figures

List of Symbols and Abbreviations

2D	two dimension
3D	three dimension
BEC	Bose-Einstein condensate
GLSE	Ginzburg–Landau–Schrödinger equation
GLE	Ginburg–Landau equation
NLSE	Nonlinear Schrödinger equation
CGLE	complex Ginburg–Landau equation
GPE	Gross–Pitaevskii equation
RDL	reduced dynamical law
BC	boundary condition
CNFD	Crank–Nicolson finite difference
TSCNFD	time–splitting Crank–Nicolson finite difference
TSCP	time–splitting cosine pseudospectral
FEM	finite element method
SAM	surface adiabatic model
SDM	surface density model
Fig.	figure
$\hbar$	Planck constant

(r, θ)	polar coordinate
∇	gradient
$\Delta = \nabla \cdot \nabla$	Laplacian
$\mathbf{x}$	Cartesian coordinate
$\tilde{\mathbf{x}}$	rotating Lagrangian coordinate
τ	time step size
h	space mesh size
i	imaginary unit
$\hat{f}$	Fourier transform of function f
f^*	conjugate of of a complex function f
$f * g$	convolution of function f with function g
$\mathrm{Re}(f)$	real part of a complex function f
$\mathrm{Im}(f)$	imaginary part of a complex function f
Ω	angular velocity
ω_x, ω_y, ω_z	trapping frequencies in x-, y-, and z- direction
$L_z = -i(x\partial_y - y\partial_x)$	z-component of angular momentum
$\langle L_z \rangle(t)$	angular momentum expectation
$\mathbf{x}_c(t)$	center of mass of a condensate
$\sigma_\alpha(t)$ $(\alpha = x, y, \mathrm{or}\, z)$	condensate width in α-direction
$\psi(\mathbf{x}, t)$, $\psi^\varepsilon(\mathbf{x}, t)$	macroscopic wave function
$\phi(\mathbf{x}, t)$, $\phi_m^\varepsilon(\mathbf{x}, t)$	stationary state
$\rho^\varepsilon(\mathbf{x}, t) = \|\phi^\varepsilon(\mathbf{x}, t)\|^2$	position density
$S^\varepsilon(\mathbf{x}, t) = \mathrm{Arg}(\phi^\varepsilon(\mathbf{x}, t))$	phase of the wave function

Chapter 1

Introduction

Vortex, which can exist in vast areas, is any spiral motion with closed stream lines. It can survive not only in macro scale such as in the air, liquid or the turbulent flow, but also in micro scale such as the Bose-Einstein condensate (BEC), the superfluidity and superconductivity, etc. The micro-vortices differ from those macro-vortices by the so-called ‘vorticity’, which is a mathematical concept related to the amount of ‘circulation’ or ‘rotation’. Among those micro-vortices, the quantized vortex that arises from quantum mechanics distinguish itself from others by the signature of ‘quantized vorticity’.

1.1 Vortex in superfluidity and superconductivity

Quantized vortices are topological defects that arise from the order parameter in superfluids, Bose-Einstein condensate (BEC) and superconductors in which frictionless fluids flow with circulation being quantized around each vortex.

Bose-Einstein condensation, superconductivity and superfluidity are among the most intriguing phenomena in nature. Their astonishing properties are direct consequences of quantum mechanics. While most other quantum effects only appear in matter on the atomic or subatomic scale, superfluids and superconductors show the effects of quantum mechanics acting on the bulk properties of matter on a large scale. They are macroscopic quantum phenomena. This is an essential origin of superfluidity and superconductivity, in which macroscopically phase coherence allows a dissipationless current to flow. Bulk superfluids are distinguished from normal fluids by their ability to support dissipationless flow.

Superconductivity is a phenomenon of exactly zero electrical resistance occurring in certain materials at low temperature. It was discovered by Heike Kamerlingh Onnes in 1911. Type-I superconductivity is characterized by the so-called Meissner effect, which introduce the complete exclusion of magnetic from the superconductor. While for the type-II superconductors in the so-called mixed vortex state, quantized amount of magnetic flux carried by the vortex lines is allowed to penetrate the superconductors [56, 58].

A Bose-Einstein condensate (BEC) is a state of matter of a dilute gas of weakly interacting bosons below some critical temperature. It supports the quantum effects in macroscopic scale since numbers of the bosons will condense into the single-particle state, at which point we can treat those condensed bosons as one-particle [2,86,121,124,129]. The phenomena of BEC was predicted in 1924 by Albert Einstein based on the work of Satyendra Bath Bose and was first realized in experiments in 1955 [7, 37, 50]. Later, with the observation of quantized vortices [2, 38, 106, 107, 109, 122, 148], plenty of work have been devoted to study the phenomenological properties of vortices in the rotating BEC, dipolar BEC, multi-component BEC and spinor BEC, etc, which has now opened the door to the study of superfluidity in the Bose-system [4, 89].

Superfluid is a state of matter characterized by the complete absence of viscosity. In other words, if placed in a closed loop, superfluids can flow endlessly without friction. Known as a major facet in the study of quantum hydrodynamics, the superfluidity effect was discovered by Kapitsa, Allen and Misener in 1937. The formation of the superfluid is known to be related to the formation of a BEC. This is made obvious by the fact that superfluidity occurs in liquid helium-4 at far higher temperatures than it does in helium-3. Each molecule of helium-4 is a boson particle, by virtue of its zero spin. Helium-3, however, is a fermion particle, which can form bosons only by pairing with itself at much lower temperatures, in a process similar to the electron pairing in superconductivity.

Feynman [61] predicted that the rotation of superfluids might be subject to the quantized vortices in 1955, while in 1957 Abrikosov [3] predicted the existence of the vortex lattice in superconductors. Studies on phenomena related to quantized vortex has since boomed and the Nobel Prize in Physics was recently awarded to Cornell, Weimann and Ketterle in 2001 for their decisive contributions to Bose-Einstein condensation and to Ginzburg, Abrikosov and Leggett in 2003 for their pioneering contributions to superfluidity and superconductivity.

1.2 Problems and contemporary studies

In recent years, phenomenological properties of quantized vortices in superfluidity and superconductivity have been extensively studied by both mathematical analysis and numerical simulations. It is remarkable that many of those properties can be well characterized by relatively simple models such as the Ginzburg-Landau-Schrödinger equation (GLSE) [11] and the Gross-Pitaesvkii equation (GPE) [18,121]. In this thesis, we focus on the following two subjects.

1.2.1 Ginzburg-Landau-Schrödinger equation

First, we are concerned with the vortex dynamics and interactions in a specific form of 2D Ginzburg-Landau-Schrödinger equation , which describe a vast variety of phenomena in physics community, ranging from superconductivity and superfluidity to strings in field theory, from the second order phase transition to nonlinear waves [11, 62, 64, 85, 120, 123]:

$$(\lambda_\varepsilon + i\beta)\partial_t \psi^\varepsilon(\mathbf{x}, t) = \Delta\psi^\varepsilon + \frac{1}{\varepsilon^2}(V(\mathbf{x}) - |\psi^\varepsilon|^2)\psi^\varepsilon, \qquad \mathbf{x} \in \mathcal{D}, \quad t > 0, \tag{1.1}$$

with initial condition

$$\psi^\varepsilon(\mathbf{x},0)=\psi_0^\varepsilon(\mathbf{x}),\qquad \mathbf{x}\in\overline{\mathcal{D}},\tag{1.2}$$

and under either Dirichlet boundary condition (BC)

$$\psi^\varepsilon(\mathbf{x},t)=g(\mathbf{x})=e^{i\omega(\mathbf{x})},\qquad \mathbf{x}\in\partial\mathcal{D},\quad t\geq 0,\tag{1.3}$$

or homogeneous Neumann BC

$$\frac{\partial\psi^\varepsilon(\mathbf{x},t)}{\partial\nu}=0,\qquad \mathbf{x}\in\partial\mathcal{D},\quad t\geq 0.\tag{1.4}$$

Here, $\mathcal{D}\subset\mathbb{R}^2$ is a smooth and bounded domain, t is time, $\mathbf{x}=(x,y)\in\mathbb{R}^2$ is the Cartesian coordinate vector, $V(\mathbf{x})$ satisfying $\lim_{|x|\to\partial\mathcal{D}}V(\mathbf{x})=1$ is a positive real-valued smooth function, $\psi^\varepsilon:=\psi^\varepsilon(\mathbf{x},t)$ is a complex-valued wave function (order parameter), ω is a given real-valued function, ψ_0^ε and g are given smooth and complex-valued functions satisfying the compatibility condition $\psi_0^\varepsilon(\mathbf{x})=g(\mathbf{x})$ for $\mathbf{x}\in\partial\mathcal{D}$, $\nu=(\nu_1,\nu_2)$ and $\nu_\perp=(-\nu_2,\nu_1)\in\mathbb{R}^2$ satisfying $|\nu|=\sqrt{\nu_1^2+\nu_2^2}=1$ are the outward normal and tangent vectors along $\partial\mathcal{D}$, respectively, $i=\sqrt{-1}$ is the unit imaginary number, $0<\varepsilon<1$ is a given dimensionless constant, and λ_ε, β are two nonnegative constants satisfying $\lambda_\varepsilon+\beta>0$. The GLSE covers many different equations arise in various different physical fields. For example, when $\lambda_\varepsilon\neq 0$, $\beta=0$, it reduces to the Ginzburg-Landau equation (GLE) for modelling superconductivity. When $\lambda_\varepsilon=0$, $\beta=1$, the GLSE collapses to the nonlinear Schrödinger equation (NLSE) which is well known for modelling, for example, BEC or superfluidity. While $\lambda_\varepsilon>0$ and $\beta>0$, the GLSE is the so-called complex Ginzburg-Landau equation (CGLE) or nonlinear Schrödinger equation with damping term which arise in the study of the hall effect in type II superconductor.

In superconductivity, $V(\mathbf{x})\equiv 1$ stands for the equilibrium density of superconducting electron [42, 43, 55]. When $V(\mathbf{x})\equiv 1$, the medium is uniform, while if $V(\mathbf{x})\not\equiv 1$, the medium is inhomogeneous which is used to, for example, describe the pining effect in superconductor with impurities.

Denote the Ginzburg-Landau (GL) functional ('energy') as [46,74,104]

$$\mathcal{E}^\varepsilon(t) := \int_{\mathcal{D}} \left[\frac{1}{2}|\nabla\psi^\varepsilon|^2 + \frac{1}{4\varepsilon^2}\left(V(\mathbf{x}) - |\psi^\varepsilon|^2\right)^2\right] d\mathbf{x} = \mathcal{E}^\varepsilon_{\text{kin}}(t) + \mathcal{E}^\varepsilon_{\text{int}}(t), \quad t \geq 0, \tag{1.5}$$

whose corresponding Euler–Lagrange equation reads as:

$$\Delta\psi^\varepsilon + \frac{1}{\varepsilon^2}(V(\mathbf{x}) - |\psi^\varepsilon|^2)\psi^\varepsilon = 0, \qquad \mathbf{x} \in \mathcal{D}. \tag{1.6}$$

In (1.5), the kinetic and interaction energies are defined as

$$\mathcal{E}^\varepsilon_{\text{kin}}(t) := \frac{1}{2}\int_{\mathcal{D}} |\nabla\psi^\varepsilon|^2 d\mathbf{x}, \quad \mathcal{E}^\varepsilon_{\text{int}}(t) := \frac{1}{4\varepsilon^2}\int_{\mathcal{D}} \left(V(\mathbf{x}) - |\psi^\varepsilon|^2\right)^2 d\mathbf{x}, \quad t \geq 0,$$

respectively. The GLSE (1.1) now can be rewritten as

$$(\lambda_\varepsilon + i\beta)\partial_t\psi^\varepsilon(\mathbf{x}, t) = -\frac{\delta\mathcal{E}(\psi)}{\delta\psi^*}, \tag{1.7}$$

where ψ^* denotes the complex conjugate of function ψ. Moreover, it is easy to show that the GLE or CGLE dissipates the total energy, i.e., $\frac{d\mathcal{E}^\varepsilon}{dt} \leq 0$, while the NLSE conserve the total energy, i.e., $\frac{d\mathcal{E}^\varepsilon}{dt} = 0$.

During the last several decades, constructions and analysis of the solutions of (1.6) as well as vortex dynamics and interaction related to the GLSE (1.1) under different scalings have been extensively studied in the literatures.

For GLE defined in $\mathbb{R}^2$, under the normal scaling $\lambda_\varepsilon = \varepsilon \equiv 1$ and homogeneous potential $V(\mathbf{x}) \equiv 1$, Neu [113] found numerically that quantized vortices with winding number $m = \pm 1$ are dynamically stable, and respectively, $|m| > 1$ dynamically unstable. Based on the assumption that the vortices are well separated and of winding number $+1$ or -1, he also obtained formally the reduced dynamical law (RDL) governing the motion of the vortex centers by method of asymptotic analysis. However, this RDL is only correct up to the first collision time and cannot indicate the motion of multi-degree vortices. Recently, in a series of papers [30,32,33], Bethuel et al. investigated the asymptotic behaviour of vortices as $\varepsilon \to 0$ under the accelerating time scale $\lambda_\varepsilon = \frac{1}{\ln\frac{1}{\varepsilon}}$. Under very general assumptions (which release those constrains in Neu's work), they proved that the limiting vortices, which can be of multiple degree, move according to a RDL, which is a set of simple ordinary differential equations (ODEs). Much stronger than Neu's RDL, this RDL is always valid except for a finite number of times that representing vortex splittings, recombinations and/or collisions. Their studies also show an interesting phenomena called as "phase-vortex interaction", the phenomena that can cause an unexpected drift of the vortices, which they pointed out that cannot occur in the case of the domain being bounded. Moreover, they conducted some similar research in higher dimensional space [31].

In the bounded domain case when the potential is homogeneous, i.e., $V(\mathbf{x}) \equiv 1$ Lin [96, 97, 99] extended Neu's results by considering the dynamics of vortices in the asymptotic limit $\varepsilon \to 0$ under various scales of λ_ε and with different BCs. Based on the well-preparation assumption similar to Neu's, he derived the RDLs that govern the motion of these vortices and rigorously proved that vortices move with velocities of the order of $|\ln \varepsilon|^{-1}$ if $\lambda_\varepsilon = 1$. Similar studies have also been conducted by E [59], Jerrard et al. [73], Jimbo et al. [80, 83] and Sandier et al. [128]. Unfortunately, all those RDLs are only valid up to the first time that the vortices collide and/or exit the domain and cannot describe the motion of multiple degree vortices. Recently, Serfaty [132] extended the RDL of the vortices after collisions, but still under the assumption that those vortices are of degree $+1$ or -1 and that only simple collision could happen during dynamics (i.e, the situation that more than two vortices meet at the same time and place are not allowed). Actually, the motion of the multiple degree vortices and the dynamics of vortices after collision and/or splittings still remain as interesting open problems. When the potential is inhomogeneous, i.e., $V(\mathbf{x}) \not\equiv 1$, Jian et al. [75–77] investigated the pinning effect of the vortices asymptotically as $\varepsilon \to 0$ in the GLE with Dirichlet BC under the scale $\lambda_\varepsilon = 1$. They established the corresponding RDLs that govern the dynamics of limiting vortices.

As for the steady states of GLE or the solution of Euler–Lagrange equation (1.6), situations are quite different case by case. In the whole plane case, as indicated by

Neu's results [113], it was generally believed that two vortices with winding number of opposite sign undergo attractive interaction and tend to coalesce and annihilation. Hence, for the steady states of the GLE in whole plane, either there are no vortices or all the vortices are of the same sign. However, when the domain is bounded, Lin [98] proved the existence of the mixed vortex-antivortex solution of the Euler–Lagrange equation subject to the Dirichlet BC (1.3) for sufficiently small ε, i.e., the steady states of GLE under Dirichlet BC (1.3) allows vortices with winding number of opposite sign. Nevertheless, Jimbo et al. [81] and Serfaty [131] obtained that any solutions with vortices to (1.1) and (1.4) are unstable in a convex or simple connected domain, while recently del Pino et al. [51] proved the existence of the solution with exactly k vortices of degree one for any integer number k if the domain were not simply connected by the approach of variational reduction. Hence, all the vortices in the initial data (1.2) will either collide with each other and annihilate or simply exit the domain finally. Actually, several studies had been established in both the planar domains and/or higher dimensional domains for the stability of the steady state solution of GLE with Neumann BC (1.4) [49, 79, 81, 82, 84], which imply the close relation between the stability of the equilibrium solution with vortices and the geometrical property of the domain.

For NLSE defined in $\mathbb{R}^2$, when $V(\mathbf{x}) = 1$ and $\varepsilon = 1$, Bethuel et al. [34] proved global well-posedness of NLSE for classes of initial data that have vortices. For the vortex dynamics, Fetter [60] predicted that, to the leading order, the motion of vortices in the NLSE would be governed by the same law as that in the ideal incompressible fluid. Then, the same prediction was given by Neu [113]. He conjectured the stability of the vortex states under NLSE dynamics as an open problem, based on which he found that the vortices behave like point vortices in ideal fluid, and obtained the corresponding RDLs. However, these RDLs are only correct up to the leading order. Corrections to this leading order approximation due to radiation and/or related questions when long-time dynamics of vortices is considered still remain as important open problems. In fact, using the method of effective action and geometric solvability, Ovichinnikov and Sigal confirmed Neu's approximation and derived some leading radiative corrections [116, 117] based on the assumption that the vortices are well separated, which was extended by Lange and Schroers [95] to study the dynamics of overlapping vortices. Recently, Bethuel et al. [29] derived the asymptotic behaviour of the vortices as $\varepsilon \to 0$.

In the bounded domain case, when $V(\mathbf{x}) = 1$, many papers have been dedicated to the study of the vortex states and dynamics after Neu's work [113]. Mironescu [111] investigated stability of the vortices in NLSE with (1.3) and showed that for fixed winding number m: a vortex with $|m| = 1$ is always dynamical stable; while for those of winding number $|m| > 1$, there exists a critical ε_m^c such that if $\varepsilon > \varepsilon_m^c$, the vortex is stable, otherwise unstable. Mironescu's results were then improved by Lin [100] using the spectrum of a linearized operator. Subsequently, Lin and Xin [104] studied the vortex dynamics on a bounded domain with either Dirichlet or Neumann BC, which was further investigated by Jerrard and Spirn [74]. In addition, Colliander and Jerrard [46, 47] studied the vortex structures and dynamics on a torus or under periodic BC. In these studies, the authors derived the RDLs which govern the dynamics of vortex centers under the NLSE dynamics when $\varepsilon \to 0$ with fixed distances between different vortex centers initially. They obtained that to the leading order the vortices move according to the Kirchhoff law in the bounded domain case. However, these reduced dynamical laws cannot indicate radiation and/or sound propagations created by highly co-rotating or overlapping vortices. In fact, it remains as a very fascinating and fundamental open problem to understand the vortex-sound interaction [114], and how the sound waves modify the motion of vortices [62].

For the CGLE under scaling $\lambda_\varepsilon = \frac{1}{\ln \frac{1}{\varepsilon}}$ and homogeneous potential, based on some proper assumptions, Miot [110] studied the dynamics of vortices asymptotically as $\varepsilon \to 0$ in the whole plane case while Kurzke et al. [92] investigated that in the bounded domain case, the corresponding RDLs were derived to govern the motion of the limiting vortices in the whole plane and/or the bounded domain, respectively.

The results shows that the RDLs in the CGLE is actually a hybrid of RDL for GLE and that for NLSE. More recently, Serfaty and Tice [133] studied the vortex dynamics in a more complicated CGLE which involves electromagnetic field and pinning effect.

On the numerical aspects, finite element methods were proposed to investigate numerical solutions of the Ginzburg-Landau equation and related Ginzburg-Landau models of superconductivity [5, 44, 54, 58, 87]. Recently, by proposing efficient and accurate numerical methods for discretizing the GLSE in the whole space, Zhang et al. [152, 153] compared the dynamics of quantized vortices from the reduced dynamical laws obtained by Neu with those obtained from the direct numerical simulation results from GLE and/or NLSE under different parameters and/or initial setups. They solved numerically Neu's open problem on the stability of vortex states under the NLSE dynamics, i.e., vortices with winding number $m = \pm 1$ are dynamically stable, and resp., $|m| > 1$ dynamically unstable [152, 153], which agree with those derived by Ovchinnikov and Sigal [115]. In addition, they identified numerically the parameter regimes for quantized vortex dynamics when the reduced dynamical laws agree qualitatively and/or quantitatively and fail to agree with those from GLE and/or NLSE dynamics.

However, to our limited knowledge, there were few numerical studies on the vortex dynamics and interaction of the GLSE (1.1) in bounded domain, much less for the sound-vortex interaction in the NLSE dynamics.

1.2.2 Gross-Pitaevskii equation with angular momentum

The occurrence of quantized vortices is a hallmark of the superfluid nature of Bose–Einstein condensates. In addition, condensation of bosonic atoms and molecules with significant dipole moments whose interaction is both nonlocal and anisotropic has recently been achieved experimentally in trapped ^{52}Cr and ^{164}Dy gases [1, 48, 67, 94, 105, 108, 143].

Using the mean field approximation, when the temperature T is much smaller than the critical temperature T_c, the properties of a BEC in a rotating frame with long-range dipole-dipole interaction are well described by the macroscopic complex-valued wave function $\psi = \psi(\mathbf{x}, t)$, whose evolution is governed by the following three-dimensional (3D) Gross-Pitaevskii equation (GPE) with angular momentum rotation term and long-range dipole-dipole interaction [1, 16, 39, 130, 140, 144, 154]:

$$i\hbar\partial_t\psi(\mathbf{x},t) = \left[-\frac{\hbar^2}{2m}\nabla^2 + V(\mathbf{x}) + U_0|\psi|^2 + \left(V_{\text{dip}} * |\psi|^2\right) - \Omega L_z\right]\psi(\mathbf{x},t),\ t > 0, \tag{1.8}$$

where t denotes time, $\mathbf{x} = (x, y, z)^T \in \mathbb{R}^3$ is the Cartesian coordinate vector, $\hbar$ is the Planck constant, m is the mass of a dipolar particle and $V(\mathbf{x})$ is an external trapping potential, which reads as

$$V(\mathbf{x}) = \frac{m}{2}(\omega_x^2 x^2 + \omega_y^2 y^2 + \omega_z^2 z^2) \tag{1.9}$$

if a harmonic trap potential is concerned with. Here, ω_x, ω_y and ω_z are the trap frequencies in x-, y- and z-directions, respectively. $U_0 = \frac{4\pi\hbar^2 a_s}{m}$ represents short-range (or local) interaction between dipoles in the condensate with a_s the s-wave scattering length. $V_{\text{dip}}(\mathbf{x})$ describes the long-range dipolar interaction potential between dipoles, which is defined as

$$V_{\text{dip}}(\mathbf{x}) = \frac{\mu_0\mu_{\text{dip}}^2}{4\pi}\frac{1 - 3(\mathbf{x}\cdot\mathbf{n})^2/|\mathbf{x}|^2}{|\mathbf{x}|^3} = \frac{\mu_0\mu_{\text{dip}}^2}{4\pi}\frac{1 - 3\cos^2(\vartheta)}{|\mathbf{x}|^3}, \qquad \mathbf{x} \in \mathbb{R}^2,$$

where μ_0 and μ_{dip} are the vacuum permeability and permanent magnetic dipole moment, respectively (e.g., $\mu_{\text{dip}} = 6\mu_B$ for $^{52}\mathrm{C_r}$ with μ_B being the Bohr magneton), $\mathbf{n} = (n_1, n_2, n_3)^T \in \mathbb{R}^3$ is a given unit vector, i.e., $|\mathbf{n}| = \sqrt{n_1^2 + n_2^2 + n_3^2} = 1$, representing the dipole axis (or dipole moment) and $\vartheta = \vartheta_{\mathbf{n}}(\mathbf{x})$ is the angle between the dipole axis $\mathbf{n}$ and the vector $\mathbf{x}$. In addition, Ω is the angular velocity of the laser beam and $L_z = -i\hbar(x\partial_y - y\partial_x)$ is the z-component of the angular momentum $\mathbf{L} = \mathbf{x} \times \mathbf{P}$ with the momentum operator $\mathbf{P} = -i\hbar\nabla$. The wave function is normalized to

$$||\psi||_2^2 := \int_{\mathbb{R}^3} |\psi(\mathbf{x},t)|^2 d\mathbf{x} = N,$$

with N being the total number of dipolar particles in the dipolar BEC. Introducing the dimensionless variables, $t \to t/\omega_0$ with $\omega_0 = \min\{\omega_x, \omega_y, \omega_z\}$, $\mathbf{x} \to a_0\mathbf{x}$ and $\psi \to \sqrt{N}\psi/a_0^{\frac{3}{2}}$, we have the dimensionless rotational dipolar GPE [18, 144, 145]:

$$i\partial_t\psi(\mathbf{x},t) = \left[-\frac{1}{2}\nabla^2 + V(\mathbf{x}) + \kappa|\psi|^2 + \lambda\left(U_{\text{dip}} * |\psi|^2\right) - \Omega L_z\right]\psi(\mathbf{x},t), \qquad (1.10)$$

where $\kappa = \frac{4\pi N a_s}{x_s}$, $\lambda = \frac{mN\mu_0\mu_{\text{dip}}^2}{3\hbar^2 x_s}$, $V(\mathbf{x}) = \frac{1}{2}(\gamma_x^2\mathbf{x}^2 + \gamma_y^2 y^2 + \gamma_z^2 z^2)$ is the dimensionless harmonic trapping potential with $\gamma_x = \omega_x/\omega_0$, $\gamma_y = \omega_y/\omega_0$, $\gamma_z = \omega_z/\omega_0$, and U_{dip} is the dimensionless long-range dipole-dipole interaction potential defined as

$$U_{\text{dip}}(\mathbf{x}) = \frac{3}{4\pi|\mathbf{x}|^3}\left[1 - \frac{3(\mathbf{x}\cdot\mathbf{n})^2}{|\mathbf{x}|^2}\right] = \frac{3}{4\pi|\mathbf{x}|^3}\left[1 - 3\cos^2(\vartheta)\right], \quad \mathbf{x} \in \mathbb{R}^3. \qquad (1.11)$$

The wave function is normalized to

$$\|\psi\|^2 := \int_{\mathbb{R}^3} |\psi(\mathbf{x},t)|^2\, d\mathbf{x} = 1. \qquad (1.12)$$

In addition, similar to [16, 39], the above GPE (1.10) can be re-formulated as the following Gross-Pitaevskii-Poisson system [13, 16, 39]

$$i\partial_t\psi(\mathbf{x},t) = \left[-\frac{1}{2}\nabla^2 + V(\mathbf{x}) + (\kappa - \lambda)|\psi|^2 - 3\lambda\varphi(\mathbf{x},t) - \Omega L_z\right]\psi(\mathbf{x},t), \qquad (1.13)$$

$$\varphi(\mathbf{x},t) = \partial_{\mathbf{nn}}u(\mathbf{x},t), \quad -\nabla^2 u(\mathbf{x},t) = |\psi(\mathbf{x},t)|^2 \ \text{ with } \lim_{|\mathbf{x}|\to\infty} u(\mathbf{x},t) = 0, \qquad (1.14)$$

where $\partial_{\mathbf{n}} = \mathbf{n}\cdot\nabla$ and $\partial_{\mathbf{nn}} = \partial_{\mathbf{n}}(\partial_{\mathbf{n}})$. From (1.14), it is easy to see that for $t \geq 0$

$$u(\mathbf{x},t) = \left(\frac{1}{4\pi|\mathbf{x}|}\right) * |\psi|^2 := \int_{\mathbb{R}^3} \frac{1}{4\pi|\mathbf{x}-\mathbf{x}'|}|\psi(\mathbf{x}',t)|^2 d\mathbf{x}', \quad \mathbf{x} \in \mathbb{R}^3. \qquad (1.15)$$

Recently, many numerical and theoretical studies have been done on rotating (dipolar) BECs. There have been many numerical methods proposed to study the dynamics of non-rotating BECs, i.e. when $\Omega = 0$ and $\lambda = 0$ [5, 18, 24, 40, 88, 112, 138]. Among them, the time-splitting sine/Fourier pseudospectral method is one of the most successful methods. It has spectral accuracy in space and is easy to implement. In addition, as shown in [16], this method can also be easily generalized to simulate the dynamics of dipolar BECs when $\lambda \neq 0$. However, in rotating condensates, i.e., when $\Omega \neq 0$, we can not directly apply the time-splitting pseudospectral method proposed in [24] to study their dynamics due to the appearance of angular rotational term. So far, there have been several methods introduced to solve the GPE with an angular momentum term. For example, a pseudospectral type method was proposed in [17] by reformulating the problem in the two-dimensional polar coordinates (r, θ) or three-dimensional cylindrical coordinates (r, θ, z). The method is of second-order or fourth-order in the radial direction and spectral accuracy in other directions. A time-splitting alternating direction implicit method was proposed in [23], where the authors decouple the angular terms into two parts and apply the Fourier transform in each direction. Furthermore, a generalized Laguerre-Fourier-Hermite pseudospectral method was presented in [20]. These methods have higher spatial accuracy compared to those in [5, 15, 88] and are also valid in dissipative variants of the GPE (1.10), cf. [139]. On the other hand, the implementation of these methods can become quite involved.

1.3 Purpose and scope of this thesis

As shown in the last two subsections, a vast number of researches have been done and plenty of results have been obtained for the vortex dynamics in BEC, superfluidity and superconductivity. However, there are still some limitations.

- For the vortex dynamics in superconductivity and superfluidity on bounded domain, most studies are primarily researches of the RDLs of well separated vortices. Vortex phenomena related to overlapping vortices and/or vortex collision as well as the effect of the boundary condition and effect of the domain geometry on the vortex dynamics still remains unknown. Numerical simulations have become powerful and useful to figure out those exotic phenomena. However, few numerical studies for the bounded domain case were reported.

- For the vortex dynamics in GPE with angular momentum, there have been only a few reports about the interactions between a few vortices. Moreover, the existing numerical methods have their own limitations. (i). The finite difference method (FDM) or finite element method (FEM) usually need a very fine mesh size, and their order of accuracy are usually low, hence they are time–consuming and inefficient. (ii). Although time splitting spectral method with alternative direction technique is of spectral accuracy, they might cause some problems when the rotating frequency is large. (iii). Additionally, the generalized Laguerre-Fourier-Hermite pseudospectral method is not easy to implement.

Hence, in this thesis, we mainly focus on the following two parts:

- (i). to present efficient and accurate numerical methods for discretizing the reduced dynamical laws and the GLSE (1.1) on bounded domains under different BCs, (ii). to understand numerically how the boundary condition and radiation as well as geometry of the domain affect vortex dynamics and interaction, (iii). to investigate the pining effect of the vortices in CGLE and GLE dynamics, (iv). to study numerically vortex interaction in the GLSE dynamics and/or compare them with those from the reduced dynamical laws with different initial setups and parameter regimes, and (v). to identify cases where the reduced dynamical laws agree qualitatively and/or quantitatively as well as fail to agree with those from GLSE on vortex interaction.

- to propose a simple and efficient numerical method to solve the GPE with angular momentum rotation term which may include a dipolar interaction term. One novel idea in this method consists in the use of rotating Lagrangian coordinates as in [10] in which the angular momentum rotation term vanishes. Hence, we can easily apply the method for non-rotating BECs in [24] to solve the rotating case.

Studies for the first part will be carried out in chapter 2 to chapter 5, while research on the second part will be conducted in chapter 6. In chapter 7, conclusions and possible directions of future work will be summarized and discussed.

Chapter 2

Methods for GLSE on bounded domain

In this chapter, begin with the stationary vortex state of the Ginzburg-Landau-Schrödinger (GLSE) equation, various RDLs that governed the motion of the vortex centers under different boundary conditions (BCs) are reviewed and their equivalent forms are presented and proved. Then, accurate and efficient numerical methods are proposed for computing the GLSE in a disk or rectangular domain under Dirichlet or homogeneous Neumann BC. These methods will be applied to study various phenomena on the vortex dynamics and interaction in following chapters.

2.1 Stationary vortex states

To consider the vortex solution of the GLSE (1.1), we consider the following time independent GLSE with $V(\mathbf{x}) = 1$ in a disk domain centered at origin with radius R_0, i.e., $\mathcal{D} = B_{R_0}(0)$:

$$\Delta\phi^\varepsilon + \frac{1}{\varepsilon^2}(1 - |\phi^\varepsilon|^2)\phi^\varepsilon = 0, \quad \mathbf{x} \in \mathcal{D}, \tag{2.1}$$

$$|\phi^\varepsilon(\mathbf{x}, t)| = 1, \qquad \text{if } \mathbf{x} \in \partial\mathcal{D}, \tag{2.2}$$

where $\phi^\varepsilon(\mathbf{x}, t)$ is a complex-valued function which can be viewed as the steady states of the GLSE (1.1) in a disk domain. The vortex solution takes the form of:

$$\phi^\varepsilon_m(\mathbf{x}) = f^\varepsilon_m(r)e^{im\theta}, \quad \mathbf{x} = (r\cos(\theta), r\sin(\theta)) \in \mathcal{D}, \tag{2.3}$$

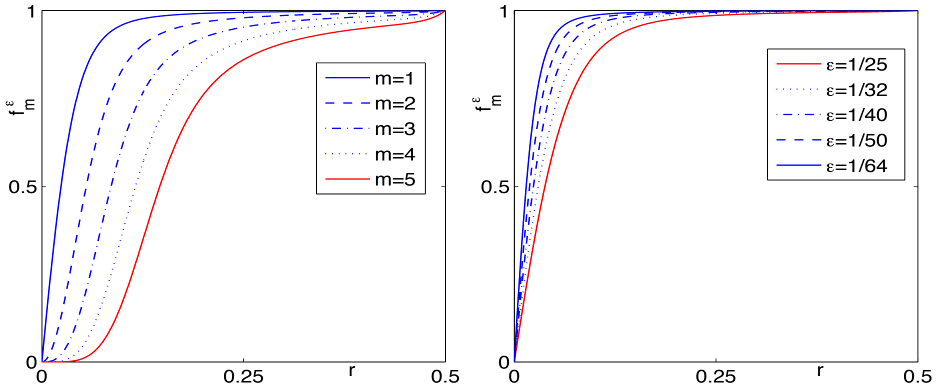

Figure 2.1: Plot of the function $f_m^\varepsilon(r)$ in (2.4) with $R_0 = 0.5$. left: $\varepsilon = \frac{1}{40}$ with different winding number m. right: $m = 1$ with different different ε.

whose existence and qualitative properties were carried out in [69, 70]. Here, $m \in \mathbb{Z}$ is called as the topological charge or winding number or index that represents the singularity of the vortex, the modulus $f_m^\varepsilon(r)$ is a real-valued function satisfying:

$$\left[\frac{1}{r}\frac{d}{dr}\left(r\frac{d}{dr}\right) - \frac{1}{r^2} + \frac{1}{\varepsilon^2}\left(1 - (f_m^\varepsilon(r))^2\right)\right] f_m^\varepsilon(r) = 0, \quad 0 < r < R_0, \tag{2.4}$$

$$f_m^\varepsilon(r = 0) = 0, \quad f_m^\varepsilon(r = R_0) = 1. \tag{2.5}$$

Numerically, the solution f_m^ε can be obtained by either employing a shooting method [45] or a finite difference method with Newton iteration being used for the resulted non-linear system [152]. Fig. 2.1 depicts the results for function $f_m^\varepsilon(r)$ with different ε and m, while Fig. 2.2 shows the surf plots of the density $|\phi_m^\varepsilon|^2$ and the contour plots of the corresponding phase for $m = 1$ and $m = 5$. The stability of the vortex was investigated by Mironescu [111]. He showed that for fixed winding number m, the vortex with $|m| = 1$ is always dynamical stable while for those of winding number $|m| > 1$, there is a critical ε_m^c such that if $\varepsilon > \varepsilon_m^c$, the vortex is stable, otherwise unstable. Mironescu's results was then improved by Lin [100] by considering the spectrum of a linearized operator. It might be interesting to study how the stability of a vortex depends on the perturbation, and how the vortices of high index split if they are not stable.

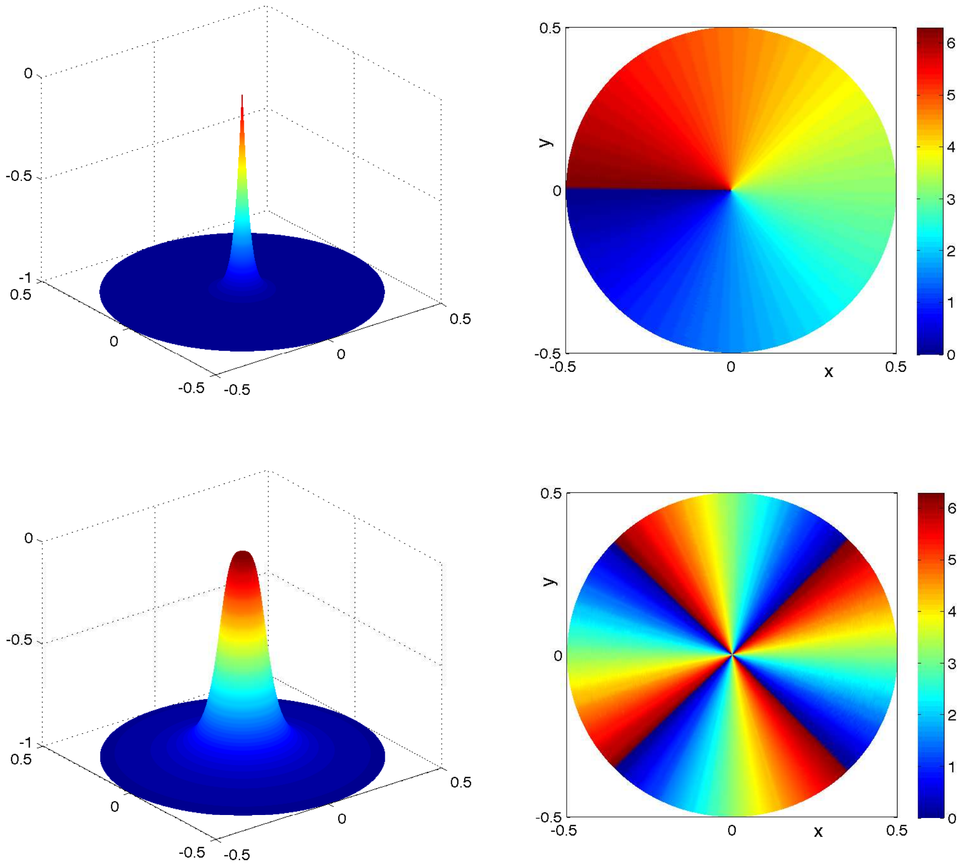

(a)

(b)

Figure 2.2: Surf plot of the density $|\phi_m^\varepsilon|^2$ (left column) and the contour plot of the corresponding phase (right column) for $m = 1$ (a) and $m = 4$ (b).

2.2 Reduced dynamical laws

It had been pointed out that the vortex of index $|m| = 1$ is always stable, and those of index $|m| > 1$ is stable only up to some condition. Thus, it should be interesting to understand how those vortices of winding number $|m| = 1$ dynamic and interact with each other, and how the BC, the geometry of the domain affect their motion. To this end, we choose the initial data in (1.2) as:

$$\psi_0^\varepsilon(\mathbf{x}) = e^{ih(\mathbf{x})} \prod_{j=1}^{M} \tilde{\phi}_{n_j}^\varepsilon(\mathbf{x} - \mathbf{x}_j^0) = e^{ih(\mathbf{x})} \prod_{j=1}^{M} \tilde{\phi}_{n_j}^\varepsilon(x - x_j^0, y - y_j^0), \quad \mathbf{x} \in \bar{\mathcal{D}}, \tag{2.6}$$

here $M > 0$ is the total number of vortices in the initial data, the phase shift $h(\mathbf{x})$ is a harmonic function and for $j = 1, 2, \ldots, M$, $n_j = 1$ or -1, and $\mathbf{x}_j^0 = (x_j^0, y_j^0) \in \mathcal{D}$ are the winding number and initial location of the j-th vortex, respectively. Moreover, $\tilde{\phi}_{n_j}^{\varepsilon}$ is chosen as

$$\tilde{\phi}_{n_j}^{\varepsilon} = \begin{cases} f_{n_j}^{\varepsilon}(|\mathbf{x}|)e^{in_j\theta(\mathbf{x})}, & \text{if } 0 \leq |\mathbf{x}| \leq R_0, \\ e^{in_j\theta(\mathbf{x})}, & \text{if } |\mathbf{x}| \geq R_0, \end{cases} \tag{2.7}$$

where $f_{n_j}^{\varepsilon}$ is the modulus of the vortex solution in (2.3) with winding number n_j and R_0 is constant which is small than the diameter of the domain $\mathcal{D}$.

It is well known that to the leading order in the limit $\varepsilon \to 0$, the M well separated vortices move according to the reduced dynamical law, which are ODE systems. In this section, we review various reduced dynamical laws in different cases and present some equivalent forms. We divide into three parts. The first part and second part are devoted to the case of the GLSE (1.1) under Dirichlet and/or homogeneous BC without pinning effect, i.e., $V(\mathbf{x}) \equiv 1$, respectively. The third part is concerned with the GLE with inhomogeneous potential, i.e., $V(\mathbf{x}) \not\equiv 1$ under Dirichlet BC.

2.2.1 Under homogeneous potential

In this section, we let $\lambda_\varepsilon = \frac{\alpha}{\ln(1/\varepsilon)}$. To simplify our presentation, for $j = 1, \cdots, N$, hereafter we let $\mathbf{x}_j^{\varepsilon}(t) = (x_j^{\varepsilon}(t), y_j^{\varepsilon}(t))$ be the location of the M distinct and isolated vortex centers in the solution of the GLSE (1.1) with initial condition (2.6) at time $t \geq 0$, and denote

$$X^0 := (\mathbf{x}_1^0, \mathbf{x}_2^0, \ldots, \mathbf{x}_M^0), \qquad X^{\varepsilon} := X^{\varepsilon}(t) = (\mathbf{x}_1^{\varepsilon}(t), \mathbf{x}_2^{\varepsilon}(t), \ldots, \mathbf{x}_M^{\varepsilon}(t)), \quad t \geq 0,$$

then we have [46, 72, 92, 97]:

Theorem 2.2.1. *As $\varepsilon \to 0$, for $j = 1, \cdots, N$, the vortex center $\mathbf{x}_j^{\varepsilon}(t)$ will converge to point $\mathbf{x}_j(t)$ satisfying:*

$$(\alpha I + \beta n_j J)\frac{d\mathbf{x}_j(t)}{dt} = -\nabla_{\mathbf{x}_j} W(X), \quad 0 \leq t < T, \tag{2.8}$$

$$\mathbf{x}_j(t = 0) = \mathbf{x}_j^0. \tag{2.9}$$

In equation (2.8), T is the first time that either two vortex collide or any vortex exit the domain, $X := X(t) = (\mathbf{x}_1(t), \mathbf{x}_2(t), \dots, \mathbf{x}_M(t))$,

$$I = \begin{pmatrix} 1 & 0 \\ 0 & 1 \end{pmatrix}, \qquad J = \begin{pmatrix} 0 & -1 \\ 1 & 0 \end{pmatrix},$$

are the 2×2 identity and symplectic matrix, respectively. Moreover, the function $W(X)$ is the so called renormalized energy defined as:

$$W(X) =: W_{\text{cen}}(X) + W_{\text{bc}}(X), \tag{2.10}$$

where W_{cen} is the renormalized energy associated to the M vortex centers that defined as

$$W_{\text{cen}}(X) = -\sum_{1 \le i \ne j \le N} n_i n_j \ln |\mathbf{x}_i - \mathbf{x}_j|, \tag{2.11}$$

and $W_{\text{bc}}(X)$ is the renormalized energy involving the effect of the BC (1.3) and/or (1.4), which takes different formations in different cases.

Under Dirichlet boundary condition

For the GLSE (1.1) with initial condition (2.6) under Dirichlet BC (1.3), it has been derived formally and rigorously [28,46,92,99,103,132] that $W_{\text{bc}}(X) = W_{\text{dbc}}(X)$ in the renormalized energy (2.10) admits the form:

$$W_{\text{dbc}}(X) =: -\sum_{j=1}^{M} n_j R(\mathbf{x}_j; X) + \int_{\partial \mathcal{D}} \left[R(\mathbf{x}; X) + \sum_{j=1}^{M} n_j \ln |\mathbf{x} - \mathbf{x}_j| \right] \frac{\partial_{\nu_\perp} \omega(\mathbf{x})}{2\pi} \, ds, \tag{2.12}$$

where, for any fixed $X \in \mathcal{D}^M$, $R(\mathbf{x}; X)$ is a harmonic function in $\mathbf{x}$, i.e.,

$$\Delta R(\mathbf{x}; X) = 0, \qquad \mathbf{x} \in \mathcal{D}, \tag{2.13}$$

satisfying the following Neumann BC

$$\frac{\partial R(\mathbf{x}; X)}{\partial \nu} = \partial_{\nu_\perp} \omega(\mathbf{x}) - \frac{\partial}{\partial \nu} \sum_{l=1}^{M} n_l \ln |\mathbf{x} - \mathbf{x}_l|, \qquad \mathbf{x} \in \partial \mathcal{D}. \tag{2.14}$$

Notice that to calculate $\nabla_{\mathbf{x}_j} W(X)$, we need to calculate $\nabla_{\mathbf{x}_j} R$, and since for $j = 1, \cdots, N$, $\mathbf{x}_j$ is implicitly included in $R(\mathbf{x}, X)$ as a parameter, hence it is difficult to calculate $\nabla_{\mathbf{x}_j} R$ and thus difficult to solve the reduced dynamical law (2.8) with (2.10)–(2.12) even numerically. However, by using an identity in [28] (see Eq. (51) on page 84),

$$\nabla_{\mathbf{x}_j} \left[W(X) + W_{\text{dbc}}(X)\right] = -2n_j \nabla_{\mathbf{x}} \left[R(\mathbf{x}; X) + \sum_{l=1 \& l\neq j}^{M} n_l \ln |\mathbf{x} - \mathbf{x}_l| \right]_{\mathbf{x}=\mathbf{x}_j},$$

we have the following simplified equivalent form for (2.8).

Lemma 2.2.1. *For* $1 \leq j \leq M$ *and* $t > 0$, *system (2.8) can be simplified as*

$$(\alpha I + \beta m_j J) \frac{d}{dt} \mathbf{x}_j(t) = 2n_j \left[\nabla_{\mathbf{x}} R\left(\mathbf{x}; X\right)|_{\mathbf{x}=\mathbf{x}_j(t)} + \sum_{l=1 \& l\neq j}^{M} n_l \frac{\mathbf{x}_j(t) - \mathbf{x}_l(t)}{|\mathbf{x}_j(t) - \mathbf{x}_l(t)|^2} \right]. \tag{2.15}$$

Moreover, for any fixed $X \in \mathcal{D}^M$, by introducing function $H(\mathbf{x}, X)$ and $Q(\mathbf{x}, X)$ that both are harmonic in $\mathbf{x}$ satisfying respectively the boundary condition [73,104]:

$$\frac{\partial H(\mathbf{x}; X)}{\partial \nu_\perp} = \partial_{\nu_\perp} \omega(\mathbf{x}) - \frac{\partial}{\partial \nu} \sum_{l=1}^{M} n_l \ln |\mathbf{x} - \mathbf{x}_l|, \qquad \mathbf{x} \in \partial \mathcal{D}, \tag{2.16}$$

$$Q(\mathbf{x}; X) = \omega(\mathbf{x}) - \sum_{l=1}^{M} n_l \theta(\mathbf{x} - \mathbf{x}_l), \qquad \mathbf{x} \in \partial \mathcal{D}, \tag{2.17}$$

with the function $\theta : \mathbb{R}^2 \to [0, 2\pi)$ defined as

$$\cos(\theta(\mathbf{x})) = \frac{x}{|\mathbf{x}|}, \qquad \sin(\theta(\mathbf{x})) = \frac{y}{|\mathbf{x}|}, \qquad 0 \neq \mathbf{x} = (x, y) \in \mathbb{R}^2, \tag{2.18}$$

we have the following lemma for the equivalence of the reduced dynamical law (2.15) [21, 22]:

Lemma 2.2.2. . *For any fixed* $X \in \mathcal{D}^M$, *we have the following identity*

$$J \nabla_{\mathbf{x}} Q\left(\mathbf{x}; X\right) = \nabla_{\mathbf{x}} R\left(\mathbf{x}; X\right) = J \nabla_{\mathbf{x}} H\left(\mathbf{x}; X\right), \qquad \mathbf{x} \in \mathcal{D}, \tag{2.19}$$

which immediately implies the equivalence between system (2.15) and the following *two systems: for* $t>0$

$$(\alpha I+\beta n_j J)\frac{d}{dt}\mathbf{x}_j(t)=2n_j\left[J\nabla_{\mathbf{x}}H\left(\mathbf{x};X\right)|_{\mathbf{x}=\mathbf{x}_j(t)}+\sum_{l=1\&l\neq j}^{M}n_l\frac{\mathbf{x}_j(t)-\mathbf{x}_l(t)}{|\mathbf{x}_j(t)-\mathbf{x}_l(t)|^2}\right],$$

$$(\alpha I+\beta n_j J)\frac{d}{dt}\mathbf{x}_j(t)=2n_j\left[J\nabla_{\mathbf{x}}Q\left(\mathbf{x};X\right)|_{\mathbf{x}=\mathbf{x}_j(t)}+\sum_{l=1\&l\neq j}^{M}n_l\frac{\mathbf{x}_j(t)-\mathbf{x}_l(t)}{|\mathbf{x}_j(t)-\mathbf{x}_l(t)|^2}\right].$$

Proof. For any fixed $X\in\mathcal{D}^M$, since Q is a harmonic function, there exists a function $\varphi_1(\mathbf{x})$ such that

$$J\nabla_{\mathbf{x}}Q\left(\mathbf{x};X\right)=\nabla\varphi_1(\mathbf{x}),\qquad \mathbf{x}\in\mathcal{D}.$$

Thus, $\varphi_1(\mathbf{x})$ satisfies the Laplace equation

$$\Delta\varphi_1(\mathbf{x})=\nabla\cdot(J\nabla_{\mathbf{x}}Q(\mathbf{x};X))=\partial_{yx}\varphi_1(\mathbf{x})-\partial_{xy}\varphi_1(\mathbf{x})=0,\quad \mathbf{x}\in\mathcal{D},\tag{2.20}$$

with the following Neumann BC

$$\partial_\nu\varphi_1(\mathbf{x})=(J\nabla_{\mathbf{x}}Q(\mathbf{x};X))\cdot\nu=\nabla_{\mathbf{x}}Q(\mathbf{x};X)\cdot\nu_\perp=\partial_{\nu_\perp}Q(\mathbf{x};X),\quad \mathbf{x}\in\partial\mathcal{D}.\tag{2.21}$$

Noticing (2.17), we obtain for $\mathbf{x}\in\partial\mathcal{D}$,

$$\partial_\nu\varphi_1(\mathbf{x})=\partial_{\nu_\perp}\omega(\mathbf{x})-\frac{\partial}{\partial\nu_\perp}\sum_{l=1}^{M}n_l\theta(\mathbf{x}-\mathbf{x}_l)=\partial_{\nu_\perp}\omega(\mathbf{x})-\frac{\partial}{\partial\nu}\sum_{l=1}^{M}n_l\ln|\mathbf{x}-\mathbf{x}_l|.\tag{2.22}$$

Combining (2.20), (2.22), (2.13) and (2.14), we get

$$\Delta(R(\mathbf{x};X)-\varphi_1(\mathbf{x}))=0,\quad \mathbf{x}\in\mathcal{D},\qquad \partial_\nu\left(R(\mathbf{x};X)-\varphi_1(\mathbf{x})\right)=0,\quad \mathbf{x}\in\partial\mathcal{D}.\tag{2.23}$$

Thus

$$R(\mathbf{x};X)=\varphi_1(\mathbf{x})+\text{constant},\qquad \mathbf{x}\in\mathcal{D},$$

which immediately implies the first equality in (2.19).

Similarly, since H is a harmonic function, there exists a function $\varphi_2(\mathbf{x})$ such that

$$J\nabla_{\mathbf{x}}H\left(\mathbf{x};X\right)=\nabla\varphi_2(\mathbf{x}),\qquad \mathbf{x}\in\mathcal{D}.$$

Thus, $\varphi_2(\mathbf{x})$ satisfies the Laplace equation

$$\Delta\varphi_2(\mathbf{x})=\nabla\cdot(J\nabla_{\mathbf{x}}H(\mathbf{x};X))=\partial_{yx}\varphi_2(\mathbf{x})-\partial_{xy}\varphi_2(\mathbf{x})=0,\qquad \mathbf{x}\in\mathcal{D},\tag{2.24}$$

with the following Neumann BC

$$\partial_\nu \varphi_2(\mathbf{x}) = (J\nabla_{\mathbf{x}} H(\mathbf{x};X))\cdot\nu = \nabla_{\mathbf{x}} H(\mathbf{x};X)\cdot\nu_\perp = \partial_{\nu_\perp} H(\mathbf{x};X), \qquad \mathbf{x}\in\partial\mathcal{D}. \tag{2.25}$$

Combining (2.24), (2.25), (2.13), (2.14) and (2.16), we get

$$\Delta(R(\mathbf{x};X)-\varphi_2(\mathbf{x})) = 0, \quad \mathbf{x}\in\mathcal{D}, \qquad \partial_\nu\left(R(\mathbf{x};X)-\varphi_2(\mathbf{x})\right) = 0, \quad \mathbf{x}\in\partial\mathcal{D}. \tag{2.26}$$

Thus

$$R(\mathbf{x};X) = \varphi_2(\mathbf{x}) + \text{constant}, \qquad \mathbf{x}\in\mathcal{D},$$

which immediately implies the second equality in (2.19). □

Under homogeneous Neumann boundary condition

For the GLSE (1.1) with initial condition (2.6) under homogeneous Neumann BC (1.4), it has been derived formally and rigorously [46,74,92] that $W_{\text{bc}}(X)$ in the renormalized energy (2.10) admit the form:

$$W_{\text{bc}}(X) = W_{\text{nbc}}(X) := -\sum_{j=1}^{M} n_j \tilde{R}(\mathbf{x}_j;X), \tag{2.27}$$

and by using the following identity

$$\nabla_{\mathbf{x}_j}\left[W(X)+W_{\text{nbc}}(X)\right] = -2n_j\nabla_{\mathbf{x}}\left[\tilde{R}(\mathbf{x};X) + \sum_{l=1\&l\neq j}^{M} n_l \ln|\mathbf{x}-\mathbf{x}_l|\right]_{\mathbf{x}_j}, \tag{2.28}$$

we have the following simplified equivalent form for (2.8):

Lemma 2.2.3. *For $1\le j\le M$ and $t>0$, system (2.8) can be simplified as*

$$(\alpha I+\beta n_j J)\frac{d}{dt}\mathbf{x}_j(t) = 2n_j\left[\nabla_{\mathbf{x}}\tilde{R}\left(\mathbf{x};X\right)|_{\mathbf{x}=\mathbf{x}_j(t)} + \sum_{l=1\&l\neq j}^{M} n_l \frac{\mathbf{x}_j(t)-\mathbf{x}_l(t)}{|\mathbf{x}_j(t)-\mathbf{x}_l(t)|^2}\right]. \tag{2.29}$$

Moreover, for any fixed $X\in\mathcal{D}^M$, by introducing function $\tilde{H}(\mathbf{x},X)$ and $\tilde{Q}(\mathbf{x},X)$ that both are harmonic in $\mathbf{x}$ satisfying respectively the boundary condition [80,81,83,104]:

$$\frac{\partial\tilde{H}(\mathbf{x};X)}{\partial\nu_\perp} = -\frac{\partial}{\partial\nu}\sum_{l=1}^{M} n_l\theta(\mathbf{x}-\mathbf{x}_l), \qquad \mathbf{x}\in\partial\mathcal{D}, \tag{2.30}$$

$$\frac{\partial\tilde{Q}(\mathbf{x};X)}{\partial\nu} = -\frac{\partial}{\partial\nu}\sum_{l=1}^{M} n_l\theta(\mathbf{x}-\mathbf{x}_l), \qquad \mathbf{x}\in\partial\mathcal{D}, \tag{2.31}$$

with the function $\theta : \mathbb{R}^2 \to [0, 2\pi)$ being defined in (2.18), we have the following lemma for the equivalence of the reduced dynamical law (2.29) [21,22]:

Lemma 2.2.4. *For any fixed $X \in \mathcal{D}^M$, we have the following identity*

$$J\nabla_{\mathbf{x}}\tilde{Q}\left(\mathbf{x}; X\right) = \nabla_{\mathbf{x}}\tilde{R}\left(\mathbf{x}; X\right) = J\nabla_{\mathbf{x}}\tilde{H}\left(\mathbf{x}; X\right), \qquad \mathbf{x} \in \mathcal{D}, \tag{2.32}$$

which immediately implies the equivalence of system (2.29) and the following two systems: for $t > 0$

$$(\alpha I + \beta n_j J)\frac{d}{dt}\mathbf{x}_j(t) = 2n_j\left[\nabla_{\mathbf{x}}\tilde{H}\left(\mathbf{x}; X\right)|_{\mathbf{x}=\mathbf{x}_j(t)} + \sum_{l=1\&l\neq j}^{M} n_l\frac{\mathbf{x}_j(t) - \mathbf{x}_l(t)}{|\mathbf{x}_j(t) - \mathbf{x}_l(t)|^2}\right],$$

$$(\alpha I + \beta n_j J)\frac{d}{dt}\mathbf{x}_j(t) = 2n_j\left[J\nabla_{\mathbf{x}}\tilde{Q}\left(\mathbf{x}; X\right)|_{\mathbf{x}=\mathbf{x}_j(t)} + \sum_{l=1\&l\neq j}^{M} n_l\frac{\mathbf{x}_j(t) - \mathbf{x}_l(t)}{|\mathbf{x}_j(t) - \mathbf{x}_l(t)|^2}\right].$$

Proof. Follow the line in the proof of lemma 2.2.1 and we omit the details here for brevity. ☐

2.2.2 Under inhomogeneous potential

It has been shown in last section that in a homogeneous potential, vortices in the GLE dynamics under Dirichlet BC will move according to gradient flow of the so called renormalized energy, which is associated to the BC. However, in an inhomogeneous potential, i.e $V(\mathbf{x}) \not\equiv 1$, the phenomena is quite different. Generally speaking, vortices no longer move along the gradient flow of the renomalized energy, they move toward the critical points of the potential $V(\mathbf{x})$ instead [42,76,78]. And it has been proved that they obey the following reduced dynamical law [76]:

Theorem 2.2.2. *As $\varepsilon \to 0$, for $j = 1, \cdots, N$, the vortex center $\mathbf{x}_j^\varepsilon(t)$ in the GLE dynamics with $\lambda_\varepsilon = 1$ under Dirichlet BC will converge to point $\mathbf{x}_j(t)$, which satisfies:*

$$\frac{d\mathbf{x}_j(t)}{dt} = -\frac{\nabla V(\mathbf{x}_j)}{V(\mathbf{x}_j)}, \qquad 0 \leq t < +\infty, \tag{2.33}$$

$$\mathbf{x}_j(t = 0) = \mathbf{x}_j^0. \tag{2.34}$$

In addition, for each j*, if there is a Lipschitz domain* $G_j \subset \mathcal{D}$ *such that*

$$\mathbf{x}_j^0 \in G_j, \qquad \min_{\mathbf{x}\in\partial G_j} V(\mathbf{x}) > V(\mathbf{x}_j^0), \quad , j = 1, \cdots, M,$$

the solution in (2.33) will satisfy:

$$\text{for } t > 0, \mathbf{x}_j(t) \neq \mathbf{x}_l(t) \text{ if } j \neq l, \text{ and } \mathbf{x}_j(t) \in G_j.$$

Hence, the vortices will all be pinned together to the critical points of $V(\mathbf{x})$ and further to the minimum points if $V(\mathbf{x})$ has no other critical points.

Unfortunately, to our limited knowledge, there are no existing studies that deal with the vortex dynamics in the inhomogeneous potential in the GLE dynamics under Neumann BC, or in the CGLE or NLSE dynamics in the limiting process $\varepsilon \to 0$.

2.3 Numerical methods

In this section, we present efficient and accurate numerical methods for discretizing the GLSE (1.1) with a time dependent potential $U(\mathbf{x}, t)$ in either a rectangle or a disk with initial condition (1.2) and under either Dirichlet BC (1.3) or homogeneous Neumann BC (1.4):

$$(\lambda_\varepsilon + i\beta)\partial_t \psi^\varepsilon(\mathbf{x}, t) = \Delta\psi^\varepsilon + \frac{1}{\varepsilon^2}(U(\mathbf{x}, t) - |\psi^\varepsilon|^2)\psi^\varepsilon, \qquad \mathbf{x} \in \mathcal{D}, \quad t > 0, \quad (2.35)$$

here $U(\mathbf{x}, t) = V(\mathbf{x}) + W(\mathbf{x}, t)$ with $W(\mathbf{x}, t)$ an external potential. The key idea in our numerical methods are based on: (i) applying a time-splitting technique which has been widely used for nonlinear partial differential equations [65, 137] to decouple the nonlinearity in the GLSE [19, 27, 141, 152]; and (ii) adapt proper finite difference and/or spectral method to discretize a gradient flow with constant coefficient [17, 21, 22].

2.3.1 Time-splitting

Let $\tau > 0$ be the time step size, denote $t_n = n\tau$ for $n \geq 0$. For $n = 0, 1, \ldots$, from time $t = t_n$ to $t = t_{n+1}$, the GLSE (1.1) is solved in two splitting steps. One first solves

$$(\lambda_\varepsilon + i\beta)\partial_t \psi^\varepsilon(\mathbf{x}, t) = \frac{1}{\varepsilon^2}(U(x, t) - |\psi^\varepsilon|^2)\psi^\varepsilon, \qquad \mathbf{x} \in \mathcal{D}, \quad t \geq t_n, \tag{2.36}$$

for the time step of length τ, followed by solving

$$(\lambda_\varepsilon + i\beta)\partial_t \psi^\varepsilon(\mathbf{x}, t) = \Delta\psi^\varepsilon, \qquad \mathbf{x} \in \mathcal{D}, \quad t \geq t_n, \tag{2.37}$$

for the same time step. Equation (2.37) is discretized in the next two subsections on a rectangle and a disk, respectively. For $t \in [t_n, t_{n+1}]$, to solve equation (2.36), we rewrite

$$\psi^\varepsilon(\mathbf{x}, t) = \sqrt{\rho^\varepsilon(\mathbf{x}, t)}e^{iS^\varepsilon(\mathbf{x},t)} \tag{2.38}$$

with ρ^ε and S^ε being the density and phase of ψ^ε, respectively. From (2.36), we can easily obtain the following ODE for $\rho^\varepsilon(\mathbf{x}, t) = |\psi^\varepsilon(\mathbf{x}, t)|^2$:

$$\partial_t \rho^\varepsilon(\mathbf{x}, t) = \eta[U(\mathbf{x}, t) - \rho^\varepsilon(\mathbf{x}, t)]\rho^\varepsilon(\mathbf{x}, t), \quad \mathbf{x} \in \mathcal{D}, \quad t_n \leq t \leq t_{n+1}, \tag{2.39}$$

where $\eta = 2\lambda_\varepsilon/\varepsilon^2(\lambda_\varepsilon^2 + \beta^2)$. Solving equation (2.39), we have

$$\rho^\varepsilon(\mathbf{x}, t) = \frac{\rho^\varepsilon(\mathbf{x}, t_n)\exp[\eta U_n(\mathbf{x}, t)]}{1 + \eta\rho^\varepsilon(\mathbf{x}, t_n)\int_{t_n}^t \exp[\eta U_n(\mathbf{x}, s)ds]}, \tag{2.40}$$

where $U_n(\mathbf{x}, t) = \int_{t_n}^t U(\mathbf{x}, s)ds$. Moreover, if $W(\mathbf{x}, t) \equiv 0$, i.e., $U(\mathbf{x}, t) = V(\mathbf{x})$, $\rho(\mathbf{x}, t)$ can be analytically integrated to have

$$\rho^\varepsilon(\mathbf{x}, t) = \begin{cases} \rho^\varepsilon(\mathbf{x}, t_n), & \lambda_\varepsilon = 0, \\ \frac{\rho^\varepsilon(\mathbf{x},t_n)}{1+\eta\rho^\varepsilon(\mathbf{x},t_n)(t-t_n)}, & V(\mathbf{x}) = 0 \,\&\, \lambda_\varepsilon \neq 0, \\ \frac{V(\mathbf{x})\rho^\varepsilon(\mathbf{x},t_n)}{\rho^\varepsilon(\mathbf{x},t_n)+(V(\mathbf{x})-\rho^\varepsilon(\mathbf{x},t_n))\exp[-\eta V(\mathbf{x})(t-t_n)]}, & V(\mathbf{x}), \lambda_\varepsilon \neq 0. \end{cases} \tag{2.41}$$

Plugging (2.38) back into (2.36), we obtain the equation for the phase $S^\varepsilon(\mathbf{x}, t)$:

$$\partial_t S^\varepsilon(\mathbf{x}, t) = -\frac{\beta}{\varepsilon^2(\lambda_\varepsilon^2 + \beta^2)}[U(\mathbf{x}, t) - \rho^\varepsilon(\mathbf{x}, t)], \quad \mathbf{x} \in \mathcal{D}, \quad t_n \leq t \leq t_{n+1}. \tag{2.42}$$

Combining (2.40) and (2.42), we obtain for $t \in [t_n, t_{n+1}]$,

$$\psi^\varepsilon(\mathbf{x}, t) = \psi^\varepsilon(\mathbf{x}, t_n)\sqrt{P_n(\mathbf{x}, t)}\exp\left[-\frac{i\beta}{\varepsilon^2(\lambda_\varepsilon^2 + \beta^2)}(U_n(\mathbf{x}, t) - \int_{t_n}^t \rho^\varepsilon(\mathbf{x}, s)ds)\right], \tag{2.43}$$

where

$$P_n(\mathbf{x},t) = \frac{\exp[\eta U_n(\mathbf{x},t)]}{1+\eta|\psi^\varepsilon(\mathbf{x},t_n)|^2\int_{t_n}^{t}\exp[\eta U_n(\mathbf{x},s)]ds}. \tag{2.44}$$

Furthermore, if $U(\mathbf{x},t)=V(\mathbf{x})$, we have the explicit formation of ψ^ε:

$$\psi^\varepsilon(\mathbf{x},t) = \psi^\varepsilon(\mathbf{x},t_n)\begin{cases} \exp\left[-\frac{i\beta}{\varepsilon^2\beta^2}(V(\mathbf{x})-|\psi^\varepsilon(\mathbf{x},t_n)|^2)(t-t_n)\right], & \lambda_\varepsilon = 0,\\ \sqrt{\hat{P}(\mathbf{x},t)}\exp\left[-\frac{i\beta}{2\lambda_\varepsilon^2}\ln\hat{P}(\mathbf{x},t)\right], & \lambda_\varepsilon \neq 0 \end{cases} \tag{2.45}$$

where

$$\hat{P}(\mathbf{x},t) = \begin{cases} \frac{1}{1+\eta|\psi^\varepsilon(\mathbf{x},t_n)|^2(t-t_n)}, & V(\mathbf{x})\equiv 0,\\ \frac{V(\mathbf{x})}{|\psi^\varepsilon(\mathbf{x},t_n)|^2+(V(\mathbf{x})-|\psi^\varepsilon(\mathbf{x},t_n)|^2)\exp(-\eta V(\mathbf{x})(t-t_n))}, & V(\mathbf{x})\not\equiv 0, \end{cases} \tag{2.46}$$

Remark 2.3.1. *If functions $U_n(\mathbf{x},t)$ and other integrals in (2.43) cannot be calculated analytically, numerical quadrature such as the trapezoidal rule can be applied to solve them.*

Remark 2.3.2. *In practice, we always use the second-order Strang splitting [137], that is, from time $t=t_n$ to $t=t_{n+1}$: (i) evolve (2.36) for half time step $\tau/2$ with initial data given at $t=t_n$; (ii) evolve (2.37) for one step τ starting with the new data; and (iii) evolve (2.36) for half time step $\tau/2$ again with the newer data.*

2.3.2 Discretization in a rectangular domain

Let $\mathcal{D}=[a,b]\times[c,d]$ be a rectangular domain, and denote mesh sizes $h_x{=}\frac{b-a}{N}$ and $h_y{=}\frac{d-c}{L}$ with N and L being two even positive integers.

First we present a Crank-Nicolson 4th-order compact finite difference (CNFD) method for discretizing the equation (2.37) with Dirichlet BC (1.3) by using the 4th-order compact finite difference discretization for spatial derivatives followed by a Crank-Nicolson scheme for temporal derivative. In order to do so, denote the grid points as $x_j=a+jh_x$ for $j=0,1,\ldots,N$ and $y_l=c+lh_y$ for $l=0,1,\ldots,L$; and $\psi_{j,l}^{\varepsilon,n}$

be the numerical approximation of $\psi^\varepsilon(x_j, y_l, t_n)$ for $j = 0, 1, \ldots, N$, $l = 0, 1, \ldots, L$ and $n \geq 0$. Define the finite difference operators as

$$\delta_x^2 \psi_{j,l}^{\varepsilon,n} = \frac{\psi_{j+1,l}^{\varepsilon,n} - 2\psi_{j,l}^{\varepsilon,n} + \psi_{j-1,l}^{\varepsilon,n}}{h_x^2}, \qquad \delta_y^2 \psi_{j,l}^{\varepsilon,n} = \frac{\psi_{j,l+1}^{\varepsilon,n} - 2\psi_{j,l}^{\varepsilon,n} + \psi_{j,l-1}^{\varepsilon,n}}{h_y^2},$$

then a CNFD discretization for (2.37) reads, i.e., for $1 \leq j \leq N-1$ and $1 \leq l \leq L-1$

$$\frac{(\lambda_\varepsilon + i\beta)}{\tau}\left[I + \frac{h_x^2}{12}\delta_x^2 + \frac{h_y^2}{12}\delta_y^2\right]\left(\psi_{j,l}^{\varepsilon,n+1} - \psi_{j,l}^{\varepsilon,n}\right) = \left[\delta_x^2 + \delta_y^2 + \frac{h_x^2 + h_y^2}{12}\delta_x^2\delta_y^2\right]\left(\frac{\psi_{j,l}^{\varepsilon,n+1} + \psi_{j,l}^{\varepsilon,n}}{2}\right), \tag{2.47}$$

where I is the identity operator and the boundary condition (1.3) is discretized as

$$\begin{aligned}
&\psi_{0,l}^{\varepsilon,n+1} = g(a, y_l), \qquad &&\psi_{M,l}^{\varepsilon,n+1} = g(b, y_l), \qquad &&l = 0, 1, \ldots, L,\\
&\psi_{j,0}^{\varepsilon,n+1} = g(x_j, c), \qquad &&\psi_{j,L}^{\varepsilon,n+1} = g(x_j, d), \qquad &&j = 0, 1, \ldots, N.
\end{aligned}$$

Here although an implicit time discretization is applied for (2.37), the linear system in (2.47) can be solved explicitly via direct Poisson solver through DST [90] at the computational cost of $O\left(NL\ln(NL)\right)$.

Combining the above CNFD discretization with the second order Strang splitting presented in the previous subsection, we obtain a time-splitting Crank-Nicolson finite difference (TSCNFD) discretization for the GLSE (1.1) on a rectangle with Dirichlet BC (1.3). This TSCNFD discretization is unconditionally stable, second order in time and fourth order in space, the memory cost is $O(NL)$ and the computational cost per time step is $O\left(NL\ln(NL)\right)$.

Next we present a cosine pseudospectral method for the equation (2.37) with homogeneous Neumann BC (1.4) by using cosine spectral discretization for spatial derivatives followed by integrating in time *exactly*. To this end, let

$$Y_{NL} = \text{span}\{\phi_{pq}(\mathbf{x}) = \cos(\mu_p^x(x-a))\cos(\mu_q^y(y-c)), 0 \leq p \leq N-1,\ 0 \leq q \leq L-1\},$$

with

$$\mu_p^x = \frac{p\pi}{b-a}, \quad p = 0, 1, \ldots, N-1; \qquad \mu_q^y = \frac{q\pi}{d-c}, \quad q = 0, 1, \ldots, L-1.$$

Then the cosine spectral discretization for (2.37) with (1.4) is as follows: Find $\psi^\varepsilon_{NL}(\mathbf{x},t) \in Y_{NL}$, i.e.,

$$\psi^\varepsilon_{NL}(\mathbf{x},t) = \sum_{p=0}^{N-1}\sum_{q=0}^{L-1} \hat{\psi}^\varepsilon_{pq}(t)\phi_{pq}(\mathbf{x}), \qquad \mathbf{x} \in \mathcal{D}, \quad t \geq t_n, \tag{2.48}$$

such that

$$(\lambda_\varepsilon + i\beta)\partial_t \psi^\varepsilon_{NL}(\mathbf{x},t) = \Delta\psi^\varepsilon_{NL}(\mathbf{x},t), \qquad \mathbf{x} \in \mathcal{D}, \quad t \geq t_n. \tag{2.49}$$

Plugging (2.48) into (2.49), noticing the orthogonality of the cosine functions, for $0 \leq p \leq N-1$ and $0 \leq q \leq L-1$, we find

$$(\lambda_\varepsilon + i\beta)\frac{d}{dt}\hat{\psi}^\varepsilon_{pq}(t) = -\left[(\mu^x_p)^2 + (\mu^y_q)^2\right]\hat{\psi}^\varepsilon_{pq}(t), \qquad t \geq t_n. \tag{2.50}$$

The above ODE can be integrated *exactly* in time, i.e.,

$$\hat{\psi}^\varepsilon_{pq}(t) = e^{\tilde{\eta}\left[(\mu^x_p)^2+(\mu^y_q)^2\right](t-t_n)}\,\hat{\psi}^\varepsilon_{pq}(t_n), \quad t \geq t_n,\ 0 \leq p \leq N-1,\ 0 \leq q \leq L-1, \tag{2.51}$$

where $\tilde{\eta} = \frac{i\beta-\lambda_\varepsilon}{\lambda^2_\varepsilon+\beta^2}$. The above procedure is not suitable in practice due to the difficulty of computing the integrals in (2.48). In practice, we need approximate the integrals by a quadrature rule on grids. Define the grid points as $x_{j+\frac{1}{2}} = a + (j+\frac{1}{2})h_x$ for $j = 0,1,\ldots,N-1$ and $y_{l+\frac{1}{2}} = c + (l+\frac{1}{2})h_y$ for $j = 0,1,\ldots,L-1$; denote $\psi^{\varepsilon,n}_{j+\frac{1}{2},l+\frac{1}{2}}$ be the numerical approximation of $\psi^\varepsilon(x_{j+\frac{1}{2}}, y_{l+\frac{1}{2}}, t_n)$ for $j = 0,1,\ldots,N-1$, $l = 0,1,\ldots,L-1$ and $n \geq 0$; and $\psi^{\varepsilon,n}$ be the solution vector at time $t = t_n$ with components $\{\psi^{\varepsilon,n}_{j+\frac{1}{2},l+\frac{1}{2}}, 0 \leq j \leq N-1, 0 \leq l \leq L-1\}$ for $n \geq 0$. Choose $\psi^{\varepsilon,0}_{j+\frac{1}{2},l+\frac{1}{2}} = \psi^\varepsilon_0(x_{j+\frac{1}{2}}, y_{l+\frac{1}{2}})$ for $0 \leq j \leq N-1$ and $0 \leq l \leq L-1$, then a cosine pseudospectral approximation for (2.37) with (1.4) reads as, for $0 \leq j \leq N-1$ and $0 \leq l \leq L-1$

$$\psi^{\varepsilon,n+1}_{j+\frac{1}{2},l+\frac{1}{2}} = \sum_{p=0}^{N-1}\sum_{q=0}^{L-1} \alpha^x_p\alpha^y_q e^{\tilde{\eta}\left[(\mu^x_p)^2+(\mu^y_q)^2\right]\tau}\,\hat{\psi}^{\varepsilon,n}_{pq}\phi_{pq}(x_{j+\frac{1}{2}}, y_{l+\frac{1}{2}}), \quad n \geq 0, \tag{2.52}$$

where

$$\hat{\psi}^{\varepsilon,n}_{p,q} = \alpha^x_p\alpha^y_q \sum_{j=0}^{N-1}\sum_{l=0}^{L-1} \psi^{\varepsilon,n}_{j+\frac{1}{2},l+\frac{1}{2}}\phi_{pq}(x_{j+\frac{1}{2}}, y_{l+\frac{1}{2}}), \quad 0 \leq p \leq N-1,\ 0 \leq q \leq L-1,$$

with

$$\alpha_p^x = \begin{cases} \sqrt{\frac{1}{N}}, & p = 0, \\ \sqrt{\frac{2}{N}}, & 1 \le p \le N-1, \end{cases} \qquad \alpha_q^y = \begin{cases} \sqrt{\frac{1}{L}}, & q = 0, \\ \sqrt{\frac{2}{L}}, & 1 \le q \le L-1. \end{cases}$$

Again, combining the above cosine pseudospectral discretization with the second order Strang splitting presented in the subsection 3.1, we obtain a time-splitting cosine pseudospectral (TSCP) discretization for the GLSE (1.1) on a rectangle with homogeneous Neumann BC (1.4). This TSCP discretization is unconditionally stable, second order in time and spectral order in space, the memory cost is $O(NL)$ and the computational cost per time step is $O\left(NL \ln(NL)\right)$ via DCT [134].

Remark 2.3.1. *If the homogeneous Neumann BC (1.4) is replaced by periodic BC, the above TSCP discretization for the GLSE (1.1) is still valid provided that we replace the cosine basis functions by the Fourier basis functions in the spectral discretization and use the quadrature rule associated to the Fourier functions [134]. We omit the details here for brevity.*

2.3.3 Discretization in a disk domain

Let $\mathcal{D} = \{\mathbf{x} \mid |\mathbf{x}| < R\}$ be a disk with $R > 0$ a fixed constant. In this case, it is natural to adopt the polar coordinate (r, θ). In order to discretize (2.37) with either (1.3) or (1.4), we apply the standard Fourier pseudospectral method in θ-direction [134], finite element method in r-direction, and Crank-Nicolson method in time [12, 17, 152]. With the following truncated Fourier expansion

$$\psi^\varepsilon(r,\theta,t) = \sum_{l=-L/2}^{l=L/2-1} \hat{\psi}_l(r,t) e^{il\theta}, \qquad 0 \le r \le R, \quad 0 \le \theta \le 2\pi, \tag{2.53}$$

where L is an even positive number and $\hat{\psi}_l$ is the Fourier coefficients for the l-th mode, plugging (2.53) into (2.37) and using the orthogonality of the Fourier functions, we obtain for $l{=}-\frac{L}{2}, \cdots, \frac{L}{2}-1$:

$$(\lambda_\varepsilon + i\beta)\partial_t \hat{\psi}_l(r,t) = \frac{1}{r}\partial_r \left(r \partial_r \hat{\psi}_l(r,t)\right) - \frac{l^2}{r^2}\hat{\psi}_l(r,t), \quad 0 < r < R, \quad t \ge t_n, \tag{2.54}$$

with the following boundary condition at $r = 0$

$$\partial_r \hat{\psi}_0(0,t) = 0, \qquad \hat{\psi}_l(0,t) = 0, \quad l \neq 0, \qquad t \geq t_n. \tag{2.55}$$

When the Dirichlet BC (1.3) is used for (2.37), we then impose the following boundary condition at $r = R$:

$$\hat{\psi}_l(R,t) = \hat{g}_l := \frac{1}{2\pi}\int_0^{2\pi} g(\theta)e^{-il\theta}d\theta, \qquad -\frac{L}{2} \leq l \leq \frac{L}{2} - 1, \quad t \geq t_n. \tag{2.56}$$

Let P^k denote all polynomials with degree at most k, denote $0 = r_0 < r_1 < \cdots < r_N = R$ be a partition for the interval $[0, R]$ with N a positive integer and a mesh size $h = \max_{0\leq j\leq N-1}(r_{j+1} - r_j)$, and define a finite element space by

$$U^h = \left\{u^h \in C[0,R] \mid u^h|_{[r_j,r_{j+1}]} \in P^k, \ 0 \leq j \leq N-1\right\}.$$

Introducing the following finite element approximate sets associated to the Dirichlet BCs for $-\frac{L}{2} \leq l \leq \frac{L}{2} - 1$ as

$$U_l^g = \begin{cases} \left\{u^h \in U^h \mid u^h(R) = \hat{g}_0\right\}, & l = 0, \\ \left\{u^h \in U^h \mid u^h(0) = 0, \ u^h(R) = \hat{g}_l\right\}, & l \neq 0; \end{cases} \tag{2.57}$$

then we obtain the FEM approximation for (2.54) with (2.55) and (2.56):

Find $\hat{\psi}_l^h(\cdot,t) \in U_l^g$ with $-\frac{L}{2} \leq l \leq \frac{L}{2} - 1$ such that

$$\frac{d}{dt}A(\hat{\psi}_l^h, \phi^h) = B(\hat{\psi}_l^h, \phi^h) + l^2 C(\hat{\psi}_l^h, \phi^h), \quad \forall \phi^h \in U_l^0, \quad t_n \leq t \leq t_{n+1}; \tag{2.58}$$

where the bilinear forms A, B and C are defined as

$$A(u^h, v^h) = (\lambda_\varepsilon + i\beta)\int_0^R r u^h v^h dr, \quad B(u^h, v^h) = -\int_0^R r\partial_r u^h \partial_r v^h dr,$$
$$C(u^h, v^h) = -\int_0^R \frac{1}{r} u^h v^h dr, \qquad \forall u^h, \ v^h \in U^h.$$

The above ODE system (2.58) is then discretized by the standard Crank-Nicolson scheme in time. Here although an implicit time discretization is applied for (2.58), the one-dimensional nature of the problem makes the coefficients matrix for the linear system band limited. For example, if the piecewise linear polynomial is used, i.e., $k = 1$ in U^h, the matrix is tridiagonal. Thus for each fixed $-\frac{L}{2} \le l \le \frac{L}{2} - 1$, fast algorithms can be applied to solve the resulting linear systems at the cost of $O(N)$.

Similarly, when the homogeneous Neumann BC (1.4) is used for (2.37), the above discretization is still valid provided that we replace the boundary condition at $r = R$ in (2.56) by

$$\partial_r \hat{\psi}_l(R, t) = 0, \qquad -\frac{L}{2} \le l \le \frac{L}{2} - 1, \quad t \ge t_n, \tag{2.59}$$

the finite element subsets U_l^g in (2.57) and U_l^0 in (2.58) by the following finite element spaces

$$U_l^n = \begin{cases} U^h, & l = 0, \\ \left\{ u^h \in U^h \mid u^h(0) = 0 \right\}, & l \ne 0. \end{cases} \tag{2.60}$$

The detailed discretization is omitted here for brevity.

Remark 2.3.2. *The equation (2.54) with (2.55) can also be discretized in space by either Legendre or Chebyshev pseudospectral method [134] and in time by the Crank-Nicolson method.*

Chapter 3

Vortex dynamics in GLE

Formal analysis indicate that, if initially ψ_0^ε has isolated vortices, these vortices move with velocities of the order of $|\ln\varepsilon|^{-1}$ in the GLE dynamics with $\lambda_\varepsilon = 1$ [26, 96, 99]. Therefore, to obtain nontrivial vortex dynamics, in this chapter, we always assume $0 < \varepsilon < 1$ and choose

$$\lambda_\varepsilon = \frac{1}{|\ln\varepsilon|} = \frac{1}{\ln(1/\varepsilon)}, \qquad 0 < \varepsilon < 1. \tag{3.1}$$

We then apply the numerical method presented in chapter 2 to simulate quantized vortex interaction of GLE, i.e., $\beta = 0, \lambda_\varepsilon = \frac{1}{\ln(1/\varepsilon)}$ in the GLSE (1.1), with different ε and under different initial setups including single vortex, vortex pair, vortex dipole and vortex lattice. We study how the dimensionless parameter ε, initial setup, boundary value and geometry of the domain $\mathcal{D}$ affect the dynamics and interaction of vortices. Moreover, we compare the results obtained from the GLE with those from the corresponding reduced dynamical laws, and identify the cases where the reduced dynamical laws agree qualitatively and/or quantitatively as well as fail to agree with those from GLE on vortex interaction. Finally, we also obtain numerically different patterns of the steady states for quantized vortex lattices and study the alignment of the vortices in the steady state.

3.1 Initial setup

For a given bounded domain $\mathcal{D}$, the GLSE (1.1) is unchanged by the re-scaling $\mathbf{x} \to l\mathbf{x}$, $t \to l^2 t$ and $\varepsilon \to l\varepsilon$ with l the diameter of $\mathcal{D}$. Thus without lose of generality, hereafter, without specification, we always assume that the diameter of $\mathcal{D}$ is $O(1)$. The initial data ψ_0^ε in (1.2) for simulating GLE thus is chosen as (2.6) with $R_0 = 0.25$ in (2.7). To simulate GLE under Dirichlet BC, we choose the function $g(\mathbf{x})$ in (1.3) as

$$g(\mathbf{x}) = e^{i(h(\mathbf{x})+\sum_{j=1}^{M} n_j\theta(\mathbf{x}-\mathbf{x}_j^0))}, \qquad \mathbf{x} \in \partial\mathcal{D}, \tag{3.2}$$

and we consider following six kinds of modes for the phase shift $h(\mathbf{x})$ in (3.2) and (2.6):

- Mode 0: $h(\mathbf{x}) = 0$, Mode 1: $h(\mathbf{x}) = x + y$,
- Mode 2: $h(\mathbf{x}) = x - y$, Mode 3: $h(\mathbf{x}) = x^2 - y^2$,
- Mode 4: $h(\mathbf{x}) = x^2 - y^2 - 2xy$, Mode 5: $h(\mathbf{x}) = x^2 - y^2 - 2xy$.

Moreover, to simulate GLE under homogeneous Neumann BC, we choose the phase shift $h(\mathbf{x})$ to be the solution of the following problem:

$$\begin{cases} \Delta h(\mathbf{x}) = 0, & \mathbf{x} \in \mathcal{D}, \\ \frac{\partial}{\partial \nu} h(\mathbf{x}) = -\frac{\partial}{\partial \nu} \sum_{l=1}^{M} n_l \theta(\mathbf{x} - \mathbf{x}_l), & \mathbf{x} \in \partial\mathcal{D}, \\ \int_{\mathcal{D}} h(\mathbf{x}) d\mathbf{x} = 0. \end{cases} \tag{3.3}$$

Without specification, this initial setup will also be used in chapter 4 in studying vortex interaction in the NLSE dynamics and chapter 5 in the CGLE dynamics. To simplify our presentation, for $j = 1, 2, \ldots, M$, hereafter we let $\mathbf{x}_j^\varepsilon(t)$ and $\mathbf{x}_j^{\mathrm{r}}(t)$ be the j-th vortex center in the GLE dynamics and corresponding reduced dynamics, respectively, and denote $d_j^\varepsilon(t) = |\mathbf{x}_j^\varepsilon(t) - \mathbf{x}_j^{\mathrm{r}}(t)|$ as their difference. Moreover, in the presentation of figures, the initial location of a vortex with winding number $+1$, -1 and the location that two vortices merge are marked as '$+$', '$\circ$' and '$\diamond$', respectively.

Furthermore, if a vortex could finally stay steady in somewhere, we denote its final location as '*'. Finally, in our computations, if not specified, we take $\mathcal{D} = [-1, 1]^2$, mesh sizes $h_x = h_y = \frac{\varepsilon}{10}$ and time step $\tau = 10^{-6}$. The GLE with (1.3), (1.2) and (2.6) is solved by the method TSCNFD presented in section 3.

3.2 Numerical results under Dirichlet BC

3.2.1 Single vortex

Here we present numerical results of the motion of a single quantized vortex under the GLE dynamics and its corresponding reduced dynamical laws. We take $M = 1$, $n_1 = 1$ and consider following cases: case I. $\mathbf{x}_1^0 = (0, 0)$, $h(\mathbf{x}) = x + y$; case II. $\mathbf{x}_1^0 = (0, 0)$, $h(\mathbf{x}) = x - y$; case III. $\mathbf{x}_1^0 = (0, 0)$, $h(\mathbf{x}) = x^2 - y^2$; case IV. $\mathbf{x}_1^0 = (0.1, 0.2)$, $h(\mathbf{x}) = x + y$; case V. $\mathbf{x}_1^0 = (0.1, 0.2)$, $h(\mathbf{x}) = x - y$; and case VI. $\mathbf{x}_1^0 = (0.1, 0.2)$, $h(\mathbf{x}) = x^2 - y^2$. Fig. 3.1 depicts trajectory of the vortex center when $\varepsilon = \frac{1}{32}$ for the above 6 cases and d_1^ε with different ε for case II, IV and VI. From Fig. 3.1 and additional numerical experiments not shown here for brevity, we can draw following conclusions: (i). When $h(\mathbf{x}) \equiv 0$, the vortex center doesn't move and this is similar to the case in the whole space. (ii). When $h(\mathbf{x}) = (x+by)(x-\frac{y}{b})$ with $b \neq 0$, the vortex does not move if $\mathbf{x}_0 = (0, 0)$, while it does move if $\mathbf{x}_0 \neq (0, 0)$ (cf. case III and VI for $b = 1$). (iii). When $h(\mathbf{x}) \neq 0$ and $h(\mathbf{x}) \neq (x + by)(x - \frac{y}{b})$ with $b \neq 0$, in general, the vortex center does move to a different point from its initial location and stays there forever. This is quite different from the situation in the whole space, where a single vortex may move to infinity under the initial data (2.6) with $h(\mathbf{x}) \neq 0$ and $\mathcal{D} = \mathbb{R}^2$. (iv). In general, the initial location, the geometry of the domain and the boundary value will all affect the motion of the vortex center. (v). When $\varepsilon \to 0$, the dynamics of the vortex center in the GLE dynamics converges uniformly in time to that in the reduced dynamics (cf. Fig. 3.1) which verifies numerically the validation of the reduced dynamical laws. In fact, based on our extensive numerical experiments, the motion of the vortex center from the reduced dynamical laws agree

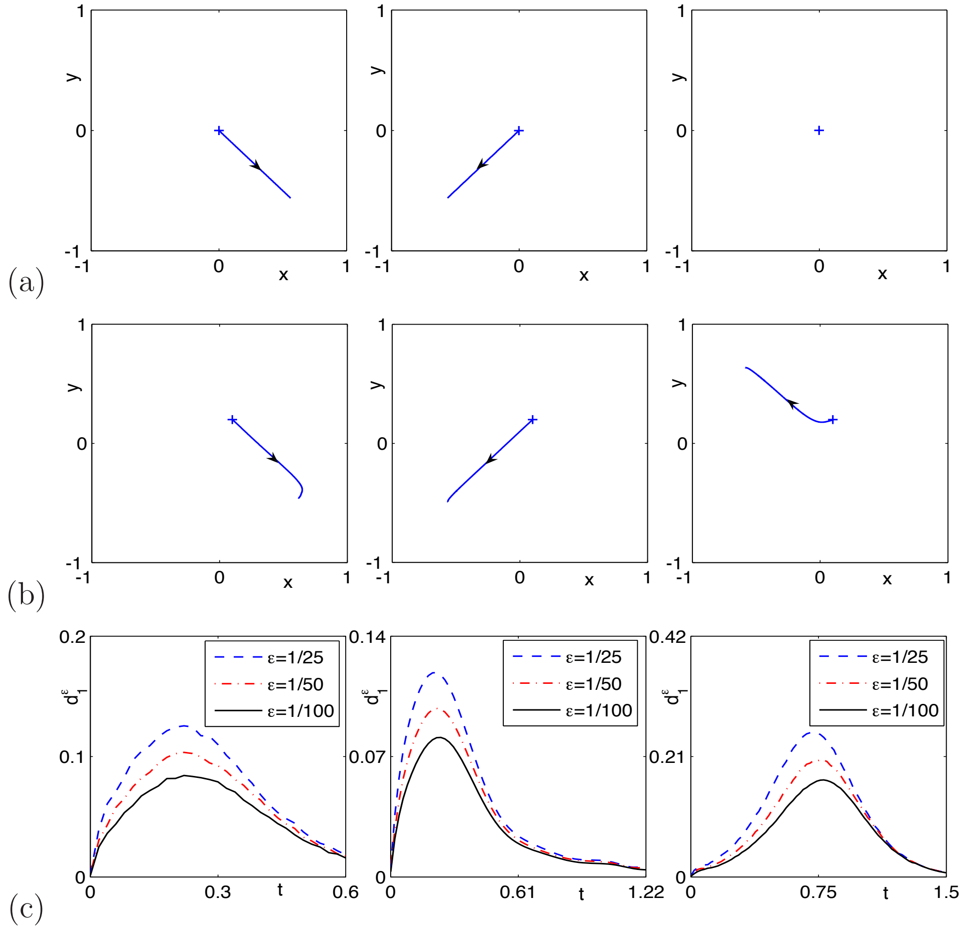

Figure 3.1: (a)-(b): Trajectory of the vortex center in GLE under Dirichlet BC when $\varepsilon = \frac{1}{32}$ for cases I-VI (from left to right and then from top to bottom), and (c): d_1^ε for different ε for cases II, IV and VI (from left to right) in section 3.2.1.

with those from the GLE dynamics qualitatively when $0 < \varepsilon < 1$ and quantitatively when $0 < \varepsilon \ll 1$.

3.2.2 Vortex pair

Here we present numerical results of the interaction of vortex pair under the GLE dynamics and its corresponding reduced dynamical laws, i.e., we take $M = 2$, $n_1 = n_2 = 1$, $\mathbf{x}_1^0 = (-0.5, 0)$ and $\mathbf{x}_2^0 = (0.5, 0)$ in (2.6). Fig. 3.2 depicts time evolution of the amplitude $|\psi^\varepsilon|$, while Fig. 3.3 shows that of the GL functionals as well as the trajectory of the vortex centers when $\varepsilon = \frac{1}{32}$ in with different $h(\mathbf{x})$ in (2.6). Fig. 3.4 shows time evolution of $\mathbf{x}_1^r(t)$, $\mathbf{x}_1^\varepsilon(t)$ and $d_1^\varepsilon(t)$ with different $h(\mathbf{x})$ in (2.6).

From Figs. 3.2, 3.3 & 3.4 and additional numerical results not shown here for brevity, we can draw the following conclusions for the interaction of vortex pair under the GLE dynamics with Dirichlet BC: (i). The two vortices undergo a repulsive interaction, they never collide, both of them move towards the boundary of $\mathcal{D}$ for a while and finally stop somewhere near the boundary which indicate that the boundary imposes a repulsive force on the vortices when t is large enough (cf. Figs. 3.2 & 3.3). (ii). When $h(\mathbf{x}) \equiv 0$, the two vortex centers move outward along the line connecting them initially, and their trajectories are symmetric, i.e., $\mathbf{x}_1^\varepsilon(t) = -\mathbf{x}_2^\varepsilon(t)$, while when $h(\mathbf{x}) \neq 0$, it affects the motion of the two vortex centers significantly (cf. Fig. 3.3). (iii). When $\varepsilon \to 0$, the dynamics of the two vortex centers in the GLE dynamics converges uniformly in time to that in the reduced dynamics (cf. Fig. 3.4) which verifies numerically the validation of the reduced dynamical laws in this case. In fact, based on our extensive numerical experiments, the motions of the two vortex centers from the reduced dynamical laws agree with those from the GLE dynamics qualitatively when $0 < \varepsilon < 1$ and quantitatively when $0 < \varepsilon \ll 1$. (iv). During the dynamics of GLE, the GL functional and its kinetic part decrease when time increases, its interaction part changes dramatically when t is small, and when $t \to \infty$, all the three quantities converge to constants (cf. Fig. 3.3), which immediately imply that a steady state solution will be reached when $t \to \infty$.

3.2.3 Vortex dipole

Here we present numerical results of the interaction of vortex dipole under the GLE dynamics and its corresponding reduced dynamical laws, i.e., we take $M = 2$, $n_1 = -1$, $n_2 = 1$, $\mathbf{x}_1^0 = (-d_0, 0)$ and $\mathbf{x}_2^0 = (d_0, 0)$ in (2.6). Fig. 3.5 depicts time evolution of the amplitude $|\psi^\varepsilon|$, while Fig. 3.6 shows that of the GL functionals as well as the trajectory of the vortex centers when $\varepsilon = \frac{1}{32}$ in GLE with different d_0

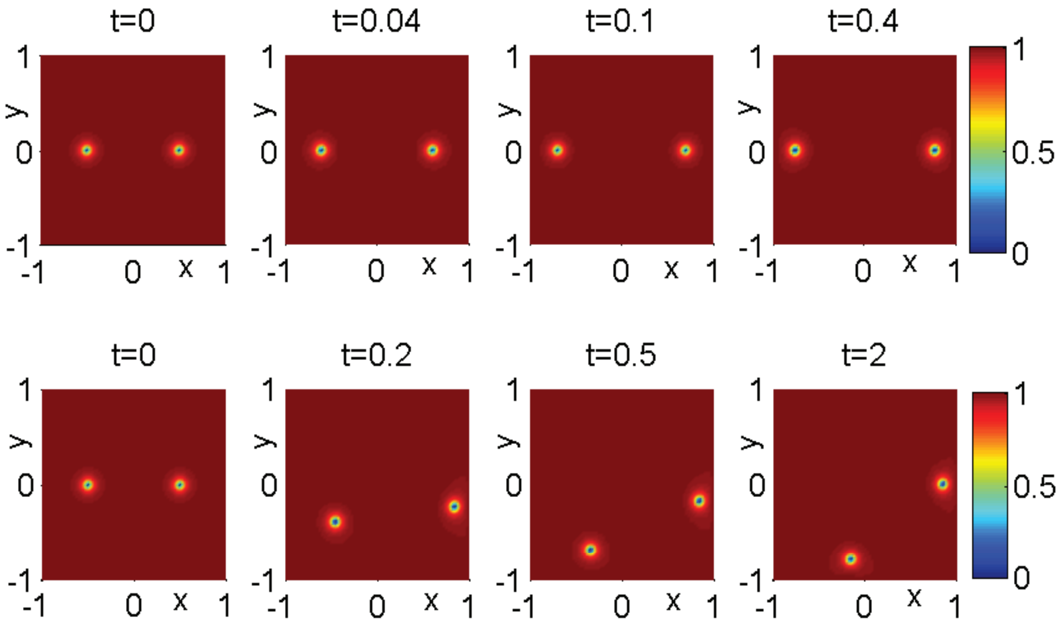

(a)

(b)

Figure 3.2: Contour plots of $|\psi^\varepsilon(\mathbf{x},t)|$ at different times for the interaction of vortex pair in GLE under Dirichlet BC with $\varepsilon = \frac{1}{32}$ and different $h(\mathbf{x})$ in (2.6): (a) $h(\mathbf{x}) = 0$, (b) $h(\mathbf{x}) = x + y$.

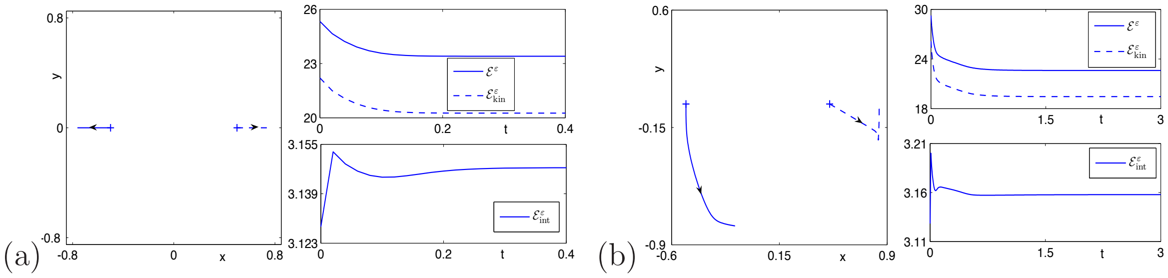

(a) (b)

Figure 3.3: Trajectory of vortex centers (left) and time evolution of the GL functionals (right) for the interaction of vortex pair in GLE under Dirichlet BC with $\varepsilon = \frac{1}{32}$ for different $h(\mathbf{x})$ in (2.6): (a) $h(\mathbf{x}) = 0$, (b) $h(\mathbf{x}) = x + y$.

and $h(\mathbf{x})$ in (2.6) as well as the critical value d_c^ε for different ε when $h(\mathbf{x}) \equiv x + y$. Fig. 3.7 shows time evolution of $\mathbf{x}_1^r(t)$, $\mathbf{x}_1^\varepsilon(t)$ and $d_1^\varepsilon(t)$ with $d_0 = 0.5$ for different ε and $h(\mathbf{x})$ in (2.6).

From Figs. 3.5, 3.6 & 3.7 and additional numerical results not shown here for

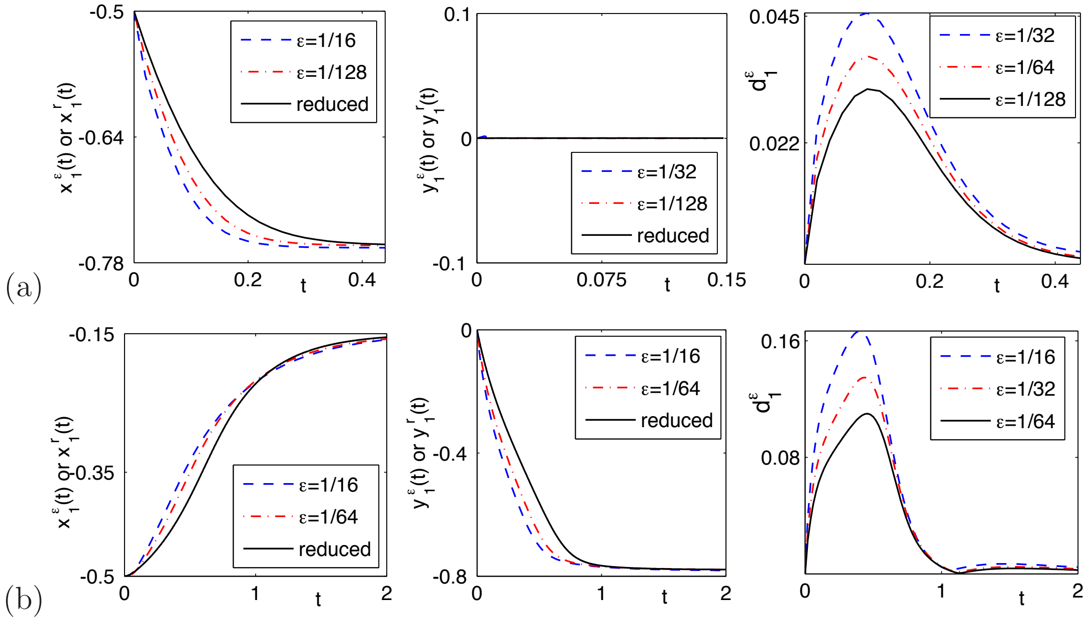

Figure 3.4: Time evolution of $\mathbf{x}_1^\varepsilon(t)$ and $\mathbf{x}_1^r(t)$ (left and middle) and their difference d_1^ε (right) for different ε for the interaction of vortex pair in GLE under Dirichlet BC for different $h(\mathbf{x})$ in (2.6): (a) $h(\mathbf{x}) = 0$, (b) $h(\mathbf{x}) = x + y$.

brevity, we can draw the following conclusions for the interaction of vortex dipole under the GLE dynamics with Dirichlet BC: (i). Both boundary value, i.e., $h(\mathbf{x})$, and distance between the two vortex centers initially, i.e., $2d_0$, affect the motion of the vortices significantly. (ii). When $h(\mathbf{x}) \equiv 0$, for any initial location of the vortex dipole, the two vortices always undergo an attractive interaction and their centers move toward each other along the line connecting them initially, their trajectory are symmetric with respect to the line perpendicular to the segment connecting them initially, and finally, they merge at the middle point of this segment, i.e., the point $\mathbf{x}_{\text{merge}} = \frac{1}{2}(\mathbf{x}_1^0 + \mathbf{x}_2^0)$ (cf. Figs. 3.5 & 3.6). At the collision, both vortices in the vortex dipole merge/annihilate with each other; and after the collision, they will disappear and no vortex is left afterwards during the dynamics. For any fixed $0 < \varepsilon < 1$, there is a collision time T_ε which increases when ε decreases. (iii). When $h(\mathbf{x}) = x + y$, the two vortices move along a symmetric trajectory, i.e., $\mathbf{x}_1^\varepsilon(t) = -\mathbf{x}_2^\varepsilon(t)$. Moreover, for the reduced dynamical laws, there exists a critical value d_c^r, which is found

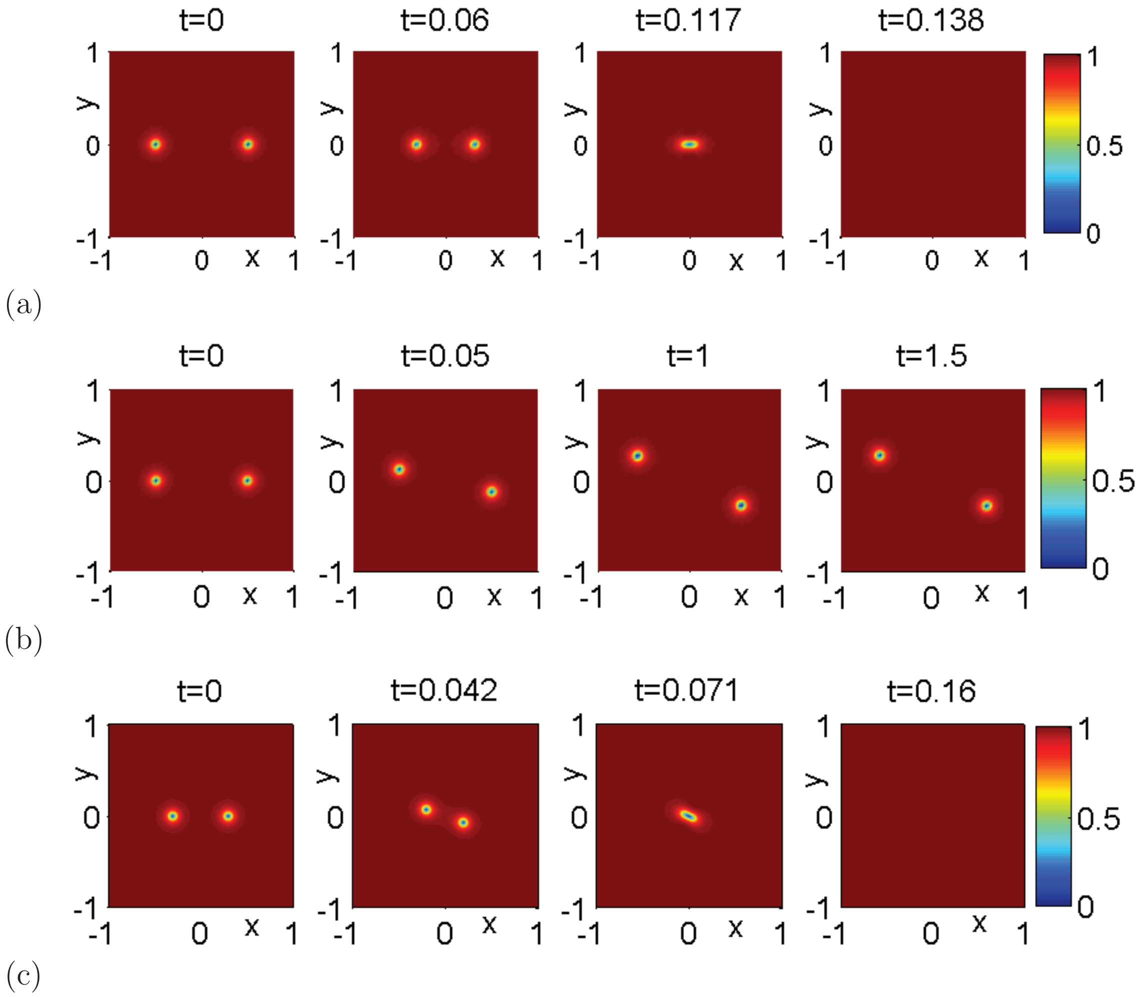

Figure 3.5: Contour plots of $|\psi^\varepsilon(\mathbf{x},t)|$ at different times for the interaction of vortex dipole in GLE under Dirichlet BC with $\varepsilon = \frac{1}{32}$ for different d_0 and $h(\mathbf{x})$ in (2.6): (a) $h(\mathbf{x}) = 0$, $d_0 = 0.5$, (b) $h(\mathbf{x}) = x + y$, $d_0 = 0.5$, (c) $h(\mathbf{x}) = x + y$, $d_0 = 0.3$.

numerically as $d_c^r \approx 0.4142$, such that when $d_0 < d_c^r$, then the vortex dipole will merge at finite time, and respectively, when $d_0 > d_c^r$, the vortex dipole will never collide. Similarly, for the vortex dipole under the GLE dynamics, for each fixed $0 < \varepsilon < 1$, there exists a critical value d_c^ε such that when $d_0 < d_c^\varepsilon$, then the vortex dipole will merge at finite time, and respectively, when $d_0 > d_c^\varepsilon$, the vortex dipole will never collide (cf. Figs. 3.5 & 3.6). We find numerically the critical distance d_c^ε for $0 < \varepsilon < 1$ and depict them in Fig. 3.8. From these values, we can fit the

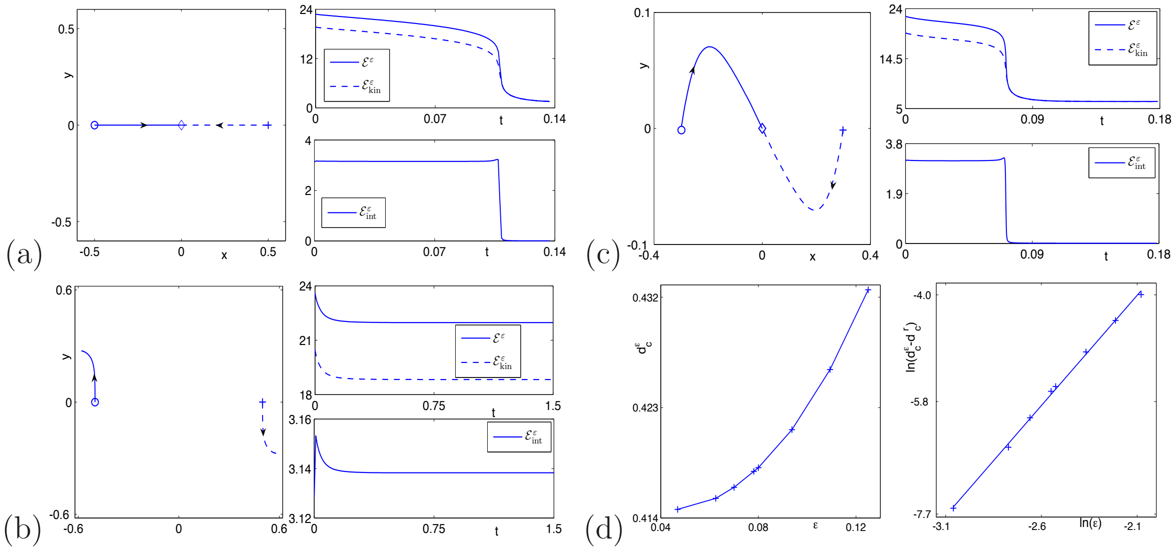

Figure 3.6: (a)-(c): Trajectory of vortex centers (left) and time evolution of the GL functionals (right) for the interaction of vortex dipole in GLE under Dirichlet BC with $\varepsilon = \frac{1}{32}$ for different d_0 and $h(\mathbf{x})$ in (2.6): (a) $h(\mathbf{x}) = 0$, $d_0 = 0.5$, (b) $h(\mathbf{x}) = x + y$, $d_0 = 0.5$, (c) $h(\mathbf{x}) = x + y$, $d_0 = 0.3$. (d): Critical value d^ε_c for different ε when $h(\mathbf{x}) \equiv x + y$.

following relationship between d^ε_c and d^r_c:

$$d^\varepsilon_c \approx d^r_c + 41.26\varepsilon^{3.8}, \qquad 0 \le \varepsilon < 1.$$

(iv). When $\varepsilon \to 0$, the dynamics of the two vortex centers under the GLE dynamics converges uniformly in time to that of the reduced dynamical laws before the collision happens (cf. Fig. 3.7) which verifies numerically the validation of the reduced dynamical laws in this case. In fact, based on our extensive numerical experiments, the motion of the two vortex centers from the reduced dynamical laws agree with those from the GLE dynamics qualitatively when $0 < \varepsilon < 1$ and quantitatively when $0 < \varepsilon \ll 1$ if the initial distance between the two vortex centers satisfies either $0 < d_0 < d^r_c$ or $d_0 > d^\varepsilon_c$. On the contrary, if $d^r_c < d_0 < d^\varepsilon_c$, then the motion of the vortex dipole from the reduced dynamical laws is different qualitatively from that of the GLE dynamics. (v). During the dynamics of GLE, the GL functional decreases when time increases, its kinetic and interaction parts change dramatically

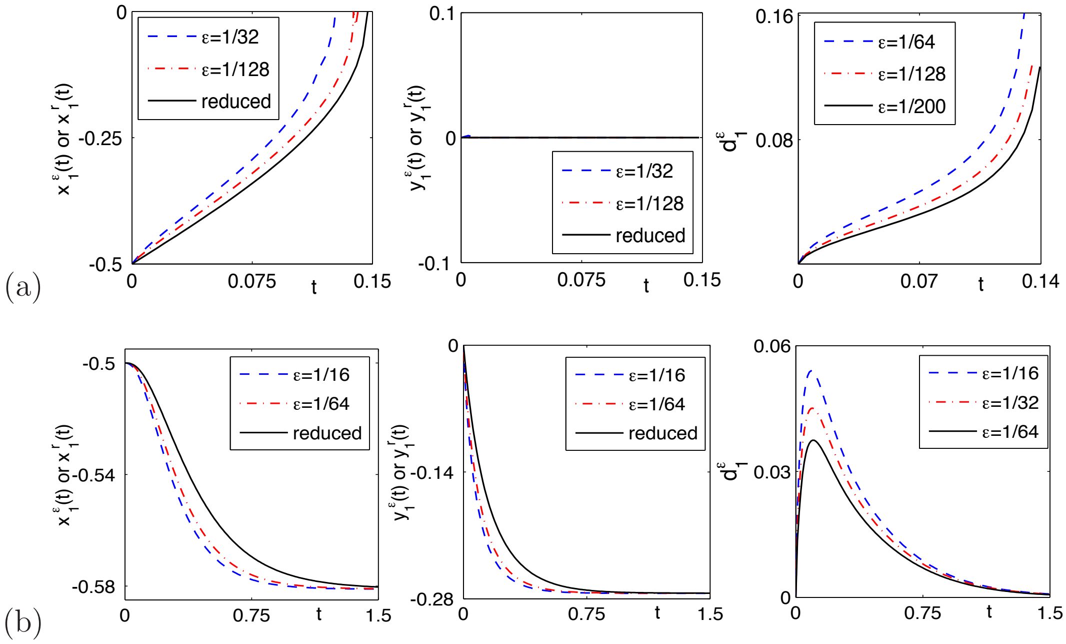

Figure 3.7: Time evolution of $\mathbf{x}_1^\varepsilon(t)$, $\mathbf{x}_1^r(t)$ (left and middle) and their difference d_1^ε (right) for different ε for the interaction of vortex dipole in GLE under Dirichlet BC with $d_0 = 0.5$ for different $h(\mathbf{x})$ in (2.6): (a) $h(\mathbf{x}) = 0$, (b) $h(\mathbf{x}) = x + y$.

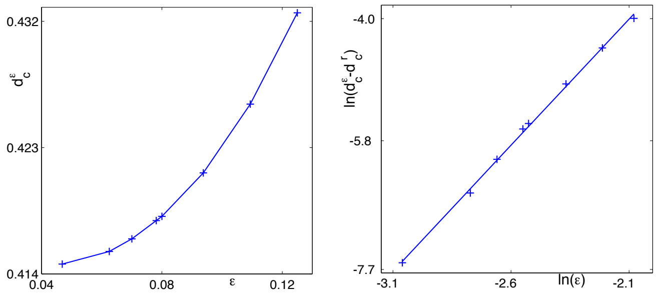

Figure 3.8: Critical value d_c^ε for the interaction of vortex dipole of the GLE under Dirichlet BC with $h(\mathbf{x}) \equiv x + y$ in (2.6) for different ε.

when t is small, and when $t \to \infty$, all the three quantities converge to constants (cf. Fig. 3.6). Moreover, if finite time merging/annihilation happens, the GL functional and its kinetic and interaction parts change significantly during the collision. In addition, when $t \to \infty$, the interaction energy goes to 0 which immediately implies that a steady state will be reached in the form of $\phi^\varepsilon(\mathbf{x}) = e^{ic(\mathbf{x})}$, where $c(\mathbf{x})$ is a harmonic function satisfying $c(\mathbf{x})|_{\partial\mathcal{D}} = h(\mathbf{x}) + \sum_{j=1}^{M} n_j\theta(\mathbf{x}-\mathbf{x}_j^0)$.

3.2.4 Vortex lattices

Here we present numerical results of the interaction of vortex lattices under the GLE dynamics. We will consider the following cases: case I. $M = 3$, $n_1 = n_2 = n_3 = 1$, $\mathbf{x}_1^0 = (-0.25, \frac{\sqrt{3}}{4})$, $\mathbf{x}_2^0 = (-0.25, -\frac{\sqrt{3}}{4})$, $\mathbf{x}_3^0 = (0.5, 0)$; case II. $M = 3$, $n_1 = n_2 = n_3 = 1$, $\mathbf{x}_1^0 = (-0.4, 0)$, $\mathbf{x}_2^0 = (0, 0)$, $\mathbf{x}_3^0 = (0.4, 0)$; case III. $M = 3$, $n_1 = n_2 = n_3 = 1$, $\mathbf{x}_1^0 = (0, 0.3)$, $\mathbf{x}_2^0 = (0.15, 0.15)$, $\mathbf{x}_3^0 = (0.3, 0)$; case IV. $M = 3$, $n_1 = -1$, $n_2 = n_3 = 1$, $\mathbf{x}_1^0 = (-0.25, \frac{\sqrt{3}}{4})$, $\mathbf{x}_2^0 = (-0.25, -\frac{\sqrt{3}}{4})$, $\mathbf{x}_3^0 = (0.5, 0)$; case V. $M = 3$, $n_2 = -1$, $n_1 = n_3 = 1$, $\mathbf{x}_1^0 = (-0.4, 0)$, $\mathbf{x}_2^0 = (0, 0)$, $\mathbf{x}_3^0 = (0.4, 0)$; case VI. $M = 3$, $n_1 = -1$, $n_2 = n_3 = 1$, $\mathbf{x}_1^0 = (0.2, 0.3)$, $\mathbf{x}_2^0 = (-0.3, 0.4)$, $\mathbf{x}_3^0 = (-0.4, -0.2)$; case VII. $M = 4$, $n_1 = n_2 = n_3 = n_4 = 1$, $\mathbf{x}_1^0 = (0, 0.5)$, $\mathbf{x}_2^0 = (-0.5, 0)$, $\mathbf{x}_3^0 = (0, -0.5)$, $\mathbf{x}_4^0 = (0.5, 0)$; case VIII. $M = 4$, $n_1 = n_3 = -1$, $n_2 = n_4 = 1$, $\mathbf{x}_1^0 = (0, 0.5)$, $\mathbf{x}_2^0 = (-0.5, 0)$, $\mathbf{x}_3^0 = (0, -0.5)$, $\mathbf{x}_4^0 = (0.5, 0)$; and case IX. $M = 4$, $n_1 = n_2 = -1$, $n_3 = n_4 = 1$, $\mathbf{x}_1^0 = (0, 0.5)$, $\mathbf{x}_2^0 = (-0.5, 0)$, $\mathbf{x}_3^0 = (0, -0.5)$, $\mathbf{x}_4^0 = (0.5, 0)$. Fig. 3.9 shows trajectory of the vortex centers when $\varepsilon = \frac{1}{32}$ in and $h(\mathbf{x}) = 0$ in (2.6) for the above 9 cases. From Fig. 3.9 and additional numerical experiments not shown here for brevity, we can draw the following conclusions: (i). The interaction of vortex lattices under the GLE dynamics with Dirichlet BC is very interesting and complicated. The detailed dynamics and interaction pattern of a lattice depends on its initial alignment of the lattice, geometry of the domain $\mathcal{D}$ and the boundary value $g(\mathbf{x})$. (ii). For a lattice of M vortices, if they have the same index, then no collision will happen for any time $t \geq 0$. On the other hand, if they have opposite index, e.g. $M^+ > 0$ vortices with index '+1' and $M^- > 0$ vortices with index '−1' satisfying $M^+ + M^- = M$, collision will always happen at finite time. In addition, when t is sufficiently large, there exist exactly $|M^+ - M^-|$ vortices of winding number '+1' if $M^+ > M^-$, and resp. '−1' if $M^+ < M^-$, left in the domain.

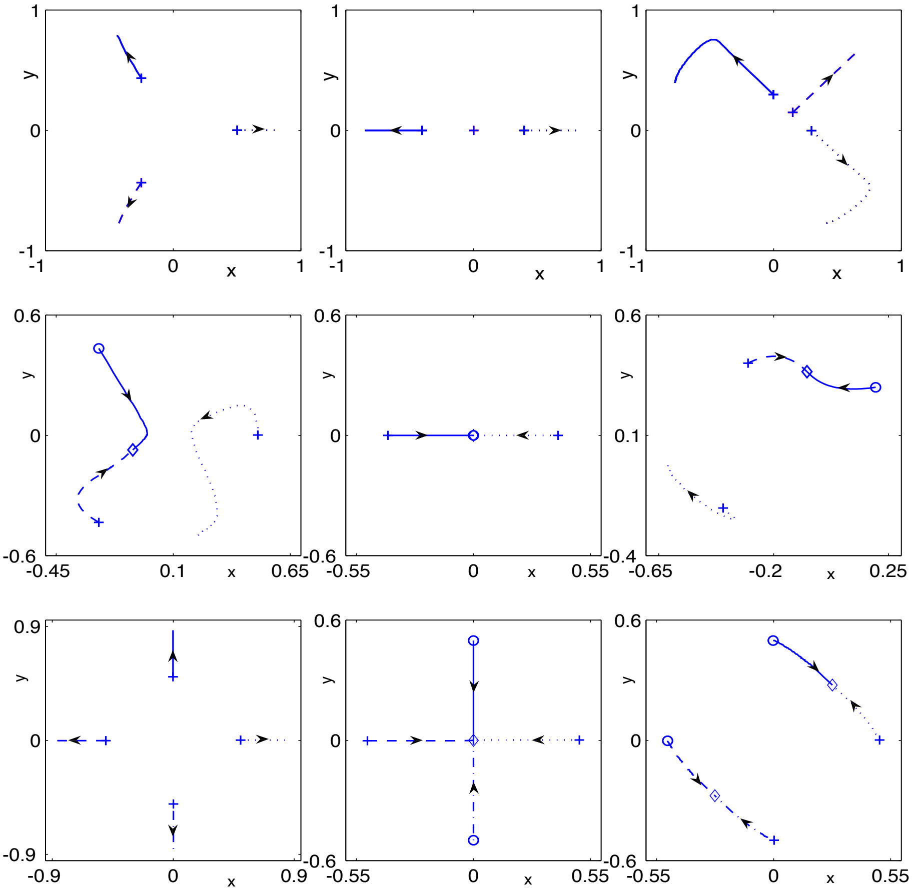

Figure 3.9: Trajectory of vortex centers for the interaction of different vortex lattices in GLE under Dirichlet BC with $\varepsilon = \frac{1}{32}$ and $h(\mathbf{x}) = 0$ for cases I-IX (from left to right and then from top to bottom) in section 3.2.4.

3.2.5 Steady state patterns of vortex lattices

Here we present the steady state patterns of vortex lattices in the GLE dynamics under Dirichlet BC. We study how the geometry of the domain $\mathcal{D}$ and boundary condition affect the alignment of vortices in the steady states. To this end, we take $\varepsilon = \frac{1}{16}$ in,

$$n_j = 1, \qquad \mathbf{x}_j^0 = 0.5\left(\cos\left(\frac{2j\pi}{M}\right), \sin\left(\frac{2j\pi}{M}\right)\right), \qquad j = 1, 2, \ldots, M,$$

i.e., initially we have M like vortices which are located uniformly in a circle centered at origin with radius $R_1 = 0.5$.

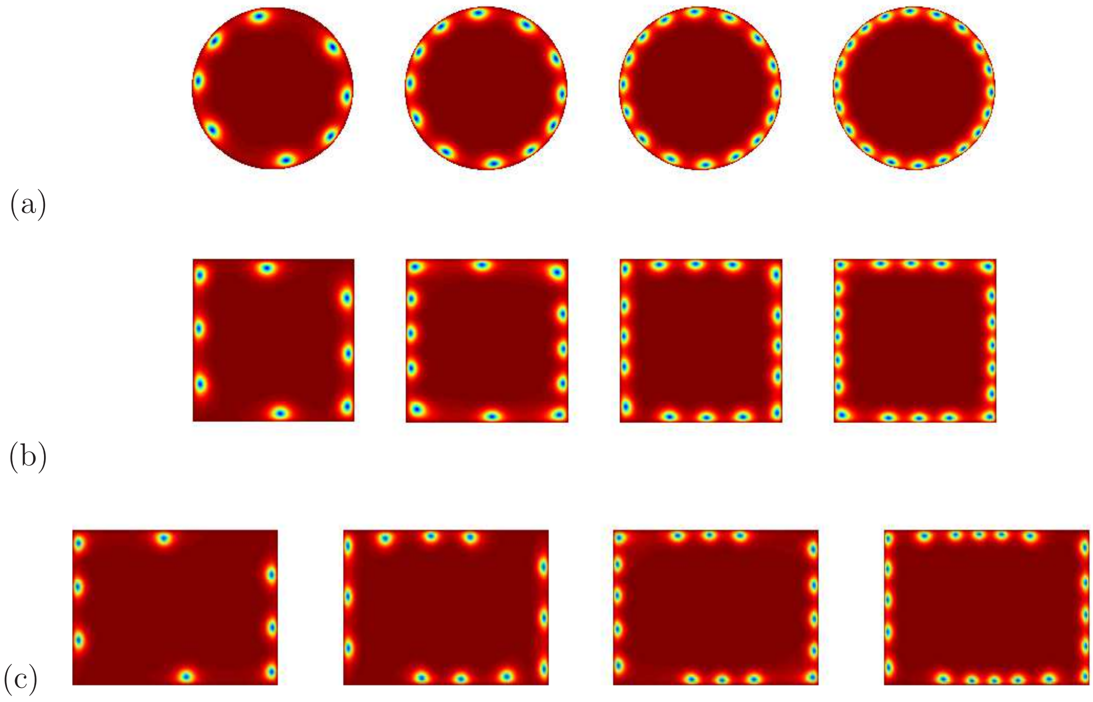

Figure 3.10: Contour plots of $|\phi^\varepsilon(\mathbf{x})|$ for the steady states of vortex lattice in GLE under Dirichlet BC with $\varepsilon = \frac{1}{16}$ for $M = 8,\ 12,\ 16,\ 20$ (from left column to right column) and different domains: (a) unit disk $\mathcal{D} = B_1(\mathbf{0})$, (b) square domain $\mathcal{D} = [-1, 1]^2$, (c) rectangular domain $\mathcal{D} = [-1.6, 1.6] \times [-1, 1]$.

Denote $\phi^\varepsilon(\mathbf{x})$ as the steady state, i.e., $\phi^\varepsilon(\mathbf{x}) = \lim_{t\to\infty} \psi^\varepsilon(\mathbf{x}, t)$ for $\mathbf{x} \in \mathcal{D}$. Fig. 3.10 depicts the contour plots of the amplitude $|\phi^\varepsilon|$ of the steady state in the GLE dynamics with $h(\mathbf{x}) = x^2 - y^2 + 2xy$ in (2.6) for different M and domains, while Fig. 3.11 depicts similar results on a rectangular domain $\mathcal{D} = [-1.6, 1.6] \times [-1, 1]$ for different M and $h(\mathbf{x})$ in (2.6). In addition, Fig. 3.11 shows similar results with $M = 8$ for different $h(\mathbf{x})$ and domain $\mathcal{D}$.

From Figs. 3.10, 3.11 & 3.12 and additional numerical results not shown here for brevity, we can draw the following conclusions for the steady state patterns of vortex lattices under the GLE dynamics with Dirichlet BC: (i). The vortex undergo repulsive interaction between each other and they move to locations near the boundary of $\mathcal{D}$, there is no collision and a steady state pattern is formed when

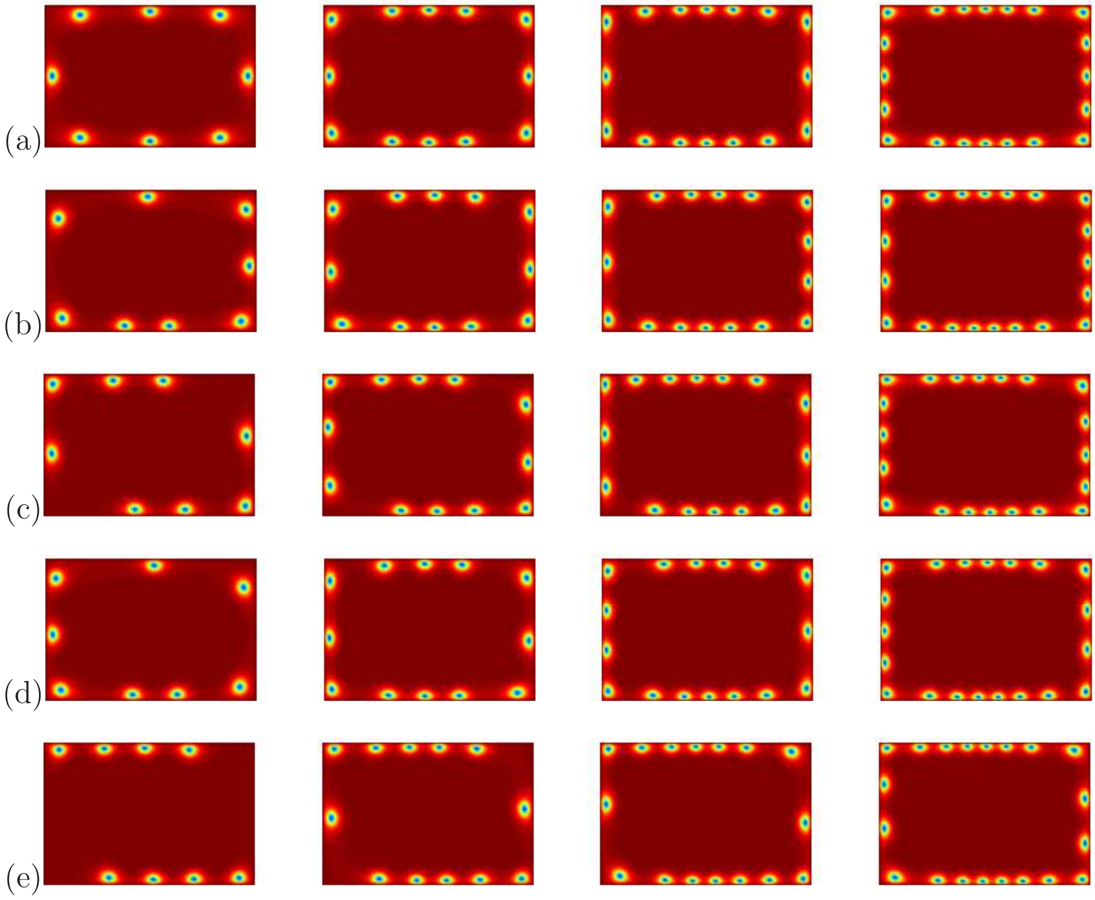

Figure 3.11: Contour plots of $|\phi^\varepsilon(\mathbf{x})|$ for the steady states of vortex lattice in GLE under Dirichlet BC with $\varepsilon = \frac{1}{16}$ on a rectangular domain $\mathcal{D} = [-1.6, 1.6] \times [-1, 1]$ for $M = 8,\ 12,\ 16,\ 20$ (from left column to right column) and different $h(\mathbf{x})$: (a) $h(\mathbf{x}) = 0$, (b) $h(\mathbf{x}) = x + y$, (c) $h(\mathbf{x}) = x^2 - y^2$, (d) $h(\mathbf{x}) = x - y$, (e) $h(\mathbf{x}) = x^2 - y^2 - 2xy$.

$t \to \infty$. In fact, the steady state is also the solution of the following minimization problem

$$\phi^\varepsilon = \text{argmin}_{\phi(\mathbf{x})|_{\mathbf{x}\in\partial\mathcal{D}} = \psi_0^\varepsilon(\mathbf{x})|_{\mathbf{x}\in\partial\mathcal{D}}} \mathcal{E}^\varepsilon(\phi).$$

Actually, based on our extensive numerical experiments, we found that for a vortex lattice of any configuration, i.e., vortices in the vortex lattice may be opposite winding number, the vortices either merge and annihilate and all the leftover vortices are

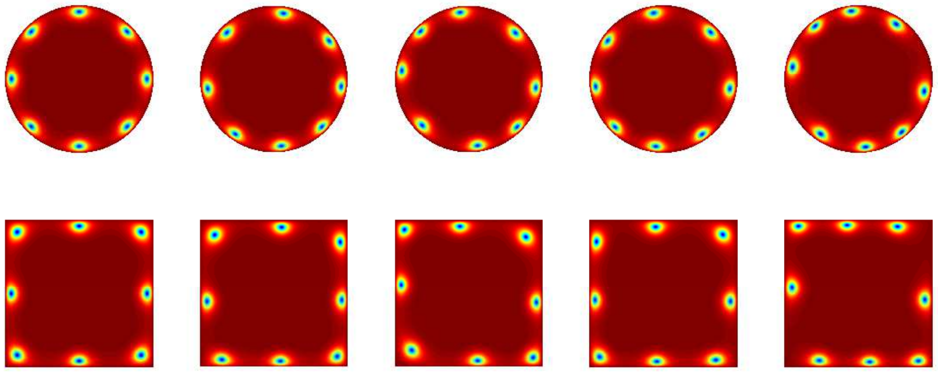

Figure 3.12: Contour plots of $|\phi^\varepsilon(\mathbf{x})|$ for the steady states of vortex lattice in GLE under Dirichlet BC with $\varepsilon = \frac{1}{16}$ and $M = 8$ on a unit disk $\mathcal{D} = B_1(\mathbf{0})$ (top row) or a square $\mathcal{D} = [-1, 1]^2$ (bottom row) under different $h(\mathbf{x}) = 0,\ x + y,\ x^2 - y^2,\ x - y,\ x^2 - y^2 - 2xy$ (from left column to right column).

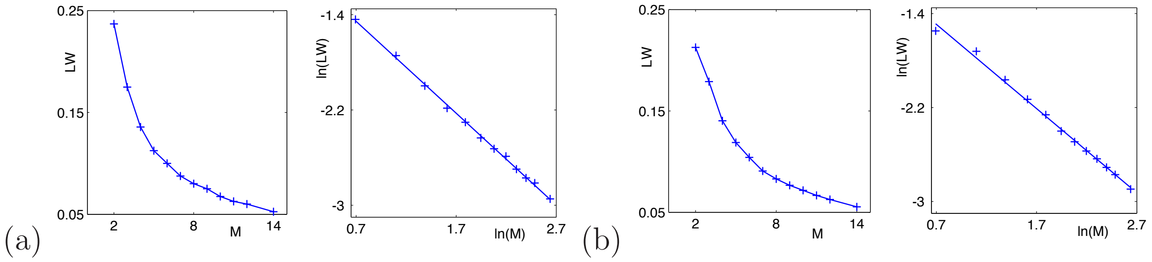

Figure 3.13: Width of the boundary layer LW vs M (the number of vortices) under Dirichlet BC on a square $\mathcal{D} = [-1, 1]^2$ when $\varepsilon = \frac{1}{16}$ for different $h(\mathbf{x})$: (a) $h(\mathbf{x}) = 0$, (b) $h(\mathbf{x}) = x + y$.

all pinned in near the boundary finally. This phenomena is similar with the one in the superconductor involving magnetic field [101].

(ii). During the dynamics, the GL functional decreases when time increases. (iii). Both the geometry of the domain and the boundary condition, i.e., $h(\mathbf{x})$, affect the final steady states significantly. The configuration of a vortex lattice at the steady state follows the symmetry of $\mathcal{D}$ and $h(\mathbf{x})$. For example, in the disk domain, when $h(\mathbf{x}) = x^2 - y^2 + 2xy$, the vortex lattice is symmetric with respect to the two lines $y = (1-\sqrt{2})x$ and $y = (1+\sqrt{2})x$ which satisfy $h(\mathbf{x}) = 0$ (cf. Fig. 3.10). (iv). At the steady state, the distance between the vortex centers and $\partial\mathcal{D}$ depends on ε and M. For fixed M, when ε decreases, the distance decreases; and respectively, for fixed ε, when M increases, the distance decreases. In order to characterize this distance, we denote

$$LW := LW(M,\varepsilon) = \lim_{t\to\infty} \min_{1\le j\le M} \operatorname{dist}(\mathbf{x}_j^\varepsilon(t), \partial\mathcal{D}), \qquad M \ge 2.$$

For a square domain $\mathcal{D} = [-1,1]^2$, we find these distances numerically and depict $LW(M,\varepsilon)$ with $\varepsilon = \frac{1}{16}$ for different M in Fig. 3.13. From these results, we can fit the following relations between $LW(M, \varepsilon = 1/16)$ as a function of M as

$$\text{LW} \approx 0.4M^{-0.7713}, \qquad M \gg 1,$$

for $h(\mathbf{x}) \equiv 0$, and respectively,

$$\text{LW} \approx 0.3714M^{-0.7164}, \qquad M \gg 1,$$

for $h(\mathbf{x}) = x + y$. For other cases, we can also fit out similar results, we omit here for brevity.

3.2.6 Validity of RDL under small perturbation

It is well known that in the NLSE dynamics highly co-rotating vortex will radiate out sound waves, which will in turn modify their motion. In other words, the reduced dynamical law which does not take the radiation into account will become invalid after the sound wave coming up, or equivalent to say, a small perturbation comes up in the field. To understand if there were same bad situations in the GLE dynamics, i.e., if the RDL in the GLE dynamics is valid under small perturbation or not, we take the initial data (1.2) as

$$\psi^\varepsilon(\mathbf{x},0) = \psi_0^{\delta,\varepsilon}(\mathbf{x}) = \psi_0^\varepsilon(\mathbf{x}) + \delta e^{-20((|x|-0.48)^2+y^2)}, \qquad \mathbf{x} = (x,y) \in \mathcal{D}, \qquad (3.4)$$

where ψ_0^ε is given in (2.6) with $h(\mathbf{x}) \equiv 0$, $M = 2$, $n_1 = n_2 = 1$ and $\mathbf{x}_1^0 = -\mathbf{x}_2^0 = (0.5, 0)$, i.e., we perturb the initial data for studying the interaction of a vortex pair

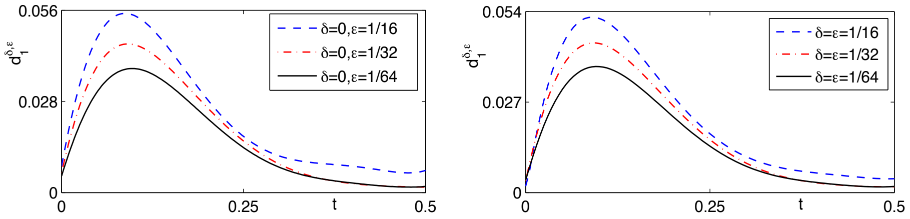

Figure 3.14: Time evolution of $d_1^{\delta,\varepsilon}(t)$ for non-perturbed initial data (left) and perturbed initial data (right) in section 3.2.6

by a Gaussian function with amplitude δ. Then we take $\delta = \varepsilon$ and let ε go to 0, and solve the GLE with initial condition (3.4) for the vortex centers $\mathbf{x}_1^{\delta,\varepsilon}(t)$ and $\mathbf{x}_2^{\delta,\varepsilon}(t)$ and compare them with those from the reduced dynamical law. We denote $d_j^{\delta,\varepsilon}(t) = |x_j^{\delta,\varepsilon}(t) - x_j^r(t)|$ for $j = 1, 2$ as the error. Fig. 3.14 depicts time evolution of $d_1^{\delta,\varepsilon}(t)$ for the case when $\delta = \varepsilon$, i.e., small perturbation, and the case when $\delta = 0$, i.e., no perturbation. From this figure, we can see that small perturbation in the initial data does not affect the motion of the vortices much, same as that with non-perturbed initial setups, the dynamics of the two vortex centers under the GLE dynamics with perturbed initial setups converge to those obtained from the reduced dynamical law when $\varepsilon \to 0$ as well. Actually, from our extensive numerical examples, we see that any kind of small perturbations that we consider in the initial setup does not affect the motion of the vortex dynamics much, the RDL always hold valid.

3.3 Numerical results under Neumann BC

3.3.1 Single vortex

Here we present numerical results of the motion of a single quantized vortex under the GLE dynamics and its corresponding reduced dynamical laws, i.e., we take $M = 1$ and $n_1 = 1$ in (2.6). Fig. 3.15 depicts trajectory of the vortex center for different $\mathbf{x}_1^0$ in (2.6) when $\varepsilon = \frac{1}{32}$ in and d_1^ε for different ε. From Fig. 3.15 and

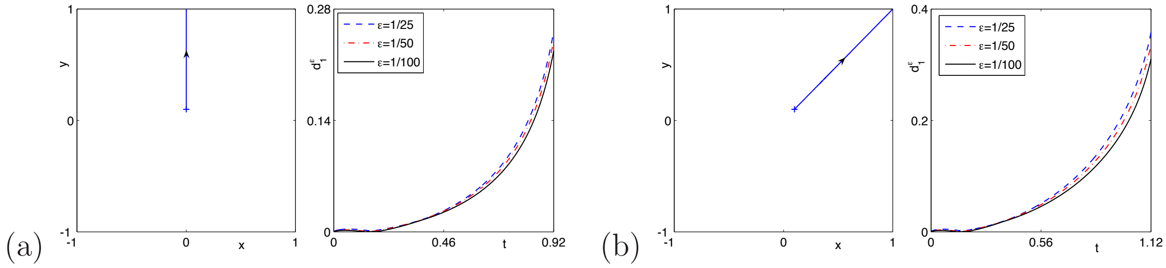

Figure 3.15: Trajectory of the vortex center when $\varepsilon = \frac{1}{32}$ (left column) and d_1^ε for different ε (right column) for the motion of a single vortex in GLE under homogeneous Neumann BC with different $\mathbf{x}_1^0$ in (2.6): (a) $\mathbf{x}_1^0 = (0, 0.1)$, (b) $\mathbf{x}_1^0 = (0.1, 0.1)$.

additional numerical results not shown here for brevity, we can see that: (i). The initial location of the vortex, i.e., value of $\mathbf{x}_0$ affects the motion of the vortex a lot and this shows the effect on the vortex from the Neumann BC. (ii). If $\mathbf{x}_1^0 = (x_0, y_0) \neq (0, 0)$ satisfies $x_0 = 0$ or $y_0 = 0$ or $x_0 = \pm y_0$, the trajectory is a straight line. (iii). If $\mathbf{x}_1^0 = (0, 0)$, the vortex will not move all the time, otherwise, the vortex will move and finally exit the domain and never come back. This is quite different from the situations in bounded domain with Dirichlet BC where a single vortex can never move outside the domain or in the whole space where a single vortex doesn't move at all under the initial condition (2.6) when $\mathcal{D} = \mathbb{R}^2$. (iv). As $\varepsilon \to 0$, the dynamics of the vortex center under the GLE dynamics converges uniformly in time to that of the reduced dynamical laws well before it exits the domain, which verifies numerically the validation of the reduced dynamical laws in this case. Of course, when the vortex center is being exited the domain or after it moves out of the domain, the reduced dynamics laws are no longer valid. However, the dynamics of GLE is still physically interesting. In fact, based on our extensive numerical experiments, the motion of the vortex centers from the reduced dynamical law agrees with that from the GLE dynamics qualitatively when $0 < \varepsilon < 1$ and quantitatively when $0 < \varepsilon \ll 1$ well before it moves out of the domain.

3.3.2 Vortex pair

Here we present numerical results of the interaction of vortex pair under the GLE dynamics and its corresponding reduced dynamical laws, i.e., we take $M = 2$, $n_1 = n_2 = 1$, $\mathbf{x}_1^0 = (-0.5, 0)$ and $\mathbf{x}_2^0 = (0.5, 0)$ in (2.6).

Fig. 3.16 depicts time evolution of the amplitude $|\psi^\varepsilon|$, time evolution of the GL functionals, $\mathbf{x}_1^r(t)$, $\mathbf{x}_1^\varepsilon(t)$ and $d_1^\varepsilon(t)$, and trajectory of the vortex centers for GLE under homogeneous Neumann BC.

From Fig. 3.16 and additional numerical results not shown here for brevity, we can draw the following conclusions for the interaction of vortex pair under the GLE dynamics with homogeneous Neumann BC: (i). The two vortices undergo a repulsive interaction, their centers move outwards along the line connected them initially with symmetric trajectories, i.e., $\mathbf{x}_1^\varepsilon(t) = -\mathbf{x}_2^\varepsilon(t)$ (cf. Fig. 3.16 (a) & (b)). Moreover, if the two vortices are not located symmetrically initially, the one closer to the boundary will first move outside the domain and the other one will exit the domain later. All the vortices will exit the domain $\mathcal{D}$ at finite time T_ε which increases when ε decreases. (ii). When $\varepsilon \to 0$, the dynamics of the two vortex centers under the GLE dynamics converge uniformly in time to that of the reduced dynamical laws before any one of them exit the domain (cf. Fig. 3.16(c)), which verifies numerically the validation of the reduced dynamical laws in this case. In fact, based on our extensive numerical experiments, the motion of the two vortex centers from the reduced dynamical laws agree with those from the GLE dynamics qualitatively when $0 < \varepsilon < 1$ and quantitatively when $0 < \varepsilon \ll 1$. (iii). During the dynamics of GLE, the GL functional and its kinetic parts decrease when time increases, its interaction part doesn't change much when t is small and changes dramatically when any one of the two vortices move outside the domain $\mathcal{D}$. When $t \to \infty$, all the three quantities converge to 0 (cf. Fig. 3.16(c)), which imply that a constant steady state will be reached in the form of $\phi^\varepsilon(\mathbf{x}) = e^{ic_0}$ for $\mathbf{x} \in \mathcal{D}$ with c_0 a constant.

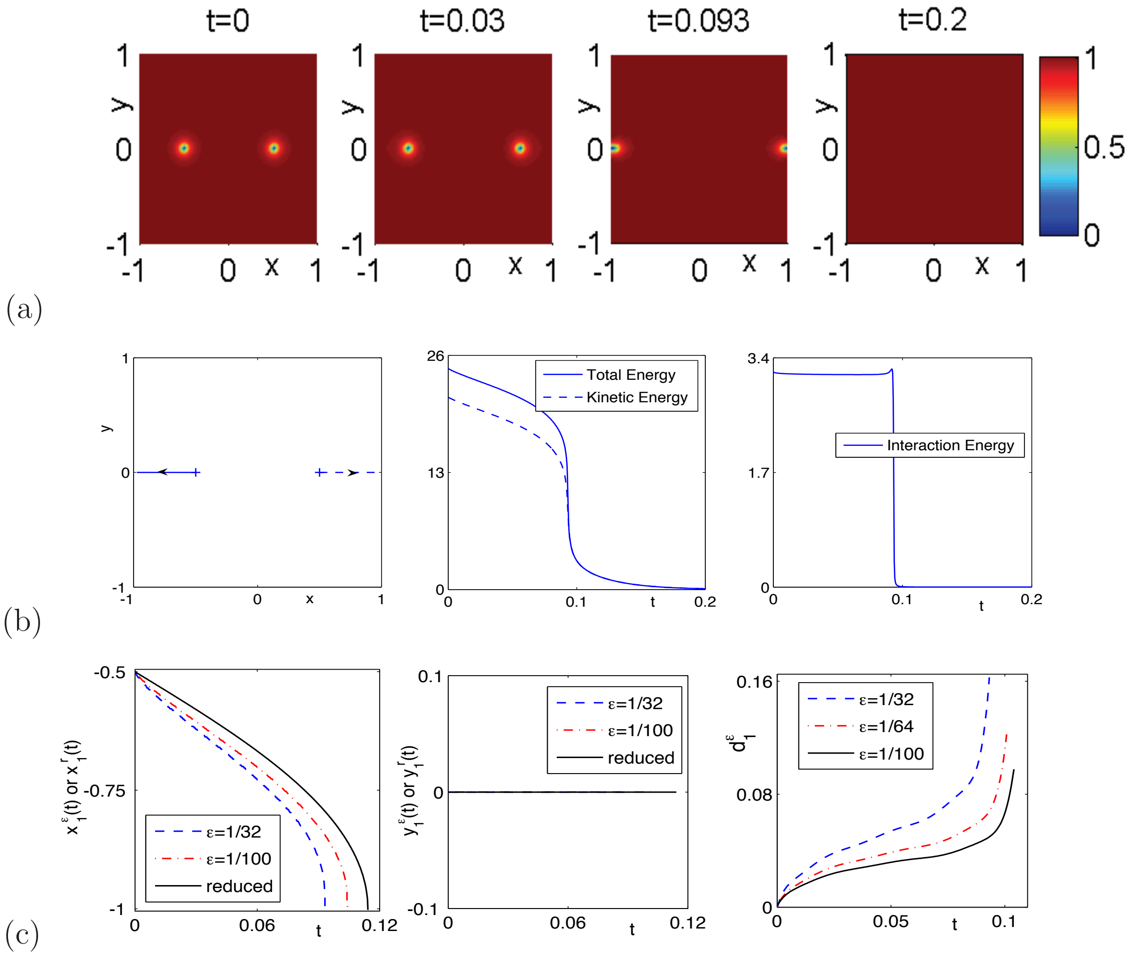

Figure 3.16: Dynamics and interaction of a vortex pair in GLE under Neumann BC: (a) contour plots of $|\psi^\varepsilon(\mathbf{x},t)|$ with $\varepsilon = \frac{1}{32}$ at different times, (b) trajectory of the vortex centers (left) and time evolution of the GL functionals (right) for $\varepsilon = \frac{1}{32}$, (c) time evolution of $\mathbf{x}_1^\varepsilon(t)$ and $\mathbf{x}_1^r(t)$ (left and middle) and their difference $d_1^\varepsilon(t)$ (right) for different ε.

3.3.3 Vortex dipole

Here we present numerical results of the interaction of vortex dipole under the GLE dynamics and its corresponding reduced dynamical laws, i.e., we take $M = 2$, $n_1 = -1$, $n_2 = 1$, $\mathbf{x}_1^0 = (-d_0, 0)$ and $\mathbf{x}_2^0 = (d_0, 0)$ with d_0 a constant.

Fig. 3.17 depicts contour plots of the amplitude $|\psi^\varepsilon|$, while Fig. 3.18 shows time evolution of GL functionals and trajectory of the vortex centers when $\varepsilon = \frac{1}{32}$ in for

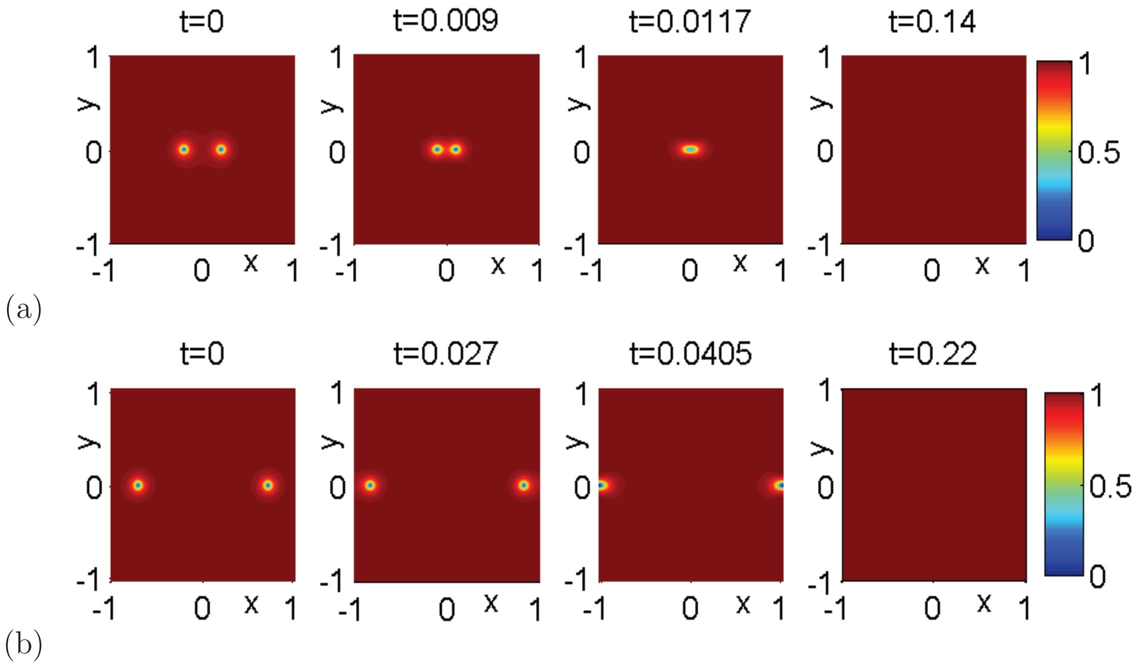

Figure 3.17: Contour plots of $|\psi^\varepsilon(\mathbf{x},t)|$ at different times for the interaction of vortex dipole in GLE under Neumann BC with $\varepsilon=\frac{1}{32}$ for different d_0: (a) $d_0=0.2$, (b) $d_0=0.7$.

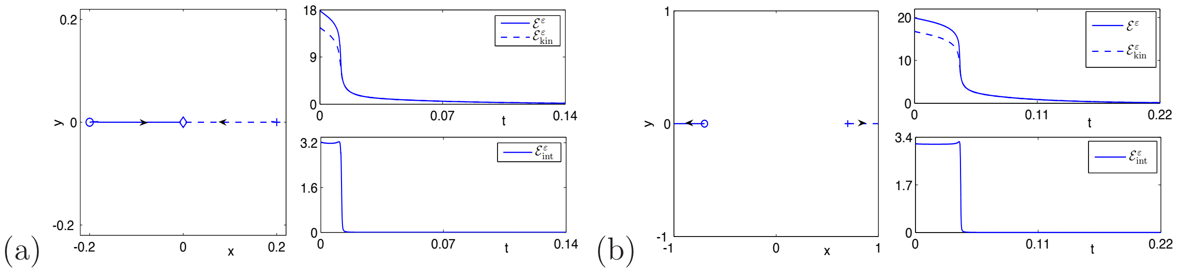

Figure 3.18: Trajectory of vortex centers (left) and time evolution of the GL functionals (right) for the interaction of vortex dipole in GLE under Neumann BC with $\varepsilon=\frac{1}{32}$ for different d_0: (a) $d_0=0.2$, (b) $d_0=0.7$.

different d_0 in (2.6). Fig. 3.19 shows time evolution of $\mathbf{x}_1^r(t)$, $\mathbf{x}_1^\varepsilon(t)$ and $d_1^\varepsilon(t)$ for different ε and d_0.

From Figs. 3.17, 3.18 & 3.19 and additional numerical results not shown here for brevity, we can draw the following conclusions for the interaction of vortex dipole

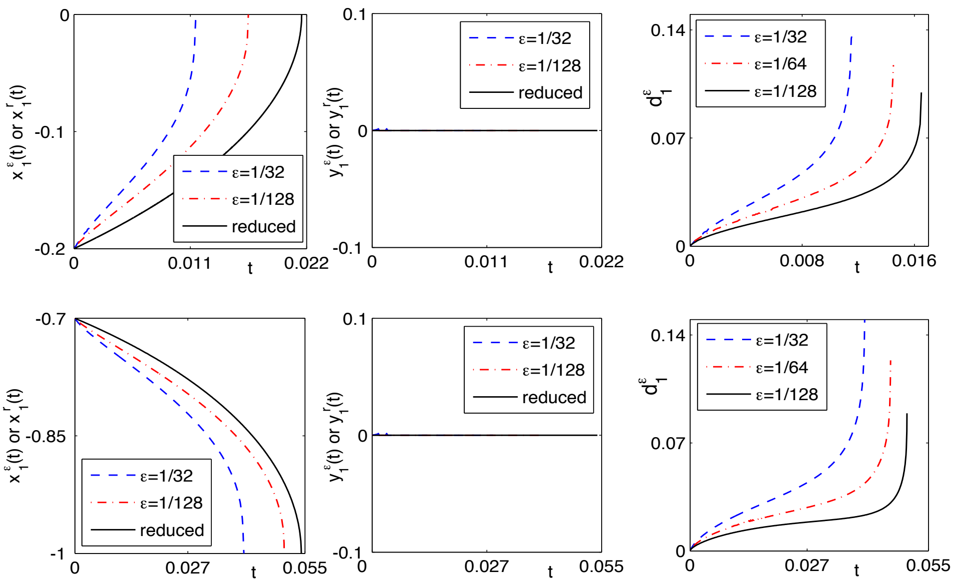

Figure 3.19: Time evolution of $\mathbf{x}^\varepsilon_1(t)$ and $\mathbf{x}^r_1(t)$ (left and middle) and their difference $d^\varepsilon_1(t)$ (right) for different ε and d_0: (a) $d_0 = 0.2$, (b) $d_0 = 0.7$.

under the GLE dynamics with homogeneous Neumann BC: (i). The initial location of the vortices, i.e., d_0, affects the motion of vortices significantly. In fact, there exists a critical value $d^r_c = d^\varepsilon_c$ for $0 < \varepsilon < 1$, which is found numerically as $d^r_c = 0.5$, such that when the distance between the two vortex centers initially $d_0 = \frac{1}{2}|\mathbf{x}^0_1 - \mathbf{x}^0_2| < d^r_c$, then the two vortices will move towards each other along the line connecting their initial locations and finally merge at the origin at finite time T_ε which increases when ε decreases, and respectively, when $d_0 > d^r_c$, the two vortices will move outwards along the line connecting their initial locations and finally move out of the domain at finite time T_ε which increases when ε decreases (cf. Figs. 3.17 & 3.18). Moreover, the trajectories of the two vortices are symmetric, i.e., $\mathbf{x}_1(t) = -\mathbf{x}_2(t)$, and finally the GLE dynamics will lead to a constant steady state with amplitude 1, i.e., $\phi^\varepsilon(\mathbf{x}) = e^{ic_0}$ for $\mathbf{x} \in \mathcal{D}$ with c_0 a real constant. (ii). When $\varepsilon \to 0$, the dynamics of the two vortex centers under the GLE dynamics converges uniformly in time to that of the reduced dynamical laws before they collide or move out of the domain (cf. Fig. 3.19) which verifies numerically the validation of the reduced dynamical laws in this case. In fact, based on our extensive numerical experiments, the motion of the two vortex centers from the reduced dynamical laws agree with those from the GLE dynamics qualitatively when $0 < \varepsilon < 1$ and quantitatively when $0 < \varepsilon \ll 1$. (iii). During the dynamics of GLE, the GL functional and its kinetic part decrease when time increases, its interaction part doesn't change much when t is small. All the three quantities changes dramatically when the two vortices collide or move across $\partial\mathcal{D}$ and eventually converge to 0 when $t \to \infty$ (cf. Fig. 3.18).

3.3.4 Vortex lattices

Here we present numerical results of the interaction of vortex lattices under the GLE dynamics. We will consider the following cases: case I. $M = 3$, $n_1 = n_2 = n_3 = 1$, $\mathbf{x}_1^0 = (-0.2, \frac{\sqrt{3}}{5})$, $\mathbf{x}_2^0 = (-0.2, -\frac{\sqrt{3}}{5})$, $\mathbf{x}_3^0 = (0.4, 0)$; case II. $M = 3$, $n_1 = n_2 = n_3 = 1$, $\mathbf{x}_1^0 = (-0.4, 0)$, $\mathbf{x}_2^0 = (0, 0)$, $\mathbf{x}_3^0 = (0.4, 0)$; case III. $M = 3$, $n_1 = n_2 = n_3 = 1$, $\mathbf{x}_1^0 = (-0.4, 0.2)$, $\mathbf{x}_2^0 = (0, 0.2)$, $\mathbf{x}_3^0 = (0.4, 0.2)$; case IV. $M = 3$, $n_2 = -1$, $n_1 = n_3 = 1$, $\mathbf{x}_1^0 = (-0.4, 0)$, $\mathbf{x}_2^0 = (0, 0)$, $\mathbf{x}_3^0 = (0.4, 0)$; case V. $M = 3$, $n_3 = -1$, $n_1 = n_2 = 1$, $\mathbf{x}_1^0 = (-0.2, \frac{\sqrt{3}}{5})$, $\mathbf{x}_2^0 = (-0.2, -\frac{\sqrt{3}}{5})$, $\mathbf{x}_3^0 = (0.4, 0)$; case VI. $M = 4$, $n_1 = n_2 = n_3 = n_4 = 1$, $\mathbf{x}_1^0 = (0.4, -0.4\sin(1))$, $\mathbf{x}_2^0 = (-0.2, 0.4\cos(1))$, $\mathbf{x}_3^0 = (-0.2, 0.4\sin(1))$, $\mathbf{x}_4^0 = (0, 0)$; case VII. $M = 4$, $n_1 = n_3 = -1$, $n_2 = n_4 = 1$, $\mathbf{x}_1^0 = (-0.4, 0)$, $\mathbf{x}_2^0 = (-\frac{2}{15}, 0)$, $\mathbf{x}_3^0 = (\frac{2}{15}, 0)$, $\mathbf{x}_4^0 = (0.4, 0)$; case VIII. $M = 4$, $n_1 = n_2 = -1$, $n_3 = n_4 = 1$, $\mathbf{x}_1^0 = (0.4, 0)$, $\mathbf{x}_2^0 = (-0.2, \frac{\sqrt{3}}{5})$, $\mathbf{x}_3^0 = (-0.2, -\frac{\sqrt{3}}{5})$, $\mathbf{x}_4^0 = (0, 0)$; and case IX. $M = 4$, $n_2 = n_3 = 1$, $n_1 = n_4 = -1$, $\mathbf{x}_1^0 = (0.4, 0)$, $\mathbf{x}_2^0 = (-0.2, \frac{\sqrt{3}}{5})$, $\mathbf{x}_3^0 = (-0.2, -\frac{\sqrt{3}}{5})$, $\mathbf{x}_4^0 = (0, 0)$.

Fig. 3.20 shows trajectory of the vortex centers when $\varepsilon = \frac{1}{32}$ in for the above 9 cases. From Fig. 3.20 and additional numerical results not shown here for brevity, we can draw the following conclusions: (i). The interaction of vortex lattices under the GLE dynamics with homogeneous Neumann BC is very interesting and complicated. The detailed dynamics and interaction pattern of a lattice depends on its initial alignment of the lattice and geometry of the domain $\mathcal{D}$. (ii). For a lattice of M vortices, if they have the same index, then at least $M - 1$ vortices will move out of

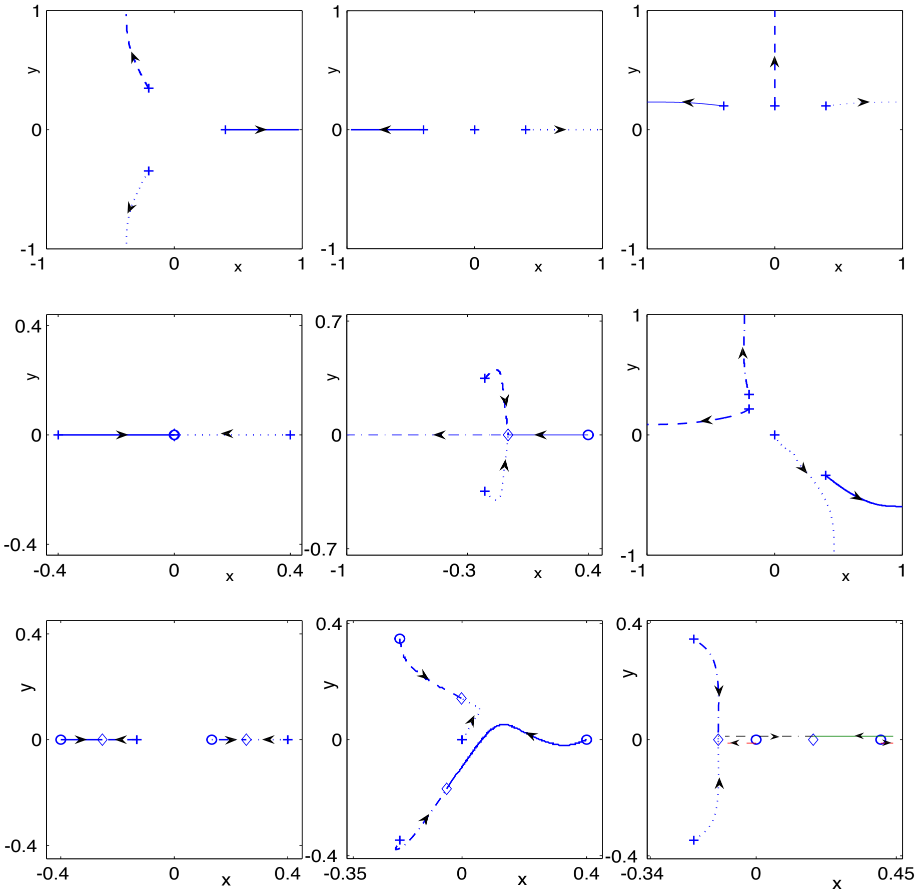

Figure 3.20: Trajectory of vortex centers for the interaction of different vortex lattices in GLE under homogeneous Neumann BC with $\varepsilon = \frac{1}{32}$ for cases I-IX (from left to right and then from top to bottom) in section 3.3.4.

the domain at finite time and no collision will happen for any time $t \geq 0$. On the other hand, if they have opposite index, collision will happen at finite time. After collisions, the leftover vortices will then move out of the domain at finite time and at most one vortex may left in the domain. When t is sufficiently large, in most cases, no vortex is left in the domain; of course, when the geometry and initial setup are properly symmetric and M is odd, there maybe one vortex left in the domain.

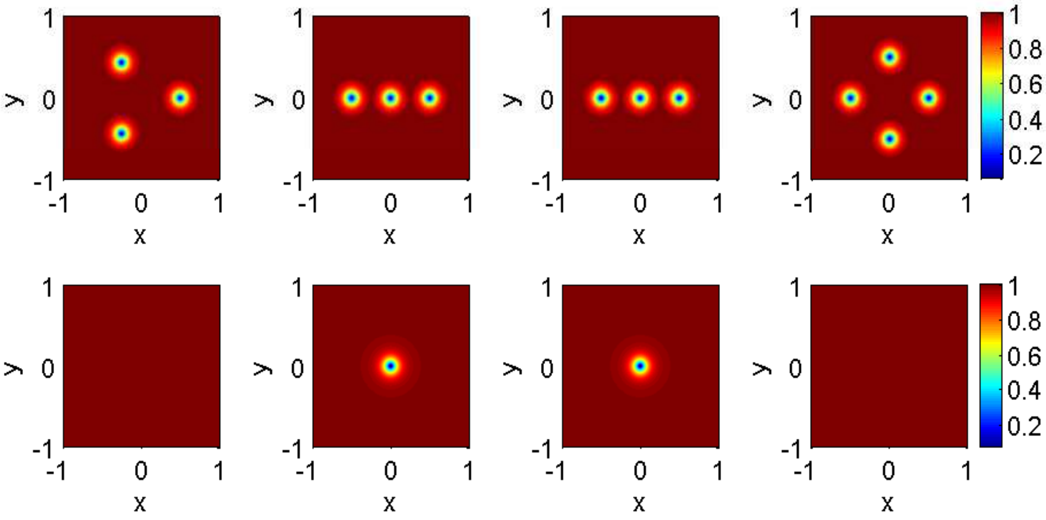

Figure 3.21: Contour plots of the amplitude $|\psi^\varepsilon(\mathbf{x},t)|$ for the initial data (top) and corresponding steady states (bottom) of vortex lattice in the GLE under homogeneous Neumann BC with $\varepsilon = \frac{1}{16}$ for different number of vortices M and winding number n_j: $M = 3, n_1 = n_2 = n_3 = 1$ (first and second columns); $M = 3, n_1 = -n_2 = n_3 = 1$ (third column); and $M = 4, n_1 = -n_2 = n_3 = -n_4 = 1$ (fourth column).

3.3.5 Steady state patterns of vortex lattices

Here we present the steady state patterns of vortex lattices under the GLE dynamics with homogeneous Neumann BC. To this end, we take $\varepsilon = \frac{1}{16}$ in and assume the M vortices are initially located uniformly on a line, i.e.,

$$\mathbf{x}_j^0 = \left(-0.5 + \frac{j-1}{M-1}, 0\right), \qquad j = 1, 2, \ldots, M,$$

or on a circle with radius $R_1 = 0.5$, i.e.,

$$\mathbf{x}_j^0 = 0.5\left(\cos\left(\frac{2j\pi}{M}\right), \sin\left(\frac{2j\pi}{M}\right)\right), \qquad j = 1, 2, \ldots, M.$$

Fig. 3.21 depicts the amplitude $|\psi^\varepsilon|$ of the initial data and final steady states under the GLE dynamics with different initial setups.

From Fig. 3.21 and additional numerical results not shown here for brevity, we can draw the following conclusions for the interaction of vortex lattices under the GLE dynamics with homogeneous Neumann BC: (i). If the three like vortices initially located uniformly on a circle, they will repel each other and finally exit outside the domain and never come back. (ii). If the three like vortices initially located uniformly on a line, the left and right vortices will finally exit outside the domain and never come back, while the middle one does not move all the time. (iii). If the three vortices initially located uniformly on a line with the middle vortex whose winding number is opposite to the other two, the middle one will not move all the time, while the left and right vortices will move toward the origin and one of them will merge with the middle vortex, finally only one vortex will stay at the origin forever. (iv). If the four vortices initially located uniformly on a circle with the sign of winding number alternatively changed, the four vortices will move toward the original point and merge with each other, and finally there will be no vortex in the domain. (v). Actually, from our extensive numerical experiments, we can conclude that for any initial setup, if the number of vortices M is even, the vortices will either merge or move outside the domain, and finally there will be no vortex leftover in the domain; while if M is odd, there will be at most one vortex leftover in the domain when $t \to \infty$.

3.3.6 Validity of RDL under small perturbation

Same as the motivation in section 3.2.6, here we study the radiation property of the GLE dynamics under homogeneous Neumann BC in this subsection. To this end, we take the initial data (1.2) as (3.4) with ψ_0^ε chosen as (2.6) with $M = 2$, $n_1 = n_2 = 1$, $\mathbf{x}_1^0 = -\mathbf{x}_2^0 = (0.5, 0)$ and $h(\mathbf{x})$ as (3.3). Then we take $\delta = \varepsilon$ and let ε go to 0, and solve the GLE with initial condition (3.4) for the vortex centers $\mathbf{x}_1^{\delta,\varepsilon}(t)$ and $\mathbf{x}_2^{\delta,\varepsilon}(t)$ and compare them with those from the reduced dynamical law. We denote $d_j^{\delta,\varepsilon}(t) = |x_j^{\delta,\varepsilon}(t) - x_j^r(t)|$ for $j = 1, 2$ as the error. Fig. 3.22 depicts time evolution of $d_1^{\delta,\varepsilon}(t)$ for the case when $\delta = \varepsilon$, i.e., small perturbation, and the case when $\delta = 0$, i.e.,

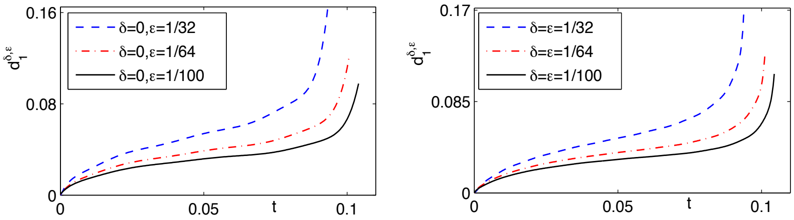

Figure 3.22: Time evolution of $d_1^{\delta,\varepsilon}(t)$ for non-perturbed initial data (left) and perturbed initial data (right) in section 3.3.6

no perturbation. From this figure, we can see that small perturbation in the initial data does not affect the motion of the vortices much, same as the non-perturbed initial setups, the dynamics of the two vortex centers under the GLE dynamics with perturbed initial setups also converge to those obtained from the reduced dynamical law when $\varepsilon \to 0$, which is simply similar as the situation in the GLE dynamics with perturbed initial data under Dirichlet BC.

3.4 Vortex dynamics in inhomogeneous potential

In this subsection, we study numerically the vortex dynamics in the GLE dynamics under Dirichlet BC in inhomogeneous potential. We let the external potential in (1.1) as:

$$V(\mathbf{x}) = \frac{1}{1 + 9e^{-\gamma_x((x-x_c^0)^2 - \gamma_y(y-y_c^0)^2)}}, \quad \mathbf{x} \in \mathcal{D}, \tag{3.5}$$

where γ_x, γ_y, x_c^0 and y_c^0 are constants, i.e., we impose a single well external potential with minimal location sitting at point (x_c^0, y_c^0). To study the joint effect of the pinning effect, the boundary effect and the interaction between vortices on the vortex dynamics, we consider two types of inhomogeneous external potential:

- Type I. Symmetric external potential, i.e., $\gamma_x = \gamma_y = 20$;
- Type II. Anisotropic external potential, i.e., $\gamma_x = 30$, $\gamma_y = 15$.

Choose the initial data as (2.6) and for simplicity, we always let $h(\mathbf{x}) = 0$ and $(x_c^0, y_c^0) = (0, 0) =: \mathcal{O}$. We study following three cases: case I: $M = 1$, $n_1 = 1$, $\mathbf{x}_1 = [0.4, 0.4]$, $V(\mathbf{x})$ is chosen as type I potential; case II: $M = 1$, $n_1 = 1$, $\mathbf{x}_1 = [0.4, 0.4]$, $V(\mathbf{x})$ is chosen as type II potential; case III: $M = 2$, $n_1 = n_2 = 1$, $\mathbf{x}_1 = [-0.3, 0]$, $\mathbf{x}_2 = [0, 0.3]$, $V(\mathbf{x})$ is chosen as type I potential.

Fig. 3.23, shows the trajectory, time evolution of the distance between the vortex center and potential center and $d_1^\varepsilon(t)$ for different ε for case I and II, as well as trajectory of vortex center for different ε of the vortices for case III. From this figure and additional numerical experiment not shown here for brevity, we can see that: (i). For the single vortex, it moves monotonically toward the points $\mathbf{x}_p = (x_c^0, y_c^0)$, where the external potential V(x) attains its minimum value (cf. Fig. 3.23 (a) & (b)), which shows clearly the pinning effect. Moreover, the trajectory depend on the type of the potential $V(\mathbf{x})$. The speed that vortex move to $\mathbf{x}_p$ as well as the final location that vortex stay steady depend on the value of ε (cf. Fig. 3.23 (a) & (b)). The smaller the ε is, the closer the final location to $\mathbf{x}_p$ and the faster the vortex move to it. (ii). As $\varepsilon \to 0$, the dynamics of the vortex center in the GLE dynamics converges uniformly in time to that in the reduced dynamics which verifies numerically the validation of the reduced dynamical laws in this case. (iii). For the vortex pair, when ε is large, the two vortices will move apart from each other for a while, then monotonically toward each other and to $\mathbf{x}_p$, which illustrate the pinning effect clearly (cf. Fig. 3.23 (c)). Then, they will move apart from each other again in the opposite direction with one toward $\mathbf{x}_p$ due to the repulsive interaction between the two vortices. Otherwise, when ε is small enough, the vortex will simply move monotonically close to each other and to $\mathbf{x}_p$ and finally they will stop and stay steady at someplace near $\mathbf{x}_p$. The smaller the ε is, the closer the two vortex to the point $\mathbf{x}_p$. As we know, in the speeded time scale $\lambda_\varepsilon = \frac{1}{\ln(\frac{1}{\varepsilon})}$, the vortex pair undergo a repulsive interaction and they always move apart from each other toward the boundary in the GLE dynamics under homogeneous potential when $h(\mathbf{x}) = 0$, and the smaller the ε is, the stronger they repulse from each other, thus, it might

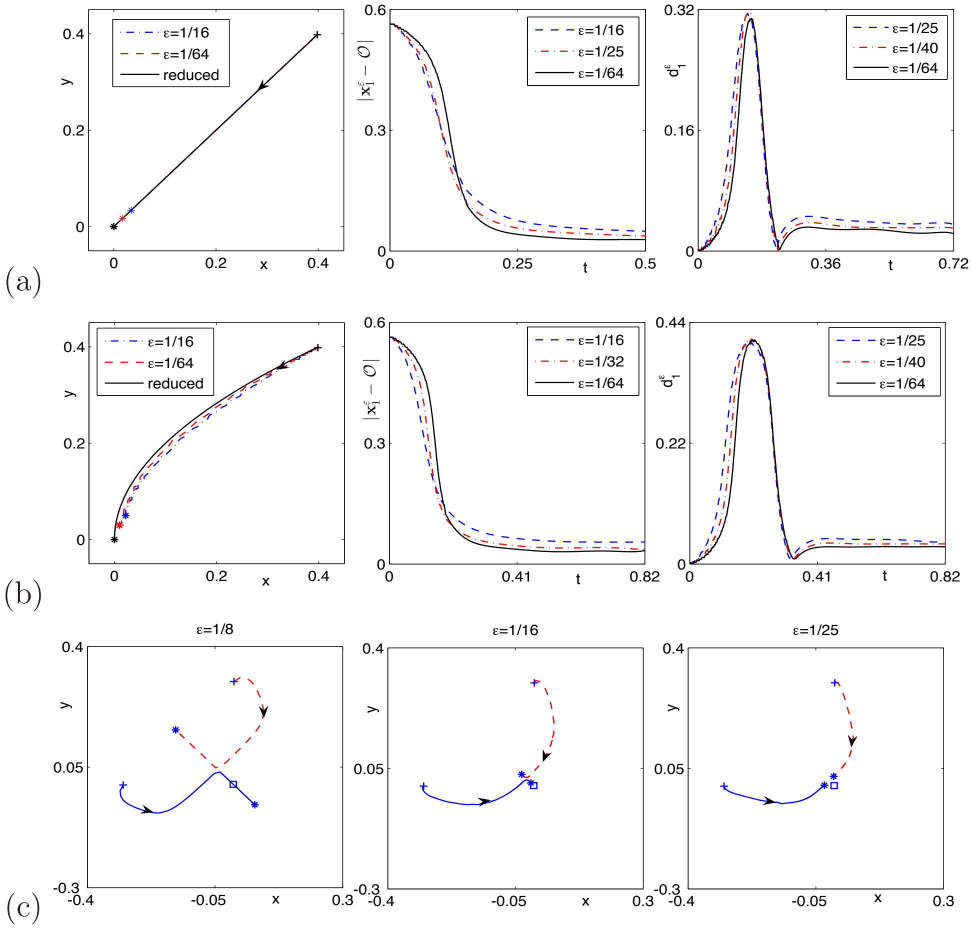

Figure 3.23: (a) and (b): trajectory, time evolution of the distance between the vortex center and potential center and $d_1^\varepsilon(t)$ for different ε for case I and II, and (c): Trajectory of vortex center for different ε of the vortices for case III in section 3.4.

be interesting that we studying the pinning effect of the vortex pair in speeded time scale to see how the vortex pair continue to move after they move close to $\mathbf{x}_p$. Will they move apart from each other again?

3.5 Conclusion

In this chapter, by applying the efficient and accurate numerical methods proposed in chapter 2 to simulate Ginzburg-Landau equation (GLE) with a dimensionless parameter $0 < \varepsilon < 1$ on bounded domains with either Dirichlet or homogenous

Neumann BC and its corresponding reduced dynamical laws (RDLs), we studied numerically quantized vortex interaction in GLE with/without impurities for superconductivity and compared numerically patterns of vortex interaction between the GLE dynamics and its corresponding reduced dynamical laws under different initial setups.

For the GLE under a homogeneous potential, based on extensive numerical results, we verified that the dynamics of vortex centers under the GLE dynamics converges to that of the reduced dynamical laws when $\varepsilon \to 0$ before they collide and/or move out of the domain. Certainly, after either vortices collide with each other or move out of the domain, the RDLs are no longer valid; however, the dynamics and interaction of quantized vortices are still physically interesting and they can be obtained from the direct numerical simulations for the GLE with fixed $\varepsilon > 0$ even after they collide and/or move out of the domain. We also identified the parameter regimes where the RDLs agree with qualitatively and/or qualitatively as well as fail to agree with those from the GLE dynamics. In the validity regimes, the RDL is still valid under small perturbation in the initial data due to the dissipative nature of the GLE. Some very interesting nonlinear phenomena related to the quantized vortex interactions in the GLE for superconductivity were also observed from our direct numerical simulation results of GLE. Different steady state patterns of vortex lattices under the GLE dynamics were obtained numerically. From our numerical results, we observed that boundary conditions and domain geometry affect significantly on vortex dynamics and interaction, which showed different interaction patterns compared to those in the whole space case [152, 153].

For the GLE in an inhomogeneous potential under the Dirichlet BC, we also numerically verified the validity of the RDL. By directly simulating the GLE, we find that vortices move in quite different ways from that in the homogeneous case. The vortices basically move toward critical points of the inhomogeneous potential in the limiting process $\varepsilon \to 0$, which show the pinning effect that caused by the impurities given by the inhomogeneities.

Chapter 4

Vortex dynamics in NLSE

In this chapter, we apply the numerical method presented in chapter 2 to simulate quantized vortex interaction of NLSE, i.e., $\lambda_\varepsilon = 0$, $\beta = 1$ in the GLSE (1.1), with different ε and under different initial setups including single vortex, vortex pair, vortex dipole and vortex lattice. We study how the dimensionless parameter ε, initial setup, boundary value and geometry of the domain $\mathcal{D}$ affect the dynamics and interaction of vortices. Moreover, we compare the results obtained from the NLSE with those from the corresponding reduced dynamical laws, and identify the cases where the reduced dynamical laws agree qualitatively and/or quantitatively as well as fail to agree with those from NLSE on vortex interaction. Finally, we also investigate the sound-vortex interaction and study the radiative nature of the vortices in NLSE dynamics.

Without specification, the initial data is chose as the same one in section 3.1 in chapter 3.

4.1 Numerical results under Dirichlet BC

4.1.1 Single vortex

In this subsection, we present numerical results of the motion of a single quantized vortex in the NLSE dynamics and the corresponding reduced dynamics, i.e we take $M = 1$, $n_1 = 1$ in (2.6). To study how the initial phase shift $h(\mathbf{x})$ and initial location of the vortex $\mathbf{x}_0$ affect the motion of the vortex and to understand the validity of the reduced dynamical law, we consider the following 11 cases:

- Case I-III: $\mathbf{x}_1^0 = (0,0)$, and $h(\mathbf{x})$ is chosen as Mode 1, 2 and 3, respectively;
- Case IV-VIII: $\mathbf{x}_1^0 = (0.1,0)$, and $h(\mathbf{x})$ is chosen as Mode 1, 2, 3, 4 and 5, respectively;
- Case IX-XI: $\mathbf{x}_1^0 = (0.1,0.1)$, and $h(\mathbf{x})$ is chosen as Mode 3, 4 and 5, respectively.

Moreover, to study the effect of domain geometry, we consider $\mathcal{D}$ of three types: type I. a square $\mathcal{D} = [-1,1] \times [-1,1]$, type II. a rectangle $\mathcal{D} = [-1,1] \times [-0.65,0.65]$, and type III. a unit disk $\mathcal{D} = B_1(\mathbf{0})$. Thus we also study the following 4 additional cases:

- Case XII-XIII: $\mathbf{x}_1^0 = (0,0)$, $h(\mathbf{x}) = x + y$, $\mathcal{D}$ is chosen as type II and III, respectively;
- Case XIV-XV: $\mathbf{x}_1^0 = (0.1,0)$, $h(\mathbf{x}) = x^2 - y^2$, $\mathcal{D}$ is chosen as type II and III, respectively.

Fig. 4.1 depicts trajectory of the vortex center when $\varepsilon = \frac{1}{40}$ for Cases I-VI and d_1^ε with different ε for Cases I, V and VI. Fig. 4.2 shows trajectory of the vortex center when $\varepsilon = \frac{1}{64}$ in NLSE for cases VI-XI, while Fig. 4.3 shows that for Cases XII-XVII when $\varepsilon = \frac{1}{32}$. From Figs. 4.1-4.3 and additional numerical experiments not shown here for brevity, we can draw the following conclusions: (i). When $h(\mathbf{x}) \equiv 0$, the vortex center doesn't move and this is similar to the case in the whole space. (ii). When $h(\mathbf{x}) = (x + by)(x - \frac{y}{b})$ with $b \neq 0$, the vortex does not move if $\mathbf{x}_1^0 = (0,0)$, while it does move if $\mathbf{x}_1^0 \neq (0,0)$ (cf. Fig. 4.1 Cases III and VI for $b = 1$). (iii). When $h(\mathbf{x}) \neq 0$ and $h(\mathbf{x}) \neq (x+by)(x - \frac{y}{b})$ with $b \neq 0$, in general, the vortex center does move. For the NLSE dynamics, there exists a critical value ε_c depending on $h(\mathbf{x})$, $\mathbf{x}_1^0$ and $\mathcal{D}$ such that if $\varepsilon < \varepsilon_c$, the vortex will move periodically in a close loop (cf. Fig. 4.1), otherwise their trajectory will not be a close loop. This differs from the situation in the reduced dynamics significantly, where the trajectory is always periodic (cf. Fig. 4.2 red dash line). Thus the reduced dynamical laws fail qualitatively when $\varepsilon > \varepsilon_c$. It should be an interesting problem to find how this critical value depends on $h(\mathbf{x})$, $\mathbf{x}_1^0$ and the geometry of $\mathcal{D}$. (iv). In general, the initial location, the geometry of the domain and the boundary value will all affect the motion of the vortex (cf. Fig. 4.3). (v). When $\varepsilon \to 0$, the dynamics of the vortex center in the NLSE dynamics converges uniformly in time to that in the reduced dynamics (cf. Fig. 4.1 bottom row) which verifies numerically the validation of the reduced dynamical laws.

4.1.2 Vortex pair

Here we present numerical results of the interaction of vortex pair under the NLSE dynamics and its corresponding reduced dynamical laws, i.e., we take $M = 2$, $n_1 = n_2 = 1$. We always suppose that the two vortices are initially located symmetric on the x-axis, i.e., we take $\mathbf{x}_2^0 = -\mathbf{x}_1^0 = (d_0, 0)$ with $0 < d_0 < 1$ in (2.6). Let $\varepsilon = \frac{1}{40}$, we consider the following three cases: case I. $d_0 = 0.1$ and $h(\mathbf{x}) = 0$, case II. $d_0 = 0.5$ and $h(\mathbf{x}) = 0$, case III. $d_0 = 0.5$ and $h(\mathbf{x}) = x + y$. Fig. 4.4 depicts the trajectory of the vortex pair, the time evolution of $\mathcal{E}^\varepsilon(t)$, $\mathcal{E}^\varepsilon_{\text{kin}}(t)$, $\mathbf{x}_1^\varepsilon(t)$, $\mathbf{x}_2^\varepsilon(t)$ and $d_1^\varepsilon(t)$ for above 3 cases.

From Figs. 4.4 and additional numerical results not shown here for brevity, we can draw the following conclusions for the interaction of vortex pair under the NLSE dynamics with Dirichlet BC: (i). The total energy is conserved during the dynamics of the NLSE in all cases. (ii). The pattern of the motion of the vortex centers depend on both the initial location of the two vortices and the initial phase shift $h(\mathbf{x})$ in (2.6). (iii). When $h(\mathbf{x}) \equiv 0$, the vortices move periodically and their trajectories are symmetric, i.e., $\mathbf{x}_1^\varepsilon(t) = -\mathbf{x}_2^\varepsilon(t)$. Moreover, for both the reduced dynamical law and NLSE dynamics, there is a critical value of d_0, say d_c^r and d_c^ε respectively, such that if $d_0 < d_c^r$ (or $d_0 < d_c^\varepsilon$ in NLSE dynamics), the two vortices will rotate with

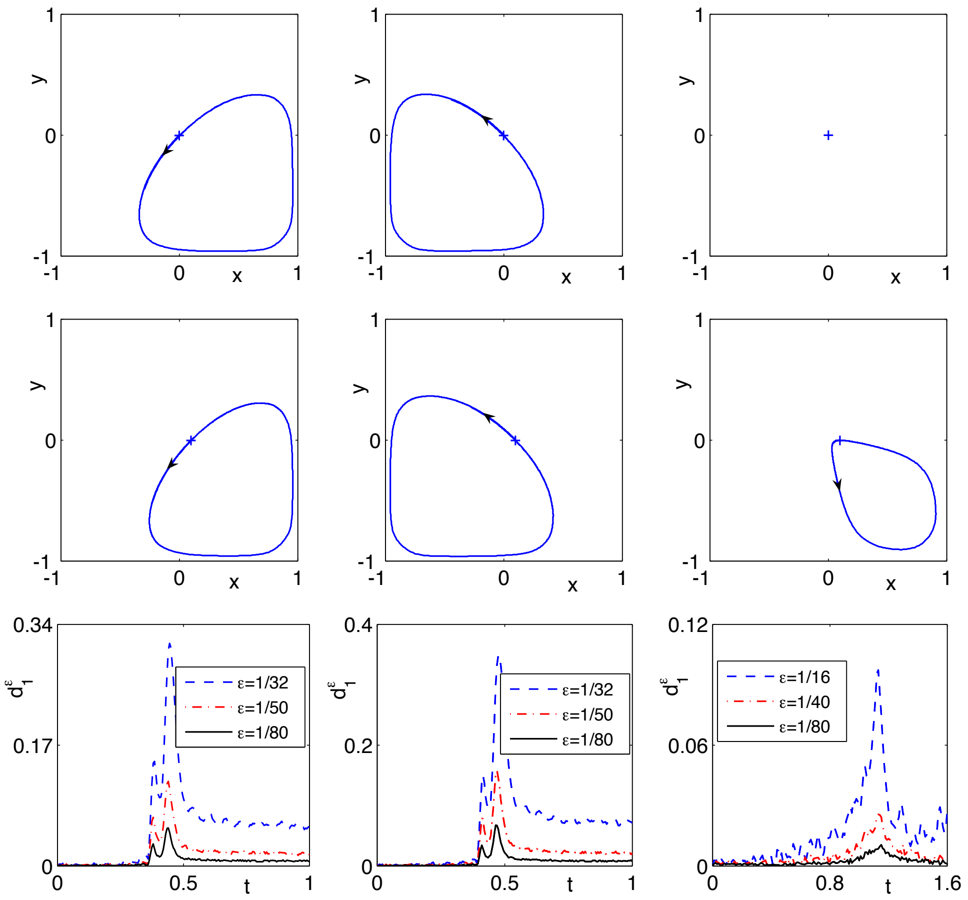

Figure 4.1: Trajectory of the vortex center in NLSE under Dirichlet BC when $\varepsilon = \frac{1}{40}$ for Cases I-VI (from left to right and then from top to bottom in top two rows), and d_1^ε for different ε for Cases I,V&VI (from left to right in bottom row) in section 4.1.1.

each other and move along a circle-like trajectory, otherwise, they will move along a crescent-like trajectory (cf. Figs.4.4 (a) & (b)). We find numerically the critical value $d_c^r \approx 0.4923$ and d_c^ε for $0 < \varepsilon < 1$ which are depicted in Fig. 4.5. From these values, we can fit the following relation for d_c^r and d_c^ε:

$$d_c^\varepsilon = d_c^r + 2.11\varepsilon^{2.08}, \qquad 0 < \varepsilon < 1.$$

(iv). When $h(\mathbf{x}) \neq 0$, it affects the motion of the two vortex centers significantly (cf. Figs.4.4 (c)). (v). For any fixed d_0, the dynamics of the two vortex centers under

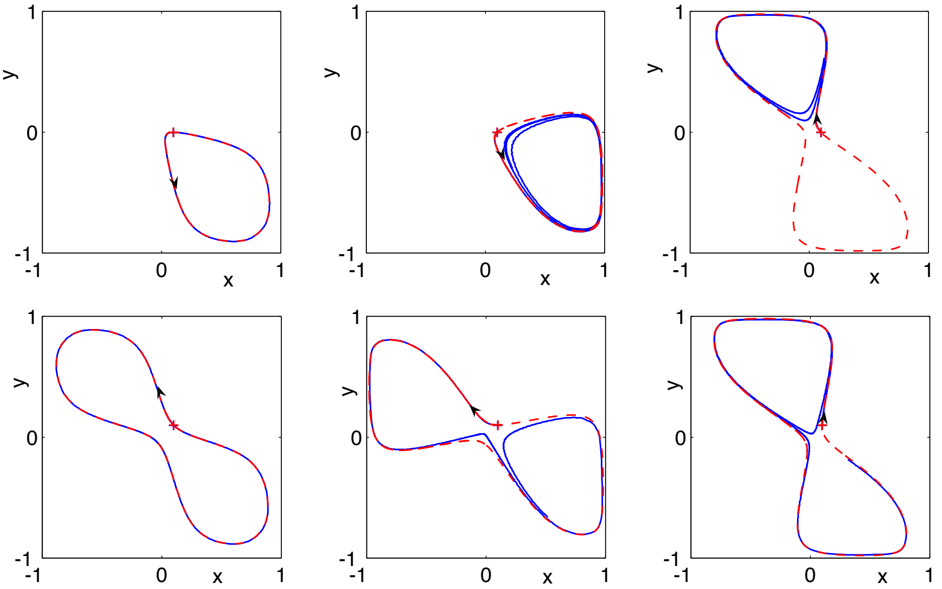

Figure 4.2: Trajectory of the vortex center in NLSE dynamics under Dirichlet BC when $\varepsilon = \frac{1}{64}$ (blue solid line) and from the reduced dynamical laws (red dash line) for Cases VI-XI (from left to right and then from top to bottom) in section 4.1.1.

the NLSE dynamics converges uniformly in time to that of the reduced dynamical laws (cf. Figs.4.4 (d)) when $\varepsilon \to 0$. However, for fixed ε, the reduced dynamical law fails qualitatively to describe the motion of vortices if $d_c^r < d_0 < d_c^\varepsilon$.

4.1.3 Vortex dipole

Here we present numerical results of the interaction of vortex dipole under the NLSE dynamics and its corresponding reduced dynamical laws, i.e., we take $M = 2$, $n_1 = -n_2 = -1$, $\mathbf{x}_2^0 = -\mathbf{x}_1^0 = (d_0, 0)$ in (2.6) with $d_0 = 0.5$ and $\varepsilon = \frac{1}{25}$. Fig. 4.6 depicts contour plots of $|\psi^\varepsilon(x,t)|$ at different times, trajectory of the vortex dipole, time evolution of $\mathbf{x}_1^\varepsilon(t)$, $\mathbf{x}_2^\varepsilon(t)$ and $d_1^\varepsilon(t)$ for different $h(\mathbf{x})$. From Fig. 4.6 and additional numerical results not shown here for brevity, we can draw the following conclusions: (i). The total energy is conserved numerically very well during the dynamics. (ii). The pattern of the motion of the vortex centers depend on both the initial location of the two vortices and the initial phase shift $h(\mathbf{x})$ in (2.6). (iii). The

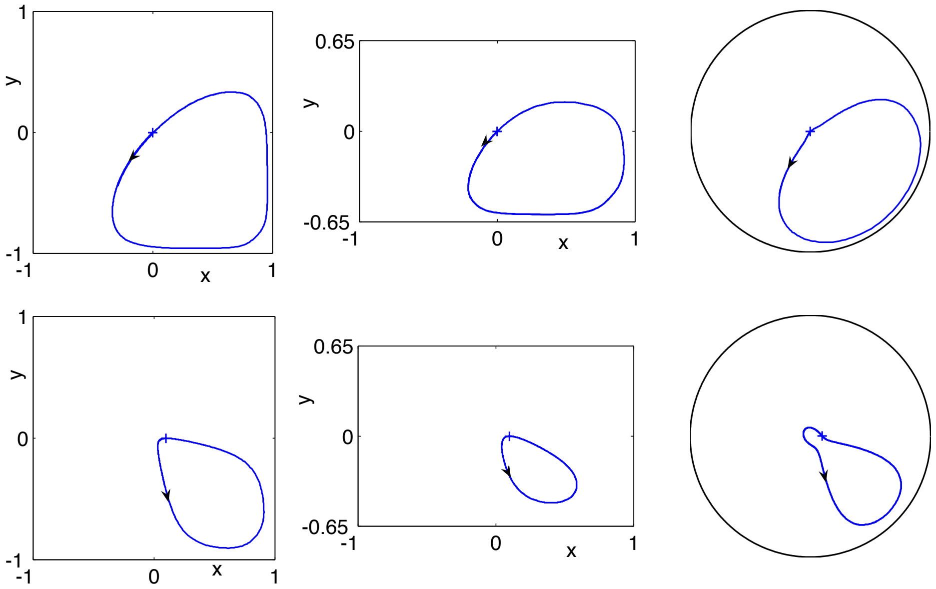

Figure 4.3: Trajectory of the vortex center in NLSE under Dirichlet BC when $\varepsilon = \frac{1}{40}$ for cases I, XII-XIII, VI and XIV-XV (from left to right and then from top to bottom) in section 4.1.1.

vortex dipole moves upward symmetrically with respect to y-axis and finally merges and annihilates somewhere near the top boundary simultaneously. The distance between the merging place and the boundary is of $O(\varepsilon)$ when ε is small. After merging, new waves will be created and reflected by the top boundary. The new waves will then move back into the domain and be reflected back into the domain again when they hit the boundaries (cf. Fig. 4.6). Moreover, the vortex dipole in the NLSE dynamics will always merge in some place near the top boundary for all d_0. However, in the reduced dynamics, they never merge inside $\mathcal{D}$, in fact, they will move outside the domain before they merge. Hence, the reduced dynamical law fails quantitatively when the vortex dipole is near the boundary. (iv). When $h(\mathbf{x}) \neq 0$, it affects the motion of the two vortex centers significantly (cf. Figs.4.4 (c)). (v). When $\varepsilon \to 0$, the dynamics of the two vortex centers under the NLSE dynamics converges uniformly to that of the reduced dynamical laws (cf. Fig. 4.6) before they merge each other or near the boundary which verifies numerically the validation of

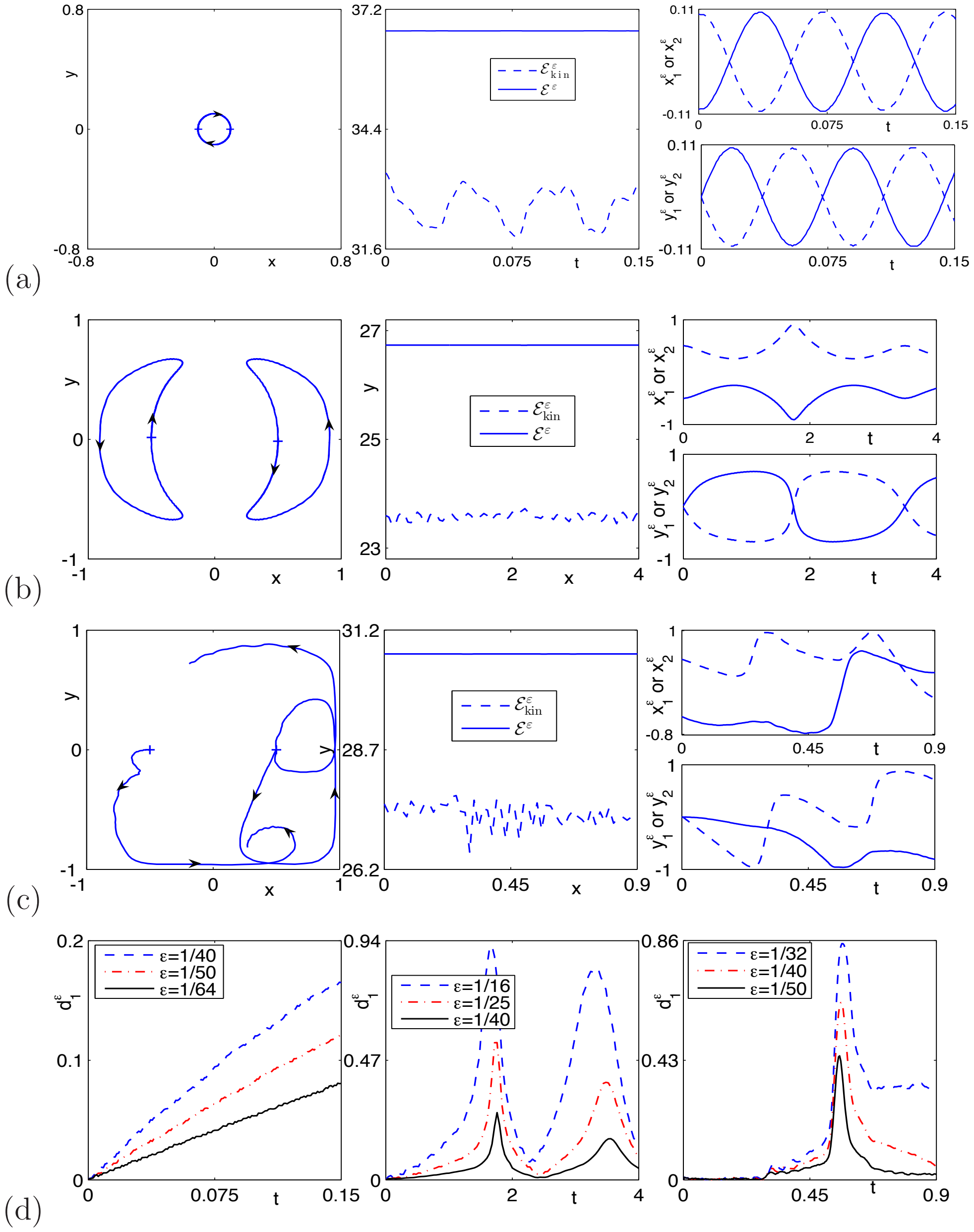

Figure 4.4: Form left to right in (a)-(c): trajectory of the vortex pair, time evolution of $\mathcal{E}^\varepsilon(t)$ and $\mathcal{E}^\varepsilon_{\rm kin}(t)$ as well as $\mathbf{x}_1^\varepsilon(t)$ and $\mathbf{x}_2^\varepsilon(t)$ for the 3 cases in section 4.1.2. (a). case I, (b). case II, (c). case III. (d). time evolution of $d_1^\varepsilon(t)$ for case I-III (form left to right).

the reduced dynamical laws in this case. In fact, based on our extensive numerical experiments, the motions of the two vortex centers from the reduced dynamical

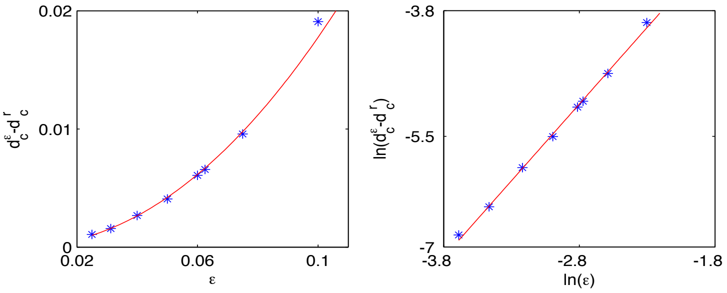

Figure 4.5: Critical value d_c^ε for the interaction of vortex pair of the NLSE under the Dirichlet BC with different ε and $h(\mathbf{x}) = 0$ in (2.6): if $d_0 < d_c^\varepsilon$, the two vortex will move along a circle-like trajectory, if $d > d_c^\varepsilon$, the two vortex will move along a crescent-like trajectory.

laws agree with those from the NLSE dynamics qualitatively when $0 < \varepsilon < 1$ and quantitatively when $0 < \varepsilon \ll 1$ when they are not too close to the boundary.

4.1.4 Vortex lattice

Here we present numerical studies on the dynamics of vortex lattices in the NLSE with Dirichlet BC (1.3), i.e., choose the initial data (1.2) as (2.6) and study four cases:

Case I. $M = 3$, $n_1 = n_2 = n_3 = 1$, $\mathbf{x}_1^0 = -\mathbf{x}_3^0 = (d_0, 0)$ and $\mathbf{x}_2^0 = (0, 0)$.

Case II. $M = 3$, $n_1 = -n_2 = n_3 = 1$, $\mathbf{x}_1^0 = -\mathbf{x}_3^0 = (d_0, 0)$ and $\mathbf{x}_2^0 = (0, 0)$.

Case III. $M = 4$, $n_1 = n_2 = -n_3 = -n_4 = 1$, $\mathbf{x}_1^0 = -\mathbf{x}_2^0 = (d_1, 0)$ and $\mathbf{x}_3^0 = -\mathbf{x}_4^0 = (0, d_2)$ with $0 < d_1, d_2 < 1$.

Case IV. $\mathcal{D} = B_5(\mathbf{0})$, $M = 9$, $n_1 = n_2 = \cdots = n_9 = 1$ and the 9 vortex centers are initially located on a 3×3 uniform mesh points for the rectangle $[-d_0, d_0] \times [-d_0, d_0]$ with $0 < d_0 < 1$.

Fig. 4.7 depicts the trajectory and time evolution of $\mathbf{x}_1^0(t)$, $\mathbf{x}_2^0(t)$ and $\mathbf{x}_3^0(t)$ in the NLSE dynamics for Cases I and II. Fig. 4.8 shows contour plots of $|\psi^\varepsilon|$ at different times in the NLSE dynamics for Case III, and Fig. 4.9 depicts contour plots of $-|\psi^\varepsilon|$, $S^\varepsilon(\mathbf{x}, t)$ as well as slice plots of $|\psi^\varepsilon(x, 0, t)|$ for showing sound wave

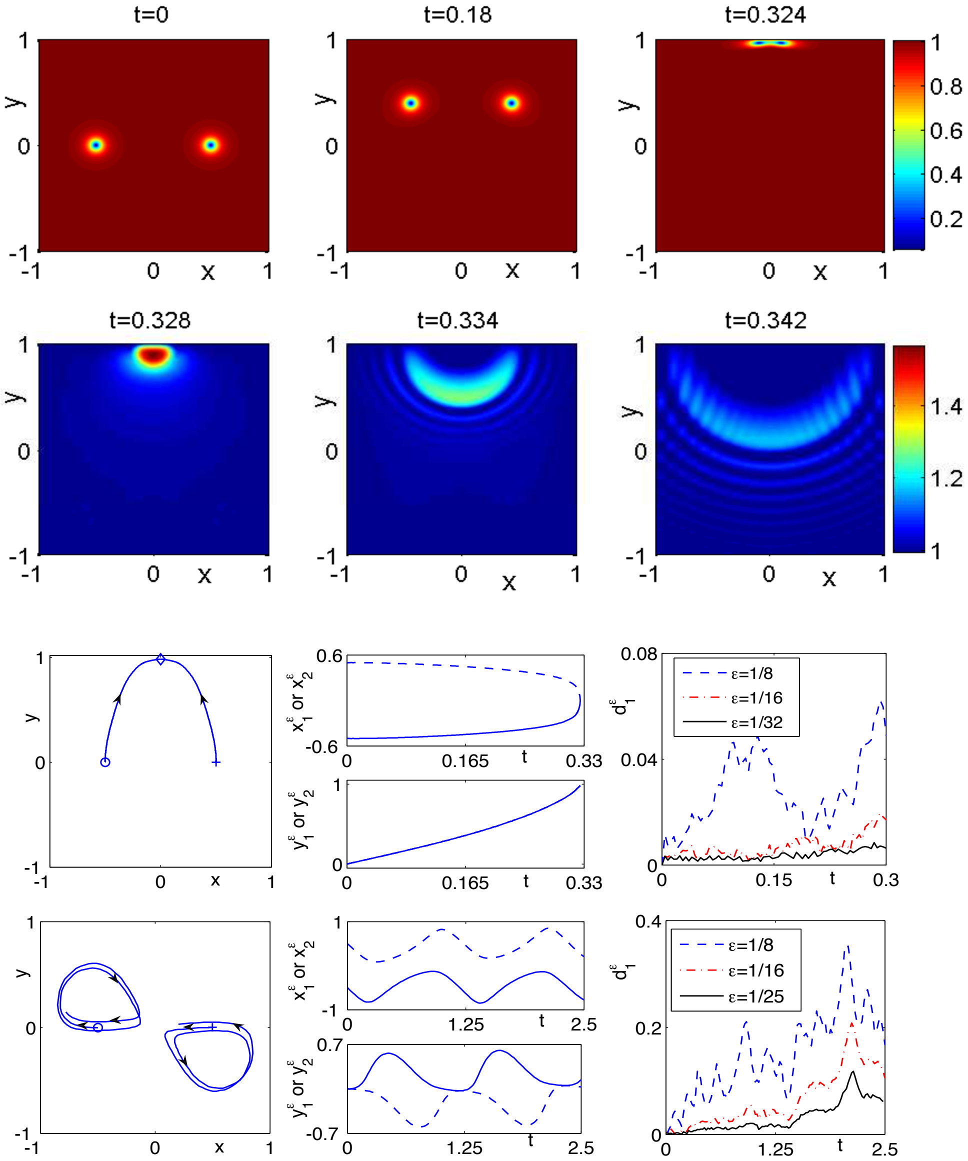

Figure 4.6: Contour plots of $|\psi^\varepsilon(\mathbf{x},t)|$ at different times (top two rows) as well as the trajectory, time evolution of $\mathbf{x}_1^\varepsilon(t)$, $\mathbf{x}_2^\varepsilon(t)$ and $d_1^\varepsilon(t)$ (bottom two rows) for the dynamics of a vortex dipole with different $h(\mathbf{x})$in section 4.1.3: (1). $h(\mathbf{x}) = 0$ (top three rows), (2). $h(\mathbf{x}) = x + y$ (bottom row).

propagation of the NLSE dynamics in Case IV. Based on Figs. 4.7-4.9 and additional computations not shown here for brevity, we can draw the following conclusions: (i). For Case I, there exits a critical time T_c depending on both d_0 and ε such that when

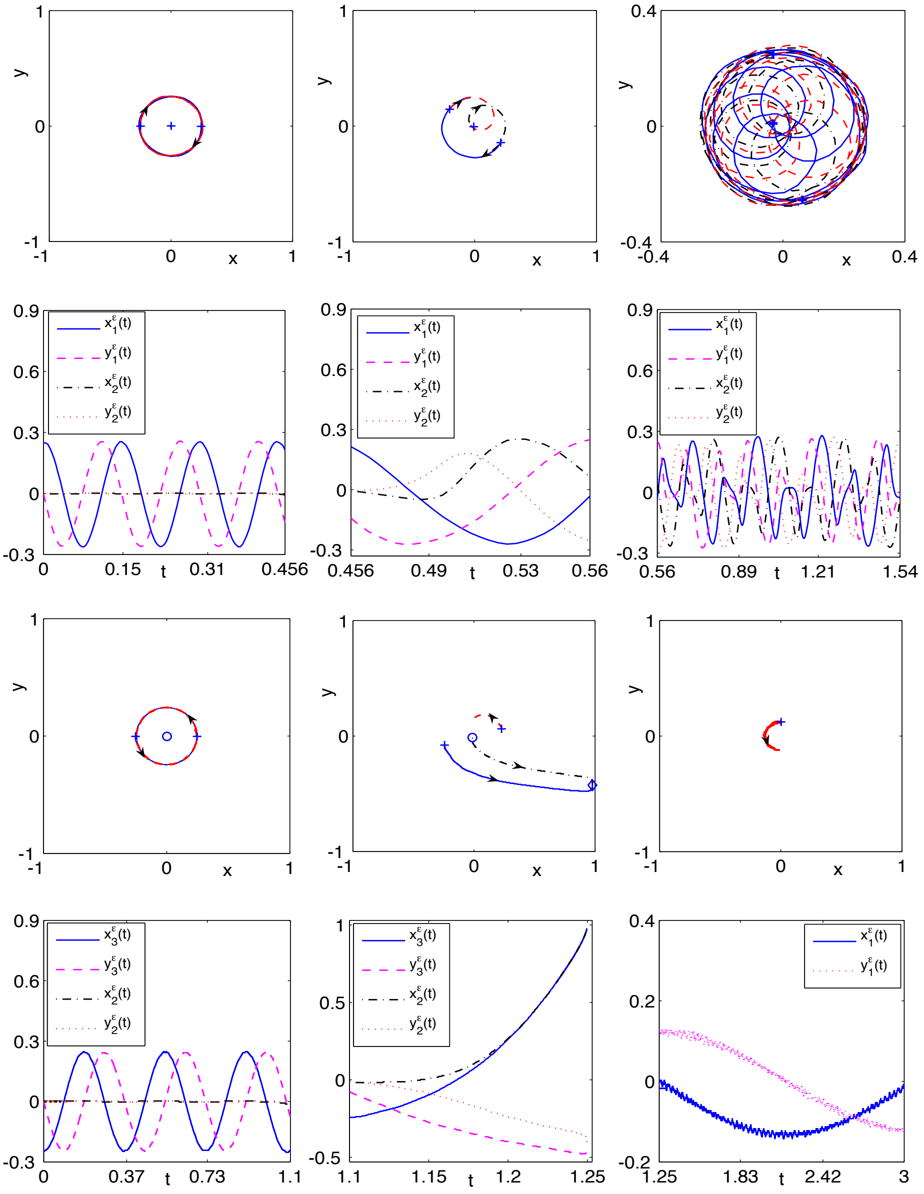

Figure 4.7: Trajectory of the vortex $\mathbf{x}_1^\varepsilon$ (blue line), $\mathbf{x}_2^\varepsilon$ (dark dash-dot line) and $\mathbf{x}_3^\varepsilon$ (red dash line) (first and third rows) and their corresponding time evolution (second and fourth rows) for Case I (top two rows) and Case II (bottom two rows) for small time (left column), intermediate time (middle column) and large time (right column) with $\varepsilon = \frac{1}{40}$ and $d_0 = 0.25$ in section 4.1.4.

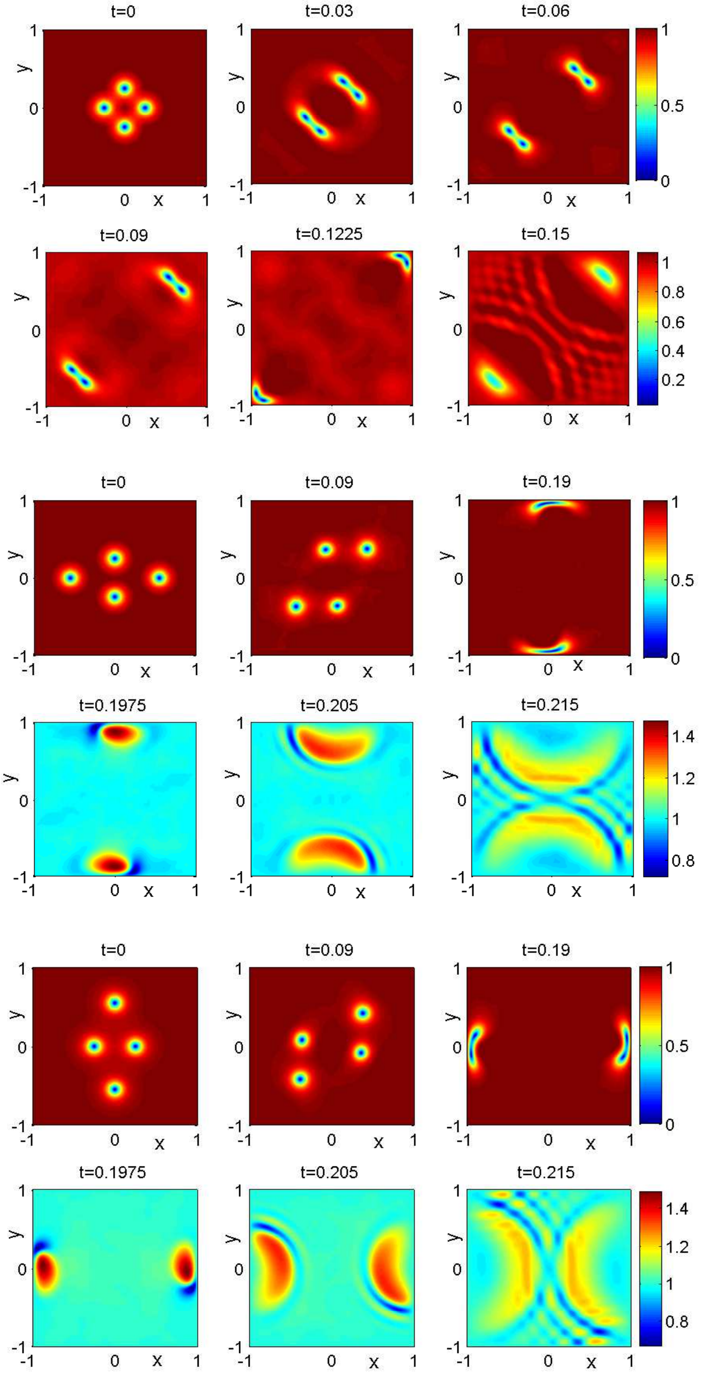

Figure 4.8: Contour plots of $|\psi^\varepsilon(\mathbf{x},t)|$ with $\varepsilon=\frac{1}{16}$ at different times for the NLSE dynamics of a vortex lattice in Case III with different initial locations: $d_1=d_2=0.25$ (top two rows); $d_1=0.55$, $d_2=0.25$ (middle two rows); $d_1=0.25$, $d_2=0.55$ (bottom two rows) in section 4.1.4.

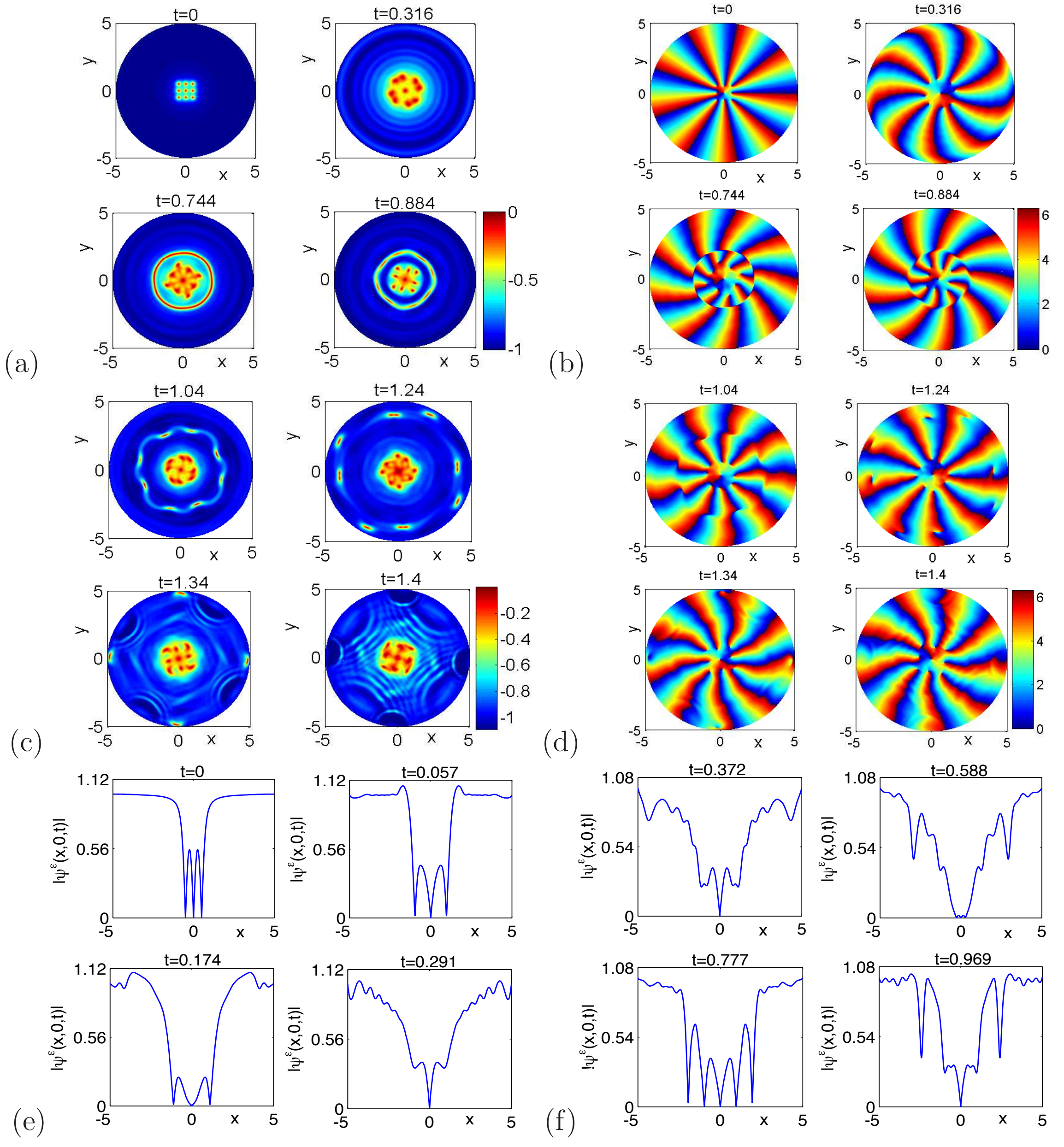

Figure 4.9: Contour plots of $-|\psi^\varepsilon(\mathbf{x},t)|$ ((a) & (c)) and the corresponding phase $S^\varepsilon(\mathbf{x},t)$ ((b) & (d)) as well as slice plots of $|\psi^\varepsilon(x,0,t)|$ ((e) & (f)) at different times for showing sound wave propagation under the NLSE dynamics of a vortex lattice in Case IV with $d_0 = 0.5$ and $\varepsilon = \frac{1}{8}$ in section 4.1.4.

$t < T_c$ the middle vortex (initially at the origin) will not move while the other two vortices rotate clockwise around the origin. This dynamics agrees very well with the

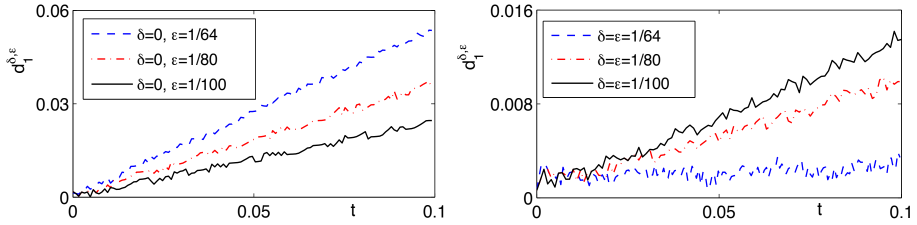

Figure 4.10: Time evolution of $d_1^{\delta,\varepsilon}(t)$ for non-perturbed initial data (left) and perturbed initial data (right) in section 4.1.5

NLSE dynamics in the whole plane [152, 153]. However, when $t > T_c$, the middle vortex will begin to move towards one of the other two vortices and form as a vortex pair which will rotate with each other and also with the other single vortex for a while. Then this pair will separate and one of them will form a new vortex pair with the single vortex, leave the other one to be a new single vortex rotating with them. This process will be repeated tautologically like three dancers exchange their partners alternatively. This shows that the boundary effect seems essentially affect the vortex dynamics and interaction (cf. Fig. 4.7). (ii). For Case II, similar as Case I, there exists a critical time T_c depending on d_0 and ε such that when $t < T_c$ the middle vortex (initially at the origin) will not move while the other two vortices rotate counterclockwise around the origin. This dynamics agrees very well with the NLSE dynamics in the whole plane [152, 153]. However, when $t > T_c$, the middle vortex will begin to move towards one of the other two vortices and form as a vortex dipole which will move nearly parallel towards the boundary and merge near the boundary. Sound waves will be created and reflected back into the domain which drive the leftover vortex in the domain to move (cf. Fig. 4.7). From section 4.1.1, we know that a single vortex in the NLSE with $h(\mathbf{x}) = 0$ does not move, hence this example illustrates clearly the sound-vortex interaction. This also indicates that the reduced dynamical law fails completely after annihilation when $t > T_c$. (iii). For Case III, the four vortices form as two vortex dipoles when t is small. Then the two dipoles will move outwards in opposite direction and finally the two vortices in each vortex dipole merge and annihilate at some place near the boundary. If

$d_1 = d_2$, the two vortex dipoles move symmetrically with respect to the line $y = x$, and merge some place near the top-right and bottom-left corners, respectively; if $d_1 > d_2$, both of them will move towards the top-bottom boundary and merge near there; and if $d_1 < d_2$, both of them will move towards the side boundary and merge near there. New waves are created after merging and they are reflected back into the domain when they hit the boundary (cf. Fig. 4.8). (iv). For Case IV, the vortex initially at the origin does not move due to symmetry, while the other eight vortices rotate clockwise and move along two circle-like trajectories (cf. Fig. 4.9). During the dynamics, sound waves are generated and they propagate outwards and are reflected back into the domain when they hit the boundary. The distances between other vortices and the one centered at the origin increase when sound waves are radiated outwards; on the other hand, they decrease and become even smaller than their initial distances when sound waves are reflected by the boundary and move back into the domain (cf. Fig. 4.9). This example clearly shows sound waves and their impact on the dynamics of vortices.

4.1.5 Radiation and sound wave

We study the radiation property of the NLSE dynamics under Dirichlet BC in this subsection. To this end, we study two types of perturbation.

Type I: Perturbation on the initial data, i.e., we take the initial data (1.2) as

$$\psi^\varepsilon(\mathbf{x}, 0) = \psi_0^{\delta,\varepsilon}(\mathbf{x}) = \psi_0^\varepsilon(\mathbf{x}) + \delta e^{-10((|x|-0.08)^2+y^2)}, \qquad \mathbf{x} = (x, y) \in \mathcal{D}, \qquad (4.1)$$

where ψ_0^ε is given in (2.6) with $h(\mathbf{x}) \equiv 0$, $M = 2$, $n_1 = n_2 = 1$ and $\mathbf{x}_1^0 = -\mathbf{x}_2^0 = (0.1, 0)$. Then we take $\delta = \varepsilon$ and let ε go to 0, and solve the NLSE with initial condition (4.1) for the vortex centers $\mathbf{x}_1^{\delta,\varepsilon}(t)$ and $\mathbf{x}_2^{\delta,\varepsilon}(t)$ and compare them with those from the reduced dynamical law. We denote $d_j^{\delta,\varepsilon}(t) = |x_j^{\delta,\varepsilon}(t) - x_j^r(t)|$ for $j = 1, 2$ as the error. Fig. 4.10 depicts time evolution of $d_1^{\delta,\varepsilon}(t)$ for the case when $\delta = \varepsilon$, i.e., small perturbation, and the case when $\delta = 0$, i.e., no perturbation. From this figure, we can see that the dynamics of the two vortex centers under the NLSE dynamics converge to those obtained from the reduced dynamical law when $\varepsilon \to 0$ without perturbation (cf. Fig. 4.10 left). On the contrary, the two vortex centers under the NLSE dynamics do not converge to those obtained from the reduced dynamical law when $\varepsilon \to 0$ with small perturbation (cf. Fig. 4.10 right). This clearly demonstrates radiation and sound wave effect on vortices in the NLSE dynamics with Dirichlet BC.

Type II: Perturbation by an external potential, i.e., we replace $V(\mathbf{x}) \equiv 1$ in NLSE by $V(\mathbf{x}, t) = 1 - W(\mathbf{x}, t)$ with

$$W(\mathbf{x}, t) = \begin{cases} -\sin(2t)^2, & t \in [0, 0.5], \\ 0, & t > 0.5, \end{cases} \qquad \mathbf{x} \in \mathcal{D}. \tag{4.2}$$

The initial data is chosen as (2.6) with $M = 1$, $n_1 = 1$, $\mathbf{x}_1^0 = (0, 0)$, $\mathcal{D} = B_5(\mathbf{0})$ and $\varepsilon = \frac{1}{4}$. In fact, the perturbation is introduced when $t \in [0, 0.5]$ and is removed after $t = 0.5$. Fig. 4.11 illustrates surface plots of $-|\psi^\varepsilon|$ and contour plots of $S^\varepsilon(\mathbf{x}, t)$ as well as the slice plots of $\psi^\varepsilon(x, 0, t)$ at different times for showing sound wave propagation. From Fig. 4.11, we can see that the perturbed vortex configuration rotates and radiates sound waves. This agrees well with some former prediction in the whole plane, for example, in Lange and Schroers [95] for the case $M = 2$. The waves will be reflected back into the domain when they hit the boundary and then be absorbed by the vortex core. Then the vortex core will radiate new waves and the process is repeated tautologically. This process explicitly illustrates the radiation in the NLSE dynamics.

Remark 4.1.1. *Based on this example and other numerical results not show here for brevity, we can conclude that the vortex with winding number $m = \pm 1$ is dynamically stable under the NLSE dynamics in a bounded domain with a perturbation in the initial data and/or external potential. Meanwhile, we also found numerically that the vortex with winding number $m = 2$ and $\varepsilon = \frac{1}{32}$ is also dynamically stable under a perturbation in the external potential. Actually, Mirionescu [111] indicated that for a vortex with winding number $|m| > 1$, there exists a critical value ε_m^c such*

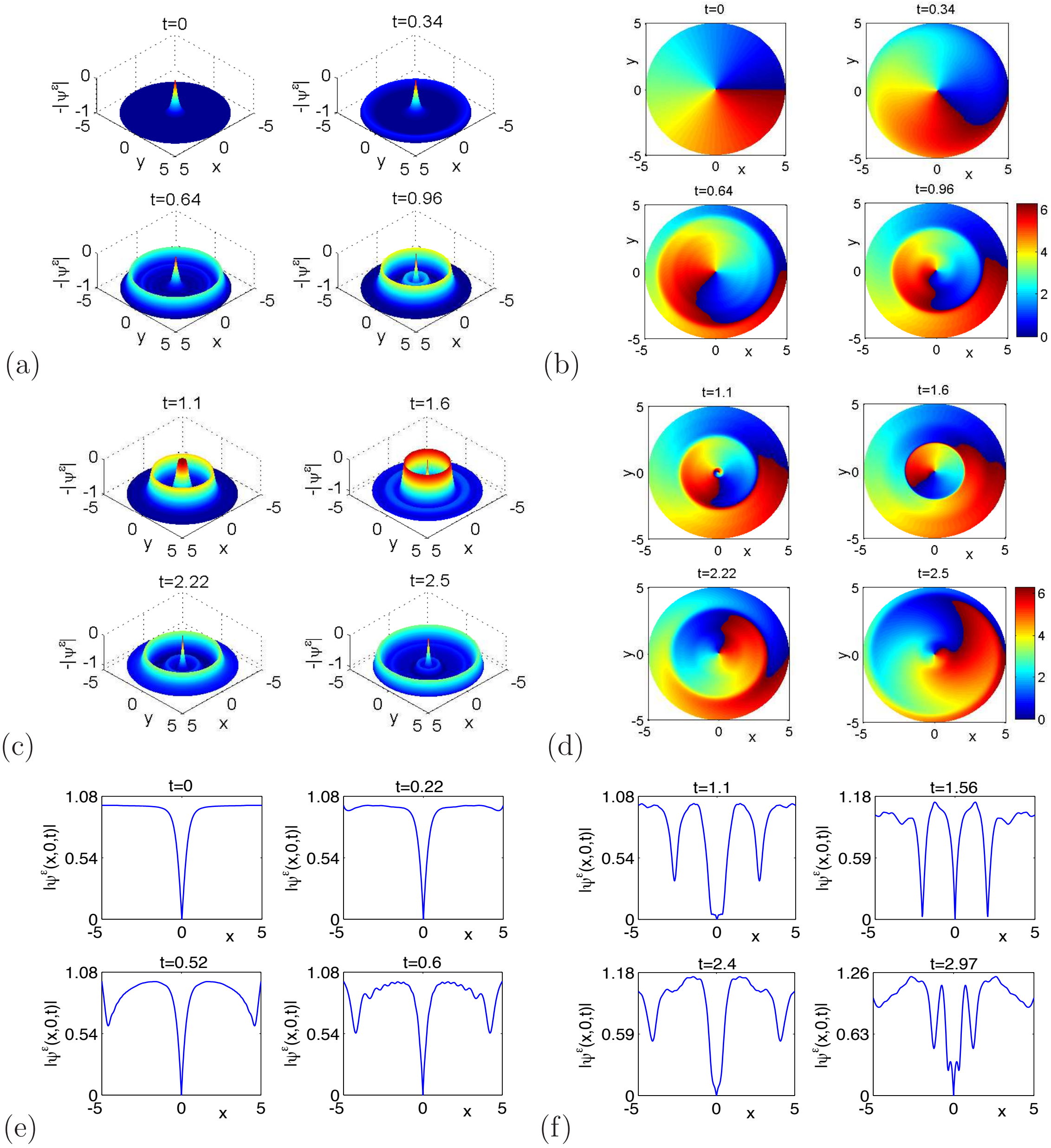

Figure 4.11: Surface plots of $-|\psi^\varepsilon(\mathbf{x},t)|$ ((a) & (c)) and contour plots of the corresponding phase $S^\varepsilon(\mathbf{x},t)$ ((b) & (d)) as well as slice plots of $|\psi^\varepsilon(x,0,t)|$ ((e) & (f)) at different times for showing sound wave propagation under the NLSE dynamics in a disk with $\varepsilon = \frac{1}{4}$ and a perturbation in the potential in section 4.1.5.

that if $\varepsilon < \varepsilon_m^c$, *the vortex is unstable, otherwise the vortex is stable. It was also numerically observed that a vortex with* $|m| > 1$ *is unstable under a perturbation in*

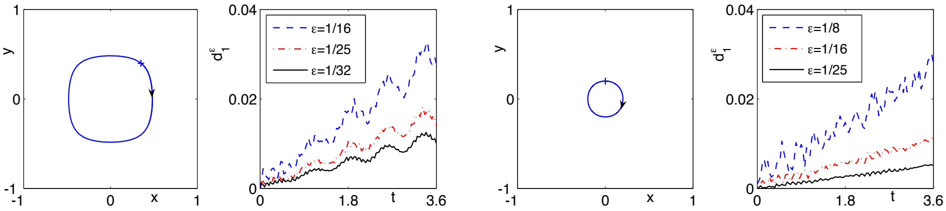

Figure 4.12: Trajectory of the vortex center when $\varepsilon = \frac{1}{32}$ and time evolution of d_1^ε for different ε for the motion of a single vortex in NLSE under homogeneous Neumann BC with $\mathbf{x}_1^0 = (0.35, 0.4)$ (left two) or $\mathbf{x}_1^0 = (0, 0.2)$ (right two) in (2.6) in section 4.2.1.

the potential but stable under a perturbation in the initial data in the whole plane case [152]. Hence, it would be an interesting problem to investigate numerically how the stability of a vortex depends on its winding number, value of ε *and strength and/or type of the perturbation under the NLSE dynamics in bounded domains.*

4.2 Numerical results under Neumann BC

4.2.1 Single vortex

Here we present numerical results of the motion of a single quantized vortex under the NLSE dynamics and its corresponding reduced dynamical laws, i.e., we take $M = 1$ and $n_1 = 1$ in (2.6). Fig. 4.12 depicts trajectory of the vortex center for different $\mathbf{x}_1^0$ in (2.6) when $\varepsilon = \frac{1}{32}$ in NLSE and d_1^ε for different ε. From Fig. 4.12 and additional numerical results not shown here for brevity, we can see that:

(i). If $\mathbf{x}_1^0 = (0, 0)$, the vortex will not move all the time, otherwise, the vortex will move and its initial location $\mathbf{x}_1^0$ does not affect its motion qualitatively. Actually, it moves periodically in a circle-like trajectory centered at the origin. This is quite different from the situation in bounded domain with Dirichlet BC where the motion of a single vortex depends significantly on its initial location for some $h(\mathbf{x})$. It is also quite different from the situation in the whole space where a single vortex doesn't move at all under the initial condition (2.6) when $\mathcal{D} = \mathbb{R}^2$.

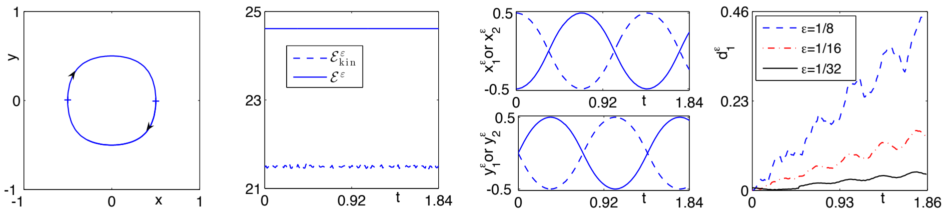

Figure 4.13: Trajectory of the vortex pair (left), time evolution of $\mathcal{E}^\varepsilon$ and $\mathcal{E}^\varepsilon_{\text{kin}}$ (second), $\mathbf{x}^\varepsilon_1(t)$ and $\mathbf{x}^\varepsilon_2(t)$ (third), and $d^\varepsilon_1(t)$ (right) in the NLSE dynamics under homogeneous Neumann BC with $\varepsilon = \frac{1}{32}$ and $d_0 = 0.5$ in section 4.2.2.

(ii). As $\varepsilon \to 0$, the dynamics of the vortex center under the NLSE dynamics converges uniformly in time to that of the reduced dynamical laws. In fact, based on our extensive numerical experiments, the motion of the vortex center from the reduced dynamical laws agrees with that from the NLSE dynamics qualitatively when $0 < \varepsilon < 1$ and quantitatively when $0 < \varepsilon \ll 1$.

4.2.2 Vortex pair

Here we present numerical results of the interaction of vortex pair under the NLSE dynamics and its corresponding reduced dynamical laws, i.e., we take $M = 2$, $n_1 = n_2 = 1$ and $\mathbf{x}^0_2 = -\mathbf{x}^0_1 = (d_0, 0)$ with $0 < d_0 < 1$ in (2.6). Fig. 4.13 depicts the trajectory of the vortex pair, time evolution of $\mathcal{E}^\varepsilon(t)$, $\mathcal{E}^\varepsilon_{\text{kin}}(t)$, $\mathbf{x}^\varepsilon_1(t)$, $\mathbf{x}^\varepsilon_2(t)$ and $d^\varepsilon_1(t)$ when $\varepsilon = \frac{1}{32}$ in NLSE and $d_0 = 0.5$ in (2.6).

From Fig. 4.13 and additional numerical results not shown here for brevity, we can draw the following conclusions for the interaction of vortex pair under the NLSE dynamics with homogeneous Neumann BC: (i). The total energy is conserved numerically very well during the dynamics. (ii). The two vortices move periodically along a circle-like trajectory for all $0 < d_0 < 1$ and their trajectories are symmetric. (iii). When $\varepsilon \to 0$, the dynamics of the two vortex centers under the NLSE dynamics converges uniformly in time to that of the reduced dynamical laws which verifies numerically the validation of the reduced dynamical laws in this case. In fact, based on our extensive numerical experiments, the motions of the two vortex centers from

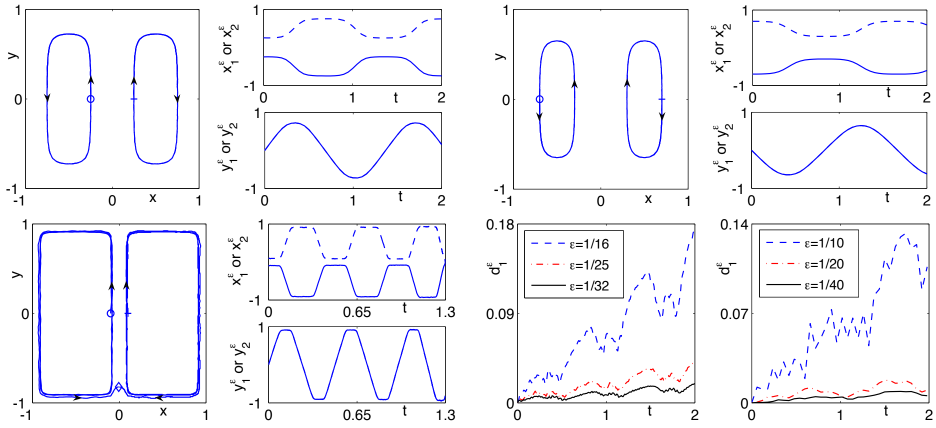

Figure 4.14: Trajectory and time evolution of $\mathbf{x}_1^\varepsilon(t)$ and $\mathbf{x}_2^\varepsilon(t)$ for $d_0 = 0.25$ (top left two), $d_0 = 0.7$ (top right two) and $d_0 = 0.1$ (bottom left two) and time evolution of $d_1^\varepsilon(t)$ for $d_0 = 0.25$ and $d_0 = 0.7$ (bottom right two) in section 4.2.3.

the reduced dynamical laws agree with those from the NLSE dynamics qualitatively when $0 < \varepsilon < 1$ and quantitatively when $0 < \varepsilon \ll 1$.

4.2.3 Vortex dipole

Here we present numerical results of the interaction of vortex dipole under the NLSE dynamics and its corresponding reduced dynamical laws, i.e., we take $M = 2$, $n_1 = -n_2 = -1$, $\mathbf{x}_2^0 = -\mathbf{x}_1^0 = (d_0, 0)$ with different d_0 and $\varepsilon = \frac{1}{32}$. Fig. 4.14 depicts the trajectory of the vortex dipole, time evolution of $\mathbf{x}_1^\varepsilon(t)$, $\mathbf{x}_2^\varepsilon(t)$ and $d_1^\varepsilon(t)$.

From Fig. 4.14 and additional numerical results not shown here for brevity, we can draw the following conclusions for the interaction of vortex dipole under the NLSE dynamics with homogeneous Neumann BC: (i). The total energy is conserved numerically very well during the dynamics. (ii). The pattern of the motion of the two vortices depends on their initial locations. (iii). The two vortices will move symmetrically (and periodically if they are well separated) with respect to y-axis. Moreover, there exists a critical value $d_c^r = d_c^\varepsilon = d_c$ for $0 < \varepsilon < 1$, which is found numerically as $d_c = 0.5$, such that if initially $d_0 < d_c$, the two vortices will move firstly upwards to the top boundary, then turn outwards to the side boundary and finally move counter-clockwise and clockwise, respectively (cf. Fig. 4.14). While if $d_0 > d_c$, then they will move firstly downwards to the bottom boundary, then turn inwards to the domain and finally move counter-clockwise and clockwise, respectively (cf. Fig. 4.14). Certainly, when $d_0 = 0.5$, the vortex dipole does not move due to symmetry. (iv). For fixed $0 < \varepsilon < 1$, there exists another critical value $\hat{d}_c^\varepsilon$ satisfying $\lim_{\varepsilon\to 0} \hat{d}_c^\varepsilon = 0$, such that if $d_0 < \hat{d}_c^\varepsilon$, the vortex dipole in the NLSE dynamics will merge at a finite time T_c depending on ε and d_0 (cf. Fig. 4.14). However, the vortex dipole from the reduced dynamical laws never merges at finite time. Hence, the reduced dynamical laws fail qualitatively if $0 < d_0 < \hat{d}_0^\varepsilon$. (v). For fixed d_0, when $\varepsilon \to 0$, the dynamics of the two vortex centers in the NLSE dynamics converges uniformly in time to that of the reduced dynamical laws before they merge (cf. Figs. 4.14) which verifies numerically the validation of the reduced dynamical laws in this case. In fact, based on our extensive numerical experiments, the motions of the two vortex centers from the reduced dynamical laws agree with those from the NLSE dynamics qualitatively when $0 < \varepsilon < 1$ and quantitatively when $0 < \varepsilon \ll 1$.

4.2.4 Vortex lattice

Here we present numerical studies on the dynamics of vortex lattices in the NLSE with homogeneous Neumann BC, i.e., we choose the initial data (1.2) as (2.6) and study four cases:

Case I. $M = 3$, $n_1 = n_2 = n_3 = 1$, $\mathbf{x}_1^0 = -\mathbf{x}_3^0 = (d_0, 0)$ and $\mathbf{x}_2^0 = (0, 0)$.

Case II. $M = 4$, $n_1 = n_2 = n_3 = n_4 = 1$, $\mathbf{x}_1^0 = -\mathbf{x}_2^0 = (d_1, 0)$ and $\mathbf{x}_3^0 = -\mathbf{x}_4^0 = (d_2, 0)$ with $0 < d_1 \neq d_2 < 1$.

Case III. $M = 4$, $n_1 = n_2 = -n_3 = -n_4 = 1$, $\mathbf{x}_1^0 = -\mathbf{x}_2^0 = (d_1, 0)$ and $\mathbf{x}_3^0 = -\mathbf{x}_4^0 = (0, d_2)$ with $0 < d_1, d_2 < 1$.

Case IV. $M = 9$, $n_1 = \cdots = n_9 = 1$, and the vortex centers are initially located on a 3×3 uniform mesh points for the rectangle $[-d_0, d_0]\times[-d_0, d_0]$ with $0 < d_0 < 1$.

Fig. 4.15 shows trajectory and time evolution of $\mathbf{x}_1^\varepsilon(t)$, $\mathbf{x}_2^\varepsilon(t)$ and $\mathbf{x}_3^\varepsilon(t)$ in the NLSE dynamics for Case I. Fig. 4.16 depicts contour plots of $|\psi^\varepsilon|$ at different times

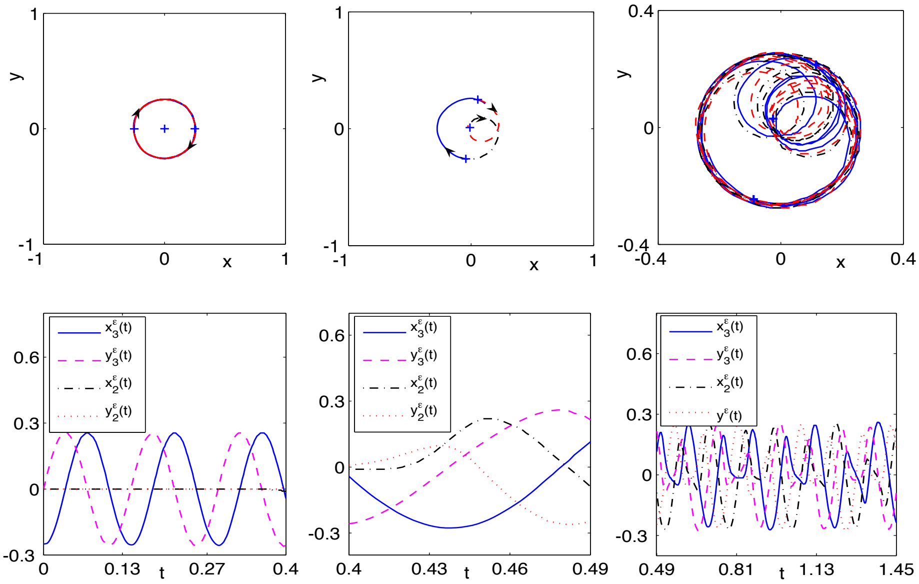

Figure 4.15: Trajectory of the vortex $\mathbf{x}_1^\varepsilon$ (blue line), $\mathbf{x}_2^\varepsilon$ (dark dash-dot line) and $\mathbf{x}_3^\varepsilon$ (red dash line) and their corresponding time evolution for Case I during small time (left column), intermediate time (middle column) and large time (right column) with $\varepsilon = \frac{1}{40}$ and $d_0 = 0.25$ in section 4.2.4.

in NLSE dynamics for Cases II and III, and Fig. 4.17 shows contour plots of $-|\psi^\varepsilon|$ and slice plots of $|\psi(0, y, t)|$ in NLSE dynamics for Case IV to show sound wave propagation. Based on Figs. 4.15-4.17 and additional results not shown here for brevity, we can draw the following conclusions: (i). For Case I, there exits a critical time T_c depending on both d_0 and ε such that when $t < T_c$ the middle vortex (initially at the origin) will not move while the other two vortices rotate clockwise around the origin. This dynamics agrees very well with the NLSE dynamics in the whole plane [152, 153]. However, when $t > T_c$, the middle vortex will begin to move towards one of the other two vortices and form as a vortex pair which will rotate with each other and also with the other single vortex for a while. Then the two vortices in the pair will separate, one of them will form a new vortex pair with the third single vortex leaving the other one to be a new single vortex that rotates around them. This process will repeat tautologically like three dancers exchange their partners

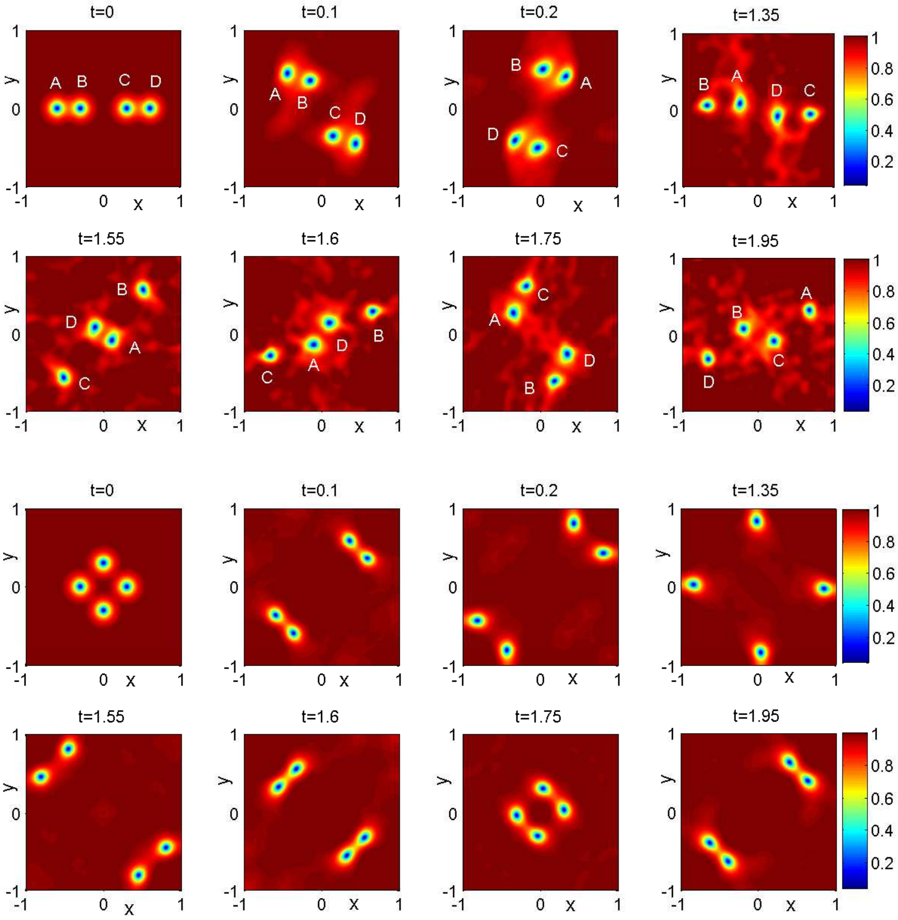

Figure 4.16: Contour plots of $|\psi^\varepsilon(\mathbf{x},t)|$ with $\varepsilon=\frac{1}{16}$ at different times for the NLSE dynamics of a vortex lattice for Case II with $d_1=0.6, d_2=0.3$ (top two rows) and Case III with $d_1=d_2=0.3$ (bottom two rows) in section 4.2.4.

alternatively. This indicates that the boundary effect essentially affects the vortex dynamics and interaction (cf. Fig. 4.15). (ii). For Case II, the four vortices form as two vortex pairs when t is small. These two pairs rotate with each other clockwise, meanwhile, the two vortices in each pair also rotate with each other clockwise, and radiations and sound waves are emitted. The sound waves propagate radially and are reflected back into the domain when they hit the boundary, which push the two vortex pairs get closer. When the two vortex pairs get close enough, the two vortices with smallest distance among the four form a new vortex pair and leave the rest

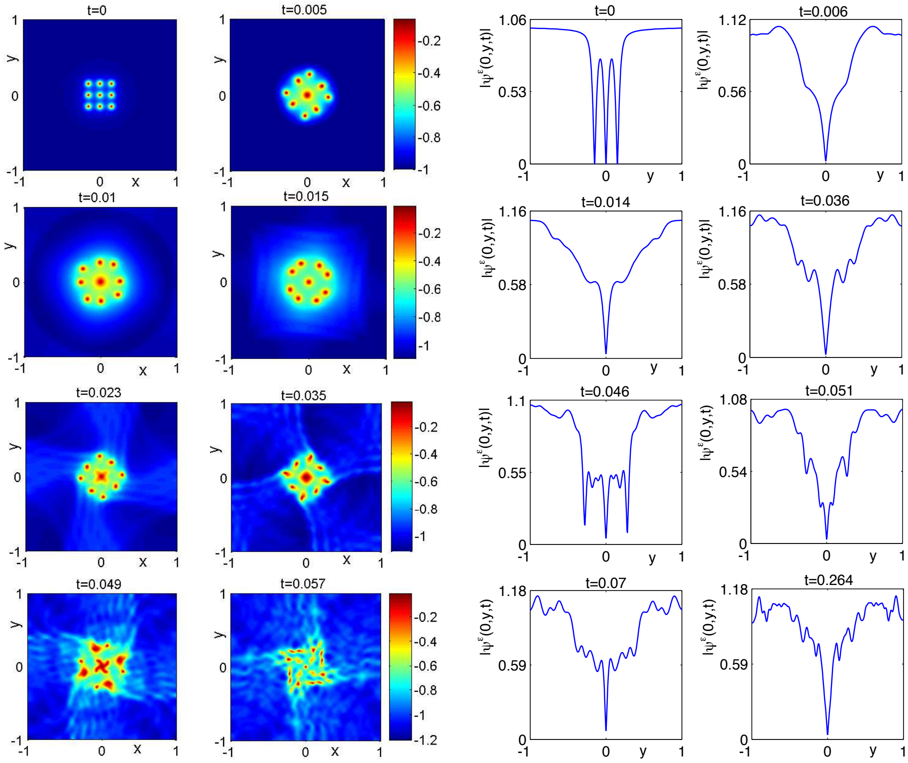

Figure 4.17: Contour plots of $-|\psi^\varepsilon(\mathbf{x},t)|$ (left) and slice plots of $|\psi^\varepsilon(0,y,t)|$ (right) at different times under the NLSE dynamics of a vortex lattice in Case IV with $d_0 = 0.15$ and $\varepsilon = \frac{1}{40}$ for showing sound wave propagation in section 4.2.4.

two as single vortex individually. The vortex pair rotates around the origin. This process is iteratively repeated during the dynamics (cf. Fig. 4.16 top two rows). (iii). For Case III, when t is small, the four vortices form as two vortex dipoles and they move symmetrically with respect to the line $y = -x$ towards the top right and bottom left corners, respectively. Meanwhile, the two vortices in each dipole move symmetrically with respect to the line $y = x$. After a while and when the two dipoles arrive at some places near the corners, the two vortices in each dipole split with each other and re-formulate two different dipoles. After this, the two vortices in each dipole move symmetrically with respect to the line $y = -x$, and the two new dipoles then move symmetrically with respect to the line $y = x$ towards their initial locations. This process is then repeated periodically (cf. Fig. 4.16 bottom two rows). (iv). For Case IV, the vortex initially centered at the origin does not move due to symmetry, and the other eight vortices rotate clockwise and move along two circle-like trajectories (cf. Fig. 4.17). During the dynamics, sound waves are generated and they propagate outwards. Some of the sound waves will exit out of the domain while others are reflected back into the domain when they hit the boundary. The distances between the one located at the origin and the other vortices become larger when the sound waves are radiated outwards, while they decrease when the sound waves are reflected from the boundary and move back into the domain (cf. Fig. 4.17).

4.2.5 Radiation and sound wave

Here we study numerically how the radiation and sound waves affect the dynamics of quantized vortices in the NLSE dynamics under homogeneous Neumann BC. To this end, we take the initial data (1.2) as (4.1) with ψ_0^ε chosen as (2.6) with $M = 2$, $n_1 = n_2 = 1$ and $\mathbf{x}_1^0 = -\mathbf{x}_2^0 = (0.1, 0)$ and $h(\mathbf{x})$ as (3.3). Then we take $\delta = \varepsilon$ and let ε goes to 0, and solve the NLSE with initial condition (4.1) for the vortex centers $\mathbf{x}_1^{\delta,\varepsilon}(t)$ and $\mathbf{x}_2^{\delta,\varepsilon}(t)$ and compare them with those from the reduced dynamical law. We denote $d_j^{\delta,\varepsilon}(t) = |x_j^{\delta,\varepsilon}(t) - x_j^r(t)|$ for $j = 1, 2$ as the error. Fig. 4.18 depicts time evolution of $d_1^{\delta,\varepsilon}(t)$ for the case when $\delta = \varepsilon$, i.e., small perturbation, and the case when $\delta = 0$, i.e., no perturbation. From this figure, we can see that the dynamics of the two vortex centers under the NLSE dynamics converge to those obtained from the reduced dynamical law when $\varepsilon \to 0$ without perturbation (cf. Fig. 4.18 left). On the contrary, the two vortex centers under the NLSE dynamics do not converge to those obtained from the reduced dynamical law when $\varepsilon \to 0$ with small perturbation (cf. Fig. 4.18 right). This clearly demonstrates radiation and sound wave effect on vortices under the NLSE dynamics with homogenous Neumann BC.

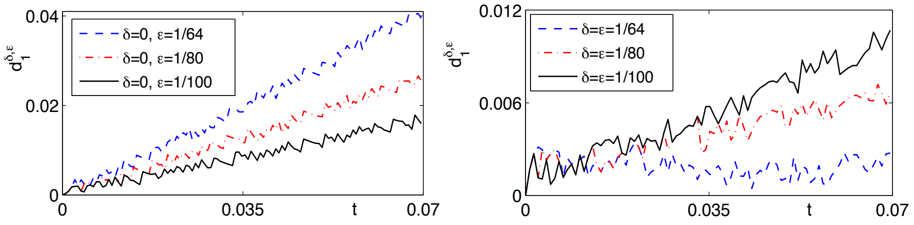

Figure 4.18: Time evolution of $d_1^{\delta,\varepsilon}(t)$ for non-perturbed initial data (left) and perturbed initial data (right) in section 4.2.5

4.3 Conclusion

In this chapter, by applying the efficient and accurate numerical methods proposed in chapter 2 to simulate nonlinear Schrödinger equation (NLSE) with a dimensionless parameter $0 < \varepsilon < 1$ in bounded domains under either Dirichlet or homogenous Neumann BC as well as its corresponding reduced dynamical laws for the dynamics of M quantized vortex centers, we studied numerically quantized vortex dynamics and interaction and investigated the sound-vortex interaction [62, 114] in NLSE for superfluidity as well as examined the validity of the corresponding reduced dynamical laws under different initial setups. Based on extensive numerical results, firstly, we verified that the dynamics of vortex centers under the NLSE dynamics converges to that of the reduced dynamical laws when $\varepsilon \to 0$ before they collide and/or move too close to the boundary. Certainly the reduced dynamical law is only valid up to the first collision time of any two vortices, therefore they cannot show the vortex dynamics after collision, which, however, can be observed and investigated by our directly numerical simulations. Secondly, we identified the parameter regimes where the reduced dynamical laws agree with quantitatively and/or qualitatively as well as fail to agree with those from the NLSE dynamics. We concluded that the dynamical pattern of two vortices depend on the initial phase shift (in the case of Dirichlet BC) as well as the initial distance of the two vortices. Thirdly, We also found that the boundary effect affect the vortex interaction very much, which lead to very different nonlinear phenomena from those observed in the whole plane case. The Dirichlet BC might correspond to introduce a tangential force (clockwise force for negative charged vortex while counter-clockwise for positive charged vortex) while the Neumann BC might correspond to apply a normal force at the boundary to the vortices, hence vortices might move according to a crescent-like trajectory, or move nearly parallel to the boundary without going outside the domain, or merge near the boundary in some situation. Moreover, we found that the radiation of NLSE dynamics which is carried by oscillating sound waves modifies the motion of vortices much, especially in the dynamics of vortex lattice, highly co-rotating vortex pairs and overlapping vortices. However, it should be reminded that the motion of the vortices still qualitatively obeys the reduced dynamical law when sound waves have moved away from them, either absorbed by the vortex core or the boundary. Finally, we would like to remark here that it should be an interesting question to find out how the dynamics pattern of the vortices depend on the domain shape and size as well as the distances between vortices, and it might be fascinating and difficult problems to extend the reduced dynamical laws for the motion of vortices involving vortex collision and splitting, which has been conducted by Serfaty [132] and Bethuel et al. [30] in the context of Ginzburg-Landau equation, as well as find possible corrections to the reduced dynamical laws due to radiation.

Chapter 5

Vortex dynamics in CGLE

In this chapter, we apply the numerical method presented in chapter 2 to simulate quantized vortex interaction of CGLE, i.e., $\lambda_\varepsilon \neq 0$, $\beta \neq 0$ in GLSE (1.1), with different ε and under different initial setups including single vortex, vortex pair, vortex dipole and vortex lattice. Let $\lambda_\varepsilon = \frac{\alpha}{\ln(1/\varepsilon)}$, we study how the dimensionless parameter ε, initial setup, boundary value and geometry of the domain $\mathcal{D}$ affect the dynamics and interaction of vortices. Moreover, we compare the results obtained from the CGLE with those from the corresponding reduced dynamical laws, and identify the cases where the reduced dynamical laws agree qualitatively and/or quantitatively as well as fail to agree with those from CGLE on vortex interaction. Finally, we also obtain numerically different patterns of the steady states for quantized vortex lattices and study the alignment of the vortices in the steady state.

Without specification, we let $\alpha = \beta = 1$ and choose the initial data as the same one in section 3.1 in chapter 3.

5.1 Numerical results under Dirichlet BC

5.1.1 Single vortex

In this subsection, we present numerical results of the motion of a single quantized vortex in the CGLE dynamics and the corresponding reduced dynamics, i.e we take $M = 1$, $n_1 = 1$ in (2.6). To study how the initial phase shift $h(\mathbf{x})$ and initial location of the vortex $\mathbf{x}_0$ affect the motion of the vortex and to understand the validity of the reduced dynamical law, we consider the following 12 cases:

- Case I-III: $\mathbf{x}_1^0 = (0, 0)$, and $h(\mathbf{x})$ is chosen as Mode 1, 2 and 3, respectively;
- Case IV-VIII: $\mathbf{x}_1^0 = (0.1, 0)$, and $h(\mathbf{x})$ is chosen as Mode 1, 2, 3, 4 and 5, respectively;
- Case IX-XII: $\mathbf{x}_1^0 = (0.1, 0.2)$, and $h(\mathbf{x})$ is chosen as Mode 2, 3, 4 and 5, respectively.

Moreover, to study the effect of domain geometry, we consider domains $\mathcal{D}$ of three types: type I: $\mathcal{D} = [-1, 1] \times [-1, 1]$, type II: $\mathcal{D} = [-1, 1] \times [-0.65, 0.65]$, type III: $\mathcal{D} = B_1(0)$, and study additionally the following 4 cases:

- Case XIII-XIV: $\mathbf{x}_1^0 = (0, 0)$, $h(\mathbf{x}) = x + y$ and domain $\mathcal{D}$ is chosen as type II and III, respectively;
- Case XV-XVI: $\mathbf{x}_1^0 = (0.1, 0.2)$, $h(\mathbf{x}) = x^2 - y^2$ and domain $\mathcal{D}$ is chosen as type II and III, respectively.

Fig. 5.1 depicts trajectory of the vortex center when $\varepsilon = \frac{1}{32}$ for cases II-IV and VI as well as time evolution of $d_1^\varepsilon(t)$ for different ε for cases II and VI. Fig. 5.2 depicts trajectory of the vortex center for cases V-XII, while Fig. 5.3 shows that for cases I, X, XIII-XVII when $\varepsilon = \frac{1}{32}$ in CGLE. From Figs. 5.1-5.3 and additional numerical experiments not shown here for brevity, we can draw following conclusions: (i). When $h(\mathbf{x}) \equiv 0$, the vortex center doesn't move, which is similar to the vortex

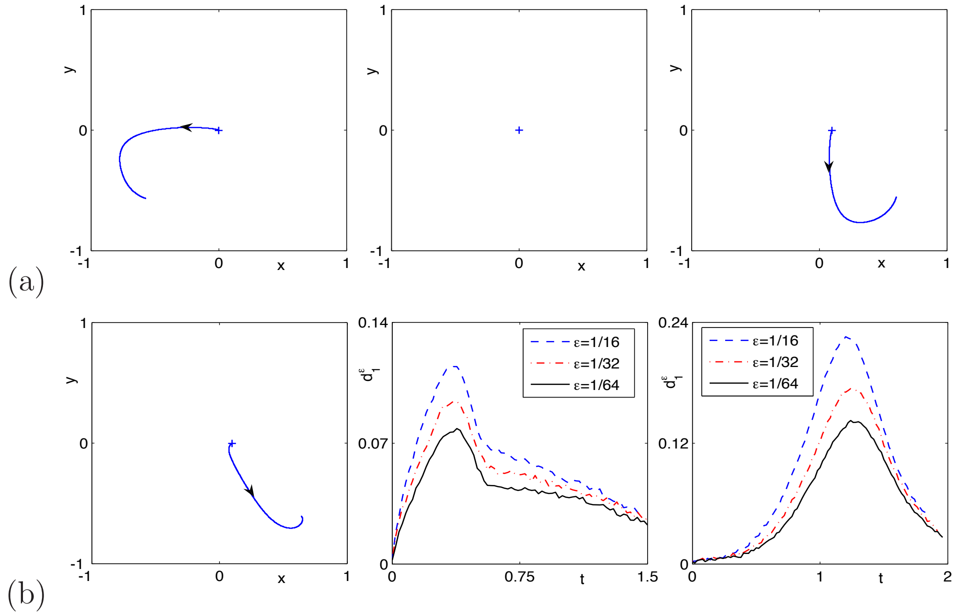

Figure 5.1: Trajectory of the vortex center in CGLE under Dirichlet BC when $\varepsilon = \frac{1}{32}$ for cases II-IV and VI and time evolution of d_1^ε for different ε for cases II and VI (from left to right and then from top to bottom) in section 5.1.1.

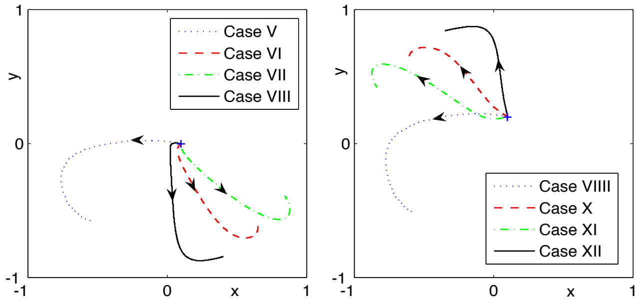

Figure 5.2: Trajectory of the vortex center in CGLE under Dirichlet BC when $\varepsilon = \frac{1}{32}$ for cases IV-VII (left) and cases V-XII (right) in section 5.1.1.

dynamics in the whole space and in GLE and NLSE dynamics. (ii). When $h(\mathbf{x}) = (x+by)(x-\frac{y}{b})$ with $b \neq 0$, the vortex does not move if $\mathbf{x}_0 = (0,0)$, while it does move if $\mathbf{x}_0 \neq (0,0)$ (cf. case III and VI for $b=1$). This is also same with the phenomena in GLE and NLSE dynamics. (iii). When $h(\mathbf{x}) \neq 0$ and $h(\mathbf{x}) \neq (x+by)(x-\frac{y}{b})$ with $b \neq 0$, in general, the vortex center does move to a different point from its

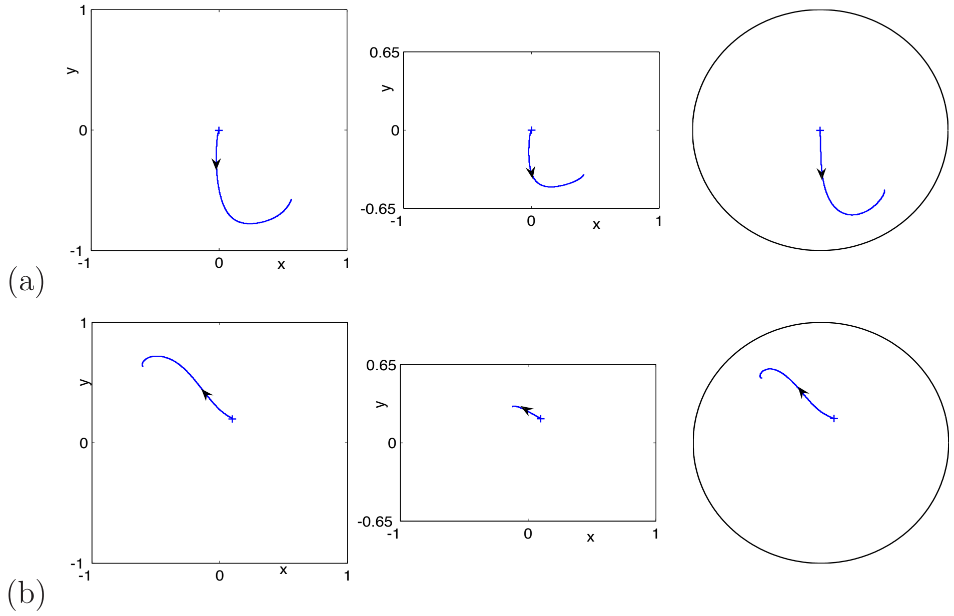

Figure 5.3: Trajectory of the vortex center in CGLE under Dirichlet BC when $\varepsilon = \frac{1}{32}$ for cases: (a) I, XIII, XIV, (b) X, XV, XVI (from left to right) in section 5.1.1.

initial location and stays there forever. This is quite different from the situation in the whole space, where a single vortex may move to infinity under the initial data (2.6) with $h(\mathbf{x}) \neq 0$. (iv). In general, the initial location, the geometry of the domain and the boundary value will all affect the motion of the vortex center. (v). When $\varepsilon \to 0$, the dynamics of the vortex center in the CGLE dynamics converges uniformly in time to that in the reduced dynamics (cf. Fig. 5.1) which verifies numerically the validation of the reduced dynamical laws. In fact, based on our extensive numerical experiments, the motion of the vortex center from the reduced dynamical laws agrees with those from the CGLE dynamics qualitatively when $0 < \varepsilon < 1$ and quantitatively when $0 < \varepsilon \ll 1$.

5.1.2 Vortex pair

Here we present numerical results of the interaction of vortex pair in the CGLE dynamics and its corresponding reduced dynamics, i.e., we take $M = 2$, $n_1 = n_2 = 1$, $\mathbf{x}_1^0 = (-0.3, 0)$ and $\mathbf{x}_2^0 = (0.3, 0)$ in (2.6). Fig. 5.4 depicts the trajectory of the vortex

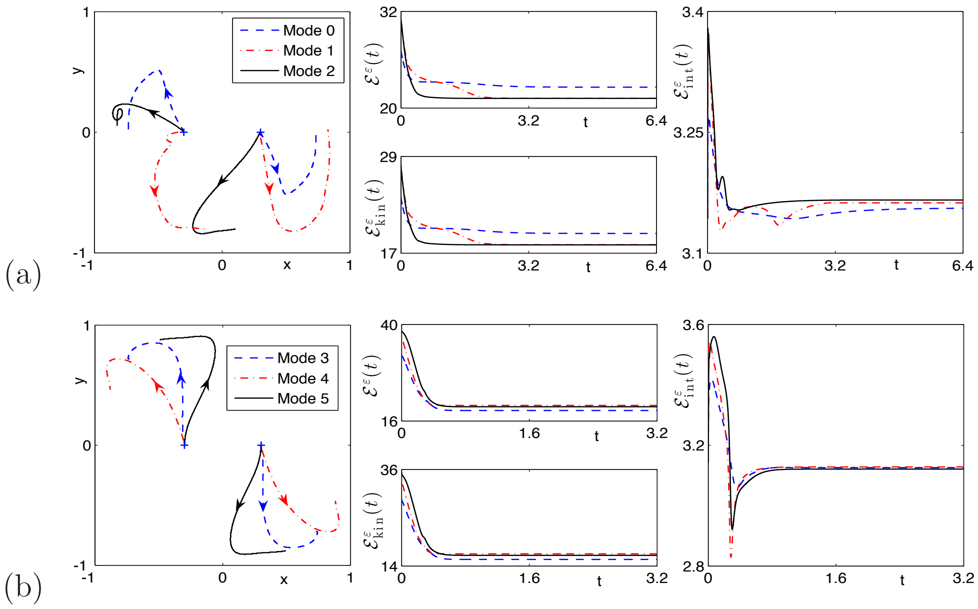

Figure 5.4: Trajectory of the vortex centers (a) and their corresponding time evolution of the GL functionals (b) in CGLE dynamics under Dirichlet BC when $\varepsilon = \frac{1}{25}$ with different $h(\mathbf{x})$ in (2.6) in section 5.1.2.

centers and their corresponding time evolution of the GL functionals when $\varepsilon = \frac{1}{25}$ in the CGLE with different $h(\mathbf{x})$ in (2.6), while Fig. 5.5 shows contour plots of $|\psi^\varepsilon(\mathbf{x},t)|$ for $\varepsilon = \frac{1}{25}$ at different times as well as the time evolution of $\mathbf{x}_1^\varepsilon(t)$, $\mathbf{x}_1^{\rm r}(t)$ and $d_1^\varepsilon(t)$ for different ε with $h(\mathbf{x}) = 0$ in (2.6).

From Figs. 5.4 and 5.5 and additional numerical experiments now shown here for brevity, we can draw the following conclusions for the interaction of vortex pair in the CGLE dynamics with Dirichlet BC: (i). The two vortices undergo a repulsive interaction, they never collide. They rotate with each other and meanwhile move apart from each other towards the boundary of $\mathcal{D}$ and finally stop somewhere near the boundary, which indicates that the boundary imposes a repulsive force on the vortices (cf. Fig. 5.4). As shown in previous chapters, a vortex pair in the GLE dynamics moves outward along the line that connects the two vortices and finally stay steady near the boundary, while in the NLSE dynamics the two vortices always rotate around each other periodically. Hence, the motion of the vortex pair here is somehow the combination of that in the GLE and NLSE dynamics. Actually, from extensive numerical results, we find that the larger the value β (α) is, the closer the motion in CGLE dynamics is to that in NLSE (GLE) dynamics, which evidence numerically that the CGLE under Dirichlet BC is somehow in between the GLE and NLSE under Dirichlet BC. (ii). The phase shift $h(\mathbf{x})$ affects the motion of the vortices significantly. When $h(\mathbf{x}) = (x + by)(x - \frac{y}{b})$ with $b \neq 0$, the vortices will move outward symmetric with respect to the origin, i.e., $\mathbf{x}_1(t) = -\mathbf{x}_2(t)$ (cf. Fig. 5.4). (iii). When $\varepsilon \to 0$, the dynamics of the two vortex centers in the CGLE dynamics converges uniformly in time to that in the reduced dynamics (cf. Fig. 5.5) which verifies numerically the validation of the reduced dynamical laws in this case. In fact, based on our extensive numerical experiments, the motions of the two vortex centers from the reduced dynamical laws agree with those from the CGLE dynamics qualitatively when $0 < \varepsilon < 1$ and quantitatively when $0 < \varepsilon \ll 1$. (iv). During the dynamics of CGLE, the GL functional and its kinetic part decrease when time increases, its interaction part changes dramatically when t is small, and when $t \to \infty$, all the three quantities converge to constants (cf. Fig. 5.4), which immediately imply that a steady state solution will be reached when $t \to \infty$.

5.1.3 Vortex dipole

Here we present numerical results of the interaction of vortex dipole under the CGLE dynamics and its corresponding reduced dynamical laws, i.e., we take $M = 2$, $n_1 = -n_2 = -1$, $\mathbf{x}_2^0 = -\mathbf{x}_1^0 = (0.3, 0)$ in (2.6). Fig. 5.6 depicts the trajectory of the vortex centers and their corresponding time evolution of the GL functionals when $\varepsilon = \frac{1}{25}$ in the CGLE with different $h(\mathbf{x})$ in (2.6), while Fig. 5.7 shows contour plot of $|\psi^\varepsilon(\mathbf{x}, t)|$ for $\varepsilon = \frac{1}{25}$ at different times as well as the time evolution of $\mathbf{x}_1^\varepsilon(t)$, $\mathbf{x}_1^{\mathrm{r}}(t)$ and $d_1^\varepsilon(t)$ for different ε with $h(\mathbf{x}) = 0$ in (2.6). From Figs. 5.6 and 5.7 and additional numerical experiments now shown here for brevity, we can draw the following conclusions for the interaction of vortex dipole in the CGLE dynamics with Dirichlet BC: (i). The two vortices undergo an attractive interaction, they

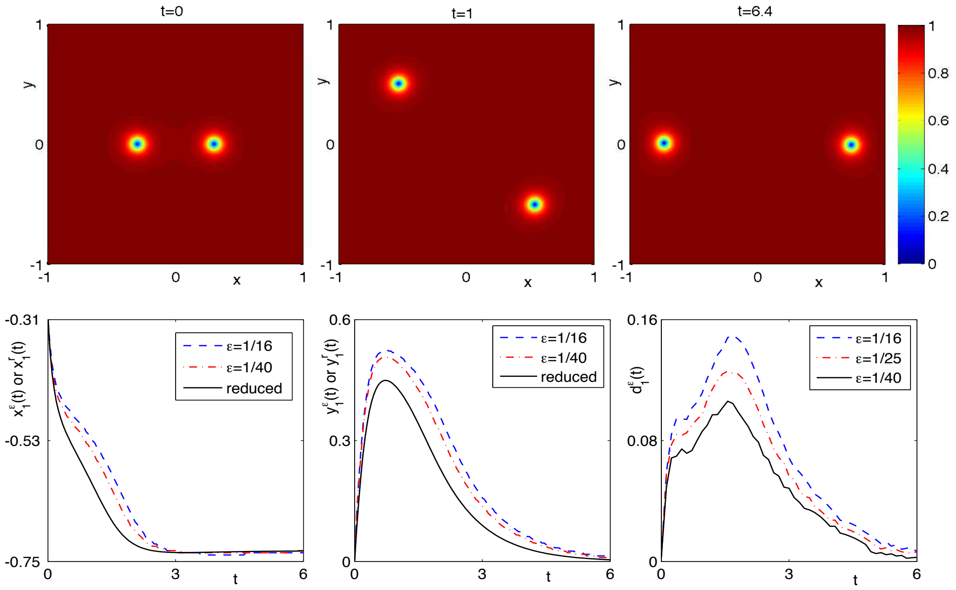

Figure 5.5: Contour plot of $|\psi^\varepsilon(\mathbf{x},t)|$ for $\varepsilon = \frac{1}{25}$ at different times as well as time evolution of $\mathbf{x}_1^\varepsilon(t)$ in CGLE dynamics and $\mathbf{x}_1^{\mathrm{r}}(t)$ in the reduced dynamics under Dirichlet BC with $h(\mathbf{x}) = 0$ in (2.6) and their difference $d_1^\varepsilon(t)$ for different ε in section 5.1.2.

will collide and annihilation with each other. (ii). The phase shift $h(\mathbf{x})$ and the initial distance of the two vortices affect the motion of the vortices significantly. If $h(\mathbf{x}) = 0$, the vortex dipole will finally merge regardless where they are initially located. However, similar as the case in GLE dynamics, if $h(\mathbf{x}) \not\equiv 0$, say $h(\mathbf{x}) = x + y$ for example, there would be a critical distance d_c^ε, which depend on the value of ε, that divide the motion of the vortex dipole into two groups: (a) if the distance between the vortex dipole initially $|\mathbf{x}_2^0 - \mathbf{x}_1^0| > d_c^\varepsilon$, the vortex will never merge, they will finally stay steady and separately at some place that near the boundary. (b) otherwise, they do finally merge and annihilation. (iii). For $h(\mathbf{x}) = 0$, when $\varepsilon \to 0$, the dynamics of the two vortex centers in the CGLE dynamics converges uniformly in time to that in the reduced dynamics (cf. Fig. 5.7) which verifies numerically the validation of the reduced dynamical laws in this case. In fact, based on our extensive numerical experiments, the motions of the two

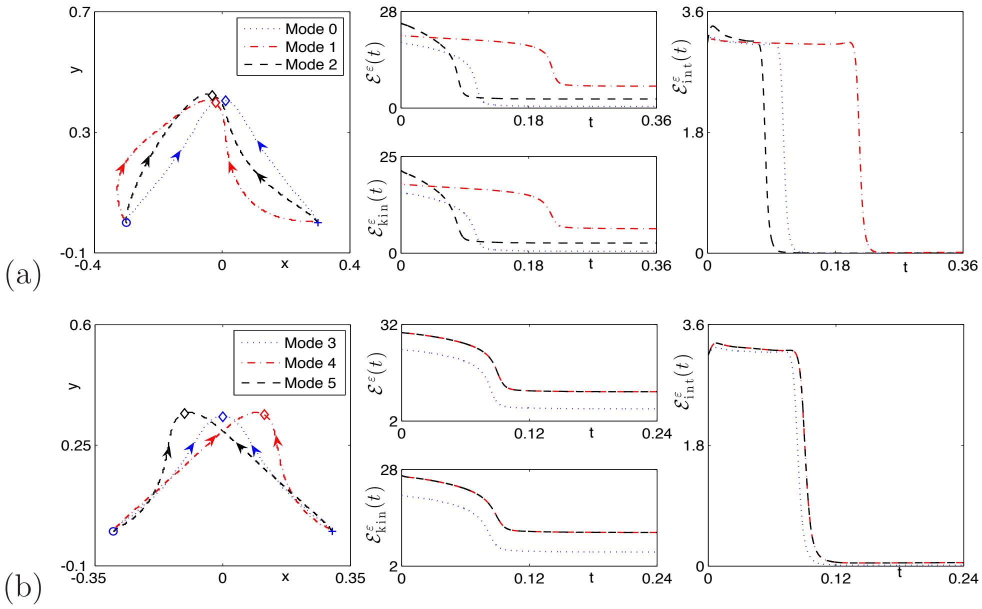

Figure 5.6: Trajectory of the vortex centers (a) and their corresponding time evolution of the GL functionals (b) in CGLE dynamics under Dirichlet BC when $\varepsilon = \frac{1}{25}$ with different $h(\mathbf{x})$ in (2.6) in section 5.1.3.

vortex centers from the reduced dynamical laws agree with those from the CGLE dynamics qualitatively when $0 < \varepsilon < 1$ and quantitatively when $0 < \varepsilon \ll 1$ before they merge. (iv). During the dynamics of CGLE, the GL functional decreases when time increases, its kinetic and interaction parts don't change dramatically when t is small, and when $t \to \infty$, all the three quantities converge to constants. Moreover, if finite time merging/annihilation happens, the GL functional and its kinetic and interaction parts change significantly during the collision. In addition, when $t \to \infty$, the interaction energy goes to 0 which immediately implies that a steady state will be reached in the form of $\phi^{\varepsilon}(\mathbf{x}) = e^{ic(\mathbf{x})}$, where $c(\mathbf{x})$ is a harmonic function satisfying $c(\mathbf{x})|_{\partial\mathcal{D}} = h(\mathbf{x}) + \sum_{j=1}^{M} n_j\theta(\mathbf{x} - \mathbf{x}_j^0)$.

5.1.4 Vortex lattice

Here we present numerical results of the interaction of vortex lattices under the CGLE dynamics. We consider the following cases: case I. $M = 3$, $n_1 = n_2 = n_3 = 1$,

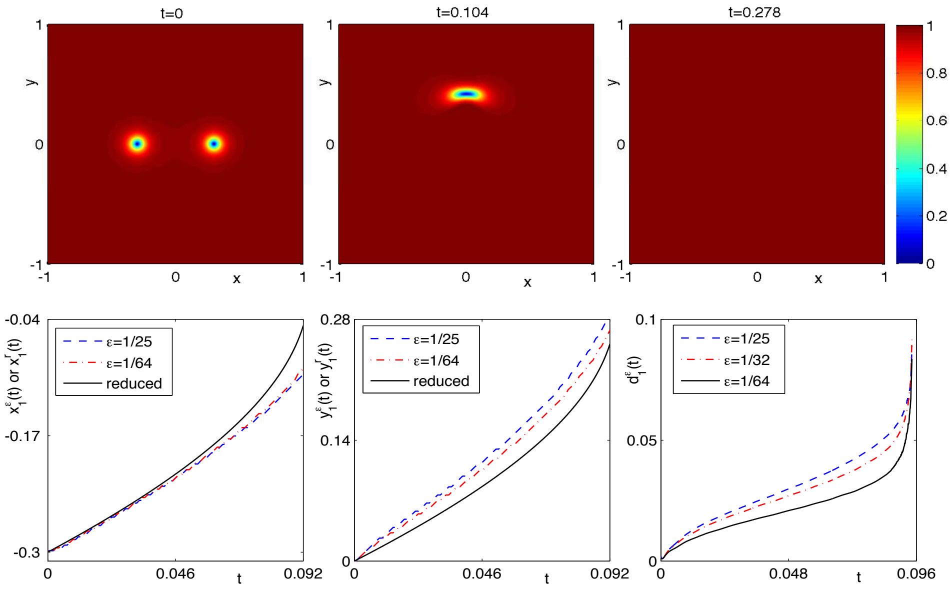

Figure 5.7: Contour plots of $|\psi^\varepsilon(\mathbf{x},t)|$ for $\varepsilon = \frac{1}{25}$ at different times as well as time evolution of $\mathbf{x}_1^\varepsilon(t)$ in CGLE dynamics, $\mathbf{x}_1^{\mathrm{r}}(t)$ in the reduced dynamics under Dirichlet BC with $h(\mathbf{x}) = 0$ in (2.6) and their difference $d_1^\varepsilon(t)$ for different ε in section 5.1.3.

$\mathbf{x}_1^0 = (0.5, 0)$; $\mathbf{x}_2^0 = (-0.25, \frac{\sqrt{3}}{4})$, $\mathbf{x}_3^0 = (-0.25, -\frac{\sqrt{3}}{4})$, case II. $M = 3$, $n_1 = n_2 = n_3 = 1$, $\mathbf{x}_1^0 = (-0.4, 0)$, $\mathbf{x}_2^0 = (0, 0)$, $\mathbf{x}_3^0 = (0.4, 0)$; case III. $M = 3$, $n_1 = n_2 = n_3 = 1$, $\mathbf{x}_1^0 = (0, 0.3)$, $\mathbf{x}_2^0 = (0.15, 0.15)$, $\mathbf{x}_3^0 = (0.3, 0)$; case IV. $M = 3$, $-n_1 = n_2 = n_3 = 1$, $\mathbf{x}_1^0 = (0.5, 0)$; $\mathbf{x}_2^0 = (-0.25, \frac{\sqrt{3}}{4})$, $\mathbf{x}_3^0 = (-0.25, -\frac{\sqrt{3}}{4})$, case V. $M = 3$, $n_2 = -1$, $n_1 = n_3 = 1$, $\mathbf{x}_1^0 = (-0.4, 0)$, $\mathbf{x}_2^0 = (0, 0)$, $\mathbf{x}_3^0 = (0.4, 0)$; case VI. $M = 3$, $n_1 = -1$, $n_2 = n_3 = 1$, $\mathbf{x}_1^0 = (0.2, 0.3)$, $\mathbf{x}_2^0 = (-0.3, 0.4)$, $\mathbf{x}_3^0 = (-0.4, -0.2)$; case VII. $M = 4$, $n_1 = n_2 = n_3 = n_4 = 1$, $\mathbf{x}_1^0 = (0.5, 0)$, $\mathbf{x}_2^0 = (0, 0.5)$, $\mathbf{x}_3^0 = (-0.5, 0)$, $\mathbf{x}_4^0 = (0, -0.5)$; case VIII. $M = 4$, $n_1 = n_3 = 1$, $n_2 = n_4 = -1$, $\mathbf{x}_1^0 = (0.5, 0)$, $\mathbf{x}_2^0 = (0, 0.5)$, $\mathbf{x}_3^0 = (-0.5, 0)$, $\mathbf{x}_4^0 = (0, -0.5)$; case IX. $M = 4$, $n_2 = n_3 = -1$, $n_1 = n_4 = 1$, $\mathbf{x}_1^0 = (0.5, 0)$, $\mathbf{x}_2^0 = (0, 0.5)$, $\mathbf{x}_3^0 = (-0.5, 0)$, $\mathbf{x}_4^0 = (0, -0.5)$; case X. $M = 4$, $n_1 = n_3 = 1$, $n_2 = n_4 = -1$, $\mathbf{x}_1^0 = (0.5, 0.5)$, $\mathbf{x}_2^0 = (-0.5, 0.5)$, $\mathbf{x}_3^0 = (-0.5, -0.5)$, $\mathbf{x}_4^0 = (0.5, -0.5)$; case XI. $M = 4$, $n_2 = n_3 = -1$, $n_1 = n_4 = 1$, $\mathbf{x}_1^0 = (0.5, 0.5)$, $\mathbf{x}_2^0 = (-0.5, 0.5)$, $\mathbf{x}_3^0 = (-0.5, -0.5)$, $\mathbf{x}_4^0 = (0.5, -0.5)$; case XII. $M = 4$, $n_1 = n_3 = -1$, $n_2 = n_4 = 1$, $\mathbf{x}_1^0 = (0.4, 0)$, $\mathbf{x}_2^0 = (-0.4/3, 0)$, $\mathbf{x}_3^0 = (0.4/3, 0)$, $\mathbf{x}_4^0 = (0.4, 0)$; case XIII. $M = 4$,

$n_2 = n_3 = -1$, $n_1 = n_4 = 1$, $\mathbf{x}_1^0 = (0.4, 0)$, $\mathbf{x}_2^0 = (-0.4/3, 0)$, $\mathbf{x}_3^0 = (0.4/3, 0)$, $\mathbf{x}_4^0 = (0.4, 0)$; case XIV. $M = 4$, $n_1 = n_2 = -1$, $n_3 = n_4 = 1$, $\mathbf{x}_1^0 = (0.4, 0)$, $\mathbf{x}_2^0 = (-0.4/3, 0)$, $\mathbf{x}_3^0 = (0.4/3, 0)$, $\mathbf{x}_4^0 = (0.4, 0)$; case XV. $M = 4$, $n_1 = n_3 = -1$, $n_2 = n_4 = 1$, $\mathbf{x}_1^0 = (0.2, 0.3)$, $\mathbf{x}_2^0 = (-0.3, 0.4)$, $\mathbf{x}_3^0 = (-0.4, -0.2)$; $\mathbf{x}_4^0 = (0.3, -0.3)$;

Fig. 5.8 shows trajectory of the vortex centers when $\varepsilon = \frac{1}{32}$ in 1.1 and $h(\mathbf{x}) = 0$ in (2.6) for the above 15 cases. From Fig. 5.8 and additional numerical experiments not shown here for brevity, we can draw the following conclusions: (i). The interaction of vortex lattices under the CGLE dynamics with Dirichlet BC is very interesting and complicated. The detailed dynamics and interaction pattern of a lattice depends on its initial alignment of the lattice, geometry of the domain $\mathcal{D}$ and the boundary value $g(\mathbf{x})$. (ii). For a lattice of M vortices, if they have the same index, then no collision will happen for any time $t \geq 0$. On the other hand, if they have opposite index, e.g. $M^+ > 0$ vortices with index '+1' and $M^- > 0$ vortices with index '-1' satisfying $M^+ + M^- = M$, collision will always happen at finite time. In addition, when t is sufficiently large, there exist exactly $|M^+ - M^-|$ vortices of winding number '+1' if $M^+ > M^-$, and resp. '-1' if $M^+ < M^-$, left in the domain.

5.1.5 Steady state patterns of vortex lattices

Here we present the steady state patterns of vortex lattices in the CGLE dynamics under Dirichlet BC. We study how the geometry of the domain $\mathcal{D}$ and boundary condition affect the alignment of vortices in the steady states. To this end, we take $\varepsilon = \frac{1}{32}$ in,

$$n_j = 1, \qquad \mathbf{x}_j^0 = 0.5\left(\cos\left(\frac{2j\pi}{M}\right), \sin\left(\frac{2j\pi}{M}\right)\right), \qquad j = 1, 2, \ldots, M,$$

i.e., initially we have M like vortices which are located uniformly in a circle centered at origin with radius $R_1 = 0.5$.

Denote $\phi^\varepsilon(\mathbf{x})$ as the steady state, i.e., $\phi^\varepsilon(\mathbf{x}) = \lim_{t\to\infty} \psi^\varepsilon(\mathbf{x}, t)$ for $\mathbf{x} \in \mathcal{D}$. Fig. 5.9 depicts the contour plots of the amplitude $|\phi^\varepsilon|$ of the steady state in the CGLE dynamics with $h(\mathbf{x}) = 0$ in (2.6) for different M and domains, while Fig. 5.10 depicts

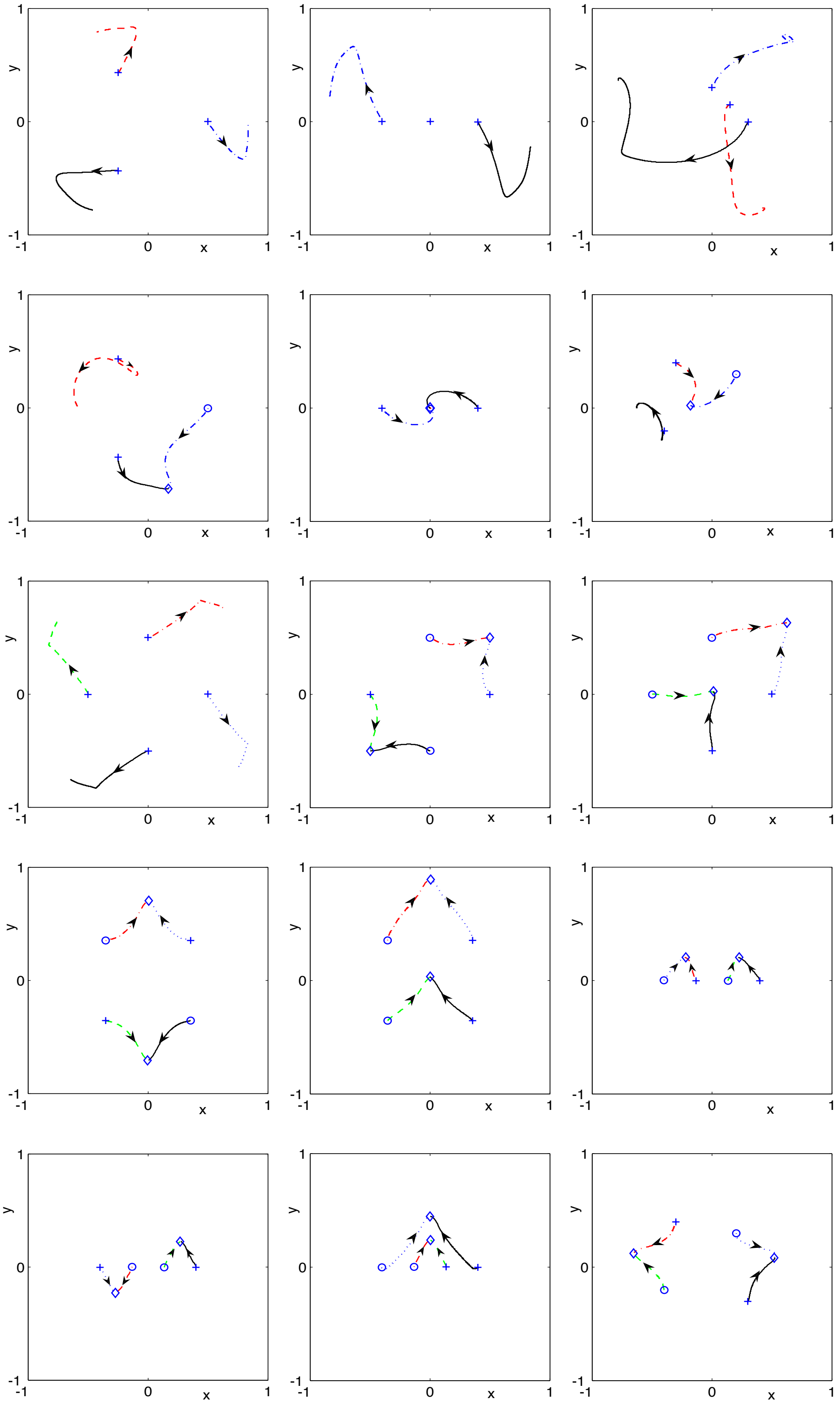

Figure 5.8: Trajectory of vortex centers for the interaction of different vortex lattices in GLE under Dirichlet BC with $\varepsilon = \frac{1}{32}$ and $h(\mathbf{x}) = 0$ for cases I-IX (from left to right and then from top to bottom) in section 5.1.4.

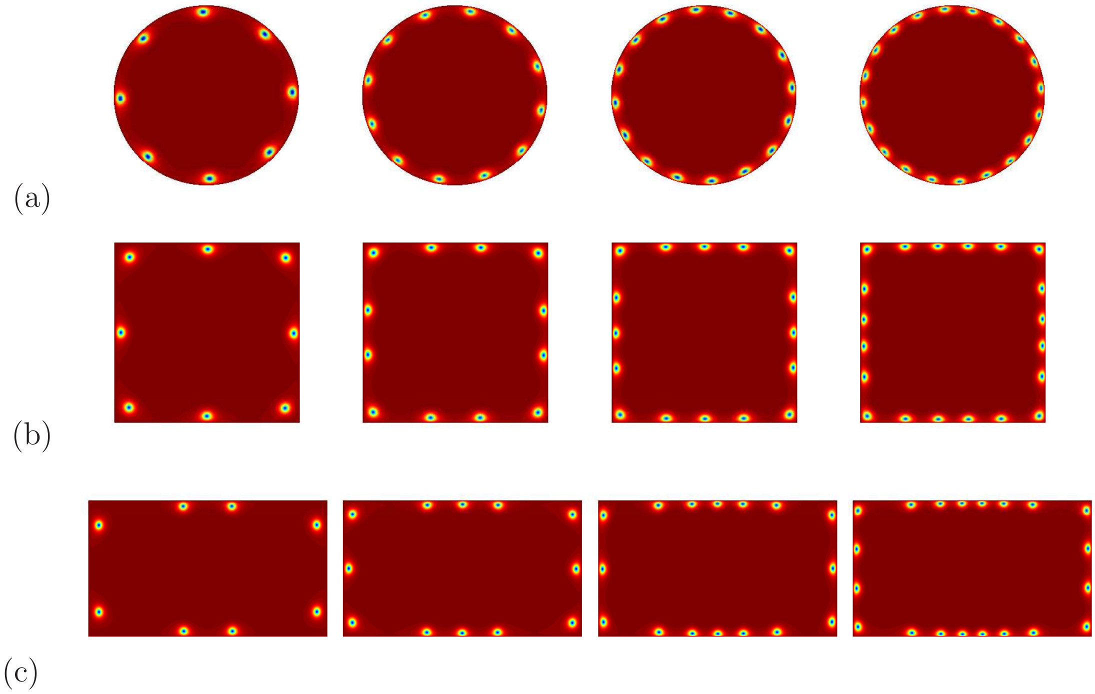

Figure 5.9: Contour plots of $|\phi^\varepsilon(\mathbf{x})|$ for the steady states of vortex lattice in CGLE under Dirichlet BC with $\varepsilon = \frac{1}{32}$ for $M = 8,\ 12,\ 16,\ 20$ (from left column to right column) and different domains: (a) unit disk $\mathcal{D} = B_1(\mathbf{0})$, (b) square domain $\mathcal{D} = [-1,1]^2$, (c) rectangular domain $\mathcal{D} = [-1.6, 1.6] \times [-0.8, 0.8]$.

similar results with $M = 12$ for different $h(\mathbf{x})$ in (2.6).

From Figs. 5.9 & 5.10 and additional numerical results not shown here for brevity, we can draw the following conclusions for the steady state patterns of vortex lattices under the CGLE dynamics with Dirichlet BC: (i). The vortex undergo repulsive interaction between each other and they move to locations near the boundary of $\mathcal{D}$, there is no collision and a steady state pattern is formed when $t \to \infty$. In fact, the steady state is also the solution of the following minimization problem

$$\phi^\varepsilon = \text{argmin}_{\phi(\mathbf{x})|_{\mathbf{x}\in\partial\mathcal{D}} = \psi_0^\varepsilon(\mathbf{x})|_{\mathbf{x}\in\partial\mathcal{D}}} \mathcal{E}^\varepsilon(\phi).$$

Actually, based on our extensive numerical experiments, we found that for a vortex lattice of any configuration, i.e., vortices in the vortex lattice may be opposite winding number, the vortices either merge and annihilate and all the leftover vortices

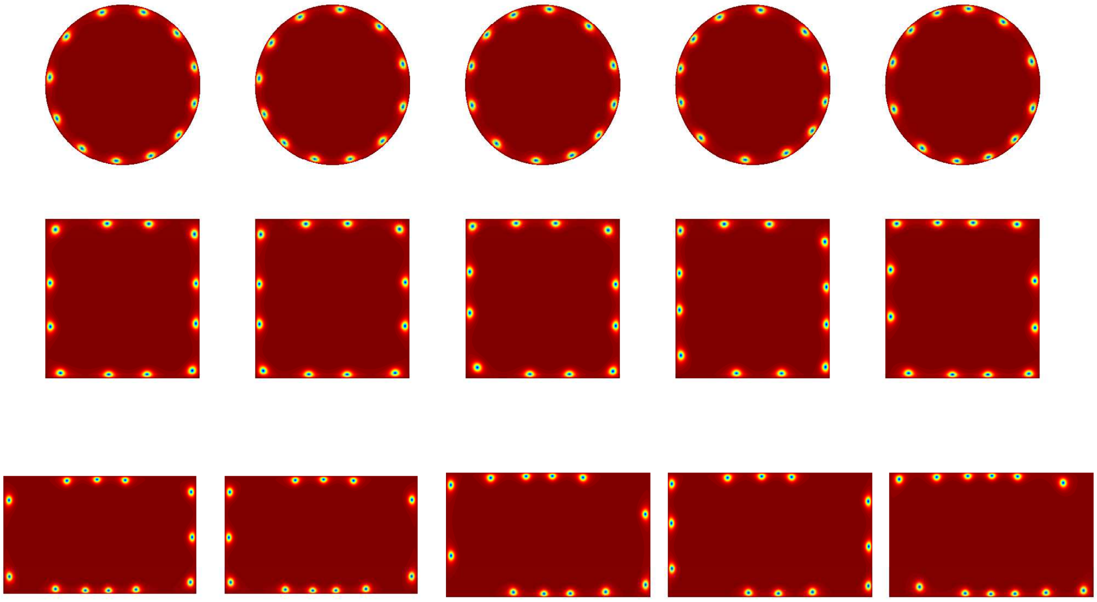

Figure 5.10: Contour plots of $|\phi^\varepsilon(\mathbf{x})|$ for the steady states of vortex lattice in CGLE under Dirichlet BC with $\varepsilon = \frac{1}{32}$ and $M = 12$ on a unit disk $\mathcal{D} = B_1(\mathbf{0})$ (top row) or a square $\mathcal{D} = [-1,1]^2$ (middle row) or a rectangular domain $\mathcal{D} = [-1.6, 1.6] \times [-0.8, 0.8]$ (bottom row) under different $h(\mathbf{x}) = x + y,\ x^2 - y^2,\ x - y,\ x^2 - y^2 + 2xy,\ x^2 - y^2 - 2xy$ (from left column to right column).

are all pinned in near the boundary finally. This phenomena is similar with the one in the superconductor involving magnetic field [101]. (ii). During the dynamics, the GL functional decreases when time increases. (iii). Both the geometry of the domain and the boundary condition, i.e., $h(\mathbf{x})$, affect the final steady states significantly. (iv). At the steady state, the distance between the vortex centers and $\partial\mathcal{D}$ depends on ε and M. For fixed M, when ε decreases, the distance decreases; and respectively, for fixed ε, when M increases, the distance decreases. We remark it here as a interesting open problem to find how the width depend on the value of ε, the boundary condition as well as the geometry of the domain.

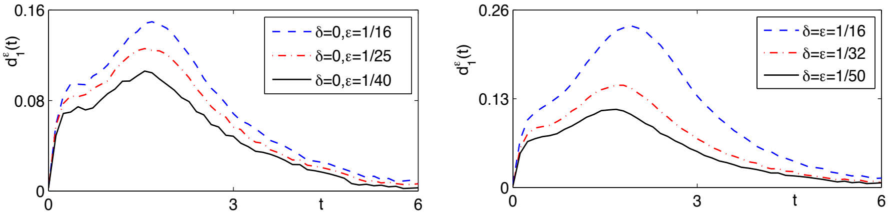

Figure 5.11: Time evolution of $d_1^{\delta,\varepsilon}(t)$ for non-perturbed initial data (left) and perturbed initial data (right) in section 5.1.6

5.1.6 Validity of RDL under small perturbation

As seen from former chapters, the small perturbation affects the motion of the vortices in NLSE dynamics much but hardly affects those in the GLE dynamics. The question that how this affects those vortex motion in CGLE dynamics now come up naturally. To this end, similar as the one studied in the GLE dynamics, we take the initial data (1.2) as (3.4) with ψ_0^ε chosen as (2.6) with $h(\mathbf{x}) \equiv 0$, $M = 2$, $n_1 = n_2 = 1$ and $\mathbf{x}_1^0 = -\mathbf{x}_2^0 = (0.3, 0)$. Then we take $\delta = \varepsilon$ and let ε go to 0, and solve the CGLE under Dirichlet BC and with initial condition (3.4) for the vortex centers $\mathbf{x}_1^{\delta,\varepsilon}(t)$ and $\mathbf{x}_2^{\delta,\varepsilon}(t)$ and compare them with those from the reduced dynamical law. We denote $d_j^{\delta,\varepsilon}(t) = |x_j^{\delta,\varepsilon}(t) - x_j^r(t)|$ for $j = 1, 2$ as the error. Fig. 5.11 depicts time evolution of $d_1^{\delta,\varepsilon}(t)$ for the case when $\delta = \varepsilon$, i.e., small perturbation, and the case when $\delta = 0$, i.e., no perturbation. From this figure, we can see that small perturbation in the initial data does not affect the motion of the vortices much, same as the non-perturbed initial setups, the dynamics of the two vortex centers under the CGLE dynamics with perturbed initial setups also converge to those obtained from the reduced dynamical law when $\varepsilon \to 0$. Same as the case in GLE dynamics, this situation is foreseeable since the CGLE is also a dissipative system, and small perturbation initially imposed for a dissipative system will not affect the system much for the dynamics.

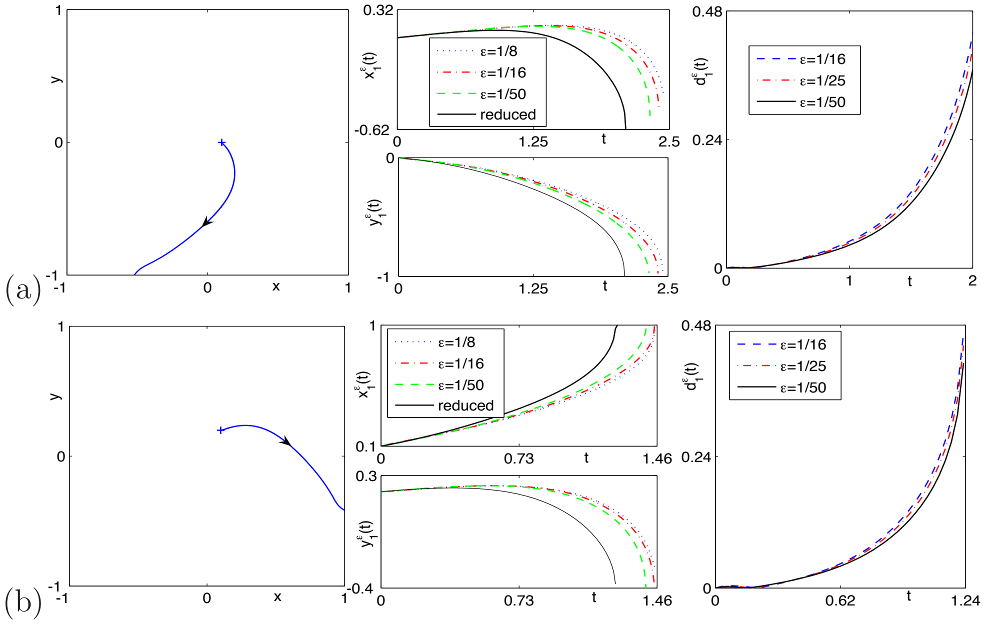

Figure 5.12: Trajectory of the vortex center when $\varepsilon = \frac{1}{25}$ (left) as well as time evolution of $\mathbf{x}_1^\varepsilon$ (middle) and d_1^ε for different ε (right) for the motion of a single vortex in CGLE under homogeneous Neumann BC with different $\mathbf{x}_1^0$ in (2.6) in section 5.2.1.: (a) $\mathbf{x}_1^0 = (0.1, 0)$, (b) $\mathbf{x}_1^0 = (0.1, 0.2)$.

5.2 Numerical results under Neumann BC

5.2.1 Single vortex

Here we present numerical results of the motion of a single quantized vortex under the CGLE dynamics and its corresponding reduced dynamical laws, i.e., we take $M = 1$ and $n_1 = 1$ in (2.6). Fig. 5.12 depicts trajectory of the vortex center for different $\mathbf{x}_1^0$ in (2.6) when $\varepsilon = \frac{1}{25}$ as well as time evolution of $\mathbf{x}_1^\varepsilon$ and d_1^ε for different ε. From Fig. 5.12 and additional numerical results not shown here for brevity, we can see that:

(i). The initial location of the vortex, i.e., value of $\mathbf{x}_0$ affects the motion of the vortex a lot and this shows the effect on the vortex from the Neumann BC.

(ii). If $\mathbf{x}_1^0 = (0, 0)$, the vortex will not move all the time, otherwise, the vortex will move and finally exit the domain and never come back. This is quite different

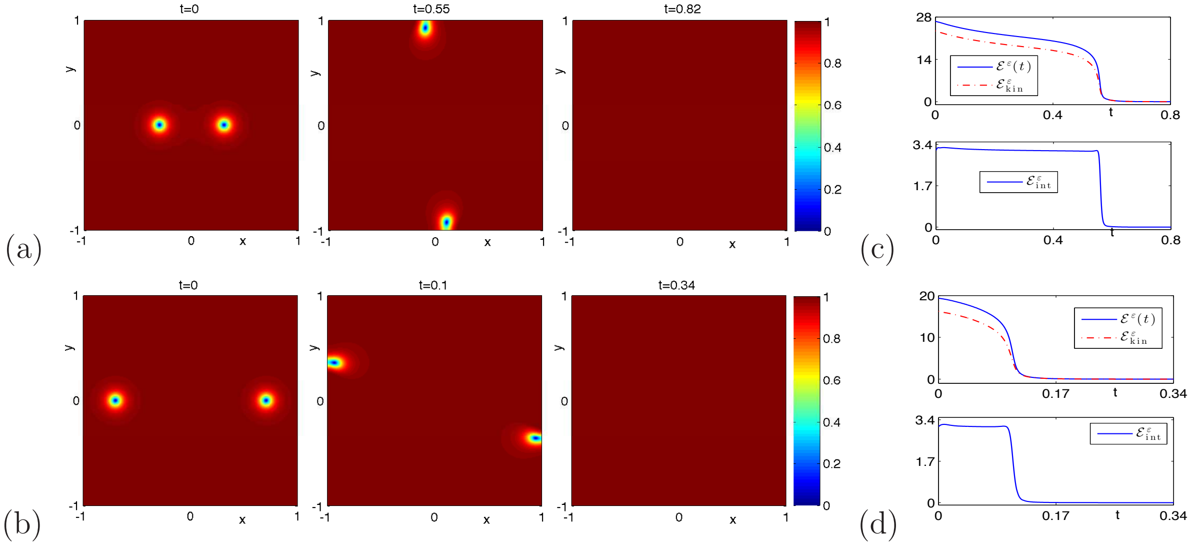

Figure 5.13: Contour plots of $|\psi^\varepsilon(\mathbf{x},t)|$ at different times when $\varepsilon = \frac{1}{25}$ ((a) & (b)) and the corresponding time evolution of the GL functionals ((c) & (d)) for the motion of vortex pair in CGLE under homogeneous Neumann BC with different d_0 in (2.6) in section 5.2.2: top row: $d_0 = 0.3$, bottom row: $d_0 = 0.7$.

from the situations in bounded domain with Dirichlet BC where a single vortex can never move outside the domain or in the whole space where a single vortex doesn't move at all under the initial condition (2.6) when $\mathcal{D} = \mathbb{R}^2$.

(iii). As $\varepsilon \to 0$, the dynamics of the vortex center under the CGLE dynamics converges uniformly in time to that of the reduced dynamical laws well before it exits the domain, which verifies numerically the validation of the reduced dynamical laws in this case. Surely, when the vortex center is being exited the domain or after it moves out of the domain, the reduced dynamics laws are no longer valid. However, the dynamics of CGLE is still physically interesting. In fact, based on our extensive numerical experiments, the motion of the vortex center from the reduced dynamical laws agrees with that from the CGLE dynamics qualitatively when $0 < \varepsilon < 1$ and quantitatively when $0 < \varepsilon \ll 1$ well before it moves out of the domain.

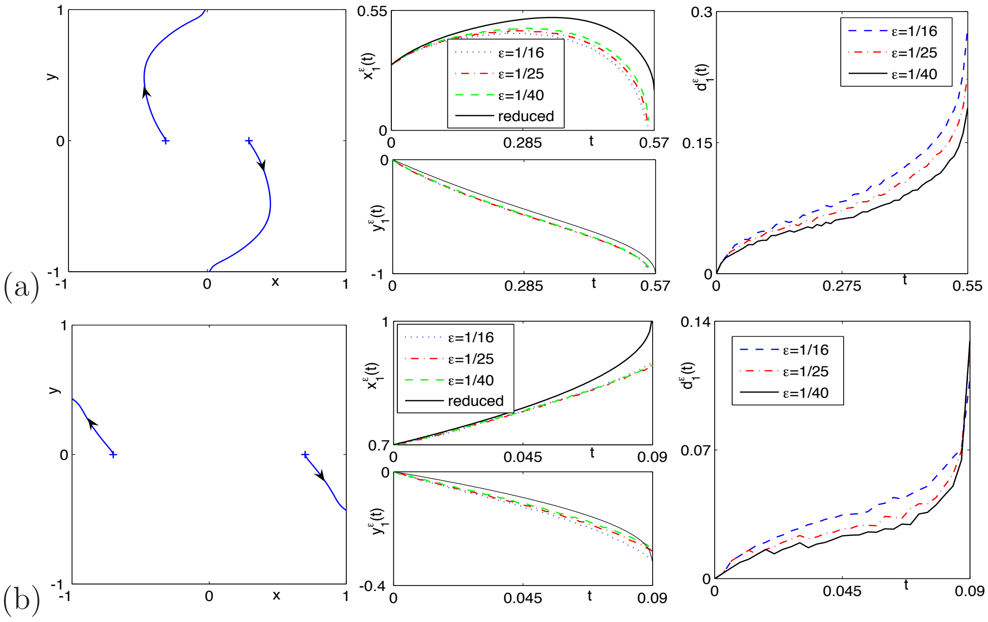

Figure 5.14: Trajectory of the vortex center when $\varepsilon = \frac{1}{25}$ (left) as well as time evolution of $\mathbf{x}_1^\varepsilon$ (middle) and d_1^ε for different ε (right) for the motion of vortex pair in CGLE under homogeneous Neumann BC with different d_0 in (2.6) in section 5.2.2: (a) $d_0 = 0.3$, (b) $d_0 = 0.7$.

5.2.2 Vortex pair

Here we present numerical results of the interaction of vortex pair under the CGLE dynamics and its corresponding reduced dynamical laws, i.e., we take $M = 2$, $n_1 = n_2 = 1$ and $\mathbf{x}_2^0 = -\mathbf{x}_1^0 = (d_0, 0)$ with $0 < d_0 < 1$ in (2.6). Fig. 5.13 shows the contour plots of $|\psi^\varepsilon(\mathbf{x}, t)|$ at different times when $\varepsilon = \frac{1}{25}$, while Fig. 5.14 depicts the trajectory of the vortex pair when $\varepsilon = \frac{1}{25}$ as well as time evolution of $x_1^\varepsilon(t)$ and $d_1^\varepsilon(t)$ for different d_0 in (2.6).

From Figs. 5.14 and 5.13 and additional numerical results not shown here for brevity, we can draw the following conclusions for the interaction of vortex pair under the NLSE dynamics with homogeneous Neumann BC:

(i). The initial location of the vortex, i.e., value of d_0 affects the motion of the vortex a lot and this shows the effect on the vortex from the Neumann BC.

(ii). For the CGLE with ε fixed, there exist a sequence of critical values $d_1^{c,\varepsilon} >$

$d_2^{c,\varepsilon} > d_3^{c,\varepsilon} > \cdots > d_k^{c,\varepsilon} > \cdots$ such that: if $d_0 > d_1^{c,\varepsilon}$, the two vortex will exit the domain from the side boundary; if $d_1^{c,\varepsilon} > d_0 > d_2^{c,\varepsilon}$, the two vortex will exit the domain from the top-bottom boundary; if $d_2^{c,\varepsilon} > d_0 > d_3^{c,\varepsilon}$, the two vortex will exit the domain from the side boundary again. Actually, they exit from the side or top-bottom boundary alternatively, i.e., for $n = 0, 1, \cdots$: if $d_{2n}^{c,\varepsilon} > d_0 > d_{2n+1}^{c,\varepsilon}$, the two vortex will exit the domain from the side boundary; otherwise, if $d_{2n+1}^{c,\varepsilon} > d_0 > d_{2n+2}^{c,\varepsilon}$, the two vortex will exit the domain from the top-bottom boundary. For the reduced dynamical law, there also exist such series of critical values $\{d_k^{c,r}, k = 0, \cdots\}$ which divide the patterns of the trajectory. It might be an interesting problem to find those $d_k^{c,\varepsilon}$ and $d_k^{c,r}$, and to study how they agree with each other.

Again, the motion here is somehow the combination of that in the GLE dynamics and that in the NLSE dynamics. The vortex pair in the GLE dynamics will always move outward along the line that connects the two vortices and finally exit the domain, while in the NLSE dynamics, they always rotate around each other periodically. Actually, from extensive numerical results, we find that for a fixed initial setups, the larger the value β is, the more rotation the pair will do before they exit the domain, i.e, the closer the motion in CGLE dynamics is to that in NLSE dynamics; on contrary, the larger the value α, the faster the vortex exit the domain, in other words, the closer the motion in CGLE dynamics is to that in NLSE dynamics. This again evidence numerically that the CGLE under Neumann BC is somehow in between the GLE and NLSE under Neumann BC.

(iii). As $\varepsilon \to 0$, the dynamics of the two vortex centers under the CGLE dynamics converge uniformly in time to that of the reduced dynamical laws well before any one of them exit the domain, which verifies numerically the validation of the reduced dynamical laws in this case. Surely, when the vortex centers are being exiting the domain or after they moves out of the domain, the reduced dynamics laws are no longer valid. However, the dynamics of CGLE is still physically interesting. In fact, based on our extensive numerical experiments, the motions of the two vortex centers from the reduced dynamical laws agree with those from the CGLE dynamics

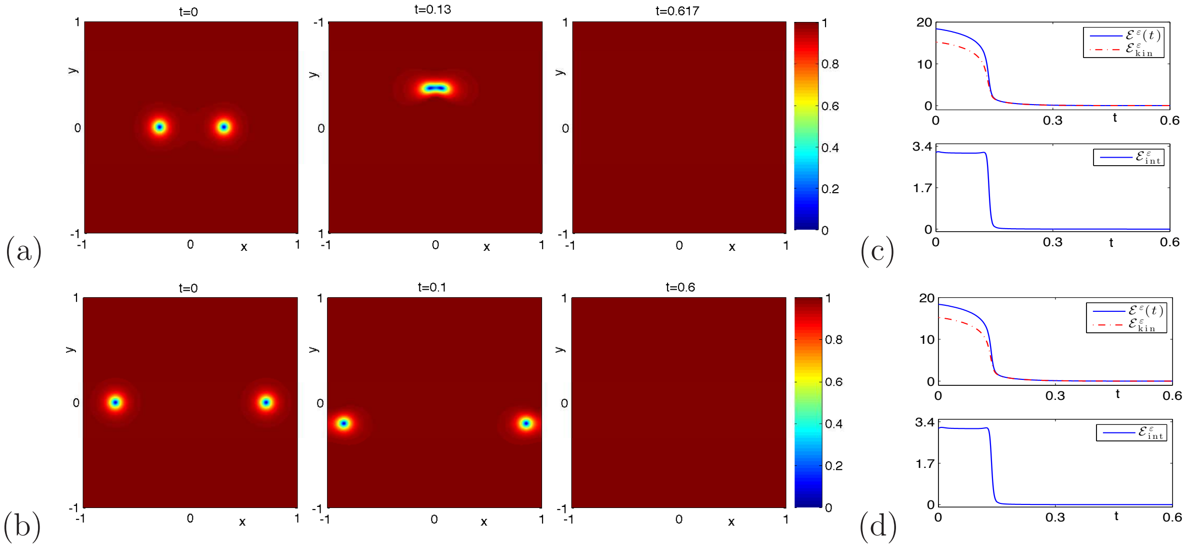

Figure 5.15: Contour plots of $|\psi^\varepsilon(\mathbf{x},t)|$ at different times when $\varepsilon = \frac{1}{25}$ and the corresponding time evolution of the GL functionals for the motion of vortex dipole in CGLE under homogeneous Neumann BC with different d_0 in (2.6) in section 5.2.3: top row: $d_0 = 0.3$, bottom row: $d_0 = 0.7$.

qualitatively when $0 < \varepsilon < 1$ and quantitatively when $0 < \varepsilon \ll 1$.

(iv). During the dynamics of CGLE, the GL functional and its kinetic parts decrease when time increases. They doesn't change much when t is small and changes dramatically when either one of the two vortices moves outside the domain $\mathcal{D}$. When $t \to \infty$, all the three quantities converge to 0 (cf. Fig. 5.13 (c) & (d)), which imply that a constant steady state will be reached in the form of $\phi^\varepsilon(\mathbf{x}) = e^{ic_0}$ for $\mathbf{x} \in \mathcal{D}$ with $c_{_0}$ a constant.

5.2.3 Vortex dipole

Here we present numerical results of the interaction of vortex dipole in the CGLE dynamics and its corresponding reduced dynamics, i.e., we take $M = 2$, $n_2 = -n_1 = 1$ and $\mathbf{x}_2^0 = -\mathbf{x}_1^0 = (d_0, 0)$ with $0 < d_0 < 1$ in (2.6).

Fig. 5.15 shows the contour plots of $|\psi^\varepsilon(\mathbf{x},t)|$ at different times when $\varepsilon = \frac{1}{25}$, while Fig. 5.16 depicts the trajectory of the vortex pair when $\varepsilon = \frac{1}{25}$ as well as time

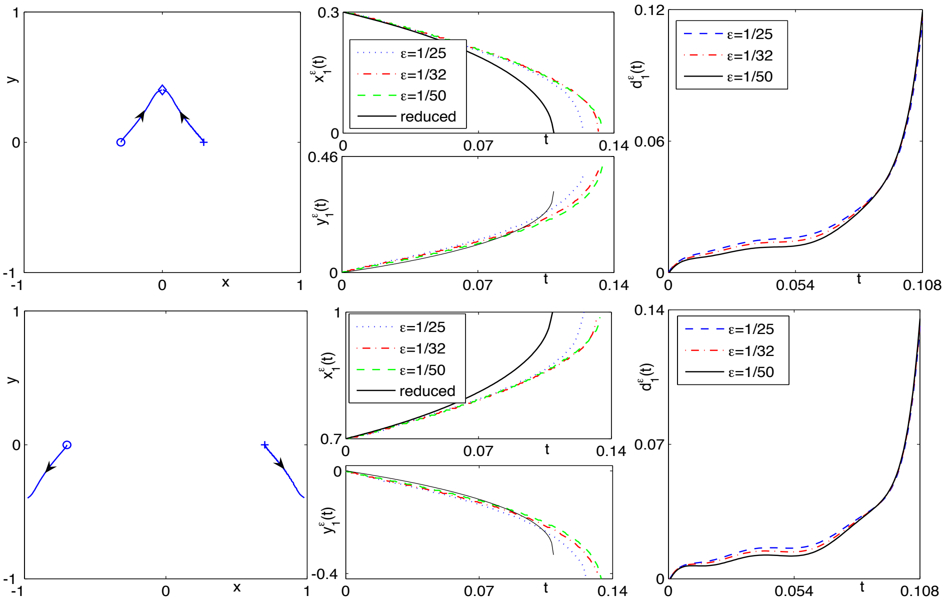

Figure 5.16: Trajectory of the vortex center when $\varepsilon = \frac{1}{25}$ (left) as well as time evolution of $\mathbf{x}_1^\varepsilon$ (middle) and d_1^ε for different ε (right) for the motion of vortex dipole in CGLE under homogeneous Neumann BC with different d_0 in (2.6) in section 5.2.2: (a) $d_0 = 0.3$, (b) $d_0 = 0.7$.

evolution of $x_1^\varepsilon(t)$ and $d_1^\varepsilon(t)$ for different d_0 in (2.6).

From Fig. 5.16 and 5.15 and additional numerical results not shown here for brevity, we can draw the following conclusions for the interaction of vortex pair under the NLSE dynamics with homogeneous Neumann BC:

(i). The initial location of the vortex, i.e., value of d_0 affects the motion of the vortex a lot and this shows the effect on the vortex from the Neumann BC. (ii). For the CGLE with ε fixed, there exists a critical value d_c^ε such that: if $d_0 > d_c^\varepsilon$, the two vortices will exit the domain from the side boundary, otherwise, they will merge somewhere in the boundary. For the reduced dynamical law, there also exists such series of critical values d_c^r which divide the patterns of the trajectory. It might be an interesting problem to find those d_c^ε and d_c^r, and to study how they agree with each other. Moreover, the trajectories of the two vortices are symmetric i.e., $\mathbf{x}_1(t) = -\mathbf{x}_2(t)$, and finally the CGLE dynamics will lead to a constant steady state with amplitude 1, i.e., $\phi^\varepsilon(\mathbf{x}) = e^{ic_0}$ for $\mathbf{x} \in \mathcal{D}$ with c_0 a real constant. (iii). As $\varepsilon \to 0$, the dynamics of the two vortex centers under the CGLE dynamics converge uniformly in time to that of the reduced dynamical laws well before they move out of the domain or merge with each other, which verifies numerically the validation of the reduced dynamical laws in this case. In fact, based on our extensive numerical experiments, the motions of the two vortex centers from the reduced dynamical laws agree with those from the CGLE dynamics qualitatively when $0 < \varepsilon < 1$ and quantitatively when $0 < \varepsilon \ll 1$.

5.2.4 Vortex lattice

Here we present numerical results of the interaction of vortex lattices under the CGLE dynamics. We consider the following 15 cases:

case I. $M = 3$, $n_1 = n_2 = n_3 = 1$, $\mathbf{x}_1^0 = (0.4, 0)$; $\mathbf{x}_2^0 = (-0.2, \frac{\sqrt{3}}{5})$, $\mathbf{x}_3^0 = (-0.2, -\frac{\sqrt{3}}{5})$, case II. $M = 3$, $n_1 = n_2 = n_3 = 1$, $\mathbf{x}_1^0 = (-0.4, 0.2)$, $\mathbf{x}_2^0 = (0, 0.2)$, $\mathbf{x}_3^0 = (0.4, 0.2)$; case III. $M = 3$, $n_1 = n_2 = n_3 = 1$, $\mathbf{x}_1^0 = (-0.4, 0)$, $\mathbf{x}_2^0 = (0, 0)$, $\mathbf{x}_3^0 = (0.4, 0)$; case IV. $M = 3$, $-n_1 = n_2 = n_3 = 1$, $\mathbf{x}_1^0 = (0.4, 0)$; $\mathbf{x}_2^0 = (-0.2, \frac{\sqrt{3}}{5})$, $\mathbf{x}_3^0 = (-0.2, -\frac{\sqrt{3}}{5})$, case V. $M = 3$, $-n_2 = n_1 = n_3 = 1$, $\mathbf{x}_1^0 = (-0.4, 0)$, $\mathbf{x}_2^0 = (0, 0)$, $\mathbf{x}_3^0 = (0.4, 0)$; case VI. $M = 3$, $-n_2 = n_1 = n_3 = 1$, $\mathbf{x}_1^0 = (-0.7, 0)$, $\mathbf{x}_2^0 = (0, 0)$, $\mathbf{x}_3^0 = (0.7, 0)$; case VII. $M = 4$, $n_1 = n_2 = n_3 = n_4 = 1$, $\mathbf{x}_1^0 = (0.4, 0)$, $\mathbf{x}_2^0 = (0, 0.4)$, $\mathbf{x}_3^0 = (-0.4, 0)$, $\mathbf{x}_4^0 = (0, -0.4)$; case VIII. $M = 4$, $n_1 = n_3 = -1$, $n_2 = n_4 = 1$, $\mathbf{x}_1^0 = (0.4, 0)$, $\mathbf{x}_2^0 = (0, 0.4)$, $\mathbf{x}_3^0 = (-0.4, 0)$, $\mathbf{x}_4^0 = (0, -0.4)$; case IX. $M = 4$, $n_1 = n_3 = -1$, $n_2 = n_4 = 1$, $\mathbf{x}_1^0 = (0.59, 0)$, $\mathbf{x}_2^0 = (0, 0.59)$, $\mathbf{x}_3^0 = (-0.59, 0)$, $\mathbf{x}_4^0 = (0, -0.59)$; case X. $M = 4$, $n_1 = n_3 = -1$, $n_2 = n_4 = 1$, $\mathbf{x}_1^0 = (0.7, 0)$, $\mathbf{x}_2^0 = (0, 0.7)$, $\mathbf{x}_3^0 = (-0.7, 0)$, $\mathbf{x}_4^0 = (0, -0.7)$; case XI. $M = 4$, $n_2 = n_3 = -1$, $n_1 = n_4 = 1$, $\mathbf{x}_1^0 = (0.4, 0)$, $\mathbf{x}_2^0 = (0, 0.4)$, $\mathbf{x}_3^0 = (-0.4, 0)$, $\mathbf{x}_4^0 = (0, -0.4)$; case XII. $M = 4$, $n_2 = n_3 = -1$, $n_1 = n_4 = 1$, $\mathbf{x}_1^0 = (0.6, 0)$, $\mathbf{x}_2^0 = (0, 0.6)$, $\mathbf{x}_3^0 = (-0.6, 0)$, $\mathbf{x}_4^0 = (0, -0.6)$; case XIII. $M = 4$, $n_1 = n_3 = -1$, $n_2 = n_4 = 1$, $\mathbf{x}_1^0 = (0.4, 0)$, $\mathbf{x}_2^0 = (-0.4/3, 0)$, $\mathbf{x}_3^0 = (0.4/3, 0)$, $\mathbf{x}_4^0 = (0.4, 0)$; case XIV. $M = 4$, $n_1 = n_3 = -1$, $n_2 = n_4 = 1$, $\mathbf{x}_1^0 = (0.4, 0)$, $\mathbf{x}_2^0 = (-0.4/3, 0)$, $\mathbf{x}_3^0 = (0.4/3, 0)$, $\mathbf{x}_4^0 = (0.4, 0)$; case XV.

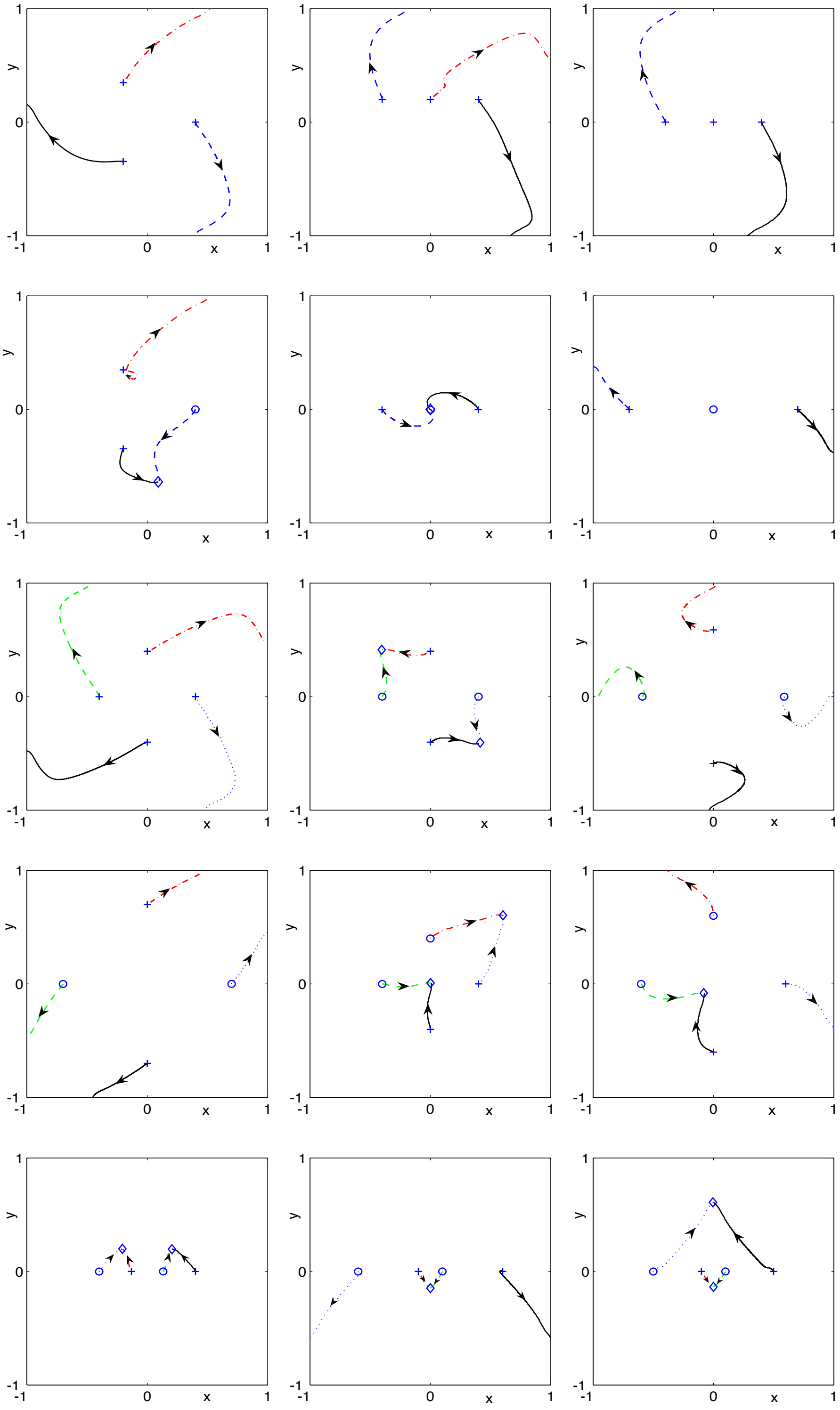

Figure 5.17: Trajectory of vortex centers for the interaction of different vortex lattices in CGLE under Neumman BC with $\varepsilon = \frac{1}{32}$ for cases I-IX (from left to right and then from top to bottom) in section 5.2.4.

$M=4$, $n_1=n_3=-1$, $n_2=n_4=1$, $\mathbf{x}_1^0=(-0.6,0)$, $\mathbf{x}_2^0=(-0.1,0)$, $\mathbf{x}_3^0=(0.1,0)$, $\mathbf{x}_4^0=(0.6,0)$;

Fig. 5.17 shows trajectory of the vortex centers for the above 15 cases when $\varepsilon=\frac{1}{32}$, while Fig. 5.18 depicts the contour plots of $|\psi^\varepsilon|$ for the initial data and corresponding steady states for cases I, III, V, VI, VII and XIV.

From Figs. 5.17 & 5.18 and additional numerical experiments not shown here for brevity, we can draw the following conclusions: (i). The interaction of vortex lattices under the CGLE dynamics with homogeneous BC is very interesting and complicated. The detailed dynamics and interaction pattern of a lattice depends on its initial alignment of the lattice and geometry of the domain $\mathcal{D}$. (ii). For a lattice of M vortices, if they have the same index, then at least $M-1$ vortices will move out of the domain at finite time and no collision will happen for any time $t\geq 0$. On the other hand, if they have opposite index, collision will happen at finite time. After collisions, the leftover vortices will then move out of the domain at finite time and at most one vortex may left in the domain. When t is sufficiently large, in most cases, no vortex is left in the domain; of course, when the geometry and initial setup are properly symmetric and M is odd, there maybe one vortex left in the domain. (iii). If finally no vortex leftover in the domain, the GL functionals will always vanish as $t\to\infty$, which indicate that the final steady states always admit the form of $\phi^\varepsilon(\mathbf{x})=e^{ic_0}$ for $\mathbf{x}\in\mathcal{D}$ with c_0 a real constant.

5.2.5 Validity of RDL under small perturbation

Same as the motivation in section 5.1.6, here we study the radiation property of the CGLE dynamics under homogeneous Neumann BC in this subsection.

To this end, we take the initial data (1.2) as (3.4) with ψ_0^ε chosen as (2.6) with $M=2$, $n_1=n_2=1$, $\mathbf{x}_1^0=-\mathbf{x}_2^0=(0.7,0)$ and $h(\mathbf{x})$ as (3.3). Then we take $\delta=\varepsilon$ and let ε go to 0, solve the CGLE with initial condition (3.4) for the vortex centers $\mathbf{x}_1^{\delta,\varepsilon}(t)$ and $\mathbf{x}_2^{\delta,\varepsilon}(t)$ and compare them with those from the reduced dynamical law. We denote $d_j^{\delta,\varepsilon}(t)=|x_j^{\delta,\varepsilon}(t)-x_j^r(t)|$ for $j=1,2$ as the error. Fig. 5.19 depicts time

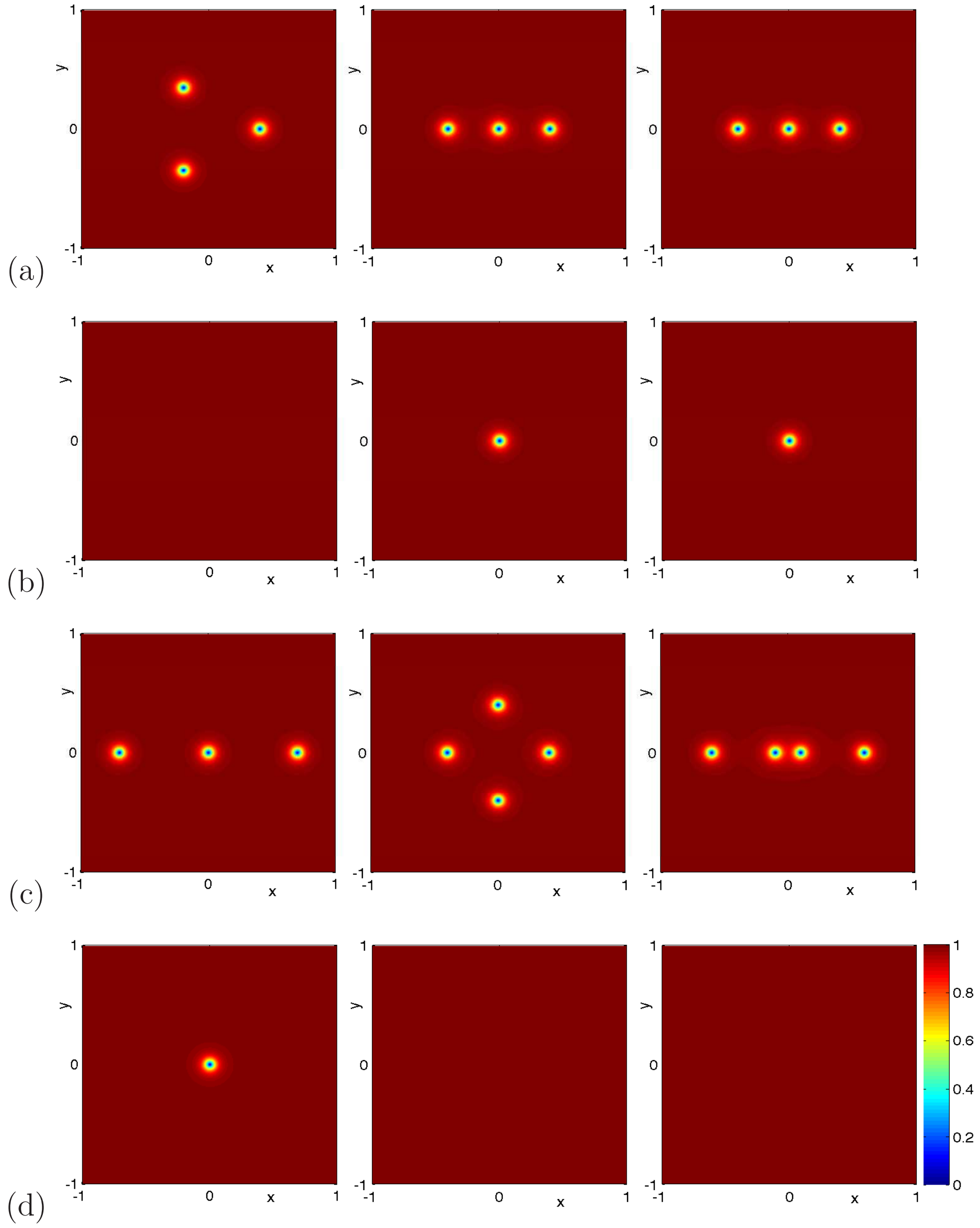

Figure 5.18: Contour plots of $|\psi^\varepsilon(\mathbf{x},t)|$ for the initial data ((a) & (c)) and corresponding steady states ((b) & (d)) of vortex lattice in CGLE dynamics under Neumman BC with $\varepsilon = \frac{1}{32}$ and for cases I, III, V, VI, VII and XIV (from left to right and then from top to bottom) in section 5.2.4.

evolution of $d_1^{\delta,\varepsilon}(t)$ for the case when $\delta = \varepsilon$, i.e., small perturbation, and the case when $\delta = 0$, i.e., no perturbation. From Fig. 5.19, we can see that small perturbation

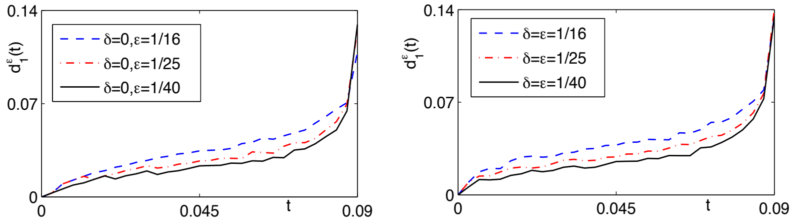

Figure 5.19: Time evolution of $d_1^{\delta,\varepsilon}(t)$ for non-perturbed initial data (left) and perturbed initial data (right) in section 5.2.5

in the initial data does not affect the motion of the vortices much, same as the non-perturbed initial setups, the dynamics of the two vortex centers under the CGLE dynamics with perturbed initial setups also converge to those obtained from the reduced dynamical law when $\varepsilon \to 0$, which is simply similar as the situation in the CGLE dynamics with perturbed initial data under Dirichlet BC.

5.3 Vortex dynamics in inhomogeneous potential

In this subsection, we study numerically the vortex dynamics in the CGLE dynamics with Dirichlet BC under inhomogeneous potential. Analogous to the one studied in section 3.4, the external potential and cases studied are chosen as the same one presented in section 3.4.

Fig. 5.20, shows the trajectory and time evolution of the distance between the vortex center and potential center for different ε for case I and II, as well as trajectory of vortex center for different ε of the vortices for case III. From this figure and additional numerical experiment not shown here for brevity, we can see that: (i). For the single vortex, it moves monotonically toward the points $\mathbf{x}_p = (x_c^0, y_c^0)$, where the external potential V(x) attains its minimum value (cf. Fig. 5.20 (a) & (b)), which shows clearly the pinning effect. Moreover, the trajectory depend on the type of the potential $V(\mathbf{x})$. The speed that vortex move to $\mathbf{x}_p$ as well as the final location that vortex stay steady depend on the value of ε (cf. Fig. 5.20 (a) & (b)). The smaller the ε is, the closer the final location to $\mathbf{x}_p$ and the faster the

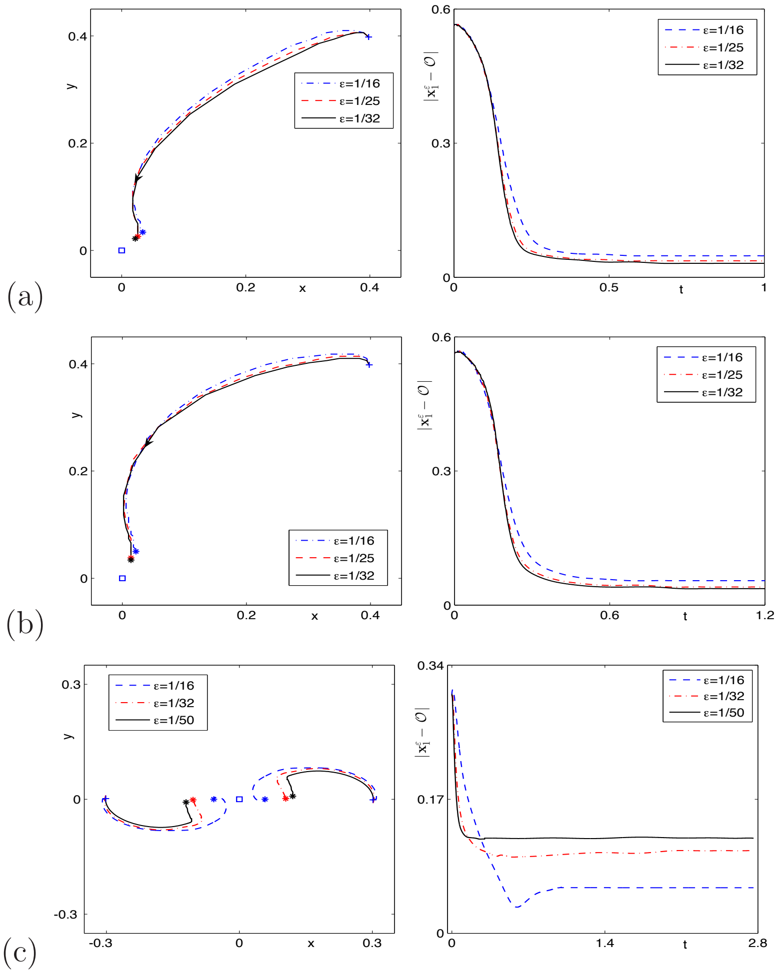

Figure 5.20: Trajectory and time evolution of the distance between the vortex center different ε for case I-III ((a)-(c)) in section 5.3.

vortex move to it. (ii). As $\varepsilon \to 0$, the trajectory seems to converge, and the final location of the vortex seems to converge to points $\mathbf{x}_p$, which are the position that the potential attain its minimum. (iii). For the vortex pair, well, the phenomena is quite different from the one in the GLE dynamics. The vortices will always move close to each other and the point $\mathbf{x}_p$ firstly, which show the pinning effect. However, they will move apart from each other and the point $\mathbf{x}_p$ after some time. And the smaller the ε is, the farther the vortex pair sit away from each other and the points $\mathbf{x}_p$.

5.4 Conclusion

In this chapter, by applying the efficient and accurate numerical methods proposed in chapter 2 to simulate complex Ginzburg-Landau equation (CGLE) with a dimensionless parameter $0 < \varepsilon < 1$ on bounded domains with either Dirichlet or homogenous Neumann BC and its corresponding reduced dynamical laws (RDLs), we studied numerically quantized vortex interaction in CGLE with/without impurities for superconductivity and compared numerically patterns of vortex interaction between the CGLE dynamics and its corresponding reduced dynamical laws under different initial setups. We find that vortex dynamics in the CGLE is somehow the combination of that in GLE and NLSE.

For the CGLE under a homogeneous potential, based on extensive numerical results, we verified that the dynamics of vortex centers under the CGLE dynamics converges to that of the reduced dynamical laws when $\varepsilon \to 0$ before they collide and/or move out of the domain. Certainly, after either vortices collide with each other or move out of the domain, the RDLs are no longer valid; however, the dynamics and interaction of quantized vortices are still physically interesting and they can be obtained from the direct numerical simulations for the CGLE with fixed $\varepsilon > 0$ even after they collide and/or move out of the domain. We also identified the parameter regimes where the RDLs agree with qualitatively and/or qualitatively as well as fail to agree with those from the CGLE dynamics. In the validity regimes, the RDL is still valid under small perturbation in the initial data due to the dissipative nature of the CGLE. Some very interesting nonlinear phenomena related to the quantized vortex interactions in the CGLE for superconductivity were also observed from our direct numerical simulation results of CGLE. Different steady state patterns of vortex lattices under the CGLE dynamics were obtained numerically. From our numerical results, we observed that boundary conditions and domain geometry affect significantly on vortex dynamics and interaction, which showed different interaction patterns compared to those in the whole space case [152, 153].

For the CGLE in an inhomogeneous potential under the Dirichlet BC, by directly simulate the GLE, we find that vortices move in a quite different ways from that in the homogeneous case. The vortices basically move toward critical points of the inhomogeneous potential in the limiting process $\varepsilon \to 0$, which show the pinning effect that caused by the impurities given by the inhomogeneities.

Chapter 6

Numerical methods for GPE with angular momentum

In this chapter, we first review how to reduce the 3D GPE (1.10) with strongly anisotropic confining potential $V(\mathbf{x})$ into 2D GPE, then we propose a simple, efficient and accurate numerical method for simulating the dynamics of rotating Bose-Einstein condensates (BECs) in a rotational frame with/without a long-range dipole-dipole interaction. We then apply the numerical method to test the dynamical laws of rotating BECs such as the dynamics of condensate width, angular momentum expectation and center-of-mass, and to investigate numerically the dynamics and interaction of quantized vortex lattices in rotating BECs without/with the long-range dipole-dipole interaction.

6.1 GPE with angular momentum

In many physical experiments of rotating BEC, the external trap $V(\mathbf{x})$ in (1.10) is strongly confined in the z-direction, i.e.,

$$V(\mathbf{x}) = V_2(x, y) + \frac{z^2}{2\varepsilon^4}, \qquad \mathbf{x} \in \mathbb{R}^3, \tag{6.1}$$

with $0 < \varepsilon \ll 1$ a given dimensionless parameter [13], resulting in a pancake-shaped BEC. Similar to the case of a non-rotating BEC, formally the GPE (1.10) or (1.13)-(1.14) can effectively be approximated by a two-dimensional (2D) GPE as [16,17,39]:

$$i\partial_t\psi(\mathbf{x}_\perp,t) = \left[-\frac{1}{2}\nabla_\perp^2 + V_2(\mathbf{x}_\perp) + \frac{\kappa+\lambda(3n_3^2-1)}{\varepsilon\sqrt{2\pi}}|\psi|^2 - \frac{3\lambda}{2}\varphi - \Omega L_z\right]\psi, \tag{6.2}$$

$$\varphi = \varphi(\mathbf{x}_\perp,t) = \left(\partial_{\mathbf{n}_\perp\mathbf{n}_\perp} - n_3^2\nabla_\perp^2\right)u(\mathbf{x}_\perp,t), \quad \mathbf{x}_\perp = (x,y)^T \in \mathbb{R}^2,\ t \geq 0, \tag{6.3}$$

where $\nabla_\perp = (\partial_x,\partial_y)^T$, $\nabla_\perp^2 = \partial_{xx} + \partial_{yy}$, $\mathbf{n}_\perp = (n_1,n_2)^T$, $\partial_{\mathbf{n}_\perp} = \mathbf{n}_\perp\cdot\nabla_\perp$, $\partial_{\mathbf{n}_\perp\mathbf{n}_\perp} = \partial_{\mathbf{n}_\perp}(\partial_{\mathbf{n}_\perp})$ and

$$u(\mathbf{x}_\perp,t) = G^\varepsilon * |\psi|^2, \quad G^\varepsilon(\mathbf{x}_\perp) = \frac{1}{(2\pi)^{3/2}}\int_{\mathbb{R}} \frac{e^{-s^2/2}}{\sqrt{|\mathbf{x}_\perp|^2+\varepsilon^2 s^2}}ds, \quad \mathbf{x}_\perp \in \mathbb{R}^2. \tag{6.4}$$

The above problem (6.2)-(6.3) with (6.4) is usually called *surface adiabatic model* (SAM) for a rotating BEC with dipole-dipole interaction in 2D. Furthermore, taking $\varepsilon \to 0^+$ in (6.4), we obtain

$$G^\varepsilon(\mathbf{x}_\perp) \to \frac{1}{2\pi|\mathbf{x}_\perp|} := G^0(\mathbf{x}_\perp), \qquad \mathbf{x}_\perp \in \mathbb{R}^2. \tag{6.5}$$

This, together with (6.4), implies that when $\varepsilon \to 0^+$,

$$u(\mathbf{x}_\perp,t) = \frac{1}{2\pi|\mathbf{x}_\perp|} * |\psi|^2 \Longleftrightarrow (-\nabla_\perp^2)^{1/2}u = |\psi|^2 \quad \text{with} \quad \lim_{|\mathbf{x}_\perp|\to\infty} u(\mathbf{x}_\perp,t) = 0. \tag{6.6}$$

The problem (6.2)-(6.3) with (6.6) is usually called *surface density model* (SDM) for a rotating BEC with dipole-dipole interaction in 2D. Note that even for the SDM we retain the ε-dependence in (6.2).

In fact, the GPE (1.10) or (1.13) in 3D and the SAM or SDM in 2D can be written in a unified way in d-dimensions ($d = 2$ or 3) with $\mathbf{x} = (x,y)^T$ when $d = 2$ and $\mathbf{x} = (x,y,z)^T$ when $d = 3$:

$$i\partial_t\psi(\mathbf{x},t) = \left[-\frac{1}{2}\nabla^2 + V(\mathbf{x}) + \beta|\psi|^2 + \eta\varphi(\mathbf{x},t) - \Omega L_z\right]\psi(\mathbf{x},t), \tag{6.7}$$

$$\varphi(\mathbf{x},t) = L_{\mathbf{n}}u(\mathbf{x},t), \qquad u(\mathbf{x},t) = G * |\psi|^2, \qquad \mathbf{x} \in \mathbb{R}^d, \quad t \geq 0, \tag{6.8}$$

where $V(\mathbf{x}) = V_2(\mathbf{x})$ when $d = 2$ and

$$\beta = \begin{cases} \frac{\kappa+\lambda(3n_3^2-1)}{\varepsilon\sqrt{2\pi}}, \\ \kappa - \lambda, \end{cases} \qquad \eta = \begin{cases} -3\lambda/2, \\ -3\lambda, \end{cases} \qquad L_{\mathbf{n}} = \begin{cases} \partial_{\mathbf{n}_\perp\mathbf{n}_\perp} - n_3^2\nabla^2, & d = 2, \\ \partial_{\mathbf{n}\mathbf{n}}, & d = 3, \end{cases} \tag{6.9}$$

$$G(\mathbf{x}) = \begin{cases} 1/2\pi|\mathbf{x}|, \\ G^\varepsilon(\mathbf{x}), \\ 1/4\pi|\mathbf{x}|, \end{cases} \Longleftrightarrow \widehat{G}(\xi) = \begin{cases} 1/|\xi|, & d=2\ \&\ \text{SDM}, \\ \frac{1}{2\pi^2}\int_{\mathbb{R}} \frac{e^{-\varepsilon^2 s^2/2}}{|\xi|^2+s^2} ds, & d=2\ \&\ \text{SAM}, \\ 1/|\xi|^2, & d=3, \end{cases} \qquad (6.10)$$

where $\widehat{f}(\xi)$ denotes the Fourier transform of the function $f(\mathbf{x})$ for $\mathbf{x}$, $\xi \in \mathbb{R}^d$. For studying the dynamics of a rotating BEC, the following initial condition is used:

$$\psi(\mathbf{x},0) = \psi_0(\mathbf{x}), \qquad \mathbf{x} \in \mathbb{R}^d, \qquad \text{with} \quad \|\psi_0\|^2 := \int_{\mathbb{R}^d} |\psi_0(\mathbf{x})|^2\, d\mathbf{x} = 1. \quad (6.11)$$

We remark here that in most BEC experiments, the following dimensionless harmonic potential is used

$$V(\mathbf{x}) = \frac{1}{2}\begin{cases} \gamma_x^2 x^2 + \gamma_y^2 y^2, & d=2, \\ \gamma_x^2 x^2 + \gamma_y^2 y^2 + \gamma_z^2 z^2, & d=3, \end{cases} \qquad (6.12)$$

where $\gamma_x > 0$, $\gamma_y > 0$ and $\gamma_z > 0$ are dimensionless constants proportional to the trapping frequencies in x-, y- and z-direction, respectively.

6.2 Dynamical properties

In this section, we analytically study the dynamics of rotating dipolar BECs. We present dynamical laws, including the conservation of angular momentum expectation, the dynamics of condensate widths and the dynamics of the center of mass. The results are quite similar to the ones in [17, 24].

6.2.1 Conservation of mass and energy

The GPE in (6.7)–(6.11) has two important invariants: the *mass* (or *normalization*) of the wave function, which is defined as

$$N(t) := \|\psi(\cdot,t)\|^2 := \int_{\mathbb{R}^d} |\psi(\mathbf{x},t)|^2 d\mathbf{x} \equiv \int_{\mathbb{R}^d} |\psi(\mathbf{x},0)|^2 d\mathbf{x} = 1, \qquad t \geq 0, \ (6.13)$$

and the *energy per particle*

$$\begin{aligned} E(t) \ &:= \ E(\psi(\cdot,t)) = \int_{\mathbb{R}^d} \left[\frac{1}{2}|\nabla\psi|^2 + V(\mathbf{x})|\psi|^2 + \frac{\beta}{2}|\psi|^4 + \frac{\eta}{2}\varphi|\psi|^2 - \Omega\psi^* L_z \psi\right] d\mathbf{x} \\ &\equiv \ E(\psi(\cdot,0)) = E(\psi_0), \qquad t \geq 0, \end{aligned} \qquad (6.14)$$

where f^* denotes the conjugate of the complex-valued function f. Stationary states, corresponding to critical points of the energy defined in (6.14), play an important role in the study of rotating dipolar BECs. Usually, to find stationary states $\phi_s(\mathbf{x})$, one can use the ansatz

$$\psi(\mathbf{x}, t) = e^{-i\mu_s t}\phi_s(\mathbf{x}), \qquad \mathbf{x} \in \mathbb{R}^d, \quad t \geq 0, \tag{6.15}$$

where $\mu_s \in \mathbb{R}$ is the chemical potential. Substituting (6.15) into (6.7) yields the nonlinear eigenvalue problem

$$\mu_s\phi_s(\mathbf{x}) = \left[-\frac{1}{2}\nabla^2 + V(\mathbf{x}) + \beta|\phi_s|^2 + \eta\varphi_s - \Omega L_z\right]\phi_s(\mathbf{x}), \qquad \mathbf{x} \in \mathbb{R}^d, \tag{6.16}$$

$$\varphi_s(\mathbf{x}) = L_{\mathbf{n}}u_s(\mathbf{x}), \qquad u_s(\mathbf{x}) = G * |\phi_s|^2, \qquad \mathbf{x} \in \mathbb{R}^d, \tag{6.17}$$

under the constraint

$$\|\phi_s\|^2 = \int_{\mathbb{R}^d} |\phi_s(\mathbf{x})|^2 d\mathbf{x} = 1. \tag{6.18}$$

Thus, by solving the constrained nonlinear eigenvalue problem (6.16)–(6.18), one can find the stationary states of rotating dipolar BECs. In physics literature, the stationary state with the lowest energy is called *ground state*, while those with larger energy are called *excited states*.

6.2.2 Conservation of angular momentum expectation

The *angular momentum expectation* of a condensate is defined as [17, 24]

$$\langle L_z\rangle(t) = \int_{\mathbb{R}^d} \psi^*(\mathbf{x}, t)L_z\psi(\mathbf{x}, t)\, d\mathbf{x}, \qquad t \geq 0. \tag{6.19}$$

This quantity is often used to measure the vortex flux. The following lemma describes the dynamics of angular momentum expectation in rotating dipolar BECs.

Lemma 6.2.1. *Suppose that $\psi(\mathbf{x}, t)$ solves the GPE (6.7)–(6.11) with $V(\mathbf{x})$ chosen as the harmonic potential (6.12). Then we have*

$$\frac{d\langle L_z\rangle(t)}{dt} = (\gamma_x^2 - \gamma_y^2)\int_{\mathbb{R}^d} xy|\psi|^2 d\mathbf{x} - \eta\int_{\mathbb{R}^d} |\psi|^2 \left[(x\partial_y - y\partial_x)\varphi\right] d\mathbf{x}, \quad t \geq 0. \tag{6.20}$$

Furthermore, the angular momentum expectation is conserved, i.e.,

$$\langle L_z \rangle(t) \equiv \langle L_z \rangle(0), \quad t \geq 0, \tag{6.21}$$

if the following two conditions are satisfied: (i). $\gamma_x = \gamma_y$*; (ii). any one of the following conditions hold true: (a).* $\eta = 0$*; (b). in 3D,* $\mathbf{n} = (0,0,1)^T$*; (c). in 2D,* $\mathbf{n} = (0,0,1)^T$ *and* ψ_0 *satisfies* $\psi_0(\mathbf{x}) = f(r)e^{im\theta}$*. That is, in a radially symmetric trap in 2D or a cylindrically symmetric trap in 3D, the angular momentum expectation is conserved when either there is no dipolar interaction or the dipole axis is parallel to the z-axis in 3-D or in 2-D with a radially symmetric or central vortex-type initial data.*

Proof. Differentiating (6.19) with respect to t, integrating by parts and taking (6.7) into account, we get

$$\begin{aligned}
\frac{d\langle L_z \rangle(t)}{dt} &= -\, i \int_{\mathbb{R}^3} \Big[\psi_t^*(x\partial_y - y\partial_x)\psi + \psi^*(x\partial_y - y\partial_x)\psi_t\Big] d\mathbf{x} \\
&= \int_{\mathbb{R}^3} \Big[(-i\psi_t^*)(x\partial_y - y\partial_x)\psi + (i\psi_t)(x\partial_y - y\partial_x)\psi^*\Big] d\mathbf{x} \\
&= \int_{\mathbb{R}^3} \Bigg[-\frac{1}{2}\left(\nabla^2\psi^*(x\partial_y - y\partial_x)\psi + \nabla^2\psi(x\partial_y - y\partial_x)\psi^*\right) \\
&\quad + \left(V(\mathbf{x}) + \beta_d|\psi|^2 + \eta\varphi\right)\left[(x\partial_y - y\partial_x)|\psi|^2\right]\Bigg] d\mathbf{x} \\
&= -\int_{\mathbb{R}^3} |\psi|^2 \Big[(x\partial_y - y\partial_x)\left(V(\mathbf{x}) + \eta\varphi\right)\Big]\, d\mathbf{x}, \quad t \geq 0.
\end{aligned} \tag{6.22}$$

Substituting (6.12) into (6.22) leads to (6.20) immediately. In 3D, due to (1.14), the second term in (6.20) further becomes

$$
\begin{aligned}
&-\eta\int_{\mathbb{R}^3}|\psi|^2(x\partial_y-y\partial_x)\varphi d\mathbf{x}=\eta\int_{\mathbb{R}^3}\nabla^2u(x\partial_y-y\partial_x)\,(\partial_{\mathbf{nn}}u)\,d\mathbf{x}\\
=&-\eta\int_{\mathbb{R}^3}(\partial_{\mathbf{n}}y\nabla^2u+y\nabla^2\partial_{\mathbf{n}}u)(\partial_x\partial_{\mathbf{n}}u)d\mathbf{x}+\eta\int_{\mathbb{R}^3}(\partial_{\mathbf{n}}x\nabla^2u+x\nabla^2\partial_{\mathbf{n}}u)(\partial_y\partial_{\mathbf{n}}u)\,d\mathbf{x}\\
=&\eta\int_{\mathbb{R}^3}\Big[n_1\partial_y(\partial_{\mathbf{n}}u)-n_2\partial_x(\partial_{\mathbf{n}}u)\Big]\nabla^2u\,d\mathbf{x}-\eta\int_{\mathbb{R}^3}\Big[x\partial_y(\partial_{\mathbf{n}}u)-y\partial_x(\partial_{\mathbf{n}}u)\Big]\nabla^2(\partial_{\mathbf{n}}u)\,d\mathbf{x}\\
=&\eta\int_{\mathbb{R}^3}\Big[n_1\partial_y(\partial_{\mathbf{n}}u)-n_2\partial_x(\partial_{\mathbf{n}}u)\Big]|\psi|^2\,d\mathbf{x}+\eta\int_{\mathbb{R}^3}\Big[y(\nabla\partial_{\mathbf{n}}u)\partial_x(\nabla\cdot\partial_{\mathbf{n}}u)\\
&+\nabla y\nabla(\partial_{\mathbf{n}}u)\partial_x(\partial_{\mathbf{n}}u)-x(\nabla\partial_{\mathbf{n}}u)\partial_y(\nabla\partial_{\mathbf{n}}u)-\nabla x\nabla(\partial_{\mathbf{n}}u)\partial_y(\partial_{\mathbf{n}}u)\Big]d\mathbf{x}\\
=&\eta\int_{\mathbb{R}^3}\Big[n_1\partial_y(\partial_{\mathbf{n}}u)-n_2\partial_x(\partial_{\mathbf{n}}u)\Big]|\psi|^2\,d\mathbf{x}+\eta\int_{\mathbb{R}^3}(\nabla\partial_{\mathbf{n}}u)(y\partial_x-x\partial_y)(\nabla\partial_{\mathbf{n}}u)d\mathbf{x}\\
=&\eta\int_{\mathbb{R}^3}\Big[n_1\partial_y(\partial_{\mathbf{n}}u)-n_2\partial_x(\partial_{\mathbf{n}}u)\Big]|\psi|^2\,d\mathbf{x},\qquad t\geq 0.
\end{aligned}
\tag{6.23}
$$

Thus, in a radially symmetric trap, i.e., $\gamma_x=\gamma_y$, if there is $\lambda=0$ or $\mathbf{n}=(0,0,1)^T$, we get

$$
\frac{d\langle L_z\rangle(t)}{dt}=0,\qquad t\geq 0,
\tag{6.24}
$$

from (6.20) and (6.23), which implies the conservation of $\langle L_z\rangle$ in (6.21).

Look into (6.20), claims in (ii) (a) is clearly and (c) is straightforward due to the radial symmetry of the solution of $\psi(\mathbf{x},t)$ under the condition given there. □

6.2.3 Dynamics of condensate width

The *condensate width* of a BEC in α-direction (where $\alpha=x,y,z$ or $r=\sqrt{x^2+y^2}$) is defined by

$$
\sigma_\alpha(t)=\sqrt{\delta_\alpha(t)},\qquad t\geq 0,\qquad \text{where}\quad \delta_\alpha(t)=\int_{\mathbb{R}^d}\alpha^2|\psi(\mathbf{x},t)|^2d\mathbf{x}.
\tag{6.25}
$$

In particular, when $d=2$, we have the following lemma for its dynamics [17]:

Lemma 6.2.2. *Consider two-dimensional BECs with radially symmetric harmonic trap (6.12), i.e., $d=2$ and $\gamma_x=\gamma_y:=\gamma_r$. If $\eta=0$, then for any initial datum $\psi_0(\mathbf{x})$ in (6.11), it holds for $t\geq 0$*

$$
\delta_r(t)=\frac{E(\psi_0)+\Omega\langle L_z\rangle(0)}{\gamma_r^2}[1-\cos(2\gamma_r t)]+\delta_r^{(0)}\cos(2\gamma_r t)+\frac{\delta_r^{(1)}}{2\gamma_r}\sin(2\gamma_r t),
\tag{6.26}
$$

where $\delta_r(t) := \delta_x(t) + \delta_y(t)$, $\delta_r^{(0)} := \delta_x(0) + \delta_y(0)$ *and* $\delta_r^{(1)} := \dot{\delta}_x(0) + \dot{\delta}_y(0)$. *Furthermore, if the initial condition* $\psi_0(\mathbf{x})$ *is radially symmetric, we have for* $t \geq 0$

$$\begin{aligned}\delta_x(t) = \delta_y(t) &= \frac{1}{2}\delta_r(t)\\ &= \frac{E(\psi_0) + \Omega\langle L_z\rangle(0)}{2\gamma_x^2}[1 - \cos(2\gamma_x t)] + \delta_x^{(0)}\cos(2\gamma_x t) + \frac{\delta_x^{(1)}}{2\gamma_x}\sin(2\gamma_x t). \qquad (6.27)\end{aligned}$$

Thus, in this case the condensate widths $\sigma_x(t)$ *and* $\sigma_y(t)$ *are periodic functions with frequency doubling trapping frequency.*

Proof. Differentiating (6.25) with respect to t, integrating by parts and taking (6.7) into account, we obtain

$$\begin{aligned}\frac{d\delta_\alpha(t)}{dt} &= \int_{\mathbb{R}^d} \alpha^2\left(\psi_t^*\psi + \psi^*\psi_t\right)d\mathbf{x} = i\int_{\mathbb{R}^d}\alpha^2\Big[(-i\psi_t^*)\psi - \psi^*(i\psi_t)\Big]d\mathbf{x}\\ &= i\int_{\mathbb{R}^d}\left[-\frac{\alpha^2}{2}\left(\psi\nabla^2\psi^* - \psi^*\nabla^2\psi\right) - i\Omega\alpha^2\left(x\partial_y - y\partial_x\right)|\psi|^2\right]d\mathbf{x}\\ &= \int_{\mathbb{R}^d}\left[i\alpha(\psi\partial_\alpha\psi^* - \psi^*\partial_\alpha\psi) - 2\Omega\alpha|\psi|^2(x\partial_y - y\partial_x)\alpha\right]d\mathbf{x}, \qquad t \geq 0. \qquad (6.28)\end{aligned}$$

Similarly, differentiating (6.28) with respect to t, integrating by parts and noticing (6.7), we have

$$\begin{aligned}\frac{d^2\delta_\alpha(t)}{dt^2} &= \int_{\mathbb{R}^d}\alpha\Big[i\Big(\psi_t\psi_\alpha^* + \psi\psi_{\alpha t}^* - \psi_t^*\psi_\alpha - \psi^*\psi_{\alpha t}\Big) - 2\Omega(\psi_t^*\psi + \psi^*\psi_t)(x\partial_y - y\partial_x)\alpha\Big]d\mathbf{x}\\ &= \int_{\mathbb{R}^d}\Big[2\alpha\Big((i\psi_t)\psi_\alpha^* + (-i\psi_t^*)\psi_\alpha\Big) + \Big(\psi^*(i\psi_t) + \psi(-i\psi_t^*)\Big)\\ &\qquad - 2i\Omega\alpha(x\partial_y\alpha - y\partial_x\alpha)\Big((-i\psi_t^*)\psi - \psi^*(i\psi_t)\Big)\Big]d\mathbf{x}\\ &= \int_{\mathbb{R}^d}\Big[\alpha\Big(-(\psi_\alpha^*\nabla^2\psi + \psi_\alpha\nabla^2\psi^*) + 2(V(\mathbf{x}) + \beta|\psi|^2 + \eta\varphi)\partial_\alpha|\psi|^2\\ &\qquad + 2i\Omega(\psi_\alpha^*(x\partial_y - y\partial_x)\psi - \psi_\alpha(x\partial_y - y\partial_x)\psi^*)\Big) + \Big(-\frac{1}{2}(\psi^*\nabla^2\psi + \psi\nabla^2\psi^*)\\ &\qquad + 2(V(\mathbf{x}) + \beta|\psi|^2 + \eta\varphi)|\psi|^2 - i\Omega(\psi(x\partial_y - y\partial_x)\psi^* - \psi^*(x\partial_y - y\partial_x)\psi)\Big)\\ &\qquad + 2i\Omega\alpha(x\partial_y\alpha - y\partial_x\alpha)\Big(\frac{1}{2}(\psi\nabla^2\psi^* - \psi^*\nabla^2\psi) + i\Omega(x\partial_y - y\partial_x)|\psi|^2\Big)\Big]d\mathbf{x};\end{aligned}$$

Moreover, we obtain for $t \geq 0$

$$\begin{aligned}
\frac{d^2\delta_\alpha(t)}{dt^2} = &\int_{\mathbb{R}^d} \Big[\Big(2|\psi_\alpha|^2 - |\nabla\psi|^2 - 2(V(\mathbf{x}) + \beta|\psi|^2 + \eta\varphi)|\psi|^2 + \beta|\psi|^4 \\
&- 2\alpha|\psi|^2\partial_\alpha(V(\mathbf{x}) + \eta\varphi) + 2i\Omega(\partial_y\alpha - \partial_x\alpha)\psi^*(x\partial_y + y\partial_x)\psi \\
&- 2i\Omega\psi^*(x\partial_y - y\partial_x)\psi\Big) + \Big(|\nabla\psi|^2 + 2(V(\mathbf{x}) + \beta|\psi|^2 + \eta\varphi)|\psi|^2 \\
&+ 2i\Omega\psi^*(x\partial_y - y\partial_x)\psi\Big) + (\partial_y\alpha - \partial_x\alpha)\Big(2i\Omega\psi^*(x\partial_y + y\partial_x)\psi \\
&+ 2\Omega^2(x^2 - y^2)|\psi|^2\Big)\Big]d\mathbf{x} \\
= &-2\gamma_\alpha^2\delta_\alpha(t) + \int_{\mathbb{R}^2}\Big[2|\psi_\alpha|^2 + \beta|\psi|^4 - 2\eta\alpha|\psi|^2\partial_\alpha\varphi \\
&+ (\partial_y\alpha - \partial_x\alpha)\Big(4i\Omega(x\partial_y + y\partial_x)\psi + 2\Omega^2(x^2 - y^2)|\psi|^2\Big)\Big]d\mathbf{x}. \qquad (6.29)
\end{aligned}$$

Hence when $d = 2$, if $\gamma_x = \gamma_y = \gamma_r$ and $\eta = 0$, combine with (6.29), (6.14) and lemma 6.2.1, we have

$$\begin{aligned}
\frac{d^2\delta_r(t)}{dt^2} =& \frac{d^2\delta_x(t)}{dt^2} + \frac{d^2\delta_y(t)}{dt^2} = -4\gamma_r^2\delta_r(t) + 2\int_{\mathbb{R}^2}\left[|\nabla\psi|^2 + \beta|\psi|^4\right]d\mathbf{x} \\
=& -4\gamma_r^2\delta_r(t) + 4\int_{\mathbb{R}^2}\left[\frac{1}{2}|\nabla\psi|^2 + V(\mathbf{x})|\psi|^2 + \frac{\beta}{2}|\psi|^4 - \Omega\mathrm{Re}(\psi^* L_z\psi)\right]d\mathbf{x} \\
&+ 4\Omega\int_{\mathbb{R}^2}\mathrm{Re}(\psi^* L_z\psi)d\mathbf{x} \\
=& -4\gamma_r^2\delta_r(t) + 4E(\psi_0) + 4\Omega\langle L_z\rangle(0), \qquad t \geq 0. \qquad (6.30)
\end{aligned}$$

Thus, (6.26) is the unique solution of the second order ODE (6.30) with the initial condition $\delta_r(0) = \delta_r^{(0)}$ and $\dot{\delta}_r(0) = \delta_r^{(1)}$.

Furthermore, if ψ_0 has radial symmetric structure, the solution $\psi(\mathbf{x}, t)$ is also radial symmetric since $\gamma_x = \gamma_y$, and can be rewritten in the form of

$$\psi(\mathbf{x}, t) = f(r, t)e^{im\theta(t)}$$

and thus

$$\begin{aligned}
\delta_x(t) &= \int_{\mathbb{R}^d} x^2|\phi|^2 d\mathbf{x} = \int_0^\infty\int_0^{2\pi} r^2\cos^2\theta|f(r,t)|^2 r d\theta dr \\
&= \pi\int_0^\infty r^2|f(r,t)|^2 r dr = \int_0^\infty\int_0^{2\pi} r^2\sin^2\theta|f(r,t)|^2 r d\theta dr \\
&= \int_{\mathbb{R}^d} y^2|\phi|^2 d\mathbf{x} = \delta_y(t) = \frac{1}{2}\delta_r(t). \qquad (6.31)
\end{aligned}$$

□

6.2.4 Dynamics of center of mass

We define the *center of mass* of a condensate at any time t by

$$\mathbf{x}_c(t) = \int_{\mathbb{R}^d} \mathbf{x}\,|\psi(\mathbf{x},t)|^2 d\mathbf{x}, \qquad t \geq 0. \tag{6.32}$$

The following lemma describes the dynamics of the center of mass.

Lemma 6.2.3. *Suppose that $\psi(\mathbf{x},t)$ solves the GPE (6.7)–(6.11) with $V(\mathbf{x})$ chosen as the harmonic potential (6.12). Then for any given initial data ψ_0, the dynamics of the center of mass are governed by the following second-order ODEs:*

$$\ddot{\mathbf{x}}_c(t) - 2\Omega J\dot{\mathbf{x}}_c(t) + (\Lambda + \Omega^2 J^2)\,\mathbf{x}_c(t) = 0, \qquad t \geq 0, \tag{6.33}$$

$$\mathbf{x}_c(0) = \mathbf{x}_c^{(0)} := \int_{\mathbb{R}^d} \mathbf{x}|\psi_0|^2 d\mathbf{x}, \tag{6.34}$$

$$\dot{\mathbf{x}}_c(0) = \mathbf{x}_c^{(1)} := \int_{\mathbb{R}^d} \mathrm{Im}\,(\psi_0^* \nabla\psi_0)\,d\mathbf{x} - \Omega J\mathbf{x}_c^{(0)}, \tag{6.35}$$

where $\mathrm{Im}(f)$ *denotes the imaginary part of the function f and the matrices*

$$J = \begin{pmatrix} 0 & 1 \\ -1 & 0 \end{pmatrix}, \qquad \Lambda = \begin{pmatrix} \gamma_x^2 & 0 \\ 0 & \gamma_y^2 \end{pmatrix}, \qquad \textit{for} \quad d = 2,$$

or

$$J = \begin{pmatrix} 0 & 1 & 0 \\ -1 & 0 & 0 \\ 0 & 0 & 0 \end{pmatrix}, \qquad \Lambda = \begin{pmatrix} \gamma_x^2 & 0 & 0 \\ 0 & \gamma_y^2 & 0 \\ 0 & 0 & \gamma_z^2 \end{pmatrix}, \qquad \textit{for} \quad d = 3.$$

Proof. For simplicity, we consider $d = 3$ in the following proof. Differentiating (6.32) with respect to t, integrating by parts and taking (6.7) into account, we obtain

$$\begin{aligned}
\frac{d\mathbf{x}_c(t)}{dt} &= \int_{\mathbb{R}^3} \mathbf{x}(\psi_t^*\psi + \psi^*\psi_t)d\mathbf{x} = i\int_{\mathbb{R}^3} \mathbf{x}\Big[(-i\psi_t^*)\psi - \psi^*(i\psi_t)\Big]d\mathbf{x} \\
&= i\int_{\mathbb{R}^3} \Big[-\frac{1}{2}\mathbf{x}\left(\psi\nabla^2\psi^* - \psi^*\nabla^2\psi\right) - i\Omega\mathbf{x}(x\partial_y - y\partial_x)|\psi|^2\Big]d\mathbf{x} \\
&= \int_{\mathbb{R}^3} \Big[-i\psi^*\nabla\psi - \Omega|\psi|^2(x\partial_y - y\partial_x)\mathbf{x}\Big]d\mathbf{x} \\
&= \int_{\mathbb{R}^3} \Big(-i\psi^*\nabla\psi + \Omega\mathbf{J}\mathbf{x}|\psi|^2\Big)d\mathbf{x} = \Omega\mathbf{J}\mathbf{x}_c(t) - i\int_{\mathbb{R}^3} (\psi^*\nabla\psi)\,d\mathbf{x}, \quad t \geq 0.
\end{aligned} \tag{6.36}$$

Differentiating (6.36) with respect to t and following the similar procedures, we have

$$\begin{aligned}
&\frac{d^2\mathbf{x}_c(t)}{dt^2} - \Omega\mathbf{J}\frac{d\mathbf{x}_c(t)}{dt} \\
&\qquad = -i\int_{\mathbb{R}^3} \left(\psi_t^*\nabla\psi + \psi^*\nabla\psi_t\right) d\mathbf{x} = \int_{\mathbb{R}^3} \Big[(-i\psi_t^*)\nabla\psi + (i\psi_t)\nabla\psi^*\Big] d\mathbf{x} \\
&\qquad = \int_{\mathbb{R}^3} \bigg[-\frac{1}{2}\left(\nabla^2\psi^*\nabla\psi + \nabla^2\psi\nabla\psi^*\right) + \left(V(\mathbf{x}) + \eta\varphi\right)\nabla|\psi|^2 \\
&\qquad\quad - i\Omega\Big((x\partial_y - y\partial_x)\psi^*\nabla\psi - (x\partial_y - y\partial_x)\psi\nabla\psi^*\Big)\bigg] d\mathbf{x} \\
&\qquad = -\int_{\mathbb{R}^3} |\psi|^2\nabla\left[V(\mathbf{x}) + \eta\varphi\right] d\mathbf{x} - i\Omega\,\mathbf{J}\int_{\mathbb{R}^3} \left(\psi^*\nabla\psi\right) d\mathbf{x}. \qquad (6.37)
\end{aligned}$$

Noticing (6.36) and $V(\mathbf{x})$ defined in (6.12), we can rewrite the ODE (6.37) as

$$\begin{aligned}
&\frac{d^2\mathbf{x}_c(t)}{dt^2} - \Omega\mathbf{J}\frac{d\mathbf{x}_c(t)}{dt} \\
&\qquad = -\mathbf{\Lambda}\int_{\mathbb{R}^3} \mathbf{x}|\psi|^2 d\mathbf{x} - \Omega\mathbf{J}\left(\frac{d\mathbf{x}_c(t)}{dt} + \Omega\mathbf{J}\mathbf{x}_c(t)\right) + \eta\int_{\mathbb{R}^3} (\nabla^2 u)\nabla\partial_{\mathbf{nn}}u\, d\mathbf{x} \\
&\qquad = -\mathbf{\Lambda}\int_{\mathbb{R}^3} \mathbf{x}|\psi|^2 d\mathbf{x} - \Omega\mathbf{J}\left(\frac{d\mathbf{x}_c(t)}{dt} + \Omega\mathbf{J}\mathbf{x}_c(t)\right) - \eta\int_{\mathbb{R}^3} \nabla|\nabla(\partial_{\mathbf{n}}u)|^2\, d\mathbf{x} \\
&\qquad = -\mathbf{\Lambda}\mathbf{x}_c(t) + \Omega\mathbf{J}\frac{d\mathbf{x}_c(t)}{dt} + \Omega^2\mathbf{x}_c(t), \quad t \geq 0. \qquad (6.38)
\end{aligned}$$

Combining (6.38) with (6.32) and (6.36) at time $t = 0$, we can get the ODEs (6.33)–(6.35). ☐

Lemma 6.2.3 shows that the dynamics of the center of mass depends on the trapping frequencies and the angular velocity, but it is independent of the interaction strength constants β and η in (6.7). For analytical solutions to the second-order ODEs (6.33)-(6.35), we refer to [151].

6.2.5 An analytical solution under special initial data

From Lemma 6.2.3, we can construct an analytical solution to the GPE (6.7)–(6.11) when the initial data is chosen as a stationary state with its center shifted.

Lemma 6.2.4. *Suppose $V(\mathbf{x})$ in (6.7) is chosen as the harmonic potential (6.12) and the initial condition $\psi_0(\mathbf{x})$ in (6.11) is chosen as*

$$\psi_0(\mathbf{x}) = \phi_s(\mathbf{x} - \mathbf{x}^0), \qquad \mathbf{x} \in \mathbb{R}^d, \qquad (6.39)$$

where $\mathbf{x}^0 \in \mathbb{R}^d$ *is a given point and* $\phi_s(\mathbf{x})$ *is a stationary state defined in (6.16)–(6.18) with chemical potential* μ_s*, then the exact solution of (6.7)–(6.11) can be constructed as*

$$\psi(\mathbf{x},t) = \phi_s(\mathbf{x}-\mathbf{x}_c(t))\, e^{-i\mu_s t}\, e^{iw(\mathbf{x},t)}, \qquad \mathbf{x}\in\mathbb{R}^d, \quad t\geq 0, \tag{6.40}$$

where $\mathbf{x}_c(t)$ *satisfies the ODE (6.33) with*

$$\mathbf{x}_c(0) = \mathbf{x}^0, \qquad \dot{\mathbf{x}}_c(0) = -\Omega J \mathbf{x}^0, \tag{6.41}$$

and $w(\mathbf{x},t)$ *is linear in* $\mathbf{x}$*, i.e.,*

$$w(\mathbf{x},t) = \mathbf{c}(t)\cdot\mathbf{x} + g(t), \quad \mathbf{c}(t) = (c_1(t),\ldots,c_d(t))^T, \quad \mathbf{x}\in\mathbb{R}^d, \quad t\geq 0$$

for some functions $\mathbf{c}(t)$ *and* $g(t)$*. Thus, up to phase shifts,* ψ *remains a stationary state with shifted center at all times.*

6.3 GPE under a rotating Lagrangian coordinate

In this section, we first introduce a coordinate transformation and derive the GPE in transformed coordinates. Then we reformulate the dynamical quantities studied in Section 6.2 in the new coordinate system.

6.3.1 A rotating Lagrangian coordinate transformation

For any time $t \geq 0$, let $A(t)$ be an orthogonal rotational matrix defined as

$$A(t) = \begin{pmatrix} \cos(\Omega t) & \sin(\Omega t) \\ -\sin(\Omega t) & \cos(\Omega t) \end{pmatrix}, \qquad \text{if} \quad d = 2, \tag{6.42}$$

and

$$A(t) = \begin{pmatrix} \cos(\Omega t) & \sin(\Omega t) & 0 \\ -\sin(\Omega t) & \cos(\Omega t) & 0 \\ 0 & 0 & 1 \end{pmatrix}, \qquad \text{if} \quad d = 3. \tag{6.43}$$

It is easy to verify that $A^{-1}(t) = A^T(t)$ for any $t \geq 0$ and $A(0) = I$ with I the identity matrix. For any $t \geq 0$, we introduce the *rotating Lagrangian coordinates* $\widetilde{\mathbf{x}}$ as [10, 63, 71]

$$\widetilde{\mathbf{x}} = A^{-1}(t)\mathbf{x} = A^T(t)\mathbf{x} \quad \Leftrightarrow \quad \mathbf{x} = A(t)\widetilde{\mathbf{x}}, \qquad \mathbf{x} \in \mathbb{R}^d, \tag{6.44}$$

and denote the wave function in the new coordinates as $\phi := \phi(\widetilde{\mathbf{x}}, t)$

$$\phi(\widetilde{\mathbf{x}}, t) := \psi(\mathbf{x}, t) = \psi\left(A(t)\widetilde{\mathbf{x}}, t\right), \qquad \mathbf{x} \in \mathbb{R}^d, \quad t \geq 0. \tag{6.45}$$

In fact, here we refer the Cartesian coordinates $\mathbf{x}$ as the *Eulerian coordinates* and Fig. 6.1 depicts the geometrical relation between the Eulerian coordinates $\mathbf{x}$ and the rotating Lagrangian coordinates $\widetilde{\mathbf{x}}$ for any fixed $t \geq 0$.

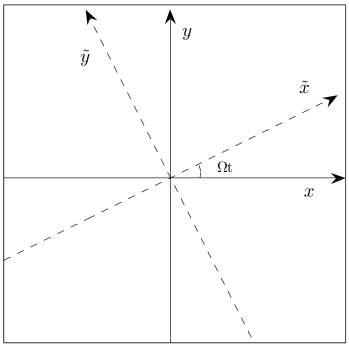

Figure 6.1: Cartesian (or Eulerian) coordinates (x, y) (solid) and rotating Lagrangian coordinates $(\tilde{x}, \tilde{y})$ (dashed) in 2D for any fixed $t \geq 0$.

Using the chain rule, we obtain the derivatives:

$$\partial_t\phi(\widetilde{\mathbf{x}}, t) = \partial_t\psi(\mathbf{x}, t) + \nabla\psi(\mathbf{x}, t) \cdot \left(\dot{A}(t)\widetilde{\mathbf{x}}\right) = \partial_t\psi(\mathbf{x}, t) - \Omega(x\partial_y - y\partial_x)\psi(\mathbf{x}, t),$$

$$\nabla\phi(\widetilde{\mathbf{x}}, t) = A^{-1}(t)\nabla\psi(\mathbf{x}, t), \qquad \nabla^2\phi(\widetilde{\mathbf{x}}, t) = \nabla^2\psi(\mathbf{x}, t).$$

Substituting them into (6.7)–(6.11) gives the following d-dimensional GPE in the rotating Lagrangian coordinates:

$$i\partial_t\phi(\widetilde{\mathbf{x}}, t) = \left[-\frac{1}{2}\nabla^2 + W(\widetilde{\mathbf{x}}, t) + \beta|\phi|^2 + \eta\varphi(\widetilde{\mathbf{x}}, t)\right]\phi(\widetilde{\mathbf{x}}, t), \;\; \widetilde{\mathbf{x}} \in \mathbb{R}^d, \;\; t > 0, \tag{6.46}$$

$$\varphi(\widetilde{\mathbf{x}}, t) = L_{\mathbf{m}(t)}u(\widetilde{\mathbf{x}}, t), \qquad u(\widetilde{\mathbf{x}}, t) = G * |\phi|^2, \qquad \widetilde{\mathbf{x}} \in \mathbb{R}^d, \quad t \geq 0, \tag{6.47}$$

where G is defined in (6.10) and

$$W(\widetilde{\mathbf{x}},t) = V(A(t)\widetilde{\mathbf{x}}), \qquad \widetilde{\mathbf{x}} \in \mathbb{R}^d, \tag{6.48}$$

$$L_{\mathbf{m}(t)} = \begin{cases} \partial_{\mathbf{m}_\perp(t)\mathbf{m}_\perp(t)} - n_3^2\nabla^2, & d=2, \\ \partial_{\mathbf{m}(t)\mathbf{m}(t)}, & d=3, \end{cases} \qquad t \geq 0, \tag{6.49}$$

with $\mathbf{m}(t) \in \mathbb{R}^3$ and $\mathbf{m}_\perp(t) \in \mathbb{R}^2$ defined as

$$\mathbf{m}(t) = \begin{pmatrix} m_1(t) \\ m_2(t) \\ m_3(t) \end{pmatrix} := A^{-1}(t)\mathbf{n} = \begin{pmatrix} n_1\cos(\Omega t) - n_2\sin(\Omega t) \\ n_1\sin(\Omega t) + n_2\cos(\Omega t) \\ n_3 \end{pmatrix}, \quad t \geq 0, \tag{6.50}$$

and $\mathbf{m}_\perp(t) = (m_1(t), m_2(t))^T$, respectively. The initial data transforms as

$$\phi(\widetilde{\mathbf{x}},0) = \psi(\mathbf{x},0) = \psi_0(\mathbf{x}) := \phi_0(\mathbf{x}) = \phi_0(\widetilde{\mathbf{x}}), \qquad \widetilde{\mathbf{x}} = \mathbf{x} \in \mathbb{R}^d. \tag{6.51}$$

We remark here again that if $V(\mathbf{x})$ in (6.7) is a harmonic potential as defined in (6.12), then the potential $W(\widetilde{\mathbf{x}},t)$ in (6.46) has the form

$$W(\widetilde{\mathbf{x}},t) = \frac{1}{4}\begin{cases} \omega_1(\widetilde{x}^2+\widetilde{y}^2) + \omega_2\left[(\widetilde{x}^2-\widetilde{y}^2)\cos(2\Omega t) + 2\widetilde{x}\widetilde{y}\sin(2\Omega t)\right], & d=2, \\ \omega_1(\widetilde{x}^2+\widetilde{y}^2) + \omega_2\left[(\widetilde{x}^2-\widetilde{y}^2)\cos(2\Omega t) + 2\widetilde{x}\widetilde{y}\sin(2\Omega t)\right] + 2\gamma_z^2\widetilde{z}^2, & d=3, \end{cases}$$

where $\omega_1 = \gamma_x^2 + \gamma_y^2$ and $\omega_2 = \gamma_x^2 - \gamma_y^2$. It is easy to see that when $\gamma_x = \gamma_y := \gamma_r$, i.e., radially and cylindrically symmetric harmonic trap in 2D and 3D, respectively, we have $\omega_1 = 2\gamma_r^2$ and $\omega_2 = 0$ and thus the potential $W(\widetilde{\mathbf{x}},t) = V(\widetilde{\mathbf{x}})$ becomes time-independent.

In contrast to (6.7), the GPE (6.46) does not have an angular momentum rotation term, which enables us to develop simple and efficient numerical methods for simulating the dynamics of rotating dipolar BEC in Section 6.4.

6.3.2 Dynamical quantities

In the above, we introduced rotating Lagrangian coordinates and cast the GPE in the new coordinate system. Next we consider the dynamical laws in terms of the new wave function $\phi(\widetilde{\mathbf{x}},t)$.

Mass and energy. In rotating Lagrangian coordinates, the conservation of mass (6.13) yields

$$\|\psi(\cdot,t)\|^2 := \int_{\mathbb{R}^d} |\psi(\mathbf{x},t)|^2 d\mathbf{x} = \int_{\mathbb{R}^d} |\phi(\widetilde{\mathbf{x}},t)|^2 d\widetilde{\mathbf{x}} = \|\phi(\cdot,t)\|^2 \equiv 1, \quad t \geq 0. \tag{6.52}$$

The energy defined in (6.14) becomes

$$\begin{aligned}\widetilde{E}(\phi(\cdot,t)) = & \int_{\mathbb{R}^d} \left[\frac{1}{2}|\nabla\phi|^2 + W(\widetilde{\mathbf{x}},t)|\phi|^2 + \frac{\beta}{2}|\phi|^4 + \frac{\eta}{2}\varphi|\phi|^2\right] d\widetilde{\mathbf{x}} \\ & - \int_{\mathbb{R}^d}\int_0^t \left[\partial_s W(\widetilde{\mathbf{x}},s) + \frac{\eta}{2}(\partial_s L_{\mathbf{m}(s)})u(\widetilde{\mathbf{x}},s)\right]|\phi|^2 ds\, d\widetilde{\mathbf{x}} \\ \equiv & \widetilde{E}(\phi(\cdot,0)), \qquad t \geq 0,\end{aligned} \tag{6.53}$$

where u is given in (6.47). Specifically, it holds

$$\partial_t L_{\mathbf{m}(t)} = 2\begin{cases}\partial_{\dot{A}^T(t)\mathbf{n}_\perp}\partial_{A^T(t)\mathbf{n}_\perp}, & d=2, \\ \partial_{\dot{A}^T(t)\mathbf{n}}\partial_{A^T(t)\mathbf{n}}, & d=3.\end{cases}$$

Angular momentum expectation. The angular momentum expectation in the new coordinates becomes

$$\begin{aligned}\langle L_z\rangle(t) &= -i\int_{\mathbb{R}^d} \psi^*(\mathbf{x},t)(x\partial_y - y\partial_x)\psi(\mathbf{x},t)\, d\mathbf{x} \\ &= -i\int_{\mathbb{R}^d} \phi^*(\widetilde{\mathbf{x}},t)(\widetilde{x}\partial_{\widetilde{y}} - \widetilde{y}\partial_{\widetilde{x}})\phi(\widetilde{\mathbf{x}},t)\, d\widetilde{\mathbf{x}}, \qquad t \geq 0,\end{aligned} \tag{6.54}$$

which has the same form as (6.19) in the new coordinates of $\widetilde{\mathbf{x}} \in \mathbb{R}^d$ and the wave function $\phi(\widetilde{\mathbf{x}},t)$. Indeed, if we denote $\widetilde{L}_z$ as the z-component of the angular momentum in the rotating Lagrangian coordinates, we have $\widetilde{L}_z = -i(\widetilde{x}\partial_{\widetilde{y}} - \widetilde{y}\partial_{\widetilde{x}}) = -i(x\partial_y - y\partial_x) = L_z$, i.e., the coordinate transform does not change the angular momentum in z-direction. In addition, noticing that for any $t \geq 0$ it holds $\phi(\widetilde{\mathbf{x}},t) = \psi(\mathbf{x},t)$ and $|A(t)| = 1$ for any $t \geq 0$ immediately yields (6.54).

Condensate width. After the coordinate transform, it holds

$$\delta_r(t) = \int_{\mathbb{R}^d} (x^2+y^2)|\psi|^2 d\mathbf{x} = \int_{\mathbb{R}^d} (\widetilde{x}^2+\widetilde{y}^2)|\phi|^2 d\widetilde{\mathbf{x}} = \delta_{\widetilde{x}}(t) + \delta_{\widetilde{y}}(t), \tag{6.55}$$

$$\delta_z(t) = \int_{\mathbb{R}^d} z^2|\psi|^2 d\mathbf{x} = \int_{\mathbb{R}^d} \widetilde{z}^2|\phi|^2 d\widetilde{\mathbf{x}} = \delta_{\widetilde{z}}(t), \tag{6.56}$$

for any $t \geq 0$.

Center of mass. The center of mass in rotating Lagrangian coordinates is defined as

$$\widetilde{\mathbf{x}}_c(t) = \int_{\mathbb{R}^d} \widetilde{\mathbf{x}}\,|\phi(\widetilde{\mathbf{x}},t)|^2 d\widetilde{\mathbf{x}}, \qquad t \geq 0. \tag{6.57}$$

Since $\det(A(t)) = 1$ for any $t \geq 0$, it holds that $\mathbf{x}_c(t) = A(t)\widetilde{\mathbf{x}}_c(t)$ for any time $t \geq 0$. In rotating Lagrangian coordinates, we have the following analogue of Lemma 6.2.4:

Lemma 6.3.1. *Suppose $V(\mathbf{x})$ in (6.7) is chosen as the harmonic potential (6.12) and the initial condition $\phi_0(\widetilde{\mathbf{x}})$ in (6.51) is chosen as*

$$\phi_0(\widetilde{\mathbf{x}}) = \phi_s(\widetilde{\mathbf{x}} - \widetilde{\mathbf{x}}^0), \qquad \widetilde{\mathbf{x}} \in \mathbb{R}^d, \tag{6.58}$$

where $\widetilde{\mathbf{x}}^0$ is a given point in $\mathbb{R}^d$ and $\phi_s(\widetilde{\mathbf{x}})$ is a stationary state defined in (6.16)–(6.18) with chemical potential μ_s, then the exact solution of (6.46)–(6.47) *is of the form*

$$\phi(\widetilde{\mathbf{x}},t) \;=\; \phi_s(\widetilde{\mathbf{x}} - \widetilde{\mathbf{x}}_c(t))\, e^{-i\mu_s t}\, e^{i\widetilde{w}(\widetilde{\mathbf{x}},t)}, \qquad t > 0, \tag{6.59}$$

where $\widetilde{\mathbf{x}}_c(t)$ satisfies the second-order ODEs:

$$\ddot{\widetilde{\mathbf{x}}}_c(t) + A^T(t)\Lambda A(t)\,\widetilde{\mathbf{x}}_c(t) = \mathbf{0}, \qquad t \geq 0, \tag{6.60}$$

$$\widetilde{\mathbf{x}}_c(0) = \widetilde{\mathbf{x}}^0, \quad \dot{\widetilde{\mathbf{x}}}_c(0) = \mathbf{0}, \tag{6.61}$$

with the matrix Λ defined in Lemma 6.2.3 and $\widetilde{w}(\widetilde{\mathbf{x}},t)$ is linear in $\widetilde{\mathbf{x}}$, i.e.,

$$\widetilde{w}(\widetilde{\mathbf{x}},t) = \widetilde{\mathbf{c}}(t)\cdot\widetilde{\mathbf{x}} + \widetilde{g}(t), \quad \widetilde{\mathbf{c}}(t) = (\widetilde{c}_1(t),\ldots,\widetilde{c}_d(t))^T, \quad \mathbf{x} \in \mathbb{R}^d, \quad t \geq 0.$$

We have seen that the form of the transformation matrix $A(t)$ in (6.43) is such that the coordinate transformation does not affect the quantities in z-direction, e.g. $\langle L_z\rangle(t)$, $\sigma_z(t)$ and $z_c(t)$.

6.4 Numerical methods

To study the dynamics of rotating dipolar BECs, in this section we propose a simple and efficient numerical method for discretizing the GPE (6.46)–(6.51) in rotating Lagrangian coordinates. The detailed discretizations for both the 2D and 3D GPEs are presented. Here we assume $\Omega \neq 0$, and for $\Omega = 0$, we refer to [14, 16, 39, 143].

In practical computations, we first truncate the whole space problem (6.46)–(6.51) to a bounded computational domain $\mathcal{D} \subset \mathbb{R}^d$ and consider

$$i\partial_t \phi(\widetilde{\mathbf{x}}, t) = -\frac{1}{2}\nabla^2 \phi + W(\widetilde{\mathbf{x}}, t)\phi + \beta|\phi|^2\phi + \eta\varphi\phi, \quad \widetilde{\mathbf{x}} \in \mathcal{D},\ t > 0, \tag{6.62}$$

$$\varphi(\widetilde{\mathbf{x}}, t) = L_{\mathbf{m}(t)} u(\widetilde{\mathbf{x}}, t), \quad u(\widetilde{\mathbf{x}}, t) = \int_{\mathbb{R}^d} G(\widetilde{\mathbf{x}} - \widetilde{\mathbf{y}})\rho(\widetilde{\mathbf{y}}, t)\, d\widetilde{\mathbf{y}}, \quad \widetilde{\mathbf{x}} \in \mathcal{D},\ t > 0; \tag{6.63}$$

where

$$\rho(\widetilde{\mathbf{y}}, t) = \begin{cases} |\phi(\widetilde{\mathbf{y}}, t)|^2, & \widetilde{\mathbf{y}} \in \mathcal{D}, \\ 0, & \text{otherwise}, \end{cases} \qquad \widetilde{\mathbf{y}} \in \mathbb{R}^d.$$

The initial condition is given by

$$\phi(\widetilde{\mathbf{x}}, 0) = \phi_0(\widetilde{\mathbf{x}}), \qquad \widetilde{\mathbf{x}} \in \overline{\mathcal{D}}. \tag{6.64}$$

The boundary condition to (6.62) will be chosen based on the kernel function G defined in (6.10). Due to the convolution in (6.63), it is natural to consider using the Fourier transform to compute $u(\widetilde{\mathbf{x}}, t)$. However, from (6.10) and (6.52), we know that $\lim_{\xi\to 0} \widehat{G}(\xi) = \infty$ and $\widehat{|\phi|^2}(\xi = 0) \neq 0$. As noted for simulating dipolar BECs in 3D [16, 35, 125], there is a numerical locking phenomena, i.e., numerical errors will be bounded below no matter how small the mesh size is, when one uses the Fourier transform to evaluate $u(\widetilde{\mathbf{x}}, t)$ and/or $\varphi(\widetilde{\mathbf{x}}, t)$ numerically in (6.63). As noticed in [13, 16], the second (integral) equation in (6.63) can be reformulated into the Poisson equation (1.14) and square-root-Poisson equation (6.6) for 3D and 2D SDM model, respectively. With these PDE formulations for $u(\widetilde{\mathbf{x}}, t)$, we can truncate them on the domain $\mathcal{D}$ and solve them numerically via spectral method with sine basis functions instead of Fourier basis functions and thus we can avoid using the 0-modes [16]. Thus in 3D and 2D SDM model, we choose the homogeneous Dirichlet boundary conditions to (6.62). Of course, for the 2D SAM model, one has to use the Fourier transform to compute $u(\widetilde{\mathbf{x}}, t)$, thus we take the periodic boundary conditions to (6.62).

The computational domain $\mathcal{D} \subset \mathbb{R}^d$ is chosen as $\mathcal{D} = [a, b] \times [c, d]$ if $d = 2$ and $\mathcal{D} = [a, b] \times [c, d] \times [e, f]$ if $d = 3$. Due to the confinement of the external potential, the wave function decays exponentially fast as $|\widetilde{\mathbf{x}}| \to \infty$. Thus if we choose $\mathcal{D}$ to be sufficiently large, the error from the domain truncation can be neglected. As long as we solve $\phi(\widetilde{\mathbf{x}}, t)$ in the bounded computational domain $\mathcal{D}$, we obtain a corresponding solution $\psi(\mathbf{x}, t)$ in the domain $A(t)\mathcal{D}$. As shown in Fig. 6.2 for the example of a 2D domain, although the domains $A(t)\mathcal{D}$ for $t \geq 0$, are in general different for different time t, they share a common disk which is bounded by the inner green solid circle in Fig. 6.2. Thus, the value of $\psi(\mathbf{x}, t)$ inside the vertical maximal square (the magenta area) which lies fully within the inner disk can be calculated easily by interpolation.

6.4.1 Time-splitting method

Next, let us introduce a time-splitting method to discretize (6.62)–(6.64). We choose a time-step size $\tau > 0$ and define the time sequence as $t_n = n\tau$ for $n \in \mathbb{N}$. Then from $t = t_n$ to $t = t_{n+1}$, we numerically solve the GPE (6.62) in two steps. First we solve

$$i\partial_t \phi(\widetilde{\mathbf{x}}, t) = -\frac{1}{2}\nabla^2 \phi(\widetilde{\mathbf{x}}, t), \qquad \widetilde{\mathbf{x}} \in \mathcal{D}, \quad t_n \leq t \leq t_{n+1} \tag{6.65}$$

for a time step of length τ, and then we solve

$$i\partial_t \phi(\widetilde{\mathbf{x}}, t) = \left[W(\widetilde{\mathbf{x}}, t) + \beta|\phi|^2 + \eta\varphi\right] \phi(\widetilde{\mathbf{x}}, t), \qquad \widetilde{\mathbf{x}} \in \mathcal{D}, \quad t_n \leq t \leq t_{n+1}, \tag{6.66}$$

$$\varphi(\widetilde{\mathbf{x}}, t) = L_{\mathbf{m}(t)} u(\widetilde{\mathbf{x}}, t), \qquad u(\widetilde{\mathbf{x}}, t) = \int_{\mathbb{R}^d} G(\widetilde{\mathbf{x}} - \widetilde{\mathbf{y}}) \rho(\widetilde{\mathbf{y}}, t) \, d\widetilde{\mathbf{y}}, \tag{6.67}$$

for the same time step.

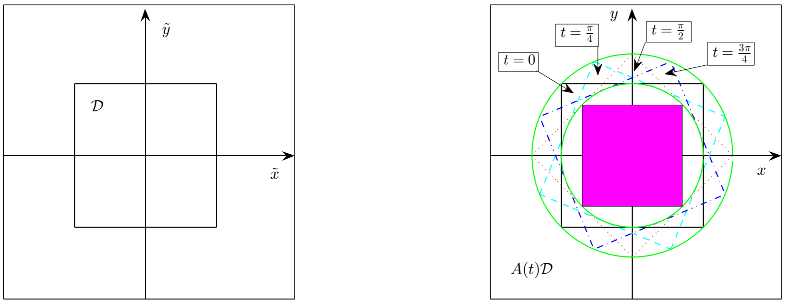

Figure 6.2: The bounded computational domain $\mathcal{D}$ in rotating Lagrangian coordinates $\widetilde{\mathbf{x}}$ (left) and the corresponding domain $A(t)\mathcal{D}$ in Cartesian (or Eulerian) coordinates $\mathbf{x}$ (right) when $\Omega = 0.5$ at different times: $t = 0$ (black solid), $t = \frac{\pi}{4}$ (cyan dashed), $t = \frac{\pi}{2}$ (red dotted) and $t = \frac{3\pi}{4}$ (blue dash-dotted). The two green solid circles determine two disks which are the union (inner circle) and the intersection of all domains $A(t)\mathcal{D}$ for $t \geq 0$, respectively. The magenta area is the vertical maximal square inside the inner circle.

Equation (6.65) can be discretized in space by sine or Fourier pseudospectral methods and then integrated exactly in time. If homogeneous Dirichlet boundary conditions are used, then we choose the sine pseudospectral method to discretize it; otherwise, the Fourier pseudospectral method is used if the boundary conditions are periodic. For more details, see e.g. [16, 24].

On the other hand, we notice that on each time interval $[t_n, t_{n+1}]$, the problem (6.66)–(6.67) leaves $|\phi(\widetilde{\mathbf{x}}, t)|$ and hence $u(\widetilde{\mathbf{x}}, t)$ invariant, i.e., $|\phi(\widetilde{\mathbf{x}}, t)| = |\phi(\widetilde{\mathbf{x}}, t_n)|$ and $u(\widetilde{\mathbf{x}}, t) = u(\widetilde{\mathbf{x}}, t_n)$ for all times $t_n \leq t \leq t_{n+1}$. Thus, for $t \in [t_n, t_{n+1}]$, Eq. (6.66) reduces to

$$i\partial_t \phi(\widetilde{\mathbf{x}}, t) = \left[W(\widetilde{\mathbf{x}}, t) + \beta|\phi(\widetilde{\mathbf{x}}, t_n)|^2 + \eta\left(L_{\mathbf{m}(t)} u(\widetilde{\mathbf{x}}, t_n)\right)\right] \phi(\widetilde{\mathbf{x}}, t), \quad \widetilde{\mathbf{x}} \in \mathcal{D}. \tag{6.68}$$

Integrating (6.68) in time gives the solution

$$\phi(\widetilde{\mathbf{x}}, t) = \phi(\widetilde{\mathbf{x}}, t_n) \exp\left[-i\left(\beta|\phi(\widetilde{\mathbf{x}}, t_n)|^2 (t - t_n) + \eta\Phi(\widetilde{\mathbf{x}}, t) + \int_{t_n}^{t} W(\widetilde{\mathbf{x}}, s) ds\right)\right] \tag{6.69}$$

for $\widetilde{\mathbf{x}} \in \mathcal{D}$ and $t \in [t_n, t_{n+1}]$, where the function $\Phi(\widetilde{\mathbf{x}}, t)$ is defined by

$$\Phi(\widetilde{\mathbf{x}}, t) = \int_{t_n}^{t} \left[L_{\mathbf{m}(s)} u(\widetilde{\mathbf{x}}, t_n)\right] ds = \left(\int_{t_n}^{t} L_{\mathbf{m(s)}}\, ds\right) u(\widetilde{\mathbf{x}}, t_n). \tag{6.70}$$

Plugging (6.50) and (6.49) into (6.70), we get

$$\Phi(\widetilde{\mathbf{x}}, t) = \tilde{L}_d(t) u(\widetilde{\mathbf{x}}, t_n), \qquad \widetilde{\mathbf{x}} \in \mathcal{D}, \quad t_n \le t \le t_{n+1}, \tag{6.71}$$

where

$$\tilde{L}_d(t) = \begin{cases} [l_e^{11}(t) - l_e^{33}(t)]\partial_{\tilde{x}\tilde{x}} + [l_e^{22}(t) - l_e^{33}(t)]\partial_{\tilde{y}\tilde{y}} + l_e^{12}(t)\partial_{\tilde{x}\tilde{y}}, & d = 2, \\ l_e^{11}(t)\partial_{\tilde{x}\tilde{x}} + l_e^{22}(t)\partial_{\tilde{y}\tilde{y}} + l_e^{33}(t)\partial_{\tilde{z}\tilde{z}} + l_e^{12}(t)\partial_{\tilde{x}\tilde{y}} + l_e^{13}(t)\partial_{\tilde{x}\tilde{z}} + l_e^{23}(t)\partial_{\tilde{y}\tilde{z}}, & d = 3, \end{cases}$$

with

$$\begin{aligned}
l_e^{11}(t) &= \int_{t_n}^{t} m_1^2(s) ds = \int_{t_n}^{t} \left[n_1^2 \cos^2(\Omega s) + n_2^2 \sin^2(\Omega s) - n_1 n_2 \sin(2\Omega s)\right] ds \\
&= \frac{n_1^2 + n_2^2}{2}(t - t_n) + \frac{n_1^2 - n_2^2}{4\Omega}\left[\sin(2\Omega t) - \sin(2\Omega t_n)\right] + \frac{n_1 n_2}{2\Omega}\left[\cos(2\Omega t) - \cos(2\Omega t_n)\right], \\
l_e^{22}(t) &= \int_{t_n}^{t} m_2^2(s) ds = \int_{t_n}^{t} \left[n_2^2 \cos^2(\Omega s) + n_1^2 \sin^2(\Omega s) + n_1 n_2 \sin(2\Omega s)\right] ds \\
&= \frac{n_1^2 + n_2^2}{2}(t - t_n) - \frac{n_1^2 - n_2^2}{4\Omega}\left[\sin(2\Omega t) - \sin(2\Omega t_n)\right] - \frac{n_1 n_2}{2\Omega}\left[\cos(2\Omega t) - \cos(2\Omega t_n)\right], \\
l_e^{12}(t) &= 2\int_{t_n}^{t} m_1(s) m_2(s) ds = \int_{t_n}^{t} \left[(n_1^2 - n_2^2)\sin(2\Omega s) + 2n_1 n_2 \cos(2\Omega t)\right] ds \\
&= \frac{n_1^2 - n_2^2}{2\Omega}\left[\cos(2\Omega t_n) - \cos(2\Omega t)\right] + \frac{n_1 n_2}{\Omega}\left[\sin(2\Omega t) - \sin(2\Omega t_n)\right], \\
l_e^{13}(t) &= 2n_3 \int_{t_n}^{t} m_1(s) ds = 2n_3 \int_{t_n}^{t} \left[n_1 \cos(\Omega s) - n_2 \sin(\Omega s)\right] ds \\
&= \frac{2n_3}{\Omega}\left[n_1\left[\sin(\Omega t) - \sin(\Omega t_n)\right] + n_2\left[\cos(\Omega t) - \cos(\Omega t_n)\right]\right], \\
l_e^{23}(t) &= 2n_3 \int_{t_n}^{t} m_2(s) ds = 2n_3 \int_{t_n}^{t} \left[n_1 \sin(\Omega s) + n_2 \cos(\Omega s)\right] ds \\
&= \frac{2n_3}{\Omega}\left[n_2\left[\sin(\Omega t) - \sin(\Omega t_n)\right] - n_1\left[\cos(\Omega t) - \cos(\Omega t_n)\right]\right], \\
l_e^{33}(t) &= \int_{t_n}^{t} n_3^2\, ds = n_3^2 (t - t_n), \qquad t_n \le t \le t_{n+1}.
\end{aligned}$$

In Section 6.4.2, we will discuss in detail the approximations to $\Phi(\widetilde{\mathbf{x}}, t)$ in (6.71). In addition, we remark here again that if $V(\mathbf{x})$ in (6.7) is a harmonic potential as defined in (6.12), then the definite integral in (6.69) can be calculated analytically as

$$\int_{t_n}^{t} W(\widetilde{\mathbf{x}}, s)ds = \frac{1}{4}\omega_1(\widetilde{x}^2+\widetilde{y}^2)(t-t_n) + H(\widetilde{\mathbf{x}}, t) + \frac{1}{2}\begin{cases} 0, & d=2, \\ \gamma_z^2\widetilde{z}^2(t-t_n), & d=3, \end{cases}$$

where

$$\begin{aligned} H(\widetilde{\mathbf{x}}, t) &= \frac{1}{4}\int_{t_n}^{t} \omega_2 \left[(\widetilde{x}^2-\widetilde{y}^2)\cos(2\Omega s) + 2\widetilde{x}\widetilde{y}\sin(2\Omega s)\right] ds \\ &= \frac{\omega_2}{8\Omega}\left[\left(\widetilde{x}^2-\widetilde{y}^2\right)\left[\sin(2\Omega t)-\sin(2\Omega t_n)\right] - 2\widetilde{x}\widetilde{y}\left[\cos(2\Omega t)-\cos(2\Omega t_n)\right]\right]. \end{aligned}$$

Of course, for general external potential $V(\mathbf{x})$ in (6.7), the integral of $W(\widetilde{\mathbf{x}}, s)$ in (6.69) might not be found analytically. In this situation, we can simply adopt a numerical quadrature to approximate it, e.g. the Simpson's rule can be used as

$$\int_{t_n}^{t} W(\widetilde{\mathbf{x}}, s)\, ds \approx \frac{t-t_n}{6}\left[W(\widetilde{\mathbf{x}}, t_n) + 4W(\widetilde{\mathbf{x}}, \frac{t_n+t}{2}) + W(\widetilde{\mathbf{x}}, t)\right].$$

We remark here that, in practice, we always use the second-order Strang splitting method [137] to combine the two steps in (6.65) and (6.66)–(6.67). For a more general discussion of the splitting method, we refer the reader to [14, 24, 65].

6.4.2 Computation of $\Phi(\widetilde{\mathbf{x}}, t)$

In this section, we present approximations to the function $\Phi(\widetilde{\mathbf{x}}, t)$ in (6.71). From the discussion in the previous subsection, we need only show how to discretize $u(\widetilde{\mathbf{x}}, t_n)$ in (6.63) and its second-order derivatives in (6.71).

Surface adiabatic model in 2D

In this case, the function $u(\widetilde{\mathbf{x}}, t_n)$ in (6.70) is given by

$$u(\widetilde{\mathbf{x}}, t_n) = \int_{\mathbb{R}^2} G(\widetilde{\mathbf{x}}-\widetilde{\mathbf{y}})\rho(\widetilde{\mathbf{y}}, t)\, d\widetilde{\mathbf{y}}, \qquad \widetilde{\mathbf{x}} \in \mathcal{D}, \tag{6.72}$$

with the kernel function G defined in the second line of (6.10). To approximate it, we consider a 2D box $\mathcal{D}$ with periodic boundary conditions.

Let M and K be two even positive integers. Then we make the (approximate) ansatz

$$u(\widetilde{\mathbf{x}}, t_n) = \sum_{p=-M/2}^{M/2-1} \sum_{q=-K/2}^{K/2-1} \widehat{u}^f_{pq}(t_n)\, e^{i\nu^1_p(\widetilde{x}-a)} e^{i\nu^2_q(\widetilde{y}-c)}, \qquad \widetilde{\mathbf{x}} = (\widetilde{x}, \widetilde{y}) \in \mathcal{D}, \tag{6.73}$$

where $\widehat{u}^f_{pq}(t_n)$ is the Fourier coefficient of $u(\widetilde{\mathbf{x}}, t_n)$ corresponding to the frequencies (p, q) and

$$\nu^1_p = \frac{2p\pi}{b-a}, \qquad \nu^2_q = \frac{2q\pi}{d-c}, \qquad (p, q) \in \mathcal{S}_{MK}.$$

The index set $\mathcal{S}_{MK}$ is defined as

$$\mathcal{S}_{MK} = \left\{(p, q) \mid -\frac{M}{2} \le p \le \frac{M}{2} - 1,\ -\frac{K}{2} \le q \le \frac{K}{2} - 1\right\}.$$

We approximate the convolution in (6.72) by a discrete convolution and take its discrete Fourier transform to obtain

$$\widehat{u}^f_{pq}(t_n) = \widehat{G}(\nu^1_p, \nu^2_q) \cdot (\widehat{|\phi^n|^2})^f_{pq}, \qquad (p, q) \in \mathcal{S}_{MK}, \tag{6.74}$$

where $(\widehat{|\phi^n|^2})^f_{pq}$ is the Fourier coefficient corresponding to the frequencies (p, q) of the function $|\phi(\widetilde{\mathbf{x}}, t_n)|^2$, and $\widehat{G}(\nu^1_p, \nu^2_q)$ are given by (see details in (6.10))

$$\widehat{G}(\nu^1_p, \nu^2_q) = \frac{1}{2\pi^2} \int_{-\infty}^{\infty} \frac{e^{-\varepsilon^2 s^2/2}}{(\nu^1_p)^2 + (\nu^2_q)^2 + s^2} ds, \qquad (p, q) \in \mathcal{S}_{MK}. \tag{6.75}$$

Since the integrand in (6.75) decays exponentially fast, in practice we can first truncate it to an interval $[s_1, s_2]$ with $|s_1|, s_2 > 0$ sufficiently large and then evaluate the truncated integral by using quadrature rules, e.g. composite Simpson's or trapezoidal quadrature rule.

Combining (6.71), (6.73) and (6.74), we obtain an approximation of $\Phi(\widetilde{\mathbf{x}}, t)$ in the solution (6.69) via the Fourier spectral method as

$$\Phi(\widetilde{\mathbf{x}}, t) = \sum_{p=-M/2}^{M/2-1} \sum_{q=-K/2}^{K/2-1} \left[L(\nu^1_p, \nu^2_q, t)\widehat{G}(\nu^1_p, \nu^2_q) \cdot (\widehat{|\phi^n|^2})^f_{pq}\right] e^{i\nu^1_p(\widetilde{x}-a)} e^{i\nu^2_q(\widetilde{y}-c)}, \tag{6.76}$$

for time $t_n \le t \le t_{n+1}$, where the function $L(\xi_1, \xi_2, t)$ is defined as

$$L(\xi_1, \xi_2, t) = -\left[\left(l^{11}_e(t) - l^{33}_e(t)\right)\xi_1^2 + \left(l^{22}_e(t) - l^{33}_e(t)\right)\xi_2^2 + l^{12}_e(t)\xi_1\xi_2\right].$$

Surface density model in 2D

In this case, the function $u(\widetilde{\mathbf{x}}, t_n)$ in (6.70) also satisfies the square-root-Poisson equation in (6.6) which can be truncated on the computational domain $\mathcal{D}$ with homogeneous Dirichlet boundary conditions as

$$(-\nabla^2)^{1/2} u(\widetilde{\mathbf{x}}, t_n) = |\phi(\widetilde{\mathbf{x}}, t_n)|^2, \qquad \widetilde{\mathbf{x}} \in \mathcal{D}; \qquad u(\widetilde{\mathbf{x}}, t_n)|_{\partial\mathcal{D}} = 0. \tag{6.77}$$

The above problem can be discretized by using a sine pseudospectral method in which the 0-modes are avoided. Letting $M, K \in \mathbb{N}$, we denote the index set

$$\mathcal{T}_{MK} = \{(p, q) \,|\, 1 \le p \le M-1,\ 1 \le q \le K-1\},$$

and define the functions

$$U_{p,q}(\widetilde{\mathbf{x}}) = \sin(\mu_p^1(\widetilde{x} - a)) \sin(\mu_q^2(\widetilde{y} - c)), \qquad (p, q) \in \mathcal{T}_{MK}, \qquad \widetilde{\mathbf{x}} = (\widetilde{x}, \widetilde{y}) \in \mathcal{D},$$

where

$$\mu_p^1 = \frac{p\pi}{b-a}, \qquad \mu_q^2 = \frac{q\pi}{d-c}, \qquad (p, q) \in \mathcal{T}_{MK}. \tag{6.78}$$

Assume that

$$u(\widetilde{\mathbf{x}}, t_n) = \sum_{p=1}^{M-1} \sum_{q=1}^{K-1} \widehat{u}_{pq}^s(t_n) U_{p,q}(\widetilde{\mathbf{x}}), \qquad \widetilde{\mathbf{x}} \in \mathcal{D}, \tag{6.79}$$

where $\widehat{u}_{pq}^s(t_n)$ is the sine transform of $u(\widetilde{\mathbf{x}}, t_n)$ at frequencies (p, q). Substituting (6.79) into (6.77) and taking sine transform on both sides, we obtain

$$\widehat{u}_{pq}^s(t_n) = \frac{(\widehat{|\phi^n|^2})_{pq}^s}{\sqrt{(\mu_p^1)^2 + (\mu_q^2)^2}}, \qquad (p, q) \in \mathcal{T}_{MK}, \tag{6.80}$$

where $(\widehat{|\phi^n|^2})_{pq}^s$ is the sine transform of $|\phi(\widetilde{\mathbf{x}}, t_n)|^2$ at frequencies (p, q).

Combining (6.79), (6.80) and (6.71), we obtain an approximation of $\Phi(\widetilde{\mathbf{x}}, t)$ in the solution (6.69) via sine spectral method as

$$\Phi(\widetilde{\mathbf{x}}, t) = \sum_{p=1}^{M-1} \sum_{q=1}^{K-1} \frac{(\widehat{|\phi^n|^2})_{pq}^s}{\sqrt{(\mu_p^1)^2 + (\mu_q^2)^2}} \left[L(\mu_p^1, \mu_q^2, t) U_{p,q}(\widetilde{\mathbf{x}}) + l_e^{12}(t) V_{p,q}(\widetilde{\mathbf{x}}) \right], \tag{6.81}$$

where the functions $L(\xi_1, \xi_2, t)$ and $V_{p,q}(\widetilde{\mathbf{x}})$ are defined as

$$L(\xi_1, \xi_2, t) = -\left[\left(l_e^{11}(t) - l_e^{33}(t) \right) \xi_1^2 + \left(l_e^{22}(t) - l_e^{33}(t) \right) \xi_2^2 \right], \tag{6.82}$$

$$V_{p,q}(\widetilde{\mathbf{x}}) = \partial_{\widetilde{x}\widetilde{y}} U_{p,q}(\widetilde{\mathbf{x}}) = \mu_p^1 \mu_q^2 \cos(\mu_p^1(\widetilde{x} - a)) \cos(\mu_q^2(\widetilde{y} - c)), \quad (p, q) \in \mathcal{T}_{MK}. \tag{6.83}$$

Approximations in 3D

In 3D case, again the function $u(\widetilde{\mathbf{x}},t_n)$ in (6.70) also satisfies the Poisson equation in (1.14) which can be truncated on the computational domain $\mathcal{D}$ with homogeneous Dirichlet boundary conditions as

$$-\nabla^2 u(\widetilde{\mathbf{x}},t_n)=|\phi(\widetilde{\mathbf{x}},t_n)|^2,\quad \widetilde{\mathbf{x}}\in\mathcal{D};\qquad\qquad u(\widetilde{\mathbf{x}},t_n)|_{\partial\mathcal{D}}=0. \tag{6.84}$$

The above problem can be discretized by using a sine pseudospectral method in which the 0-modes are avoided. Denote the index set

$$\mathcal{T}_{MKL}=\{(p,q,r)\,|\,1\le p\le M-1,\ 1\le q\le K-1,\ 1\le r\le L-1\}$$

where $M,K,L>0$ are integers and define the functions

$$U_{p,q,r}(\widetilde{\mathbf{x}})=\sin(\mu_p^1(\widetilde{x}-a))\sin(\mu_q^2(\widetilde{y}-c))\sin(\mu_r^3(\widetilde{z}-e)),\quad (p,q,r)\in\mathcal{T}_{MKL},$$

where

$$\mu_r^3=r\pi/(f-e),\qquad 1\le r\le L-1.$$

Again, we take the (approximate) ansatz

$$u(\widetilde{\mathbf{x}},t_n)=\sum_{p=1}^{M-1}\sum_{q=1}^{K-1}\sum_{r=1}^{L-1}\widehat{u}^s_{pqr}(t_n)\,U_{p,q,r}(\widetilde{\mathbf{x}}),\qquad \widetilde{\mathbf{x}}=(\widetilde{x},\widetilde{y},\widetilde{z})\in\mathcal{D}, \tag{6.85}$$

where $\widehat{u}^s_{pqr}(t_n)$ is the sine transform of $u(\widetilde{\mathbf{x}},t_n)$ corresponding to frequencies (p,q,r). Substituting (6.85) into the Poisson equation (6.84) and noticing the orthogonality of the sine functions, we obtain

$$\widehat{u}^s_{pqr}(t_n)=\frac{(\widehat{|\phi^n|^2})^s_{pqr}}{(\mu_p^1)^2+(\mu_q^2)^2+(\mu_r^3)^2},\qquad (p,q,r)\in\mathcal{T}_{MKL}, \tag{6.86}$$

where $(\widehat{|\phi^n|^2})^s_{pqr}$ is the sine transform of $|\phi(\widetilde{\mathbf{x}},t_n)|^2$ corresponding to frequencies (p,q,r).

Combining (6.71), (6.85) and (6.86), we obtain an approximation of $\Phi(\widetilde{\mathbf{x}},t)$ in the solution (6.69) via sine spectral method as

$$\begin{aligned}\Phi(\widetilde{\mathbf{x}},t)=\sum_{p=1}^{M-1}\sum_{q=1}^{K-1}\sum_{r=1}^{L-1}\widehat{u}^s_{pqr}(t_n)\Big[&L(\mu_p^1,\mu_q^2,\mu_r^3,t)U_{p,q,r}(\widetilde{\mathbf{x}})+l_e^{12}V^{(1)}_{p,q,r}(\widetilde{\mathbf{x}})\\ &+l_e^{13}V^{(2)}_{p,q,r}(\widetilde{\mathbf{x}})+l_e^{23}V^{(3)}_{p,q,r}(\widetilde{\mathbf{x}})\Big],\qquad \widetilde{\mathbf{x}}\in\mathcal{D},\end{aligned} \tag{6.87}$$

where the functions $L(\xi_1,\xi_2,\xi_3,t)$, $V^{(1)}_{p,q,r}(\widetilde{\mathbf{x}})$, $V^{(2)}_{p,q,r}(\widetilde{\mathbf{x}})$ and $V^{(3)}_{p,q,r}(\widetilde{\mathbf{x}})$ (for $(p,q,r)\in\mathcal{T}_{MKL}$) are defined as

$$\begin{aligned}
L(\xi_1,\xi_2,\xi_3,t) &= -\left[l_e^{11}(t)\xi_1^2 + l_e^{22}(t)\xi_2^2 + l_e^{33}(t)\xi_3^2\right],\\
V^{(1)}_{p,q,r}(\widetilde{\mathbf{x}}) &= \partial_{\widetilde{x}\widetilde{y}}U_{p,q,r}(\widetilde{\mathbf{x}}) = \mu_p^1\mu_q^2\cos(\mu_p^1(\widetilde{x}-a))\cos(\mu_q^2(\widetilde{y}-c))\sin(\mu_r^3(\widetilde{z}-e)),\\
V^{(2)}_{p,q,r}(\widetilde{\mathbf{x}}) &= \partial_{\widetilde{x}\widetilde{z}}U_{p,q,r}(\widetilde{\mathbf{x}}) = \mu_p^1\mu_r^3\cos(\mu_p^1(\widetilde{x}-a))\sin(\mu_q^2(\widetilde{y}-c))\cos(\mu_r^3(\widetilde{z}-e)),\\
V^{(3)}_{p,q,r}(\widetilde{\mathbf{x}}) &= \partial_{\widetilde{y}\widetilde{z}}U_{p,q,r}(\widetilde{\mathbf{x}}) = \mu_q^2\mu_r^3\sin(\mu_p^1(\widetilde{x}-a))\cos(\mu_q^2(\widetilde{y}-c))\cos(\mu_r^3(\widetilde{z}-e)).
\end{aligned}$$

Remark 6.4.1. *After obtaining the numerical solution $\phi(\widetilde{\mathbf{x}},t)$ on the bounded computational domain $\mathcal{D}$, if it is needed to recover the original wave function $\psi(\mathbf{x},t)$ over a set of fixed grid points in the Cartesian coordinates $\mathbf{x}$, one can use the standard Fourier/sine interpolation operators from the discrete numerical solution $\phi(\widetilde{\mathbf{x}},t)$ to construct an interpolation continuous function over $\mathcal{D}$ [36, 135], which can be used to compute $\psi(\mathbf{x},t)$ over a set of fixed grid points in the Cartesian coordinates $\mathbf{x}$ for any fixed time $t\ge 0$.*

Remark 6.4.2. *If the potential $V(\mathbf{x})$ in (6.7) is replaced by a time-dependent potential, e.g. $V(\mathbf{x},t)$, the rotating Lagrangian coordinates transformation and the numerical method are still valid provided that we replace $W(\widetilde{\mathbf{x}},t)$ in (6.48) by $W(\widetilde{\mathbf{x}},t) = V(A(t)\widetilde{\mathbf{x}},t)$ for $\widetilde{\mathbf{x}}\in\mathbb{R}^d$ and $t\ge 0$.*

6.5 Numerical results

In this section, we first test the accuracy of our numerical method, where throughout we apply the two-dimensional surface density model. Then study the dynamics of rotating dipolar BECs, including the center of mass, angular momentum expectation and condensate widths. In addition, the dynamics of vortex lattices in rotating dipolar BEC are presented.

Table 6.1: Spatial discretization errors $\|\phi(t) - \phi^{(\Delta\widetilde{x},\Delta\widetilde{y},\tau)}(t)\|$ at time $t = 1$.

	$\Delta\widetilde{x} = 1/2$	$\Delta\widetilde{x} = 1/4$	$\Delta\widetilde{x} = 1/8$	$\Delta\widetilde{x} = 1/16$
$\beta = 33.5914$	6.1569E-2	1.7525E-4	5.8652E-11	<1E-11
$\beta = 58.7849$	1.9746E-1	2.3333E-3	2.5738E-8	2.6124E-11
$\beta = 92.3762$	4.8133E-1	1.3385E-2	1.6620E-6	6.2264E-10
$\beta = 119.8488$	1.2984	7.7206E-2	9.5202E-5	3.0974E-8

6.5.1 Numerical accuracy

In order to test numerical accuracy, we consider a 2D GPE (6.62)-(6.63) with the SDM long-range interaction (6.6) and harmonic potential (6.12), i.e., $d = 2$ in the GPE (6.62). The other parameters are chosen as $\Omega = 0.4$, $\gamma_x = \gamma_y = 1$, $\eta = -\frac{15}{2}$ and dipole axis $\mathbf{n} = (0, 0, 1)^T$. The initial condition in (6.64) is taken as

$$\phi_0(\widetilde{\mathbf{x}}) = \frac{1}{\pi^{1/4}} e^{\frac{-(\tilde{x}^2+2\tilde{y}^2)}{2}}, \qquad \widetilde{\mathbf{x}} \in \mathcal{D}, \tag{6.88}$$

where we perform our simulations on the bounded computational domain $\mathcal{D} = [-16, 16]^2$. Denote $\phi^{(\Delta\widetilde{x},\Delta\widetilde{y},\tau)}(t)$ as the numerical solution at time t obtained with the mesh size $(\Delta\widetilde{x}, \Delta\widetilde{y})$ and time step τ. With a slight abuse of notation, we let $\phi(t)$ represent the numerical solution with very fine mesh size $\Delta\widetilde{x} = \Delta\widetilde{y} = 1/64$ and small time step $\tau = 0.0001$ and assume it to be a sufficiently good representation of the *exact* solution at time t.

Tables 6.1–6.2 show the spatial and temporal errors of our numerical method for different β in the GPE (6.62), where the errors are computed as $\|\phi(t) - \phi^{(\Delta\widetilde{x},\Delta\widetilde{y},\tau)}(t)\|_{l^2}$ (with $\Delta\widetilde{x} = \Delta\widetilde{y}$) at time $t = 1$. To calculate the spatial errors in Table 6.1, we always use a very small time step $\tau = 0.0001$ so that the errors from time discretization can be neglected compared to those from spatial discretization. Table 6.1 shows that the spatial accuracy of our method is of spectral order. In addition, the spatial errors increase with the nonlinearity coefficient β when the mesh size is kept constant.

Table 6.2: Temporal discretization errors $\|\phi(t)-\phi^{(\Delta\widetilde{x},\Delta\widetilde{y},\tau)}(t)\|$ at time $t=1$.

	$\tau=1/40$	$\tau=1/80$	$\tau=1/160$	$\tau=1/320$	$\tau=1/640$
$\beta=33.5914$	1.0434E-3	2.6018E-4	6.4992E-5	1.6233E-5	4.0456E-6
$\beta=58.7849$	2.5241E-3	6.2783E-4	1.5674E-4	3.9143E-5	9.7550E-6
$\beta=92.3762$	4.9982E-3	1.2380E-3	3.0882E-4	7.7108E-5	1.9215E-5
$\beta=119.8488$	1.1417E-2	2.7716E-3	6.9009E-4	1.7223E-4	4.2915E-5

In Table 6.2, we always use mesh sizes $\Delta\widetilde{x}=\Delta\widetilde{y}=1/64$ which are the same as those used in obtaining the 'exact' solution, so that one can regard the spatial discretization as 'exact' and the only errors are from time discretization. For different β, Table 6.2 shows second order decrease of the temporal errors with respect to time-step size τ. Similarly, for the same τ, the temporal errors increase with β.

6.5.2 Dynamics of center of mass

In the following, we study the dynamics of the center of mass by directly simulating the GPE (6.7)–(6.8) in 2D with SDM long-range interaction (6.6) and harmonic potential (6.12). To that end, we take $d=2$, $\beta=30\sqrt{10/\pi}$, $\eta=-\frac{15}{2}$ and dipole axis $\mathbf{n}=(1,0,0)^T$. The initial condition in (6.11) is taken as

$$\phi_0(\mathbf{x})=\alpha\,\zeta(\mathbf{x}-\mathbf{x}^0),\qquad \text{with}\quad \zeta(\mathbf{x})=(x+iy)e^{\frac{-(x^2+y^2)}{2}},\quad \mathbf{x}\in\mathcal{D},\tag{6.89}$$

where the constant α is chosen to satisfy the normalization condition $\|\psi_0\|^2=1$. Initially, we take $\mathbf{x}^0=(1,1)^T$. In our simulations, we use the computational domain $\mathcal{D}=[-16,16]^2$, the mesh size $\Delta\widetilde{x}=\Delta\widetilde{y}=1/16$ and the time step size $\tau=0.0001$.

We consider the following two sets of trapping frequencies: (i) $\gamma_x=\gamma_y=1$, and (ii) $\gamma_x=1$, $\gamma_y=1.1$. Fig. 6.3 shows the trajectory of the center of mass $\mathbf{x}_c(t)$ in the original coordinates as well as the time evolution of its coordinates for different angular velocities Ω, where $\gamma_x=\gamma_y=1$. On the other hand, Fig. 6.5.2 presents the same quantities for $\gamma_x = 1$ and $\gamma_y = 1.1$. In addition, the numerical results are compared with analytical ones from solving the ODEs in (6.33)–(6.35). Figs. 6.3–6.5.2 show that if the external trap is symmetric, i.e., $\gamma_x = \gamma_y$, the center of mass always moves within a bounded region which is symmetric with respect to the trap center $(0, 0)^T$. Furthermore, if the angular velocity Ω is rational, the movement is periodic with a period depending on both the angular velocity and the trapping frequencies. In contrast, when $\gamma_x \neq \gamma_y$, the dynamics of the center of mass become more complicated. The simulation results in Figs. 6.3–6.5.2 are consistent with those obtained by solving the ODE system in Lemma 6.2.3 for given Ω, γ_x, and γ_y [151] and those numerical results reported in the literatures by other numerical methods [17, 20, 23].

On the other hand, we also study the dynamics of the center of mass $\widetilde{\mathbf{x}}_c(t)$ in the new coordinates. When $\gamma_x = \gamma_y$ and Ω arbitrary, the center of mass has a periodic motion on the straight line segment connecting $-\widetilde{\mathbf{x}}^0$ and $\widetilde{\mathbf{x}}^0$. This is also true for $\mathbf{x}_c(t)$ with $\Omega = 0$ (cf. Fig. 6.3). However, the trajectories are different for different Ω if $\gamma_x \neq \gamma_y$. This observations agree with the results in Lemma 6.2.4.

In addition, our simulations show that the dynamics of the center of mass are independent of the interaction coefficients β and η, which is consistent with Lemma 6.2.3.

6.5.3 Dynamics of angular momentum expectation and condensate widths

To study the dynamics of the angular momentum expectation and condensate widths, we adapt the GPE (6.7)–(6.8) in 2D with SDM long-range interaction (6.6) and harmonic potential (6.12), i.e., we take $d = 2$ and $\Omega = 0.7$. Similarly, the initial condition in (6.11) is taken as

$$\psi_0(\mathbf{x}) = \alpha\, \zeta(\mathbf{x}), \qquad \mathbf{x} \in \mathcal{D}, \tag{6.90}$$

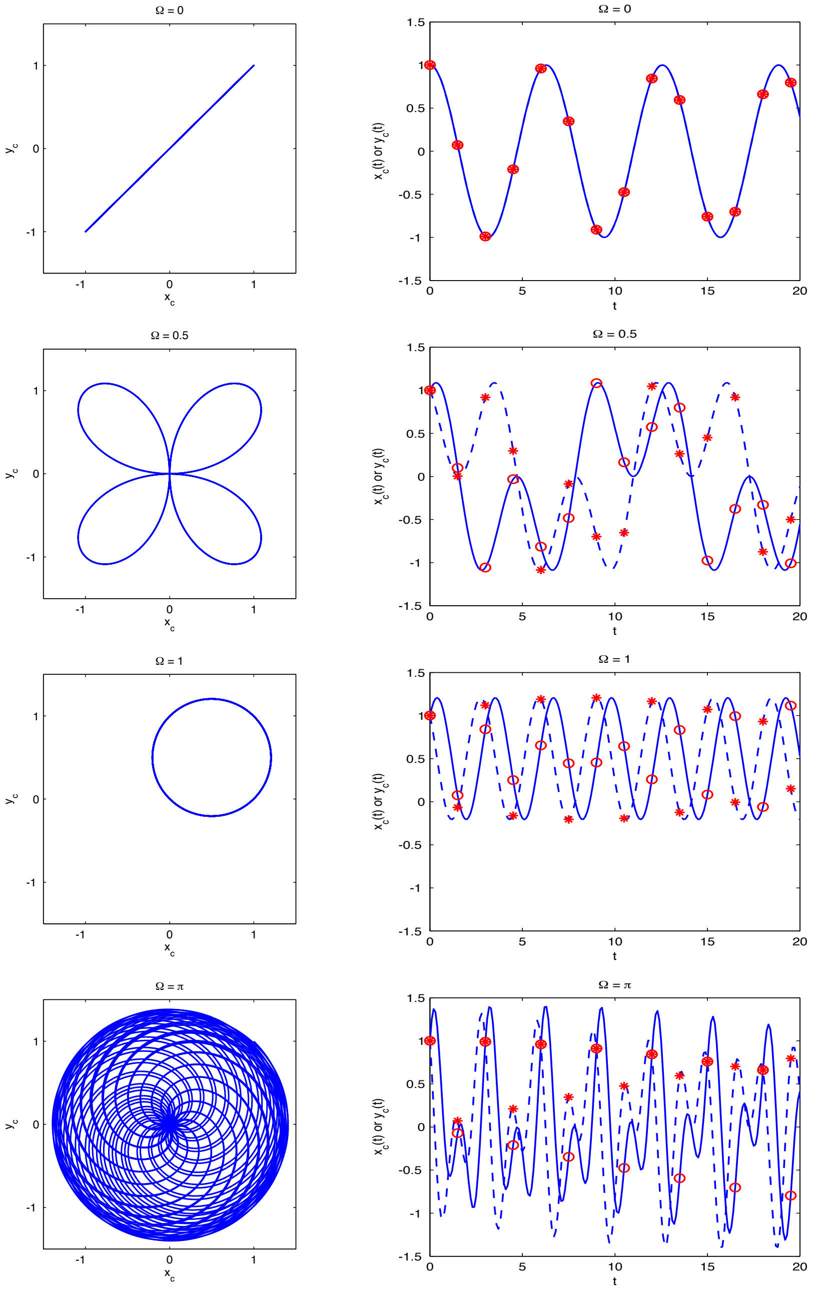

Figure 6.3: Results for $\gamma_x = \gamma_y = 1$. Left: trajectory of the center of mass, $\mathbf{x}_c(t) = (x_c(t), y_c(t))^T$ for $0 \le t \le 100$. Right: coordinates of the trajectory $\mathbf{x}_c(t)$ (solid line: $x_c(t)$, dashed line: $y_c(t)$) for different rotation speed Ω, where the solid and dashed lines are obtained by directly simulating the GPE and '*' and 'o' represent the solutions to the ODEs in Lemma 6.2.3.

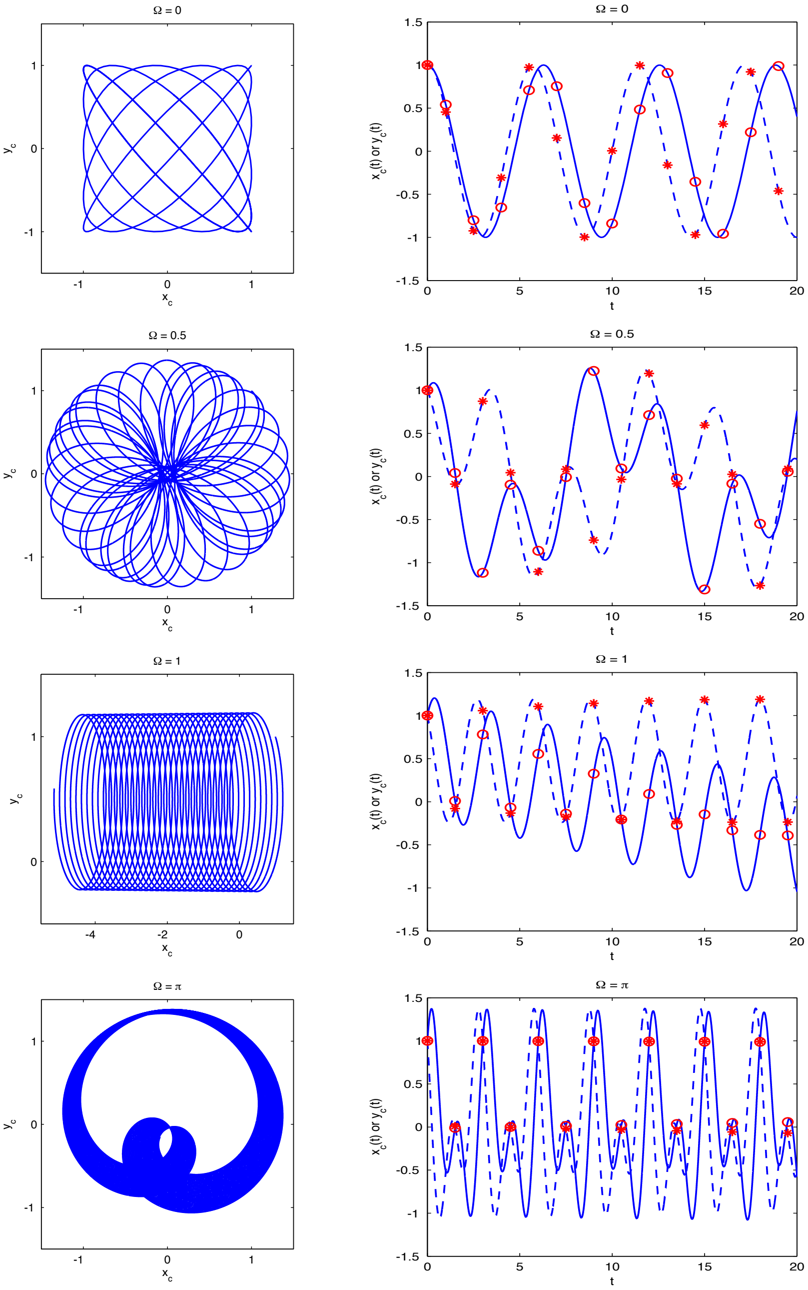

Figure 6.4: Results for $\gamma_x = 1, \gamma_y = 1.1$. Left: trajectory of the center of mass, $\mathbf{x}_c(t) = (x_c(t), y_c(t))^T$ for $0 \leq t \leq 100$. Right: coordinates of the trajectory $\mathbf{x}_c(t)$ (solid line: $x_c(t)$, dashed line: $y_c(t)$) for different rotation speed Ω, where the solid and dashed lines are obtained by directly simulating the GPE and '*' and 'o' represent the solutions to the ODEs in Lemma 6.2.3.

where $\zeta(\mathbf{x})$ is defined in (6.89) and α is a constant such that $\|\psi_0\|^2 = 1$. In our simulations, we consider the following four cases:

(i) $\gamma_x = \gamma_y = 1$, $\beta = 25\sqrt{10/\pi}$, $\eta = 0$, and $\mathbf{n} = (1,0,0)^T$;

(ii) $\gamma_x = \gamma_y = 1$, $\beta = 25\sqrt{10/\pi}$, $\eta = -15$, and $\mathbf{n} = (1,0,0)^T$;

(iii) $\gamma_x = \gamma_y = 1$, $\beta = 55\sqrt{10/\pi}$, $\eta = -15$, and $\mathbf{n} = (0,0,1)^T$;

(iv) $\gamma_x = 1$, $\gamma_y = 1.1$, $\beta = 55\sqrt{10/\pi}$, $\eta = -15$, and $\mathbf{n} = (0,0,1)^T$.

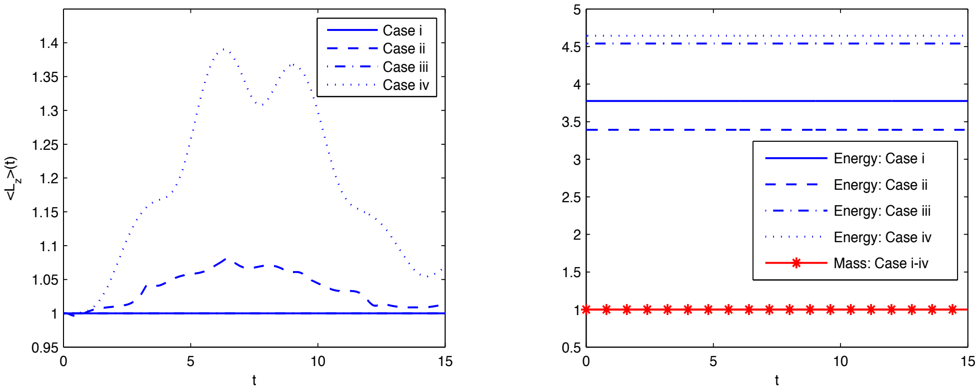

Figure 6.5: Time evolution of the angular momentum expectation (left) and energy and mass (right) for Cases (i)-(iv) in section 5.3.

In Fig. 6.5, we present the dynamics of the angular momentum expectation, energy and mass for each of the above four cases in the interval $t \in [0, 15]$. We see that if the external trap is radially symmetric in 2D, then the angular momentum expectation is conserved when either there is no dipolar interaction (Case (i)) or the dipolar axis is parallel to the z-axis (Case (iii)). Otherwise, the angular momentum expectation is not conserved. The above numerical observations are consistent with the analytical results obtained in Lemma 6.2.1. In addition, we find that our method conserves the energy and mass very well during the dynamics (cf. Fig. 6.5 right). Furthermore, from our additional numerical results not shown here for brevity, we observed that the angular momentum expectation is conserved in 3D for any initial

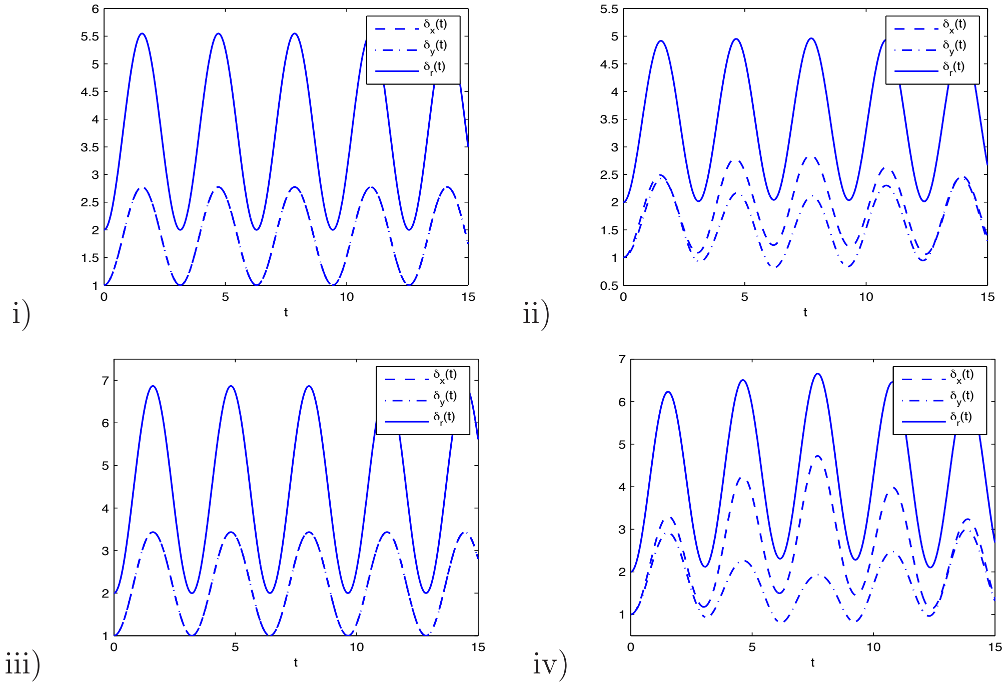

Figure 6.6: Time evolution of condensate widths in the Cases (i)–(iv) in section 5.3.

data if the external trap is cylindrically symmetric and either there is no dipolar interaction or the dipolar axis is parallel to the z-axis, which can also be justified mathematically.

The dynamics of the condensate widths are presented in Fig. 6.6. We find that $\delta_r(t)$ is periodic as long as the trapping frequencies satisfy $\gamma_x = \gamma_y$ and the influence of the dipole axis vanishes, e.g. in the Case (i), which confirms the analytical results of Lemma 6.2.2. Furthermore, from our additional numerical results not shown here for brevity, we observed that $\delta_r(t)$ is periodic and $\delta_x(t) = \delta_y(t) = \frac{1}{2}\delta_r(t)$ if $\eta = 0$ for any initial data or $\mathbf{n} = (0, 0, 1)^T$ for radially symmetric or central vortex-type initial data.

6.5.4 Dynamics of quantized vortex lattices

In the following, we apply our numerical method to study the dynamics of quantized vortex lattices in rotating dipolar BECs. Again, we adapt the GPE (6.7)–(6.8)

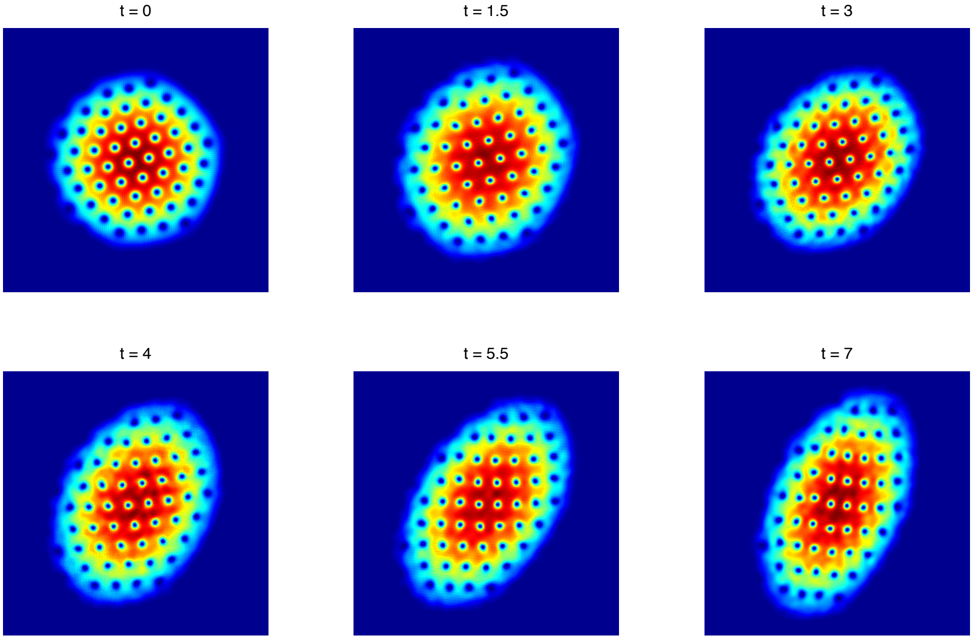

Figure 6.7: Contour plots of the density function $|\psi(\mathbf{x},t)|^2$ for dynamics of a vortex lattice in a rotating BEC (Case (i)). Domain displayed: $(x,y) \in [-13,13]^2$.

in 2D with SDM long-range interaction (6.6) and harmonic potential (6.12), i.e., we choose $d = 2$, $\beta = 1000$ and $\Omega = 0.9$. The initial datum in (6.11) is chosen as a stationary vortex lattice which is computed numerically by using the method in [149, 150] with the above parameters and $\gamma_x = \gamma_y = 1$, $\eta = 0$, i.e., no long-range dipole-dipole interaction initially. Then the dynamics of vortex lattices are studied in two cases:

(i) perturb the external potential by setting $\gamma_x = 1.05$ and $\gamma_y = 0.95$ at $t = 0$;

(ii) turn on the dipolar interactions by setting $\eta = -600$ and dipolar axis $\mathbf{n} = (1,0,0)^T$ at time $t = 0$.

In our simulations, we use $\mathcal{D} = [-16,16]^2$, $\Delta\widetilde{x} = \Delta\widetilde{y} = 1/16$ and $\tau = 0.0001$. Figs. 6.7–6.8 show the contour plots of the density function $|\psi(\mathbf{x},t)|^2$ at different time steps for Cases (i) and (ii), respectively, where the wave function $\psi(\mathbf{x},t)$ is obtained from $\phi(\widetilde{\mathbf{x}},t)$ by using interpolation via sine basis (see Remark 6.4.1). We see that during the dynamics, the number of vortices is conserved in both cases. The lattices rotate to form different patterns because of the anisotropic external potential and dipolar interaction in Cases (i) and (ii), respectively. In addition, the results in Case (i) are similar to those obtained in [17], where a spectral type method in polar coordinates was used to simulate the dynamics of vortex lattices.

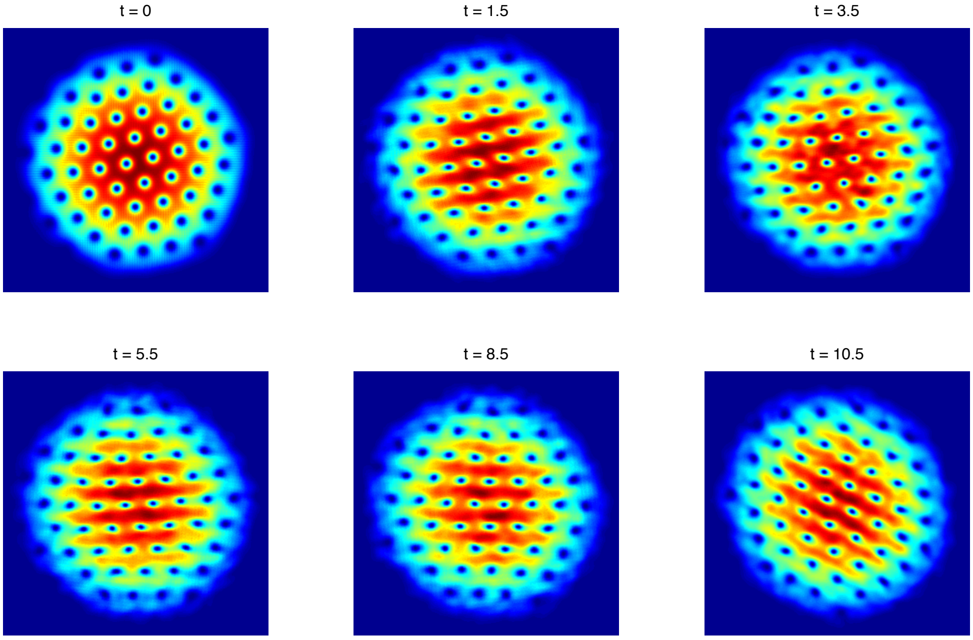

Figure 6.8: Contour plots of the density function $|\psi(\mathbf{x},t)|^2$ for dynamics of a vortex lattice in a rotating dipolar BEC (Case (ii)). Domain displayed: $(x,y)\in[-10,10]^2$.

6.6 Conclusions

We proposed a simple and efficient numerical method to simulate the dynamics of rotating dipolar Bose-Einstein condensation (BEC) whose properties are described by the Gross–Pitaevskii equation (GPE) with both the angular rotation term and the long-range dipole-dipole interaction. First, by decoupling the short-range and long-range interactions, we reformulated the GPE as a Gross-Pitaevskii-(fractional) Poisson system. Then we eliminated the angular rotation term from the GPE using a rotating Lagrangian coordinate transformation, which makes it possible to design a simple and efficient numerical method. In the new rotating Lagrangian coordinates, we presented a numerical method which combines the time-splitting techniques with Fourier/sine pseudospectral approximation to simulate the dynamics of rotating dipolar BECs. The numerical method is explicit, unconditional stable, spectral accurate in space and second order accurate in time, and conserves the mass in the discretized level. The memory cost is $O(MK)$ in 2D and $O(MKL)$ in 3D, and the computational cost per time step is $O\left(MK\ln(MK)\right)$ in 2D and $O\left(MKL\ln(MKL)\right)$ in 3D. More specifically, the method is very easy to be implemented via FFT or DST. We then numerically examined the conservation of the angular momentum expectation and studied the dynamics of condensate widths and center of mass for different angular velocities. In addition, the dynamics of vortex lattice in rotating dipolar BEC were investigated. Numerical studies show that our method is very effective in simulating the dynamics of rotating dipolar BECs.

Chapter 7

Conclusion remarks and future work

In this thesis, by proposing efficient and accurate numerical methods to solve GLSE and corresponding RDLs, we conducted an extensive numerical study on quantized vortex phenomena in GLE, NLSE and CGLE on bounded domain with a small parameter ε. Moreover, we also investigated analytically and numerically on the the dynamics of rotating dipolar BEC whose properties are described by the GPE with both the angular rotation term and the long-range dipole-dipole interaction.

In the first part, we studied quantized vortex dynamics and interaction in the GLSE. Firstly, steady vortex states of the GLSE are reviewed and an efficient and accurate numerical methods was proposed to simulate GLSE with initial data involving vortices under different boundary conditions. The numerical method is based on: (i). applying a time-splitting technique to decouple the nonlinearity in the GLSE; (ii). for the resulted linear PDE (gradient flow with constant coefficient in GLE/CGLE case or free Schrödinger equation in NLSE case), if in a rectangular domain, for the case of Dirichlet BC, we adapt a fourth-order compact finite difference method in the spatial discretization and a Crank-Nicolson method in the temporal discretization, while for the case of Neumann BC, we apply a cosine pseudospectral method to discretize it; otherwise in a disk domain, we adopt the polar coordinate in our numerical discretization, then utilized the standard Fourier pseudospectral discretization in the transverse direction, finite element discretization in the radial direction and a Crank-Nicolson discretization in temporal direction. Secondly, we reviewed various RDLs which govern the motion of the vortex centers to the leading order, and proposed some methods to solve them. Finally, we applied the proposed methods to simulate quantized vortex interaction of GLSE with different ε and initial setups including single vortex, vortex pair, vortex dipole and vortex lattices.

Based on extensive numerical results, we found that the value of ε, the boundary condition, the geometry of the domain, the initial location of the vortices and the type of the potential affect the motion of the vortices significantly. Generally, the boundary effect affect the vortex interaction very much, which lead to very different nonlinear phenomena from those observed in the case of domain being the whole plane. Moreover, we verified that the dynamics of vortex centers in the GLSE dynamics converges to that of the reduced dynamics when $\varepsilon \to 0$ before they collide and/or move out of the domain and/or after the sound wave propagate away from them. Surely, after either vortices collide with each other or move out of the domain or when sound wave is being radiating or propagate back toward them, the RDLs are no longer valid; however, the dynamics and interaction of quantized vortices are still physically interesting and they can be obtained from our direct numerical simulations. Moreover, for each fixed ε, there are regimes which at least depend on the boundary condition and the geometry of the domain, such that the RDLs failed qualitatively to describe the vortex motion.

For the case of NLSE, vortices behave like point vortices in ideal fluid on bounded domains, they never move outside domain. Moreover, we found that the radiation of NLSE dynamics which is carried by oscillating sound waves modifies the motion of vortices much, especially in the dynamics of vortex lattice, highly co-rotating vortex pairs and overlapping vortices. And due to the dispersive and radiative nature, the RDLs which does not take the radiation into account will be invalid even if there were small perturbations near around the vortex centers initially.

For the case of the GLE and/or CGLE, which are dissipative systems, vortices move in a quite different way from the case of NLSE, they can exit the domain in some circumstance. Vortices of like (opposite) winding number will undergo repulsive (attractive) interaction, they will move outside domain or merge and annihilate somewhere in the domain or move toward the boundary and finally stop somewhere near the boundary. Moreover, there are no radiation or sound waves come up during the dynamics and interaction of the vortices, the RDLs are still valid if there were small perturbations in the initial setups. We also investigated the patterns of the steady states of the vortex lattices, we found that: (i). In the case of Dirichlet BC, the vortices will all move toward the boundary to form a boundary layer, whose width is proportional to the value of ε and inverse proportional to the number of vortices in the lattice. The alignment of the vortices in the steady state depend on the initial location of the vortices, the boundary condition and the geometry of the domain. (ii). In the case of Neumann BC, the most of the vortices will exit the domain, and finally at most one vortex will leftover sitting at the center of the domain for some proper initial data. However, this steady states is not stable. If we imposed a slightly perturbation, the vortices will begin to move and finally exit the domain. These findings confirm the analytical results very well [81, 98]. Furthermore, in the presence of inhomogeneous potential, vortices generally move toward the critical points of the external potential, and finally stop steady near around those points, which illustrate clearly the pinning effect.

In the second part, we studied the dynamics of GPE with angular momentum rotation term and/or the long-range dipolar-dipolar interaction term. Firstly, we review the two-dimensional (2D) GPE obtained from the 3D GPE via dimension reduction under anisotropic external potential and derive some dynamical laws related to the 2D and 3D GPE. By introducing a rotating Lagrangian coordinate system, the original GPEs are re-formulated to GPEs without the angular momentum rotation which is replaced by a time-dependent potential in the new coordinate system. We then cast the conserved quantities and dynamical laws in the new rotating Lagrangian coordinates. Based on the new formulation of the GPE for rotating BECs in the rotating Lagrangian coordinates, we proposed a time-splitting spectral method for computing the dynamics of rotating BECs. The new numerical method is explicit, simple to implement, unconditionally stable and very efficient in computation. It is spectral order accurate in space and second-order accurate in time, and conserves the mass in the discrete level. Extensive numerical results are reported to demonstrate the efficiency and accuracy of the new numerical method. Finally, the numerical method is applied to test the dynamical laws of rotating BECs such as the dynamics of condensate width, angular momentum expectation and center-of-mass, and to investigate numerically the dynamics and interaction of quantized vortex lattices in rotating BECs without/with the long-range dipole-dipole interaction.

The topics that considered here is merely a small part of the world of vortex dynamics. Many interesting and difficult problems still remains open. The study of vortex dynamics can always be divided into two groups: (i). either to derive possible RDLs which are sets of simple ODEs that govern the motion of vortices, (ii). or to simulate the PDEs directly by some efficient and accurate numerical methods. Firstly, most of the RDLs reported in the literatures now can be valid only up to the first collision time and they were derived under some assumptions not so general. The problem that how to relax those assumptions and extend exist or derive new RDLs to describe the motion of vortices involving vortex collision, vortex of multiple degree (and thus splittings and reconnections might happen), vortex exiting domain and vortices radiating sound waves still remains as a difficult and thus interesting open problem. This is the first possible direction that we will consider in the future. Secondly, although the direct simulation can provide us as much information as we want including vortex splittings, collisions, reconnections and possible sound wave propagation in dispersive system as well as pinning effect of the vortices, the design of effective numerical algorithm itself is a difficult issue. The efficiency of the method presented in this thesis for simulating the GLSE depend on the value of ε, and it becomes useless for extreme small ε. To propose effective numerical methods which are ε-independent is another future work.

Moreover, the ideas proposed in this thesis to simulate dipolar rotating BEC is quite simple but effective. We believe that it can be easily extended to study two component rotating dipolar or spinor BEC [89], etc.

Last but not least, as mentioned in the beginning of this thesis, the GLE we consider here is the simplified model for model superconductivity, which might not be that physical interesting, which motivate us to extend our methods to study the vortex dynamics in full Ginzburg-Landau model that involving electromagnetic field [127,136]. Other topics such as vortex dynamics in the nonlinear Klein-Gorden equation [146], the nonlinear Maxwell-Klein-Gorden equation [147], the Landu-Lifshitz-Gilbert equation [93] and the coupled Ginzburg-Landau equation for modeling unconventional superconductor [102] will also be considered.

Bibliography

[1] M. Abad, M. Guilleumas, R. Mayol, M. Pi and D. M. Jazek, Vortices in Bose–Einstein condensates with dominant dipolar interactions, Phys. Rev. A, 79 (2009), article 063622.

[2] J. R. Abo-Shaeer, C. Raman, J. M. Vogels and W. Ketterle, Observation of vortex lattices in Bose–Einstein condensates, Science, 292 (2001), 476–479.

[3] A. Abrikosov, On the magnetic properties of superconductors of the second group, Soviet Physics JETP, 5 (1957), 1174–1182.

[4] A. Aftalion, Vortices in Bose–Einstein Condensates, Brikhäuser, 2006.

[5] A. Aftalion and Q. Du, Vortices in a rotating Bose–Einstein condensate: critical angular velocities and energy diagrams in the Thomas–Fermi regime, Phys. Rev. A, 64 (2001), article 063603.

[6] B. P. Anderson, Experiment with vortices in superfluid atomic gases, J. Low Temp. Phys., 161 (2010), 574–602.

[7] M. H. Anderson, J. R. Ensher, M. R. Matthewa, C. E. Wieman and E. A. Cornell, Observation of Bose–Einstein condensation in a dilute atomic vapor, Science, 269 (1995), 198–201.

[8] N. André and I. Shafrir, Asymptotic behavior for the Ginzburg–Landau functional with weight (I), Arch. Rational Mech. Anal., 142 (1998), 45–73.

[9] N. André and I. Shafrir, Asymptotic behavior for the Ginzburg–Landau functional with weight (II), Arch. Rational Mech. Anal., 142 (1998), 75–98.

[10] P. Antonelli, D. Marahrens and C. Sparber, On the Cauchy problem for nonlinear Schrödinger equations with rotation, Disc. Contin. Dyn. Syst. A, 32 (2012), 703–715.

[11] I. S. Aranson and L. Kramer, The world of the complex Ginzburg–Landau equation, Rev. Mod. Phys., 74 (2002), 99–133.

[12] W. Bao, Numerical methods for the nonlinear Schrödinger equation with nonzero far–field conditions, Methods Appl. Anal., 11 (2004), 367–388.

[13] W. Bao, N. Ben Abdallah and Y. Cai, Gross–Pitaevskii–Poisson equations for dipolar Bose–Einstein condensate with anisotropic confinement, SIAM J. Math. Anal., 44 (2012), 1713–1741.

[14] W. Bao and Y. Cai, Mathematical theory and numerical methods for Bose–Einstein condensation, Kinet. Relat. Models, 6 (2013), 1–135.

[15] W. Bao and Y. Cai, Optimal error estimates of finite difference methods for the Gross–Pitaevskii equation with angular momentum rotation, Math. Comp., 82 (2013), 99–128.

[16] W. Bao, Y. Cai and H. Wang, Efficient numerical methods for computing ground states and dynamics of dipolar Bose–Einstein condensates, J. Comput. Phys., 229 (2010), 7874–7892.

[17] W. Bao, Q. Du and Y. Zhang, Dynamics of rotating Bose–Einstein condensates and their efficient and accurate numerical computation, SIAM J. Appl. Math., 66 (2006), 758–786.

[18] W. Bao, D. Jaksch and P. A. Markowich, Numerical solution of the Gross–Pitaevskii equation for Bose–Einstein condensation, J. Comput. Phys., 187 (2003), 318–342.

[19] W. Bao, S. Jin and P. A. Markowich, On time–splitting spectral approximations for the Schrödinger equation in the semiclassical regime, J. Comput. Phys., 175 (2002), 487–524.

[20] W. Bao, H. Li and J. Shen, A generalized Laguerre–Foruier–Hermite pseudospectral method for computing the dynamics of rotating Bose–Einstein condensates, SIAM J. Sci. Comput., 31 (2009), 3685–3711.

[21] W. Bao and Q. Tang, Numerical study of quantized vortex interaction in Ginzburg–Landau equation on bounded domains, Commun. Comput. Phys., 14 (2013), 819–850.

[22] W. Bao and Q. Tang, Numerical study of quantized vortex interaction in nonlinear Schrödinger equation on bounded domains, preprint.

[23] W. Bao and H. Wang, An efficient and spectrally accurate numerical method for computing dynamics of rotating Bose–Einstein condensates, J. Comput. Phys., 271 (2006), 612–626.

[24] W. Bao and Y. Zhang, Dynamics of the ground state and central vortex state in Bose–Einstein condensation, Math. Mod. Meth. Appl. Sci., 15 (2005), 1863–1896.

[25] C. F. Barenghi, R. J. Donnelly and W. F. Vinen, Quantized Vortex Dynamics and Superfluid Turbulence, Springer, New York, 2001.

[26] P. Bauman, C. N. Chen, D. Phillips and P. Sternberg, Vortex annihilation in nonlinear heat flow for Ginzburg–Landau systems, European J. Appl. Math., 6 (1995), 115–126.

[27] C. Besse, B. Bidegaray and S. Descombes, Order estimates in time of splitting methods for the nonlinear Schrödinger equation, SIAM J. Numer. Anal., 40 (2002), 26-40.

[28] F. Bethuel, H. Brezis and F. Hélein, Ginzburg–Landau Vortices, Brikhäuser, 1994.

[29] F. Bethuel, R. L. Jerrard and D. Smets, On the NLS dynamics for infinite energy vortex configurations on the plane, Rev. Mat. Iberoamericana, 24 (2008), 671-702.

[30] F. Bethuel, G. Orlandi and D. Smets, Collisions and phase–vortex interactions in dissipative Ginzburg–Landau dynamics, Duke Math. J., 130 (2005), 523–614.

[31] F. Bethuel, G. Orlandi and D. Smets, Convergence of the parabolic Ginzburg–Landau equation to motion by mean curvature, Ann. Math., 163 (2006), 37–163.

[32] F. Bethuel, G. Orlandi and D. Smets, Dynamics of multiple degree Ginzburg-Landau vortices, Commun. Math. Phys., 272 (2007), 229–261.

[33] F. Bethuel, G. Orlandi and D. Smets, Quantization and motion law for Ginzburg–Landau vortices, Arch. Rational Mech. Anal., 183 (2007), 315–370.

[34] F. Bethuel and D. Smets, A remark on the Cauchy problem for the 2D Gross-Pitaevskii equation with non zero degree at infinity, Differential Integral Equations, 20 (2007), 325338.

[35] P. B. Blakie, C. Ticknor, A. S. Bradley, A. M. Martin, M. J. Davis and Y. Kawaguchi, Numerical method for evolving the dipolar projected Gross–Pitaevskii equation, Phy. Rev. E, 80 (2009), article 016703.

[36] J. P. Boyd, A fast algorithm for Chebyshev, Fourier, and sinc interpolation onto an irregular grid, J. Comput. Phys., 103 (1992), 243–257.

[37] C. C. Bradley, C. A. Sackett, J. J. Tollett and R. G. Hulet, Evidence of Bose–Einstein condensation in an atomic gas with attractive interaction, Phys. Rev. Lett., 75 (1995), 1687–1690.

[38] V. Bretin, S. Stock, Y. Seurin and J. Dalibard, Fast rotation of a Bose–Einstein condensate, Phys. Rev. Lett., 92 (2004), article 050403.

[39] Y. Cai, M. Rosenkranz, Z. Lei and W. Bao, Mean–field regime of trapped dipolar Bose–Einstein condensates in one and two dimensions, Phys. Rev. A, 82 (2010), article 043623.

[40] M. M. Cerimele, M. L. Chiofalo, F. Pistella, S. Succi and M. P. Tosi, Numerical solution of the Gross–Pitaevskii equation using an explicit finite difference scheme: an application to trapped Bose–Einstein condensates, Phys. Rev. E, 62 (2000), 1382–1389.

[41] S. Chapman, Q. Du and M. Gunzburger, A model for variable thickness superconducting thin film, Z. Angew. Math. Phys., 47 (1996), 410–431.

[42] S. J. Chapman and G. Richardson, Vortex pinning by inhomogeneities in type–II superconductors, Phys. D, 108 (1997), 397–407.

[43] S. J. Chapman, Q. Du, and M. D. Gunzburger, A Ginzburg-Landau type model of superconducting/normal junctions including Josephson junctions, Eur. J. Appl. Math., 6 (1995), 97-114.

[44] Z. Chen and S. Dai, Adaptive Galerkin methods with error control for a dynamical Ginzburg–Landau model in superconductivity, SIAM J. Numer. Anal., 38 (2001), 1961–1985.

[45] X. Chen, C. M. Elliot, and Q. Tang, Shooting method for votex solutions of a complex-valued Ginzburg-Landau equation, Proc. R. Soc. Edinb. A-Math., 124 (1994), 1075–1088.

[46] J. E. Colliander and R. L. Jerrard, Ginzburg–Landau vortices: weak stability and Schrödinger equation dynamics, J. Anal. Math., 77 (1999), 129–205.

[47] J. E. Colliander and R. L. Jerrard, Vortex dynamics for the Ginzburg–Landau–Schrödinger equation, IMRN Int. Math. Res. Not., 7 (1998), 333–358.

[48] N. R. Cooper, E. H. Rezayi and S. H. Simon, Vortex lattices in rotating atomic Bose gases with dipolar interactions, Phys. Rev. Lett., 95 (2005), article 200402.

[49] N. Dancer, Domain variation for certain sets of solutions and applications, Topol. Methods Nonlinear Anal., 7 (1996), 95–113.

[50] K. B. Davis, M. O. Mewes, M. R. Andrews, N. J. van Druten, D. S. Durfee, D. M. Kurn and W. Ketterle, Bose–Einstein condensation in a gas of sodium atoms, Phys. Rev. Lett., 75 (1995), 3969–3973.

[51] M. del Pino, M. Kowalczyk and M. Musso, Variational reduction for Ginzburg–Landau vortices, J. Funct. Anal., 239 (2006), 497–541.

[52] A. S. Desyatnikov, Y. S. Kivshar and L. Torner, Optical vortices and vortex solitons, Prog. Optics, 47 (2005), 291–391.

[53] R. J. Donnelly, Quantized Vortices in Helium II, Cambridge University Press, 1991.

[54] Q. Du, Finite element methods for the time dependent Ginzburg–Landau model of superconductivity, Comp. Math. Appl., 27 (1994), 119–133.

[55] Q. Du, Numerical approximations of the Ginzburg–Landau models for superconductivity, J. Math. Phys., 46 (2005), article 095109.

[56] Q. Du, "Quantized vortices in superfluids–a mathematical and computational study" in "Dynamics in Models of Coarsening, Coagulation, Condensation and Quantization", W. Bao, J.-G. Liu, World Scientific, 2007.

[57] Q. Du and M. Gunzburger, A model for superconduction thin films having variable thickness, Phys. D., 69 (1993), 215–231.

[58] Q. Du, M. Gunzburger and J. Peterson, Analysis and approximation of the Ginzburg–Landau model of superconducting, SIAM Rev., 34 (1992), 54–81.

[59] W. E, Dynamics of vortices in Ginzburg–Landau theroties with applications to superconductivity, Phys. D, 77 (1994), 38–404.

[60] A. L. Fetter, Vortices in an imperfect Bose gas. IV. Translational velocity, Phys. Rev., 151 (1966), 100–104.

[61] R. Feynman, "Application of quantum mechanics to liquid helium" in "Progress in Low Temperature Physics. Vol 1", C. J. Groter, North-Holland, 1955.

[62] T. Frisch, Y. Pomeau and S. Rica, Transition to dissipation in a model of superflow, Phys. Rev. Lett., 69 (1992), 1644–1647.

[63] J. J. García-Ripoll, V. M. Pérez-García and V. Vekslerchik, Construction of exact solution by spatial translations in inhomogeneous nonlinear Schrödinger equations, Phys. Rev. E, 64 (2001), article 056602.

[64] V. Ginzburg and L. Pitaevskii, On the theory of superfluidity, Soviet Physics JETP, 34 (1958), 858–861.

[65] R. Glowinski and P. Tallec, Augmented Lagrangian and Operator Splitting Method in Nonlinear Mechanics, SIAM, Philadelphia, PA, 1989.

[66] K. Góral, K. Rzayewski and T. Pfau, Bose–Einstein condensation with magnetic dipole–dipole forces, Phys. Rev. A, 61 (2000), article 051601.

[67] A. Griesmaier, J. Werner, S. Hensler, J. Stuhler and T. Pfau, Bose–Einstein condensation of Chromium, Phys. Rev. Lett., 94 (2005), article 160401.

[68] S. Gustafson and I. M. Sigal, Effective dynamics of magnetic vortices, Adv. Math., 199 (2006), 448–498.

[69] P. Hagan, Spiral waves in reaction diffusion equations, SIAM J. Appl. Math., 42 (1982), 762–786.

[70] R. M. Hervé and M. Hervé, Étude qualitative des solutions réelles d'une équation différentielle liée à l'équation de Ginzburg-Landau, Ann. Inst. Henri Poincaré, 11 (1994), 427–440.

[71] M. Hintermüller, D. Marahrens, P. Markowich, C. Sparber, Optimal bilinear control of Gross-Pitaevskii equations, arXiv:1202.2306 (2012).

[72] K.-H. Hoffmann, Q. Tang, Ginzburg-Landau Phase Transition Theory and Superconductivity, Brikhäuser Verlag, 2001.

[73] R. L. Jerrard and H. Soner, Dynamics of Ginzburg–Landau vortices, Arch. Rational Mech. Anal., 142 (1998), 99–125.

[74] R. L. Jerrard and D. Spirn, Refined Jacobian estimates and the Gross–Pitaevskii equations, Arch. Rational Mech. Anal., 190 (2008), 425–475.

[75] H. Jian, The dynamical law of Ginzburg–Landau vortices with a pining effect, Appl. Math. Lett., 13 (2000), 91–94.

[76] H. Jian and B. Song, Vortex dynamics of Ginzburg–Landau equations in inhomogeneous superconductors, J. Diff. Eqns., 170 (2001), 123–141.

[77] H. Jian and Y. Wang, Ginzburg–Landau vortices in inhomogeneous superconductors, J. Part. Diff. Eqns., 15 (2002), 45–60.

[78] H. Jian and X. Xu, The vortex dynamics of a Ginzburg–Landau system under pinning effect, Science in China, Ser. A, 46 (2003), 487–498.

[79] S. Jimbo, Y. Morita, Ginzburg–Landau equation and stable solutions in a rotational domain, SIAM J. Math. Anal., 27 (1996), 1360–1385.

[80] S. Jimbo and Y. Morita, Notes on the limit equation of vortex equation of vortex motion for the Ginzburg–Landau equation with Neumann condition, Japan J. Indust. Appl. Math., 18 (1972), 151–200.

[81] S. Jimbo and Y. Morita, Stability of nonconstant steady–state solutions to a Ginzburg–Landau equation in higer space dimension, Nonlinear Anal.: T.M.A., 22 (1994), 753–770.

[82] S. Jimbo, Y. Morita, Stable solutions with zeros to the Ginzburg-Landau equation with Nuemann boundary condition, J. Diff. Eqns., 128 (1996), 596–613.

[83] S. Jimbo and Y. Morita, Vortex dynamics for the Ginzburg–Landau equation with Neumann condition, Methods App. Anal., 8 (2001), 451–477.

[84] S. Jimbo, Y. Morita, J. Zhai, Ginzburg-Landau equation and stable steady state solutions in a nontrivial domain, Comm. PDE., 20 (1995), 2093–2112.

[85] C. Josserand and Y. Pomeau, Generation of vortices in a model superfluid He^4 by the KP instability, Europhys. Lett., 30 (1995), 43–48.

[86] K. T. Kapale and J. P. Dowling, Vortex phase qubit: generating arbitrary, counterrotating, coherent superposition in Bose-Einstein condensates via optical angular momentum beams, Phys. Rev. Lett., 95 (2005), article 173601.

[87] O. Karakashian and C. Makridakis, A space–time finite element method for the nonlinear Schrödinger equation: the discontinuous Galerkin method, Math. Comput., 67 (1998), 479–499.

[88] K. Kasamatsu, M. Tsubota and M. Ueda, Nonlinear dynamics of vortex lattice formation in a rotating Bose–Einstein condensate, Phys. Rev. A, 67 (2003), article 033610.

[89] Y. Kawaguchi and M. Ueda, Spinor Bose-Einstein condensates, Phys. Rep., 520 (2012), 253–381.

[90] D. Kincaid and W. Cheney, Numerical Analysis, Mathematics of Scientific Computing, Brooks–Cole, 3rd edition, 1999.

[91] R. K. Kumar and P. Muruganandam, Vortex dynamics of rotating dipolar Bose–Einstein condensates, J. Phys. B: At. Mol. Opt. Phys., 45 (2012), article 215301.

[92] M. Kurzke, C. Melcher, R. Moser and D. Spirn, Dynamics for Ginzburg–Landau vortices under a mixed flow, Indiana Univ. Math. J., 58 (2009), 2597–2622.

[93] M. Kurzke, C. Melcher, R. Moser and D. Spirn, Ginzburg–Landau vortices driven by the Landau–Lifshitz–Gilbert equation, Arch. Rational Mech. Anal., 199 (2011), 843–888.

[94] T. Lahaye, C. Menotti, L. Santos, M. Lewenstein and T. Pfau, The physics of dipolar bosonic quantum gases, Rep. Prog. Phys., 72 (2009), 126401.

[95] O. Lange and B. J. Schroers, Unstable manifolds and Schrödinger dynamics of Ginzburg–Landau vortices, Nonlinearity, 15 (2002), 1471–1488.

[96] F. Lin, A remark on the previous paper "Some dynamical properties of Ginzburg–Landau vortices", Comm. Pure Appl. Math., 49 (1996), 361–364.

[97] F. Lin, Complex Ginzburg–Landau equations and dynamics of vortices, filaments, and codimension–2 submanifolds, Comm. Pure Appl. Math., 51 (1998), 385–441.

[98] F. Lin, Mixed vortex–antivortex solutions of Ginzburg–Landu equations, Arch. Rational Mech. Anal., 133 (1995), 103–127.

[99] F. Lin, Some dynamical properties of Ginzburg–Landau vortices, Comm. Pure Appl. Math., 49 (1996), 323–359.

[100] T. Lin, The stability of the radial solution to the Ginzburg–Landau equation, Comm. PDE., 22 (1997), 619–632.

[101] F. Lin and Q. Du, Ginzburg–Landau vortices: dynamics, pining and hysteresis, SIAM J. Math. Anal., 28 (1997), 1265–1293.

[102] F. Lin and T. Lin, Multiple time scale dynamics in coupled Ginzburg-Landau equations, Comm. Math. Sci., 1 (2003), 671–695.

[103] F. Lin and J. Xin, A unified approach to vortex motion laws of complex scalar field equations, Math. Res. Lett., 5 (1998), 455–460.

[104] F. Lin and J. Xin, On the incompressible fluid limit and the vortex motion law of the nonlinear Schrödinger equation, Comm. Math. Phys., 200 (1999), 249–274.

[105] M. Lu, N. Q. Burdick, S. H. Youn and B. L. Lev, Strongly dipolar Bose–Einstein condensate of Dysprosium, Phys. Rev. Lett., 107 (2011), article 190401.

[106] K. W. Madison, F. Chevy, V. Bretin and J. Dalibard, Stationary states of a rotating Bose–Einstein condensates: routes to vortex nucleation, Phys. Rev. Lett., 86 (2001), 4443–4446.

[107] K. W. Madison, F. Chevy, W. Wohlleben and J. Dalibard, Vortex formation in a stirred Bose–Einstein condensate, Phys. Rev. Lett., 84 (2000), 806–809.

[108] F. Malet, T. Kristensen, S. M. Reimann and G. M. Kavoulakis, Rotational properties of dipolar Bose–Einstein condensates confined in anisotropic harmonic potential, Phys. Rev. A, 83 (2011), article 033628.

[109] M. R. Matthews, B. P. Anderson, P. C. Haljan, D. S. Hall, C. E. Wiemann and E. A. Cornell, Vortices in a Bose–Einstein condensate, Phys. Rev. Lett., 83 (1999), 2498–2501.

[110] E. Miot, Dynamics of vortices for the complex Ginzburg–Landau equation, Anal. PDE, 2 (2009), 159–186.

[111] P. Mironescu, On the stability of radial solutions of the Ginzburg–Landau equation, J. Funct. Anal., 130 (1995), 334–344.

[112] P. Muruganandam and S. K. Adhikari, Fortran programs for the time–dependent Gross–Pitaevskii equation in a fully anisotropic trap, Comput. Phys. Commun., 180 (2009), 1888–1912.

[113] J. Neu, Vortices in complex scalar fields, Phys. D, 43 (1990), 385–406.

[114] C. Nore, M. E. Brachet, E. Cerda and E. Tirapegui, Scattering of first sound by superfluid vortices, Phys. Rev. Lett., 72 (1994), 2593–2595.

[115] Y. N. Ovchinnikov and I. M. Sigal, Ginzbiurg–Landau equation I. Static vortices, Partial Differential Equations App. CRM Pro., 12 (1997), 199–220.

[116] Y. N. Ovchinnikov and I. M. Sigal, Long–time behaviour of Ginzburg–Landau vortices, Nonlinearity, 11 (1998), 1295–1309.

[117] Y. N. Ovchinnikov and I. M. Sigal, The Ginzburg–Landau equation III. Vortex dynamics, Nonlinearity, 11 (1998), 1277–1294.

[118] L. Peres and J. Rubinstein, Vortex dynamics for U(1)–Ginzburg–Landau models, Phys. D, 64 (1993), 299–309.

[119] L. M. Pismen, Vortices in Nonlinear Fields, Clarendon, 1999.

[120] L. Pitaevskii, Vortex lines in an imperfect Bose gas, Soviet Physics JETP, 13 (1961), 451–454.

[121] L. Pitaevskii and S. Stringari, Bose-Einstein condensation, Clarendon, 2003.

[122] C. Raman, J. R. Abo-Shaeer, J. M. Vogels, K. Xu and W. Ketterle, Vortex nucleation in a stirred Bose-Einstein condensate, Phys. Rev. Lett., 87 (2001), article 210402.

[123] P. H. Roberts and N. G. Berloff,“The nonlinear Schrödinger equation as a model of superfluidity,” in“Quantized Vortex Dynamics and Superfluid Turbulence”, C. F. Barenghi, R. J. Donnely, and W. F. Vinen, Springer, 2001.

[124] D. S. Rokhsar, Vortex stability and persistent currents in trapped Bose-gas, Phys. Rev. Lett., 79 (1997), 2164–2167.

[125] S. Ronen, D. C. E. Bortolotti and J. L. Bohn, Bogoliubov modes of a dipolar condensate in a cylindrical trap, Phys. Rev. A, 74 (2006), article 013623.

[126] J. Rubinstein and P. Sternberg, On the slow motion of vortices in the Ginaburg–Landau heat flow, SIAM J. Appl. Math., 26 (1995), 1452–1466.

[127] E. Sandier and S. Serfaty, Vortices in the Magnetic Ginzburg–Landau Model, Brikhäuser, 2007.

[128] E. Sandier and S. Serfaty, Gamma–convergence of gradient flows with applications to Ginzburg–Landau, Comm. Pure Appl. Math., 57 (2004), 1627–1672.

[129] V. Schweikhard, I. Coddington, P. Engels, V. P. Mogendorff and E. A. Cornell, Rapidly rotating Bose-Einstein condensates in and near the lowest Landau level, Phys. Rev. Lett., 92 (2004), article 040404.

[130] R. Seiringer, Ground state asymptotics of a dilute rotating gas, J. Phys. A: Math. Gen., 36 (2003), 9755–9778.

[131] S. Serfaty, Stability in 2D Ginzburg–Landau pass to the limit, Indiana U. Math. J., 54 (2005), 199–221.

[132] S. Serfaty, Vortex collisions and energy–dissipation rates in the Ginzburg–Landau heat flow. Part II: the dynamics, J. Euro. Math. Soc., 9 (2007), 383–426.

[133] S. Serfaty, I. Tice, Ginzburg-Landau vortex dynamics with pinning and strong applied currents, Arch. Rational Mech. Anal., 201 (2011), 413-464.

[134] J. Shen and T. Tang, Spectral and High–Order Method with Applications, Science Press, 2006.

[135] J. Shen, T. Tang and L. Wang, Spectral Methods: Algorithms, Analysis and Applications, Springer, 2011.

[136] D. Spirn, Vortex dynamics of the full time–dependent Ginzburg–Landau equations. Comm. Pure Appl. Math., 55 (2002), 537–581.

[137] G. Strang, On the construction and comparision of difference schemes, SIAM J. Numer. Anal., 5 (1968), 505–517.

[138] R. P. Tiwari and A. Shukla, A basis–set based Fortran program to solve the Gross–Pitaevskii equation for dilute Bose gases in harmonic and anharmonic traps, Comput. Phys. Commun., 174 (2006), 966–982.

[139] M. Tsubota, K. Kasamatsu and M. Ueda, Vortex lattice formation in a rotating Bose–Einstein condensate, Phys. Rev. A, 65 (2002), article 023603.

[140] R. M. W. van Bijnen, A. J. Dow, D. H. J. O'Dell, N. G. Parker and A. M. Martin, Exact solutions and stability of rotating dipolar Bose–Einstein condensates in the Thomas–Fermi limit, Phys. Rev. A, 80 (2009), article 033617.

[141] J. A. C. Weideman and B. M. Herbst, Split-step methods for the solution of the nonlinear Schrödinger equation, SIAM J. Numer. Anal., 23 (1986), 485–507.

[142] M. I. Weinstein and J. Xin, Dynamic stability of vortex solutions of Ginzburg–Landau and nonlinear Schrödinger equations, Comm. Math. Phys., 180 (1996), 389–428.

[143] B. Xiong, J. Gong, H. Pu, W. Bao and B. Li, Symmetry breaking and self–trapping of a dipolar Bose–Einstein condensate in a double–well potential, Phys. Rev. A, 79 (2009), article 013626.

[144] S. Yi and H. Pu, Vortex structures in dipolar condensates, Phys. Rev. A, 73 (2006), article 061602.

[145] S. Yi and L. You, Trapped condensates of atoms with dipole interactions, Phys. Rev. A, 63 (2001), article 053607.

[146] Y. Yu, Vortex dynamics for nonlinear Klein-Gordon equation, J. Diff. Eqns., 251 (2011), 970–994.

[147] Y. Yu, Vortex dynamics for nonlinear Maxwell–Klein-Gordon equation, Arch. Rational Mech. Anal., 201 (2011), 743–776.

[148] C. Yuce and Z. Oztas, Off–axis vortex in a rotating dipolar Bose–Einstein condensate, J. Phys. B: At. Mol. Opt. Phys., 43 (2010), article 135301.

[149] R. Zeng and Y. Zhang, Efficiently computing vortex lattices in fast rotating Bose–Einstein condensates, Comput. Phys. Commun., 180 (2009), 854–860.

[150] Y. Zhang, Numerical study of vortex interactions in Bose–Einstein condensation, Commun. Comput. Phys., 8 (2010), 327–350.

[151] Y. Zhang and W. Bao, Dynamics of the center of mass in rotating Bose–Einstein condensates, Appl. Numer. Math., 57 (2007), 697–709.

[152] Y. Zhang, W. Bao and Q. Du, Numerical simulation of vortex dynamics in Ginzburg–Landau–Schrödinger equation, Euro. J. Appl. Math., 18 (2007), 607–630.

[153] Y. Zhang, W. Bao and Q. Du, The dynamics and interactions of quantized vortices in Ginzburg–Landau–Schrödinger equation, SIAM J. Appl. Math., 67 (2007), 1740–1775.

[154] J. Zhang and H. Zhai, Vortex lattices in planar Bose–Einstein condensates with dipolar interactions, Phys. Rev. Lett., 95 (2005), article 200403.

List of Publications

[1] *Numerical methods and comparisions for computing dark and bright solitons in nonlinear Schrödinger equation* (with Weizhu Bao and Zhiguo Xu), Journal of Computational Physics, Vol. 235, pp. 423–445, 2013.

[2] *Numerical study of quantized vortex dynamics and interaction in Ginzburg–Landau equation on bounded domains* (with Weizhu Bao), Communication in Computational Physics, Vol. 14, pp. 819–850, 2013.

[3] *Numerical study of quantized vortex dynamics and interaction in nonlinear Schrödinger equation on bounded domains* (with Weizhu Bao), submitted to Multiscale Modeling and Simulation: a SIAM Interdisciplinary Journal.

[4] *A simple and efficient numerical method for computing dynamics of rotating dipolar Bose–Einstein condensation via a rotating Lagrange coordinate* (with Weizhu Bao, Daniel Marahrens and Yanzhi Zhang), submitted to SIAM Journal on Scientific Computing.

[5] *A simple numerical method for computing dynamics of rotating two–component Bose–Einstein condensation via a rotating Lagrange coordinate* (with Ming Ju and Yanzhi Zhang), submitted to Journal of Computational Physics.

[6] *Quantized vortex dynamics and interaction in complex Ginzburg–Landau equation on bounded domains* (with Wei Jiang), submitted to Computer Physics Communications.

[7] *Error estimates in the energy space for a Gautschi-type integrator spectral discretization for the coupled nonlinear Klein–Gordon equations* (with Xuanchun Dong), submitted to IMA Journal of Numerical Analysis.

[8] *A Variational–difference numerical method for designing progressive–addition lenses* (with Weizhu Bao and Wei Jiang), submitted to Computer–Aided Design.

[9] *Quantized vortex dynamics and interaction in Schrödinger–Ginzburg–Landau equation under pinning effect on bounded domains* (with Wei Jiang), preprint.